Università degli Studi di Genova

Scuola di Dottorato in Scienze e Tecnologie della Chimica e dei Materiali

Doctorate Course in

CHEMICAL SCIENCES AND TECHNOLOGIES
XXXII Cycle

PhD Thesis

Synthesis, characterization, optimization and application of TiO_2-based photocatalytic materials for environmental applications related to emerging pollution

Candidate
Stefano Alberti

Supervisor
Prof. Maurizio Ferretti

Defence Date: 20th March 2020

INDEX

1. ***Abstract*** **p. 5**
   - *1.1. Outline of the Thesis* p. 7

2. ***Introduction*** **p. 9**
   - *2.1. Emerging Pollution* p. 9
     - *2.1.1. Pharmaceuticals and Personal Care Products "PPCPs"* p. 13
     - *2.1.2. Antibiotic Resistance* p. 15
   - *2.2. Advanced Oxidation Processes "AOPs"* p. 16
     - *2.2.1. Heterogeneous Photocatalysis* p. 21
   - *2.3. Titanium Dioxide "TiO_2"* p. 26
   - *2.4. Supporting Materials* p. 31

3. ***Synthesis and Support of TiO_2*** **p. 33**
   - *3.1. Synthesis with Persistent Luminescence Materials "PeL"* p. 33
     - *3.1.1. ($3ZnO:Ga_2O_3:2GeO_2$): Cr^{3+}* p. 37
       - *3.1.1.1. Materials and Methods* p. 38
       - *3.1.1.2. Results and Discussion* p. 40
       - *3.1.1.3. Conclusions* p. 46
     - *3.1.2. $CaAl_2O_4$: $(La, Nd)^{3+}$* p. 47
       - *3.1.2.1. Materials and Methods* p. 48
       - *3.1.2.2. Results and Discussion* p. 49
       - *3.1.2.3. Conclusions* p. 56
     - *3.1.3. Composite Photocatalysts based on TiO_2/ZnO/PeL* p. 59
     - *3.1.4. Pilot Plant Prototype* p. 63
     - *3.1.5. Photocatalyst Recovery at pH_{IEP}* p. 65
   - *3.2. Synthesis of (Cu, N)-doped TiO_2 and Structural Refinement* p. 69
     - *3.2.1. Materials and Methods* p. 69
     - *3.2.2. Results and Discussion* p. 72
     - *3.2.3. Conclusions* p. 84
   - *3.3. Hydrothermal Synthesis of TiO_2 in presence of Ferrite Nanoparticle as Nucleation Seeds* p. 85
     - *3.3.1. Materials and Methods* p. 85
     - *3.3.2. Results and discussion* p. 89

3.3.3. Conclusions p. 94
3.4. Synthesis of PDMS Membranes loaded with N-doped TiO_2 through Electrospinning Process p. 95
3.4.1. Materials and Methods p. 96
3.4.2. Results and Discussion p. 100
3.4.3. Conclusion p. 114
3.5. Synthesis of TiO_2 supported on Magnetic Zeolite obtained from Industrial Waste p. 115
3.5.1. Materials and Methods p. 115
3.5.2. Results and Discussion p. 117
3.5.3. Conclusions p. 122

4. *Analytical Approach to Emerging Pollutants* **p. 123**
4.1. Parabens p. 124
4.1.1. Materials and Methods p. 125
4.1.2. Results and Discussion p. 126
4.1.3. Conclusions p. 132
4.2. Nicotine p. 132
4.2.1. Materials and Methods p. 134
4.2.2. Results and Discussion p. 139
4.2.3. Conclusions p. 145
4.3. Salbutamol p. 146
4.3.1. Materials and Methods p. 147
4.3.2. Results and Discussion p. 149
4.3.3. Conclusions p. 155

5. *Concluding Remarks* **p. 157**

6. *Thesis Summary – Riassunto della Tesi* **p. 160**

7. *Appendix* **p. 189**

8. *List of Tables and Figures* **p. 192**

9. *References* **p. 199**

1. Abstract

This PhD thesis deals with the exploitation of heterogeneous photocatalysis, as an Advanced Oxidation Process, for environmental issues related to the emerging pollution: in particular for wastewater remediation and bacterial decontamination purposes. During this project, several photocatalytic materials have been synthesized by coupling semiconductor (TiO_2) nanoparticles (both bare and doped) to different supporting materials, e.g. persistent luminescence materials ($3ZnO:Ga_2O_3:2GeO_2$: Cr^{3+}; $CaAl_2O_4$: $(La, Nd)^{3+}$), magnetic and porous materials (ferrite nanoparticles, magnetic zeolite obtained from industrial waste) and polymeric materials (based on polydimethylsiloxane "PDMS"). In addition, an analytical approach to the study on the abatement and the quantification of emerging pollutants was considered, an important part of which was carried out at the Water Lab of the Environmental Engineering Department at Technical University of Crete, under the supervision of Professor Elia Psillakis.

Specifically, TiO_2 was synthesized through the sol-gel technique, both in the undoped and doped form (for example with Cu and N), while its crystallization on several supporting materials was obtained with different synthetic techniques such as: sol-gel synthesis, solid-state synthesis, hydrothermal/solvothermal synthesis and electrospinning technique. Some of the synthesized materials were investigated using a chemometric approach, that is the possibility to exploit an Experimental Design mathematical model in order to investigate the optimal synthetic conditions to get enhanced photocatalytic efficiency (within the experimental domain) for the materials.

All samples synthesized within the current project were subjected to a physical-chemical characterization, by means of: X-Ray Diffraction "XRD" and crystallographic refinements (Rietveld, Pair Distribution Function "PDF", Williamson-Hall plot), Scanning and Transmission Electron Microscopy-Energy Dispersive X-Ray Spectrometry "SEM-EDS", "TEM", Porosimetry Brunauer-Emmett-Teller "BET", Dynamic Light Scattering "DLS", Differential Scanning

Calorimetry "DSC", Diffuse Reflectance (Kubelka-Munk plots for Energy Gap "E_g"), Rheological Measurements, Luminescence Properties, Turbidimetry, Inductively Coupled Plasma – Atomic Emission Spectroscopy "ICP-AES", Diffuse Reflectance Infrared Fourier Transform Spectroscopy "DRIFTS" and antibacterial properties with *E. Coli* cultures. Above all, a kinetic characterization in terms of photocatalytic efficiency evaluation was always performed for synthesized samples. In particular, kinetic behaviour of the photocatalysts was evaluated by means of Methylene Blue "MB" aqueous solutions degradation, studied as a function of time, with different initial concentrations (as required by ISO NORM 10678:2010). For MB quantification, a UV-Vis spectrophotometer was used, and experiments were usually performed in triplicate. Furthermore, during the first part of the project, a Pilot Plant Prototype was assembled (with a processing volume equal to 1L) and used for preliminary evaluations on a potential industrial scale-up. All tests and characterizations achieved were adapted according to the specific supporting material employed.

Eventually, considering the nature of emerging micro-pollutants, an analytical approach to the determination of their concentration in aqueous systems was employed. Specifically, chromatographic tests were performed with liquid and gas chromatography techniques, often coupled with mass spectrometry, for some specific emerging pollutants (Ofloxacin, Parabens, Nicotine, Salbutamol). Matrix effects were also considered in the evaluation of the pollutants' degradation during the advanced oxidation tests.

This task wouldn't have been possible without valuable National and International collaborations, which gave an essential help to the development of the project for what concerns a part of the reported characterization. My acknowledgements are directed to: Department of Chemistry and Industrial Chemistry - University of Genova (Analytical, Industrial, Physical Sections), Analytic and Photochemistry Section of the Department of Chemistry - University of Pavia; Department of Chemistry - University of Kuwait; Department of Environmental Engineering - Technical University of Crete; Institute of

Methodologies of Environmental Analysis, Institute of Matter and Institute of Superconducting and other Innovative Materials and Devices - National Research Council.

Each individual contribute will be highlighted in each dedicated section, throughout the manuscript.

1.1. Outline of the Thesis

During the PhD project I had the chance to make a deep and wide study on the application of TiO_2-based photocatalysis as an Advanced Oxidation Process and this study could range from the synthetic part, in which I could study the parameters concerning the synthesis and different suitable supporting materials, to the application part, in which model pollutants as well as real contaminants of emerging concern were degraded and quantified.

For this reason, the development of the manuscript was organized as follows: a general Introduction section (Chapter 2.), where the state of the art and the basis of the project are highlighted; two general chapters (Chapter 3. and Chapter 4.), where each single research performed within the PhD is organized according to a general scientific paper template (Materials and Methods, Results and Discussion, Conclusions); a common Concluding Remarks section (Chapter 5.), to sum up the most important highlights and suggest some future developments. A brief but thorough summary of the thesis is reported, both in English and Italian (Chapter 6.), while in the Appendix section (Chapter 7.), oral and poster communication given during these three years of Doctorate, and a list of the scientific publications related to the thesis work, are reported. In addition, the inventory of tables and figures of the thesis is stated (Chapter 8.) and eventually, the References (Chapter 9.), which are the basis of the scientific approach and of the manuscript writing.

2. Introduction

2.1. Emerging Pollution

Pollution may have both anthropic and natural causes and it can be defined as the alteration of pre-existing balances in a certain environment, thus endangering animal and vegetal life by altering the metabolism and bio-accumulating. Considerable resources and energy are spent to prevent and/or counteract the spread of pollutants throughout the environment and scientific research has made numerous steps forward on the effectiveness and the sustainability of treatments[1]. As a first approach, it is necessary to underline the difference between macro- and micro-pollution, also known as classic and emerging pollution: the former deals with polluting substances that are very well known and visible while the latter deals with very low concentrated and unknown ones[2]. Specifically, as classic pollutants, we can identify by-products coming from industrial process, chimneys, urban wastes and landfills and they are: NO_x, SO_x, I.P.A, PM_{10}, heavy metals, dioxins, furans, PO_4^{3-}, NO_3^-, NH_4^+, suspended solids, oils, and so on. First of all, there is a good comprehension on the nature of these pollutants, especially for what concerns their physical-chemical properties as they are responsible of the fate of these molecules in the environment[3–5]. Further, their impact on the environment itself and the effect on human health is often immediate, acute and thus evident. These facts allowed, over time, the development of effective strategies for their removal as well as cures and prevention approaches against human diseases. It's important to mention that, in Italy, the first law against atmospheric pollution is dated back to 1966, Law n° 615, updated later on according to European guidelines. As an example, in Figure 1 it is possible to note some transport processes in which classic pollutants are involved between the atmosphere and the soil (photo-chemical smog, formation of acids, ozone and heavy condensed matter).

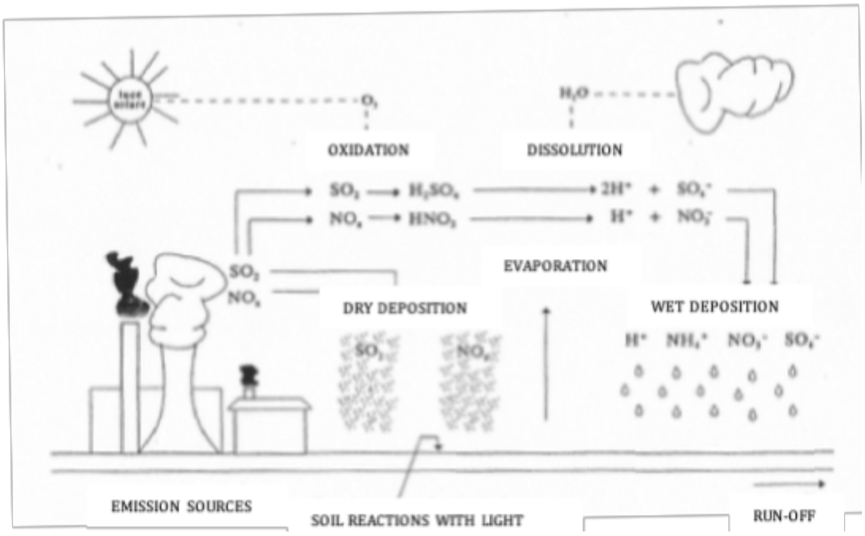

Figure 1: Scheme of classic pollutants spread in the atmosphere and transport/reaction processes involving these molecules

For what concerns water pollution, which is the main topic of this project, similar considerations can be done: main pollutants in water are well known, so that their sources, their physical-chemical properties, the transport/reactions processes among the different water compartments where they're involved and the interactions with living beings. Indeed, actual Wastewater Treatment Plants "WWTPs" result to be well equipped against the heavy load of macro-pollutants[6].

The aquatic environment represents the two-third of the Planet and it is inhabited by the majority of living beings and a lot of them are important sources of human sustainment. It represents the ultimate recipient of this increasing range of anthropogenic pollutants, a large proportion of which are potentially genotoxic and carcinogenic. It must not be forgotten that the quality of human life is directly and indirectly dependent of the health and vitality of the environment. Abiotic and biotic components constitute our environment and trough complex interactions, the equilibrium is kept. Deterioration in the health of any of these components can have serious knock-on effects on the continuity of life[7].

According to the Environmental Protection Agency "EPA" definition, emerging pollutants are all those compounds which are not subjected to precise regulation and their impact on the environment and human health is still poorly understood and known[8,9]. They are known as Concerning Emerging Contaminants “CECs” and it’s a matter of thousands of synthetic compounds with heterogeneous physical-chemical properties and unknown environmental behaviour. Among all CECs, the most alarming substances are pharmaceuticals and drugs, together with their transformation by-products, as they are designed to have a biological response, but this will be examined in Chapter 2.1.1. In the same class, it is possible to include other compounds like personal care products, fragrances, insects’ repellents, sun-screens, flame retardants (PFOA, PFAS, PFOS), gasoline additives, industrial additives, and so on[10]. It is crucial not to forget to draw the attention on the mechanisms of degradation and the by-products formation, as they are similarly involved in this pollution class and some of them may be even more harmful than original compounds. Despite the concentration of the overall class is still quite low (ppm to ppt), they’re administered and used in large quantities (the estimated annual trade of these compounds ranges from 100.000 to 200.000 tons) for different purposes, e.g. veterinary use, medical prescriptions, abuse, and so on; hence they are continuously replenished in the environment from both punctual and diffuse sources, resulting in their ubiquitous presence[11,12].

In order to preliminary evaluate the pressure on a specific environment of a certain pollutant, it’s mandatory to monitor the production, sale, use and disposal but, when it comes to deal with such different molecules, a key parameter is the physical-chemical characterization of the compounds, as their properties can be directly related to the processes and transformations occurring in the environment. Thus: vapour pressure, solubility, diffusions coefficients, boiling point, Henry constant, partition coefficients, adsorption coefficient, bio-concentrating factor and so on. For the majority of the components of this pollution class, characterization data are often inexistent and for this reason they cannot be organized in specific categories, making it even more difficult to make environmental laws on their limits and threshold values and risk characterizations. As a general overview, a scheme of the distribution paths of synthetic chemicals in the environment is reported in Figure 2.

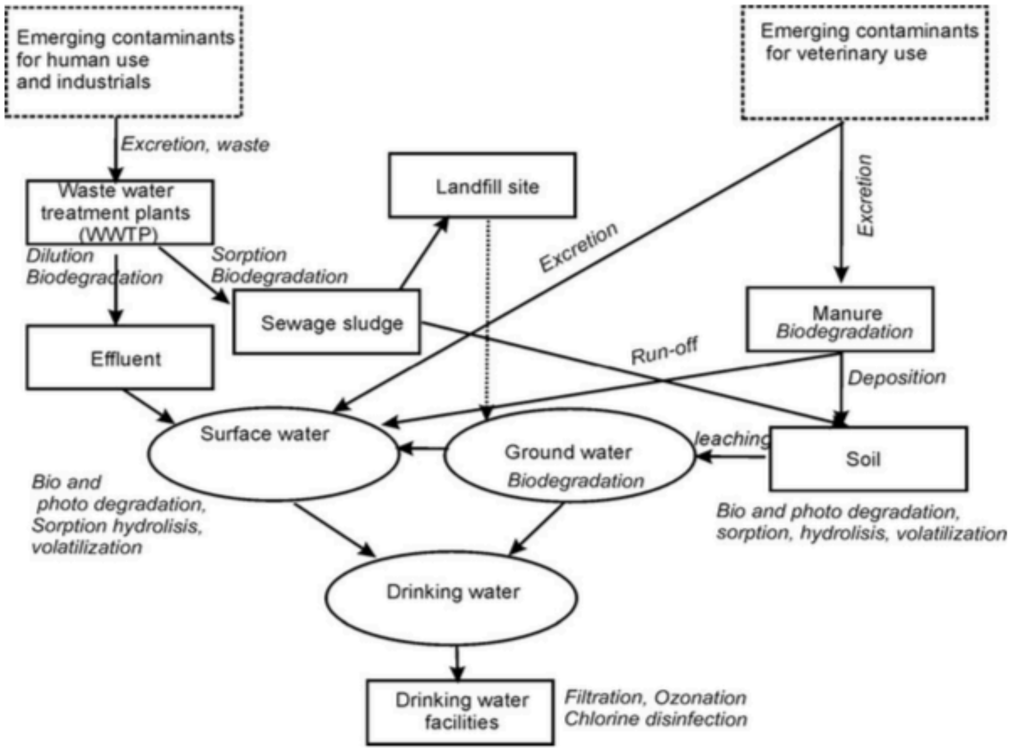

Figure 2: Distribution of synthetic chemicals and main transformation in the environment and the techno-sphere[12]

It results to be clear that, also in this case, the aquatic compartment represents the ultimate recipient of CECs collection, thus including river, lakes, sea, ground and fresh water, but conversely, the polluting load is not high. This may seem advantageous in terms of their abatement, but two main problems arise in a conventional WWTP: when high and low pollution loads are treated together, it becomes much harder to remove the smaller one (a typical situation occurring in urban WWTP) and furthermore, actual treatment plants are not designed to face emerging pollutants, but rather classic pollutants, as mentioned before, because they are not equipped with the technologies required to deal with CECs.

Luckily, in the last few years some regulations were made about environmental issues: in Italy, the law n° 152/06, later updated to law n° 172/2015, has the aim to defend the soil, to fight against the desertification, to protect water basins and to provide environmental impact evaluations or administrative fees when necessary. It is indeed possible to have a look at the "Watch List", published and updated in the EU website, where specific contaminants of high concern are identified and listed (the "Watch List" doesn't include all the compounds but the most significant ones), which is used as a guide for the environmental monitoring that should be done in the European countries (ISPRA for Italian area) for the screening of the pollution occurrence[13].

Many things could be done to act against this threat, starting from self-awareness and correct disposal procedures for consumers up to the development of efficient degradation techniques able to indiscriminately clean waters without differences of activity. Today, this problem involves all the Earth[14,15] but still there is not a single complete solution established for each micropollutant.

2.1.1. Pharmaceuticals and Personal Care Products "PPCPs"

Among all the emerging pollutants, the most concerning are pharmaceuticals, together with their degradation and metabolization by-products, because they are designed to have high chemical stability, high water solubility and strong biological interaction, even in low concentrations[16,17]. Considering the overall estimated use, 52% is for human use, hospital and prescriptions; 33% is for animal use and the residual 15% is used for illicit/illegal purposes. The variety of pharmaceuticals available today is extremely huge, in fact, as example, we can mention some families (neglecting each single molecule): antiepileptics, blood-lipid regulators, psychiatric drugs, antitumoral drugs, cardiovascular drugs, X-Rays contrasting agents, surfactants, hormones, steroids, beta-blockers, oestrogens, analgesics, antibiotics and so on[10,18]. Within this big variability, we can just imagine how easily and heterogeneously they could spread in the environment, especially in the aquatic one, even though the environmental behaviour of the single compounds is still unknown. A representation of these phenomena is reported in Figure 3.

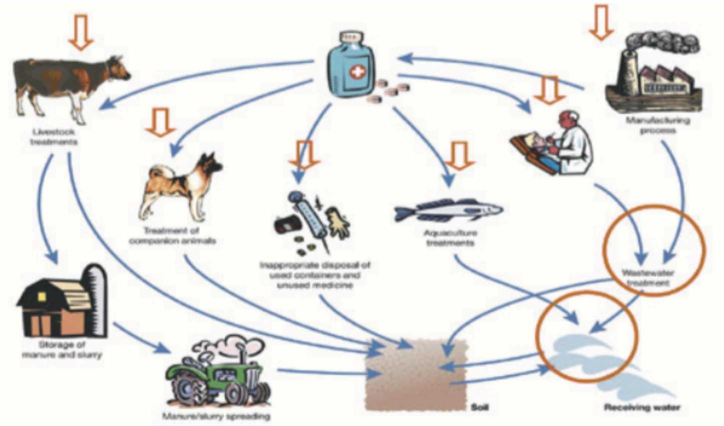

Figure 3: Routes of pharmaceuticals entering the environment[19]

The presence in the aquatic environment of all these compounds together may even represent a bigger and more dangerous threat, as the simultaneous action of different drugs can likely be synergic and thus affect in unknown ways living organisms. Pharmaceuticals can easily pass through biological membranes and here they can execute their specific activity until they are excreted as they are or partially metabolized; once removed, their activity remains unaltered, or modified if the molecules underwent transformations in the organism, thus new organisms interacting with these molecules will suffer their activity. For these reasons, the chronic exposure of living beings to the "cocktail" should be monitored along time in order to draw the attention to the risks[20,21].

Another issue related to the PPCPs presence is their very low concentrations: the daily intensities are in fact dependent on several factors, such as atmospheric conditions, quotidian use, area and specific compound. They are hardly detected, and so they would require any pre-concentrations techniques (POCIS, SPME, and so on) and/or very sensitive instruments (HPLC-MS, GC-MS, and so on) and they are in addition hardly degraded by actual available treatments.

The most commons percentage abatement of these pharmaceuticals sets up to about 2%, which is a dramatically low value for a WWTP[22]. In addition, because of this, the opposite outcome is obtained, that is the concentration of the polluting load inside the WWTP. Of course, it is very crucial to upgrade current treatment plants with new technologies able to degrade this class of compounds[23].

2.1.2. Antibiotic Resistance

Antimicrobial multidrug resistance is a critical phenomenon which has begun to be monitored in the last 20 years, to demonstrate its diffusion[24,25]. Today, it has become a serious threat for humans' and animals' health, as multi-resistant bacteria are involved in severe infections. This is due to the ability of bacteria to grow and reproduce quickly, accumulating favourable genetic mutations to adapt to the continuous alterations of their living environment[26]. For this reason, some bacteria strains have developed a resistance to the commonly used pharmaceuticals (mainly antibiotics). As an example, patients undergoing cures in intensive care units are at risk of several complications, due to the rapid colonization of biofilm-forming pathogens, which adhere to surfaces of man-made materials and have themselves responsible for sustained inflammatory processes[27]. The evolution of multidrug resistant genes is an insidious secondary effect of the emerging pollution discussed in the previous section and the enormous hazard relies in the fact that, since antibiotics are no longer active in counteracting bacterial infections, even common and harmless diseases could eventually lead to the worst outcomes[28]. Nowadays, scientific reports are monitoring those bacterial strains which developed this resistance: *Staphylococcus Aureus, Pseudomonas Aeruginosa, Escherichia Coli, Bacillus Pumilus, Acinetobacter Baumannii, Enterobacteriaceae, Enterococcus Aureus, Helicobacter Pylori, Campylobacter, Salmonella Spp, Neisseria Gonorrhoeae, Streptococcus Pneumoniae, Haemophilus Influenzae* and so on[29]. Usually, urban and hospital effluents are the source of genes and bacteria dissemination and this fact summons the necessity to have efficient treatment plants and powerful techniques.

In addition, other environmental compartments are in danger: for example, the biological treatment in wastewater plants, i.e. activated sludge, is made of bioactive microorganisms usually employed to drop the heavier organic polluting load; these microorganisms may be harmed by the pollutants' presence and this would affect the activity of the active sludge itself. Furthermore, there are also evidences about morphological and sexual disturbances in fishes and creatures living in the aquatic environments. It is indeed reported the rise of reproductive alterations due to the hormonal activity of the drugs[7].

2.2. Advanced Oxidation Processes "AOPs"

Before starting to deepen the field of the techniques included in the so-called advanced oxidation processes, it would be useful to have a general overview at the available processes in an ordinary water treatment plant, which consist in mechanical and chemical treatments also known as primary and secondary processes, employed to establish the pristine compositional equilibrium of water with considerable costs in terms of energy and commitment. They are summarized in Figure 4.

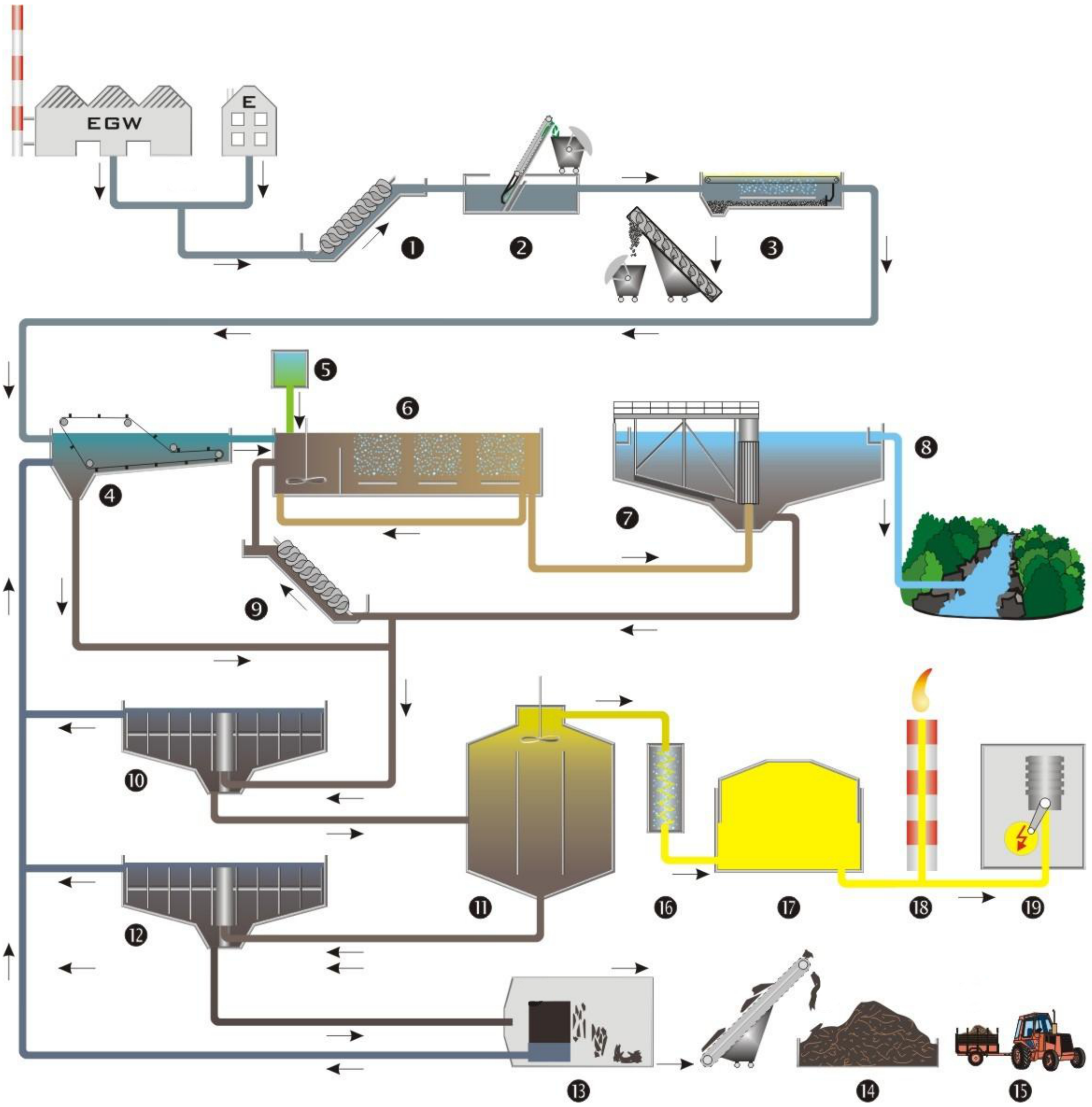

Figure 4: Scheme of a wastewater treatment plant[30]

According to the numbers reported in the Figure above, a brief description of these processes is displayed:

1- Wastewater is collected from the sewer system and conveyed by collectors to the treatment plant. This sewage is lifted before proceeding to the subsequent processes.

2- The first treatment is the sieving, used to remove the coarse material in the grit chamber, which is then washed, pressed and disposed to the landfill.

3- Sand is removed by natural sedimentation while oils and fats migrate towards the surface for their lower density. A streamline flow of air is insufflated to help this process.
4- In the primary sedimentation tank, the sedimentation of solids takes place by gravity. The sludge on the bottom is then pushed forward other treatments, while the supernatant proceeds toward different ones.

- End of primary mechanical processes; $^1/_3$ of the organic load is removed -

5- Fresh microorganisms' colonies reserve.
6- In the aeration activated sludge tank, the elimination of dissolved substances occurs by the metabolic action of microorganisms towards organic matter. This process is promoted with the insufflation of air (oxygen) from the bottom. In this section, the removal of macro-pollutants (nitrogen, phosphor) is obtained with biological and chemical processes (flocculation with $FeCl_3$ and $Fe_2(SO_4)_3$)
7- The removal of bacterial colonies flakes is obtained in the final sedimentation tank by gravity.
8- Clean water is then returned to surface water.
9- A part of the activated sludge is recovered and reused in the aeration activated sludge tank.

- End of secondary bio-chemical processes-

10- Sludges from primary and secondary sedimentations are conveyed in the pre-thickener to remove moisture and reduce volume.
11- The digestor is a closed vessel, kept at 35 °C, which treats the biomass for 20 days in anoxic conditions, where bacteria transform organic matter in inorganic substances, producing biogas.
12- A second thickener treats the remaining sludge to further decrease moisture and volume
13- With the final mechanical dehydration, the sludge volume is reduced by six times and it is semi-solid, thus can be used in:

14- Landfill disposal,
15- Composting and agriculture.
16-19- The biogas produced in the digestor is transferred to the gasometer and then burnt in order to gain electric energy and heat.

Within primary and secondary processes, the higher load of the classic pollution is removed, but it implies that micropollutants and bacterial colonies may pass through, without being degraded. As already mentioned, it is estimated the approximately 2% of removal is reached for CECs, thus after a WWTP it is even more likely a pre-concentration effect, before the introduction in the environment. Taking into account that complete transformations are not possible as thermodynamic equilibrium occurs, it is required to have experimental conditions able to shift the yield towards the complete degradation. This is exactly the case of advanced oxidation processes[31].

According to the first definition (1987), AOPs are defined as those which involve the generation of hydroxyl radicals in sufficient quantity to affect water purification. We may consider AOPs as a part of the tertiary processes, not displayed in the scheme depicted in Fig. 4, whose aim is to disinfect water with chemical and physical processes, e.g. chemical oxidation, adsorption, stripping, membrane filtration, chlorine compounds, granular/powder activated carbon, nanofiltration and reverse osmosis membranes. The main difference between AOPs and the other tertiary processes is the higher affinity to CECs for the former with respect to the latter, together with the possibility to exploit some of them with eco-friendly energy sources (and further, cheaply)[32–36].

In particular, we can make a comparison between light AOPs: ozonation (O_3), hydrogen peroxide, ultraviolet radiation (UV-C), homogeneous (Fenton) and heterogeneous (TiO_2) photocatalysis, electro-photocatalysis, and hot AOPs: wet air oxidation, non-thermal plasma, ultrasound, electron beam, vacuum UV. The difference relies on the amount of organic load to be removed: light AOPs for $0g/L < T.O.C. < 10g/L$; hot AOPs for $10g/L < T.O.C. < 220g/L$. As the definition highlights, the high activity of the AOPs is related to the formation of hydroxyl radicals[37] (E_0 2,80 eV), which main features are shown in Figure 5.

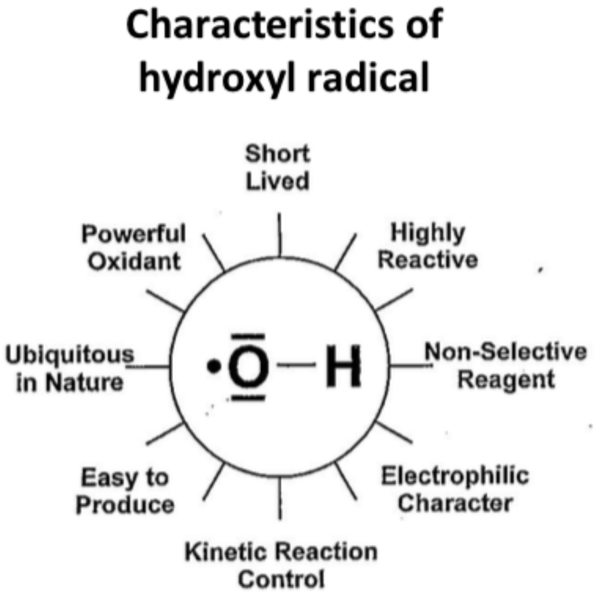

Figure 5: Main features of the hydroxyl radical

For its non-selective character, ease of production, high oxidation power and reactivity, this radical is the main responsible of the disruption of chemical bonds and functional groups which characterize each specific molecule. Furthermore, these radicals potentially lead to the complete mineralization of the CECs load, quite the opposite for other tertiary processes, whose disinfection by-products may be unavoidable[38]. The formation of hydroxyl radicals from some of the light AOPs is shown in the following equations:

$$\text{(Eq. 1)}\quad H_2O_2 + h\nu \rightarrow 2OH^*$$

$$\text{(Eq. 2)}\quad O_3 + H_2O + h\nu \rightarrow O_2 + 2OH^*$$

$$\text{(Eq. 3)}\quad 2O_3 + H_2O_2 \rightarrow 3O_2 + 2OH^*$$

$$\text{(Eq. 4)}\quad H_2O_2 \rightarrow HO_2^- + H^+$$

To be precise, the radical species produced by AOPs may be different than the only hydroxyl radical: they are generally recognized as Reactive Oxygen Species "ROS", that is oxygen-containing reactive molecules with the same reactivity features of the hydroxyl radical (OR^*, HO_2^-, O_2^{-*}, $^1O_2$, RO_2^*, CO_3^{-*}, SO_4^{-*}, and so on). The action of general AOPs can be summarized according to the following equation:

$$\textit{(Eq. }\mathbf{5}\textit{)}\quad C_nH_mX_z + \left(n+\frac{m-z}{4}\right)O_2 + \boldsymbol{AOP} \rightarrow n\,CO_2 + \frac{(m-z)}{4}H_2O + z\,HX$$

The complete mineralization of generic pollutants together with the high affinity of AOPs to CECs make them the right choice to face the emerging pollution threat and the right processes to update the WWTPs. As usual, there are some drawbacks that may reduce their effectiveness: possible formation of toxic by-products according to matrix composition, high energy demand especially for hot AOPs, interference of radicals' scavengers which react with ROS and subtract them from their aim, difficulties in the recovery of the used materials. It is thus necessary to define the conditions to have the maximum efficiency for the treatments.

2.2.1. Heterogeneous Photocatalysis

As the focus of this PhD project is the heterogeneous photocatalysis, it is useful to show how it is possible to obtain the hydroxyl and other radical species, how they react with pollutants and how they can be exploited for environmental protection.

Photocatalysis is based on the ability of a semiconductor material to absorb a photon of a proper wavelength by the promotion of an electron located in the highest electronic occupied band, the valence band "VB", to the lowest electronic unoccupied band, the conduction band "CB". This promotion is possible for the particular nature of electronic states in semiconductors: VB and CB are divided by a range of forbidden energies for electrons, also known as Energy Gap "E_g", which is an intermediate situation between the metallic and the insulator behaviour[39–42].

When the first law of photochemistry (Grotthuss-Draper law) is respected:

> "*Light must be absorbed by a chemical substance in order to activate a photochemical reaction*"

and the quantum yield "Φ", intended as the ratio of photons emitted to photons absorbed, is good; then a photon with an energy at least equal to the E_g activates the semiconductor material and a complex scenario of photo-induced processes arises. In the following equations, some of these processes are highlighted:

Thermalization of hot carriers*:*

(Eq. ***6****)* $$e_B^- \rightarrow e_{CB}^- \; ; \; h_B^+ \rightarrow h_{VB}^+$$

Bulk Recombination:

(Eq. ***7****)* $$e_{CB}^- + h_{VB}^+ \rightarrow heat, light \; (at\ recombination\ centers)$$

Migration of the carriers to the surface:

(Eq. ***8****)* $$e_{CB}^- \rightarrow e_S^- \; ; \; h_{VB}^+ \rightarrow h_S^+$$

Surface Charges Trapping:

(Eq. ***9****)* $$e_S^- \rightarrow e_{Tr}^- \; (e_S^- + \equiv TiOH \rightarrow \equiv Ti(III) + OH^-)$$

(Eq. ***10****)* $$h_S^+ \rightarrow h_{Tr}^+ \; (h_S^+ + \equiv TiOH \rightarrow \equiv TiO^* + H^+)$$

Surface Recombination:

(Eq. ***11****)* $$e_S^- + \equiv TiO^* + H^+ \rightarrow TiOH$$

(Eq. ***12****)* $h_S^+ + \equiv Ti(III) + OH^- \rightarrow TiOH$

Donor Reaction with Free or Trapped holes:

(Eq. ***13****)* $D + h^+ \rightarrow D^{*+}$

(Eq. ***14****)* $e.g. \equiv TiO^* + RH \rightarrow \equiv TiOH + R^{*+}$

(Eq. ***15****)* $e.g. \equiv H_2O + h^+ \rightarrow \equiv OH^* + H^+$

Donor Back Reaction (Donor Mediated Recombination):

(Eq. ***16****)* $D^{*+} + e^- \rightarrow D$

(Eq. ***17****)* $e.g. \equiv TiO(III) + R^{*+} + H_2O \rightarrow \equiv TiOH + RH$

Acceptor Reaction with Free or Trapped electron:

(Eq. ***18****)* $A + e^- \rightarrow A^{*-}$

(Eq. ***19****)* $e.g.\ O_2 + e^- \rightarrow \equiv O_2^{*-}$

Acceptor Back Reaction (Acceptor Mediated Recombination):

(Eq. ***20****)* $A^{*-} + h^+ \rightarrow A$

(Eq. ***21****)* $e.g.\ O_2^{*-} + \equiv TiO^* + H^+ \rightarrow O_2 + \equiv TiOH$

All these processes concur simultaneously, in a range of time included in the femto- to pico- seconds, for what concerns electron/hole processes, and from nano- to micro-seconds for what concerns ROS life.

As heterogeneous photocatalysis is a surface process, it is very important that surface characteristics of the material are optimized: the crystalline structure of the materials should enhance the migration of the carriers to the surface, rather than favouring bulk recombination; the exposed surface with respect to the bulk volume should be maximized, in order to get a better interaction with dissolved species; the electronic structure and thus bands' position should be such to have compatible e^-/h^+ redox potentials with ROS formation ones.

When the abovementioned characteristics subsist, the photocatalytic process can proceed as follows (Figure 6):

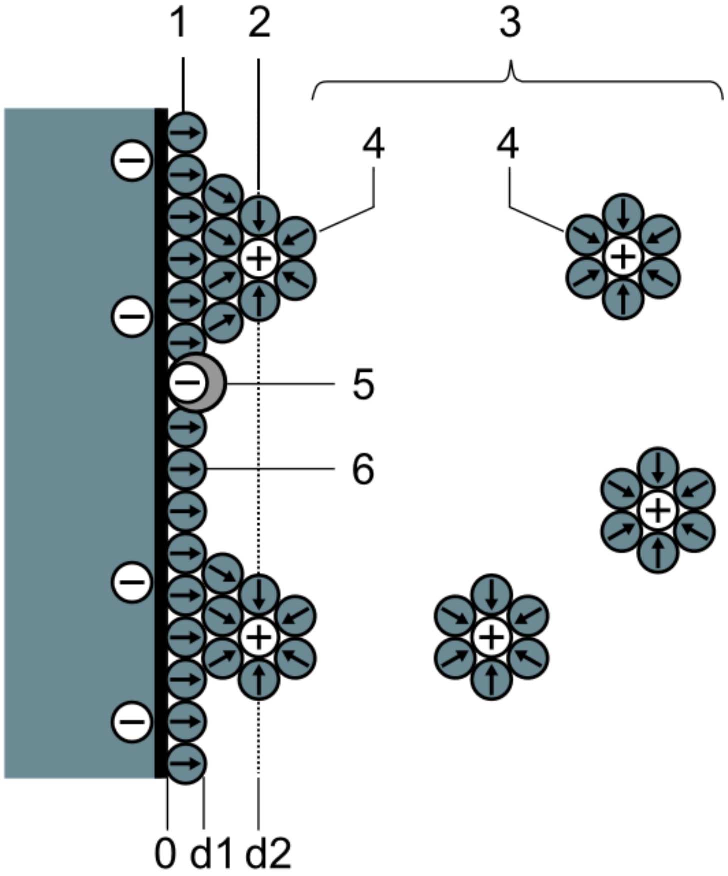

Figure 6: Schematic representation of an electrical double layer when the surface of a solid is exposed to an electrolyte[43]

1- Inner Helmholtz Plane "IHP".

2- Outer Helmholtz Plane "OHP".

3- Diffusion Layer.

4- Solvated ions.

5- Specifically adsorbed ions.

6- Molecules of the electrolyte.

The main mechanisms of charge transfer from photoactive material to the pollutants are two: direct e^-/h^+ transfer or hydroxyl mediated oxidation. Focusing on the semiconductor/electrolyte interface, it is possible to identify the double electrical layer: the IHP, where we can mainly find molecules of the solvent or some specifically adsorbed ions; the OHP, which can interact with the first one by adsorption of solvated ions within the diffusion layer (which is also a function of the life time of carriers). Direct donor/acceptor reactions with free or trapped e^-/h^+ are mainly located in the IHP, as they are formed by chemical complexes with surface groups, and the efficiency of this transfer is usually very high. Similarly, if the donors/acceptors are located in the OHP but within the diffusion layer, this mechanism can still occur. In the case of hydroxyl radical mediated oxidation, the charge transfer is intermediated by absorbed reactive species, generally formed in the IHP, with direct e^-/h^+ transfer to adsorbed electrolyte molecules (water); those species are equivalent to surface e^-/h^+ and mediate the electron transfer to the substrates.

These mechanisms are accountable for the degradation of the emerging micropollutants, independently from the various physical-chemical properties, as well as for sterilization of bacterial colonies[44–47]. For the unspecific mechanism of action, it is possible to provide sterilization from all harmful and harmless microorganisms, which are completely killed (conversely to disinfection, which is the removal of exclusively pathogenic microorganisms). The inactivation process proceeds with the partial disruption of the external bacterial membrane, followed by a partial loss of viability; if the ROS can go further (this is also depending on the dimensions of the catalyst, which can also pass through the cell wall membranes, according to their composition, and induce oxidative stress within) they are able to reach the cytoplasmic membrane: the death occurs after the complete disruption of the cell wall. It has to be underlined that, between the first two steps, the microorganism is just inhibited and it’s still able to recover.

The engineering of the photocatalytic material represents a very important part of the scientific research on heterogeneous photocatalysis. The synthetic process is extremely important to control the characteristics of the photocatalysis, like surface modifications, facets strain, quantity and distribution of pores, dopants, dimensions of particles and aggregates, nature and concentration of lattice defects, crystalline structure and so on. It is indeed possible to make a visible sensitization doping with metals or non-metals elements, but this may introduce new recombination centres (and reduce Φ). As surface features are the most important, it is also useful to know the point of zero charge, which is the pH value corresponding to the same concentration of H^+ and OH^- at the catalyst’s surface, in order to know what species are adsorbed on its surface[48,49]. Furthermore, during photocatalytic reactions, some other parameters must be fixed to enhance the efficiency: nature and concentration of the substrate to be removed, catalyst’s concentration, pH, type of irradiation source, irradiance (W/m^2) of the source, total volume and so on. A correct design of experiments is the base to deal with this problem in real water, to get solid and reproducible data and thus get to the full-scale industrial use.

2.3. Titanium Dioxide TiO_2

Titanium Dioxide TiO_2 is a semiconductor material which shows a white and solid aspect; it can be found in nature as a mineral, in particular from Ilmenite ($FeTiO_3$), Anatase and Rutile (TiO_2), from which it is purified and/or extracted[50]. There are two main industrial processes for its production, and they are the chlorine purification process[51,52]:

$$TiO_2 + 2C + 2Cl_2 \rightarrow TiCl_4 + 2CO \qquad TiCl_4 + O_2 \rightarrow TiO_2 + 2Cl_2$$

or the sulphate production process:

$$FeTiO_3 + 2H_2SO_4 \rightarrow TiOSO_4 + FeSO_4 + 2H_2O$$

$$TiOSO_4 + 2H_2O \rightarrow TiO_2 + H_2SO_4$$

This material is indeed a very well-known and studied one, as it was and still is employed in a big variety of fields for its peculiar properties: production of clean energy, part of building material, in water or air filtration systems, in self-cleaning white paints, UV absorbers sun-screen, as food additive and in personal care products formulations. All these properties arise from its semiconductor-like electronic structure, and it is in addition: abundant, eco-friendly, recyclable and easily synthesizable. For research application, it is also useful to note its characteristics of highly resistance to corrosion and photo-corrosion, chemically and thermally stable, harmless nature and especially its low cost[53–55].

The most significant polymorphs of TiO_2 are three: Anatase, Rutile and Brookite. These polymorphic structures have the same composition but different crystalline structures: in particular, Anatase and Rutile's lattices are tetragonal while Brookite is orthorhombic. These structures are characterized by edge- and corner-linked Ti cations in octahedral coordinations and they're depicted in Figure 7.

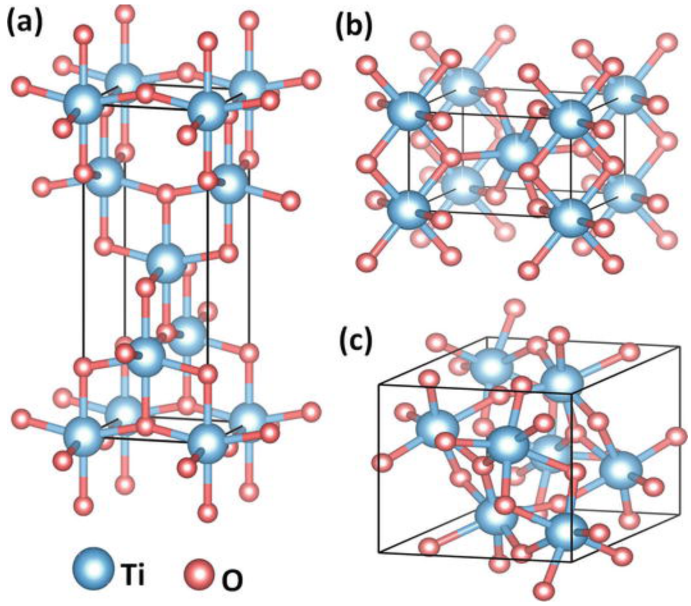

Figure 7: Crystal structure of principal TiO_2 polymorphs: a) Anatase, b) Rutile, c) Brookite[56]

Some thermodynamics considerations may be done on the stability of the different polymorphs: in standard conditions the thermodynamically stable phase is Rutile, while Anatase and Brookite are meta-stable; this is not always true because, according to the size of the particles, there may be some modifications in their range of stability (especially when dealing with nanoparticles). Apart from the stability, also electronic considerations have to be done, because, for the photocatalytic process, it is recommended to have the anatase phase (or a mixture with it), as it is reported in literature that is the crystalline lattice with the slowest charge carriers' recombination rate among the other polymorphs.

It is defined as an intrinsic n-type semiconductor, which means that, as a semiconductor, its VB is divided from the CB by a forbidden range of energies, E_g; as intrinsic n-type, it means that there is an excess of donor species, i.e. the majority carriers are electrons, and that, at the equilibrium, the redox potential of the semiconductor is equal to the Fermi energy level, which lies within the E_g. The difference in crystalline lattices among the polymorphs is also evident from their E_g values: respectively for Rutile, Anatase and Brookite, they are equal to 3,05 eV, 3,18 eV and 3,40 eV. According to the following equation:

$$\textit{(Eq. }\mathbf{22}\textit{)} \qquad E_g\ (eV) = \frac{1240}{\lambda\ (nm)}$$

it is possible to identify the energy of the photons that can interact with TiO_2 (406-365 nm, corresponding to the UV-A range of the electromagnetic spectrum). As a reminder, the activation of the semiconductor occurs through the compliance of the following conditions[55,57,58]:

$$\textit{(Eq. }\mathbf{23}\textit{)} \qquad E_{h\nu} \geq E_g$$

$$\textit{(Eq. }\mathbf{24}\textit{)} \qquad Semiconductor + h\nu \rightarrow e^-_{CB} + h^+_{VB}$$

Other semiconductor materials can be thus characterized by their E_g values and bands' positions, as they represent the description of the redox potential of the different materials (Figure 8).

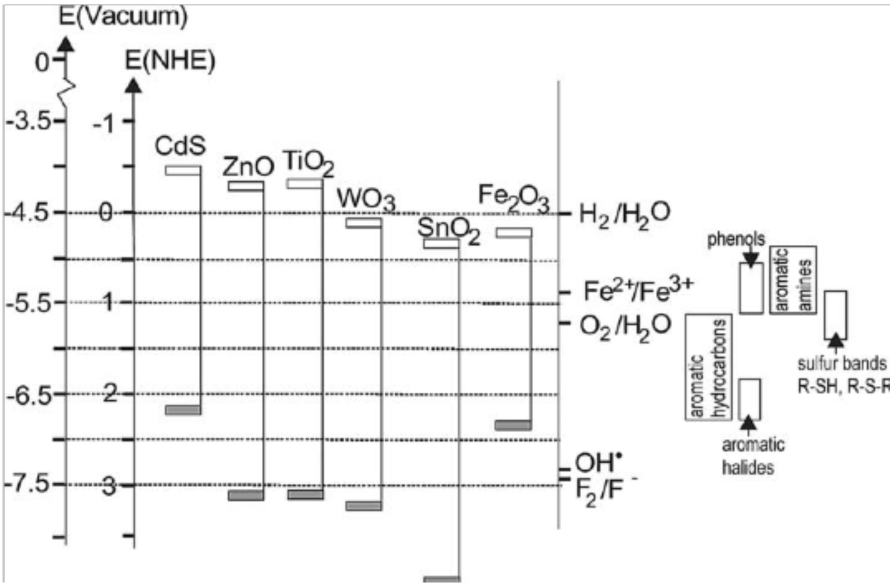

Figure 8: e^-/h^+ redox potentials for some semiconductor materials, in comparison with some redox reference potentials[59]

When TiO_2 interacts with a proper radiation, the generated electron/hole pair can promote redox reactions according to their redox potentials: the photo-electron redox potential is E_0: -0,52 eV while the photo-hole redox potential is E_0: +2,80 eV. If we take into account two reference redox potential: (O_2/O_2^{*-}) E_0: -0,28 eV and (OH^*/H_2O) E_0: +2,27 eV, related to the energy required to obtain two of the main ROS involved in advanced oxidation processes, we can immediately see that the ΔG is negative for both reactions and thus that TiO_2 is compatible with this purpose. The reactions usually proceed with hydroxylation of organic bonds, subsequently oxidized until the complete mineralization is reached (a sort of room temperature combustion)[60].

Titanium dioxide unfortunately comes along with some drawbacks that actually hinder its industrial application; fortunately, the scientific research on this topic remains still wide open. First of all, we need to make some considerations about the E_g: taking into account Anatase, the energy required for the photon to activate the material is located in the UV-A region, more specifically for wavelengths minor or equal to 390 nm. This fact can be considered a drawback for two reasons: the use of specific UV lamps brings high costs and possible danger to human safety; the possibility to exploit solar irradiation and thus eco-friendly activate the photocatalyst is impeded by the very small fraction of UV photons belonging to the solar radiation reaching Earth's surface (lower than the 8% of the total flux). In addition, as already discussed in chapter 2.2.1., the photocatalytic process proceeds through the interface between the solid and the liquid medium; hence it is highly advised to maximize the surface to volume ration, also known as surface area. Experimentally speaking, the highest ratio can be obtained with the synthesis of TiO_2 as nanoparticles, which on the contrary represent a potential threat for the environment: the spread of nano-powders throughout the different environmental compartments represent another polluting source that may modify and put in danger pre-existing equilibria and organisms. They are, for example, hardly recovered from colloidal suspensions, as they possess different physical-chemical properties with respect to the bulk material, so it would be too easy to lose and disperse the nano-material.[61–63]

The most recent scientific research on titania focused mainly on the synthetic and optimization paths in order to overcome this kind of issues. Laboratory scale synthesis is indeed very versatile, as it can be easily tuned to get specific features (shape, size, purity, homogeneity, doping, support) with also different available synthetic paths: liquid-phase and gas-phase processes, co-precipitation methods, hydrothermal treatment, sol-gel techniques, combustion synthesis, electrochemical process, sputtering, laser ablation and so on[64–74].

Thanks to the huge variety of possibilities, it results to be possible to adjust TiO_2 features towards increased efficiency: in order to overcome the UV photons required, it is possible to introduce dopants species (N^{3-}, Cu^+, Fe^{2+}) within the TiO_2 lattice that modify the electronic structure of the photocatalyst by inserting new energy levels (within the E_g, with differences according to the nature of the dopant) and thus inducing a red shift of the absorption edge towards the visible region; in order to avoid the nano-powders spreading into the environment, titania can be synthesized and coupled to other supporting materials in order to have a partial immobilization that shouldn't hinder its efficiency but just limit its dispersion. As usual, it is necessary to find a midway compromise, because both the doping and the supporting processes may lead to a decrease in the TiO_2 activity: by for example increasing the concentrations of recombination's centres (e.g. dopants and lattice defects) or just reducing TiO_2 surface area and thus inhibiting the adsorption of molecules on its surface as well as reducing surface active sites.

TiO_2 confirmed itself to be a very effective tool to counteract this widespread pollution. Its high oxidizing power is able to completely mineralize a huge spectrum of organic micropollutants to nontoxic molecules[75].

2.4. Supporting materials

As already mentioned in the previous sections, in the last years, the scientific production on titanium dioxide was focused on its optimization as heterogeneous photocatalyst, mainly undertaking the routes of doping and supporting. In addition, the application of chemometric techniques to the synthetic process e.g. multivariate analyses regressions and principal component analysis, gave the possibility to get important information on the correlation of the synthesized systems as well as on the application against emerging pollutants. The mathematical models could give an important help in the solution of complex systems, like the one of composite material or the low concentrated emerging pollutants and their dispersion paths.

With the progression of material science, it is possible to count on a big selection of new materials with fine features, in particular, properties that make them compatible with TiO_2 working conditions. These materials are actually one of the main focuses of the current thesis, as they represented the chance to bring the photocatalytic technology up to the industrial level. The main characteristics found in the materials employed for this purpose are porosity and magnetism, because they represent the ability to give an easier recovery of the suspended nano-powders without affecting their activity.

Just to mention some of them: silica, glass beads, magnetite, zeolites, ceramics, membranes, fibres, phosphors, activated carbon, semiconductors, clays, steel and so on. The noteworthy thing is that investigation is still open[6,76–83].

3. Synthesis and Support of TiO_2

In this chapter all the projects designed on the synthesis and optimization of TiO_2-based materials are reported and deepened. Every single project, when possible, is described as a scientific paper: it is possible to distinguish the "Materials and Methods" section, where reagents, instruments and techniques are explained; "Results and Discussions" section, where the experimental results are characterized and described, hypotheses are stated and confirmed or denied; and lastly "Conclusions" section, where the main results and the future perspectives are highlighted.

3.1. Synthesis with Persistent Luminescence Materials "PeL"

In this section, the synthesis of TiO_2 is performed on different persistent luminescence materials "PeL", in particular: the first (Chapter 3.1.1.) is a ($3ZnO:Ga_2O_3:2GeO_2$): Cr^{3+}, a PeL material synthesized in laboratory while the second (Chapter 3.1.2.) is a commercial PeL, based on $CaAl_2O_4$: $(La, Nd)^{3+}$. These materials were also used to test other types of composite, e.g. with ZnO nanoparticles (Chapter 3.1.3.). Furthermore, the description of a pilot plant for preliminary scale-up considerations is shown (Chapter 3.1.4.) and eventually the project on the recovery of photocatalyst's nanoparticles with zero-charge surface conditions, is reported.

Before deepening each single project, a brief description of the persistent luminescence phenomenon is described, using a PeL material based on the optically active Cr^{3+} ion as an example (Figure 9).

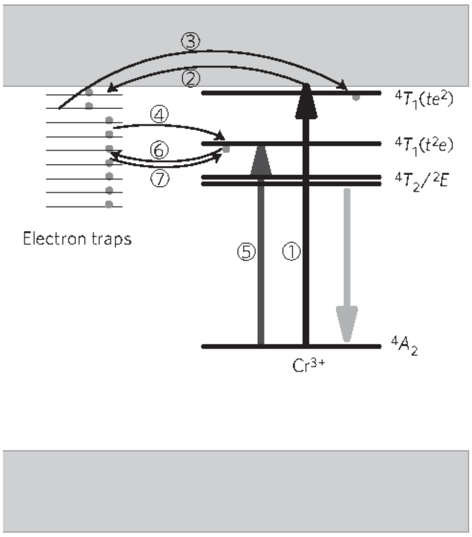

Figure 9: Mechanisms involved in the persistent luminescence phenomenon[84]

As above-mentioned, in this case Cr^{3+} ion is the optical active centre, thus it can absorb photons coming from the external excitation source. After the excitement

1- The electron is promoted from the ground state ($^4A_2$) to the excited state (te^2), which is near the CB edge,

2- Electron traps capture the promoted electron through the CB until they are completely filled.

3- In the very first moment after the stop of the source, the direct recombination between trapped electrons and Cr^{3+} ions is very fast, resulting in a very intense radiative emission.

4- Some trapped electrons, for tunnelling effect, may move towards other Cr^{3+} excited states, distant from CB,

5- As well as electrons promoted from the ground state to different excited states ($^4T_2/^2E$) or ($^4T_1(t^2e)$), 6- For the same tunnelling effect may move towards deep electron traps

7- An equilibrium between deep electronic states and deep traps occurs

The equilibrium between filling and emptying electron traps results in the possibility to have radiative emissions for a very long time. The persistent luminescence emission comes from the relaxation of excited states electrons to the ground state, with different wavelengths according to the energy of the involved electronic states, while the long duration of the phenomenon is due to the slow processes of tunnelling and thermal activation of trapped electrons among the different electronic states.

The PeL materials investigated during the project were thought to be used as supporting micrometric material (to enhance the recovery of the photocatalyst with centrifugation) for TiO_2 as well as internal excitation sources, that could provide photons required to activate the photocatalyst during the absence of an external excitation source, hence, for analogue reasons, in turbid or thick solutions[85–90].

The luminescence analyses were performed through radioluminescence and persistent luminescence intensity. In Figure 10 and Figure 11 the luminescence properties are shown respectively for ($3ZnO:Ga_2O_3:2GeO_2$): Cr^{3+} and for $CaAl_2O_4$: $(La, Nd)^{3+}$.

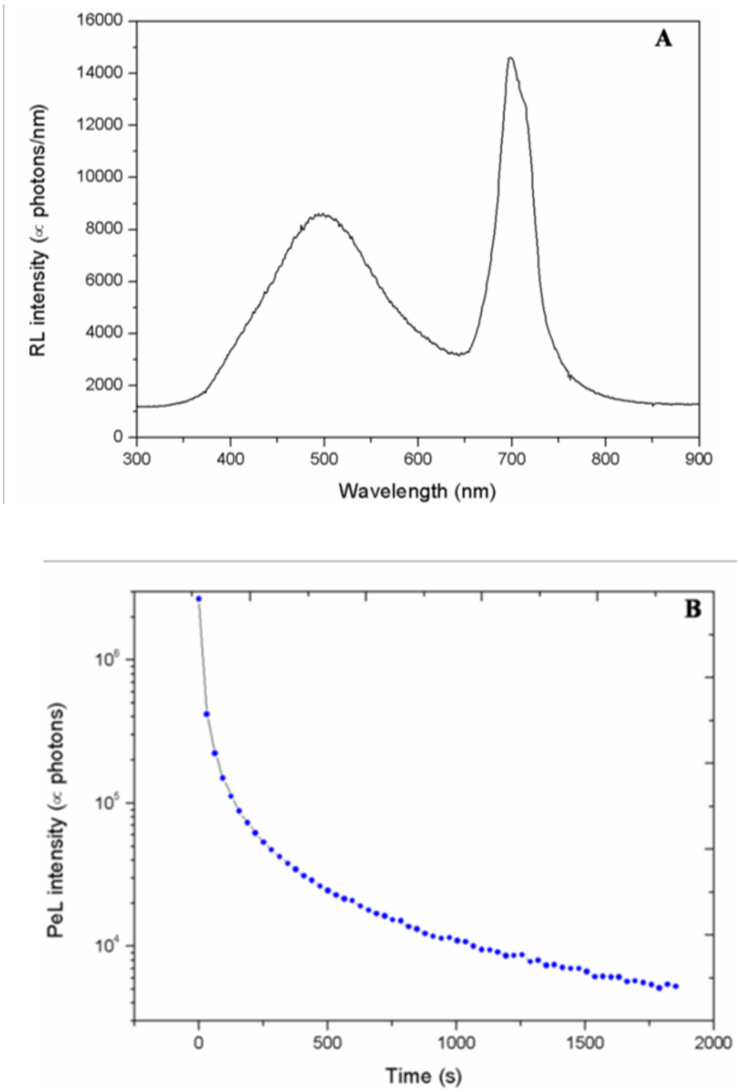

Figure 10: a) Emission spectrum of ($3ZnO:Ga_2O_3:2GeO_2$): Cr^{3+} excited with RX source; b) Decay time of emission intensity

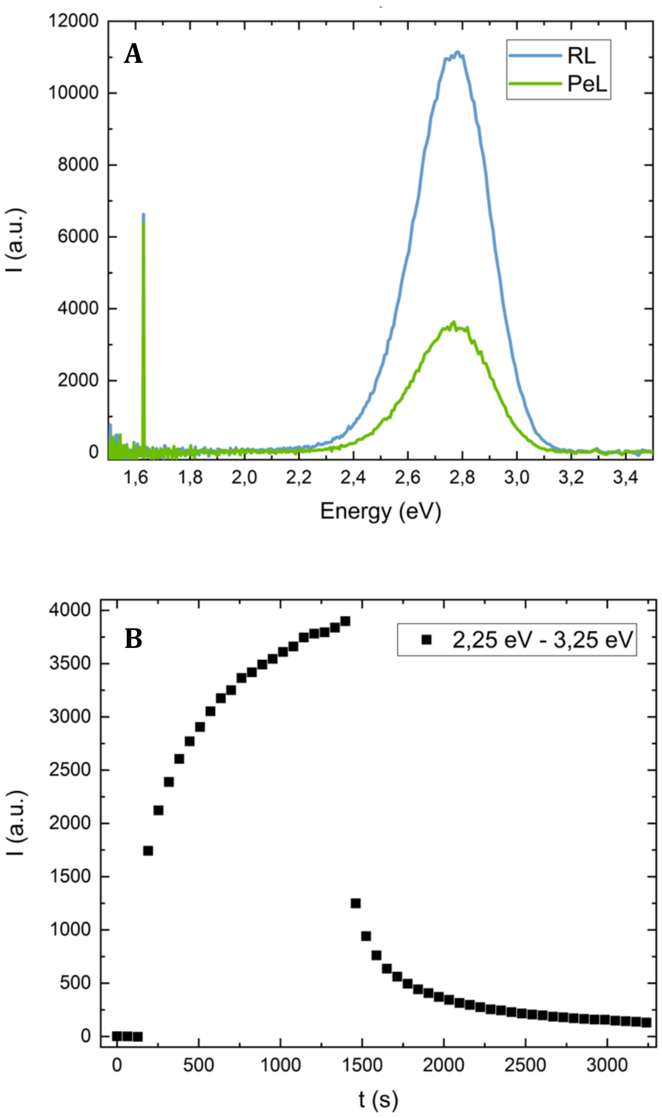

Figure 11: a) Intensity of Radioluminescence and Persistent Luminesce of $CaAl_2O_4$: (La, Nd)$^{3+}$; b) Charge/Discharge duration of persistent emission

3.1.1. *($3ZnO:Ga_2O_3:2GeO_2$): Cr^{3+}*

For this part of the project, a photocatalytic material based on TiO_2 and PeL material was produced and the synthesis was optimized using a chemometric approach. Nanometric powders of anatase TiO_2 were synthesized through the sol-gel technique, while PeL material was synthesized through a solid-state treatment. Each sample was characterized by means of XRD, SEM and BET analyses, while the photocatalytic activity was evaluated testing the percentage degradation of a methylene blue aqueous solution. In particular, the optimized sample was subjected to two kind of kinetic experiments: continuous irradiation and alternate dark/light cycles. It was demonstrated that the supporting PeL material could provide photons for the photocatalytic process during the absence of light. The synthesis of the composite material was planned through an Experimental Design 2^3, were the weight ratio between TiO_2/PeL, the heating temperature and the processing time were investigated as variables upon two levels. The evaluation of the model led to the conclusions that the monitored variables didn't affect the synthesis; thus, the most convenient values could be exploited to have an optimized sample. Eventually, the best one was tested for the degradation of a real emerging pollutant, i.e. the antibiotic ofloxacin, in tap water under simulated sunlight.

This Project was performed in collaboration with the section of Analytical and Photo- Chemistry of the Department of Chemistry of the University of Pavia, in particular with the research group of M. Sturini.

3.1.1.1. Materials and Methods

The supported $TiO_2/3ZnO{:}Ga_2O_3{:}2GeO_2{:}\ Cr^{3+}$ samples were prepared using a solid-state reaction. The PeL material was prepared using as precursor, ZnO (Alfa Aesar, 99,99%), Ga_2O_3 (Alfa Aesar, 99,999%), GeO_2 (Alfa Aesar, 99,98%) and Cr_2O_3 (Alfa Aesar, 99,97%), which were mixed together in an agate mortar and subsequently treated in a muffle furnace (Carbolite RHF1400) for 2 hours at 900 °C and then for 2 hours at 1100 °C. Between the two heat treatments, the powders were left cooling at T_{room}, grinded and homogenized again in the mortar. Titanium dioxide was prepared through the sol-gel route: 12 mL of 2-Propanol (Sigma Aldrich, 99,9%), 6 mL of Titanium Tetraisopropoxide "TTIP" (Sigma Aldrich, 97%) and 30 mL of deionized water (ARIOSO water purification system, Human Corporation) were left under vigorous magnetic stirring for 4 hours. The resulting gel was treated in an oven for 12 hours at 105 °C and then grinded in an agate mortar. The two synthesized powders were placed in 20 mL of deionized water for 30 min under magnetic stirring and eventually dried in the oven and treated in the muffle furnace. The weight ratio, the time and the temperature were set according to the model, later described. The resultant optimized sample was characterized by XRD, SEM and BET. Phase identification was performed using a Philips PW1830 Diffractometer (Bragg-Brentano geometry, Cu K_α, Ni filtered, range 20-80 2θ, step 0,025 2θ, sampling time 10 s). SEM images were collected using a Tescan Vega 3 MXV microscope, on powders coated with gold in low vacuum. Brunauer-Emmet-Teller analysis was carried out using an ASAP 2010 physisorption porosimeter (Micromeritics Instrument Corp.). Before the measurement, the sample was pre-treated at 200 °C under vacuum.

Photocatalytic activity was investigated by testing the percentage degradation of 25 mL of a 0,01 g/L MB solution (Merck), in presence of 0,0125 g of photocatalyst. MB was quantified using a Perkin Elmer UV-Vis spectrophotometer LAMBDA 35, monitoring the maximum absorbance at λ: 664 nm. The catalyst was added to the MB solution and, before irradiation, the suspension was equilibrated in the dark under magnetic stirring for 20 min. In the first kind of test, the sample was irradiated continuously, using solar simulated light (300 W - 16,6 W of UV - Osram Vitalux lamp, OSRAM) for 50 minutes; in the second one, the lamps was alternately switched on and off, for a period of time equal to 10 min for each interval, for a total time of 50 min. Later, the optimized catalyst was tested under simulated solar light (462 W/m^2 - 28 W/m^2 UV) for the degradation of ofloxacin (Sigma Aldrich, >99%). Tap water solutions of 100 mL were prepared at an ofloxacin concentration of 20 ppm, and 0,05 g of catalyst were added; after first 20 min of dark equilibration, the suspensions were subjected to alternate irradiation/darkness cycles, 10 min each. Ofloxacin was quantified by HPLC-UV, with a Shimadzu (Milan, Italy) LC-20AT solvent delivery module, equipped with a DGU-20A3 degasser and interfaced with an SPD-20A detector. The monitored λ was 275 nm. 20 μL of each sample were injected into a 250 x 4,6 mm, 5 μm Analytical Ascentis C18 (Supelco). The mobile phase was 25 mM H_3PO_4/ACN (85:15), at a flow rate of

1mL/min. All photocatalytic tests were performed in triplicate. Pictures of the samples irradiated for 5 min with solar simulated light, were collected with a Fujifilm – Finepix S1 set, with ISO equal to 12800 and acquisition time of 8 seconds.

In order to find out the best experimental conditions for the synthetic process of the photocatalytic material, a chemometric approach was chosen to evaluate the significance of the variables involved in the preparation procedure. A multivariate experimental 2^3 factorial design was carried out considering as variables: weight ratio TiO_2/PeL (X_1), temperature (X_2) and time (X_3). In table 1, the experimental domain comprised of the two levels for each variable is shown.

Table 1. Experimental Domain investigated in the Experimental Design 2^3 for $TiO_2/(3ZnO:Ga_2O_3:2GeO_2): Cr^{3+}$

Variable		Level codes	
		+1	*-1*
X_1	*$TiO_2/(3ZnO:Ga_2O_3:2GeO_2): Cr^{3+}$ wt. ratio*[a]	6	1
X_2	*Temperature (°C)*	550	350
X_3	*Time (h)*	6	1

[a]Amount of PeL: 0,5 g

Weight ratio equal to 1:1 was the minimum ratio required for the complete coverage of the support, while temperature interval was chosen considering that a treatment at 350 °C for at least 1 hour was necessary to guarantee the formation of crystalline anatase. Temperatures higher than 550 °C were not explored in order to avoid the phase transformation to rutile. Each sample was synthesized in triplicate and then tested on the photodegradation of MB solutions.

3.1.1.2. Results and Discussion

The photocatalytic activity results obtained from the synthesized samples are expressed as MB percentage degradation, calculate according to the subsequent equations, and shown in Table 2.

$$(Eq.\ \mathbf{25}) \qquad y[Abs] = 172{,}52\ \cdot x[{}^{g}/_{L}] + 0{,}1149$$

$$(Eq.\ \mathbf{26}) \qquad Degradation_{(t)}\ [\%] = [\frac{C_0 - C_t}{C_0}] \cdot 100$$

Table 2. MB percentage degradation obtained at different experimental conditions

Sample	X_1	X_2	X_3	MB Degradation (St. Dev) $^{n=3}$
1	-1	+1	-1	89 (2) %
2	-1	-1	-1	87 (1) %
3	-1	-1	+1	89 (6) %
4	-1	+1	+1	90 (4) %
5	+1	-1	-1	91 (1) %
6	+1	-1	+1	93 (2) %
7	+1	+1	+1	89 (7) %
8	+1	+1	-1	92 (3) %

According to the experimental results, a plot of the mathematical model's coefficients is elaborated, as numerical value per each variable in order to show their respective significance, and reported in Figure 12.

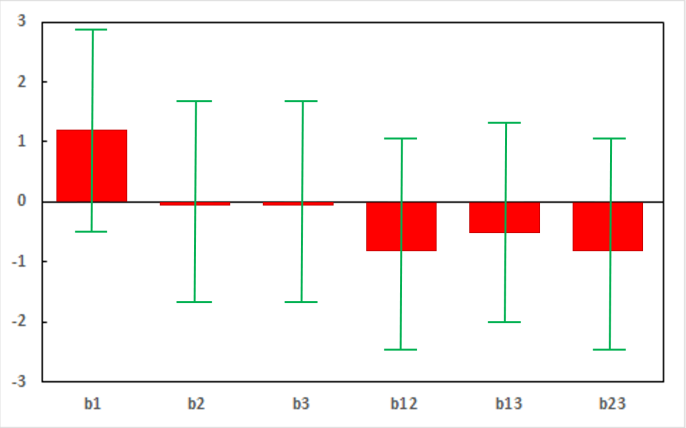

Figure 12: Plot of the coefficients of the model showing the significance of the variables considered in the chemometric study. Error bars indicate the confidence intervals at *p*=0,05

The responses were modelled according to the following equation:

$$y = b_0 + b_1X_1 + b_2X_2 + b_3X_3 + b_{12}X_1X_2 + b_{13}X_1X_3 + b_{23}X_2X_3 \quad \text{(Eq. 27)}$$

and the estimated coefficients' values of the model are reported in Table 3.

Table 3. Estimated coefficients of regression model for dependent variables. The significance of each coefficient was evaluated according to usual convention: *p<0,05, **p<0,01 and ***p<0,0001.

	Coefficient	St. Dev.
b_0	89.9	0.8
b_1	1.2	0.8
b_2	0	0.8
b_3	0	0.8
b_{12}	-0.7	0.8
b_{13}	-0.4	0.8
b_{23}	-0.7	0.8

As it is possible to see in Figure 12, the interaction among the variables was not significant: this suggest that the synthesis can be conveniently carried out at the low values of the variables reported in the experimental domain. Indeed, even working at the high value of X_1, the photocatalytic efficiency was slightly improved as can be observed from the MB percentage degradation surface responses reported in Figure 13. The model was validated on a test point (X_1=+1, X_2=0, X_3=0), chosen within the experimental domain, which shown a MB percentage degradation of 90 ± 6%, p=0,05, n=3, non-significantly different from that predicted according to the equation 27 with the estimated coefficients' values.

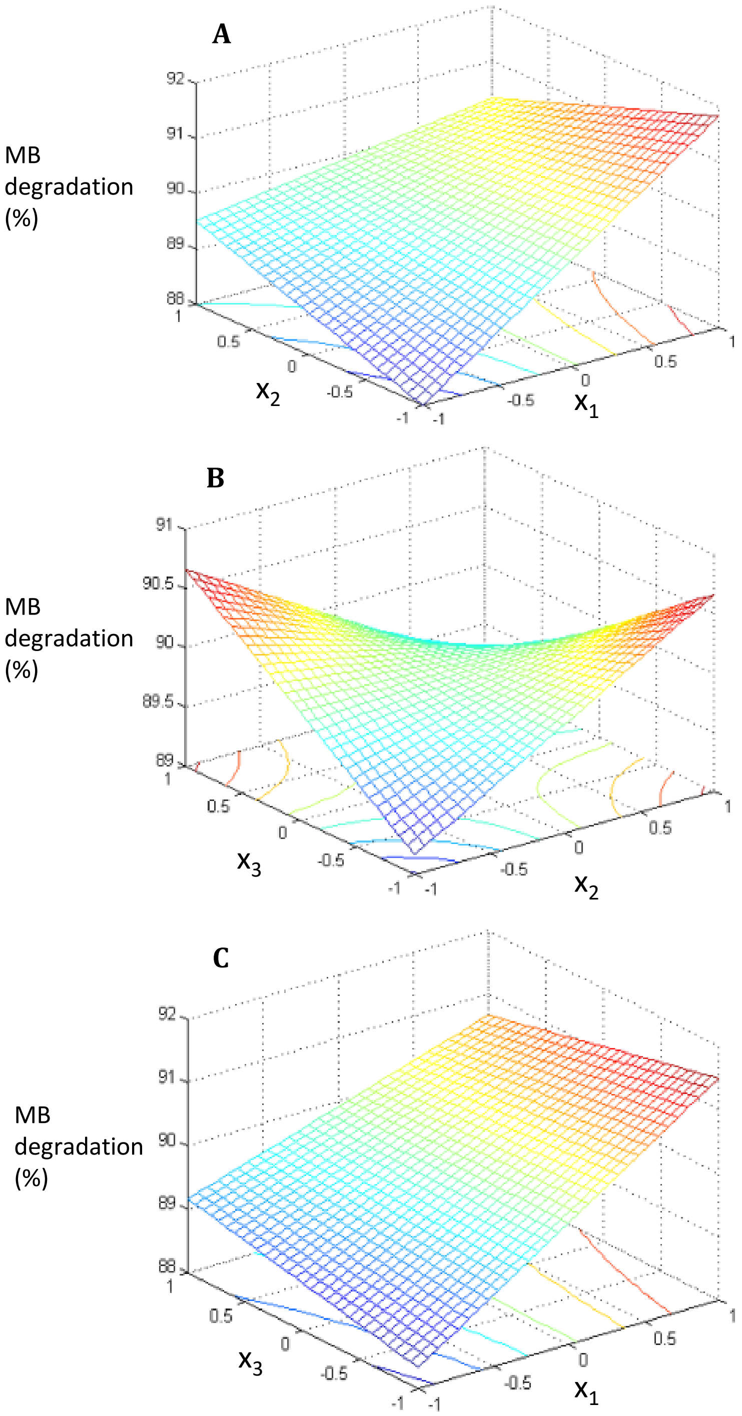

Figure 13: Response surfaces for the MB percentage abatement: a) y=f(X_1, X_2); b) y=f(X_2, X_3); c) y=f(X_1, X_3)

Thus, the optimum and most convenient sample is Sample 2, synthesized with the low values of each variable. It provides a MB percentage degradation of 87 ±

1% after 50 minutes of irradiation. As already mentioned, this sample was also subjected to alternate darkness/irradiation cycles and after this experiment the same percentage degradation was gained. This means that the PeL material can successfully emit photons during the darkness cycle which are subsequently absorbed by the photocatalyst. Three cycles were investigated to test the stability of the material and respectively, 87 ± 1%, 84 ± 1% and 88 ± 5% were obtained. Doubling starting MB concentration (to 0,02 g/L) led to a decrease of the activity of about 18% in the alternate experiments: this may be attributed to the higher absorbance of the MB solutions, which did not allow a full charge of the photoluminescence material. Moreover, for higher MB concentrations, it is reasonable to consider that the active surface sites are quickly saturated, resulting in a consequent loss in the efficiency.

In Figure 14 the XRD analysis of the Sample 2 is reported together with the experimental pattern of the PeL material and the reference anatase TiO_2 pattern. The optimized sample present both the characteristic peaks of anatase of PeL. Indeed, the signals of PeL are reasonably lower compared with the bare material, due to the effect of the presence of two crystalline phases in the composite as well as the covering of the support by TiO_2, which may smooth the intensity. It has to be noted that anatase experimental peaks show a broadening of FWHM due to the nanometric character.

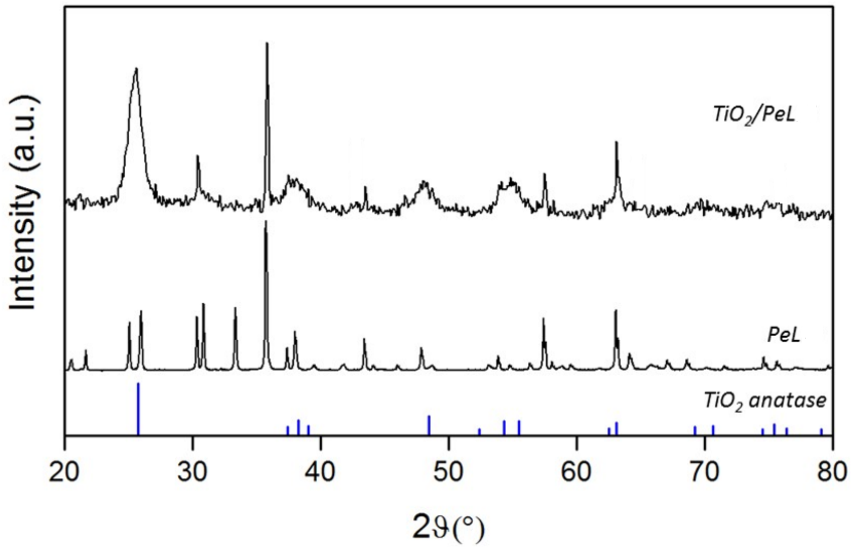

Figure 14: XRD spectra of the reference anatase TiO_2 (from Pearson's Crystal Data n° 1024705); PeL material (PeL) and Sample 2 (TiO_2/PeL)

As a further proof of the luminescence of the composite material, Figure 15 shows the behaviour of the luminescence properties of PeL and Sample 2. The latter shown a reasonable decrease in the recorded intensity, induced by the surface covering of TiO_2., which is also confirmed with SEM-EDS images, reported in Figure 16.

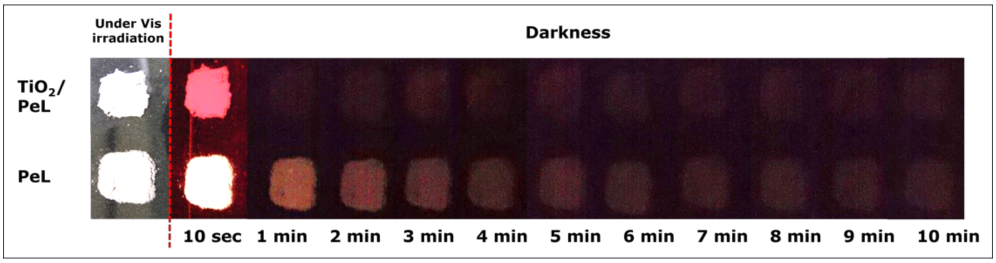

Figure 15: Behaviour of the emission intensity, in darkness, of the PeL material and of Sample 2 (solar simulated light excitation source). Pictures recorded with Fujifilm – Finepix

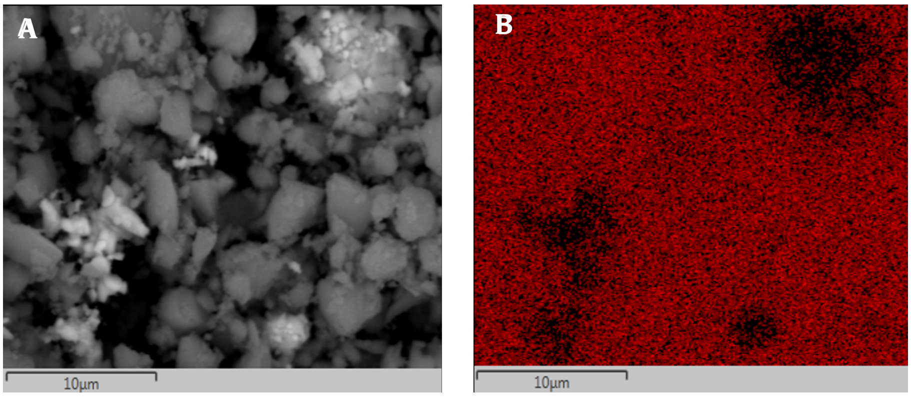

Figure 16: a) BSE image of a spot of Sample 2; b) EDS spectrum of Ti signal (red) recorded on the same spot

The morphology of the composite material results generally irregular, with micrometric particles dispersed in size, while TiO_2 coating, visible with the EDS map, results globally homogeneous and thick. BET analysis reported that the surface area of Sample 2 is equal to 62,49 ± 0,5 m^2/g. compared to previous results[90], this PeL material has a surface area of 4,49 ± 0,5 m^2/g while unsupported TiO_2 treated with the same synthetic conditions shown a surface area of 88,64 ± 0,5 m^2/g. The material provides a better photocatalytic performance due to the presence of the persistent luminesce material, and, at the same time, retains a consistent surface area, which is very important for heterogeneous processes.

Eventually, the optimized catalyst was tested for the degradation of ofloxacin in tap water under simulated sunlight irradiation. Ofloxacin, as a fluoroquinolone antibiotic, was chosen for this test as it's one of the emerging pollutants reported in the Watch List[91]. For 20 minutes, the pollutant solution is left equilibrating under magnetic stirring in the dark, where an absorption of about 26% of the initial concentration occurred onto catalyst's surface. Immediately after, the solution is subjected to 10 minutes of solar light irradiation followed by 10 minutes of dark conditions (switching off the solar box). When subjected to alternate irradiation/darkness cycles, ofloxacin was degraded as shown in Figure 17.

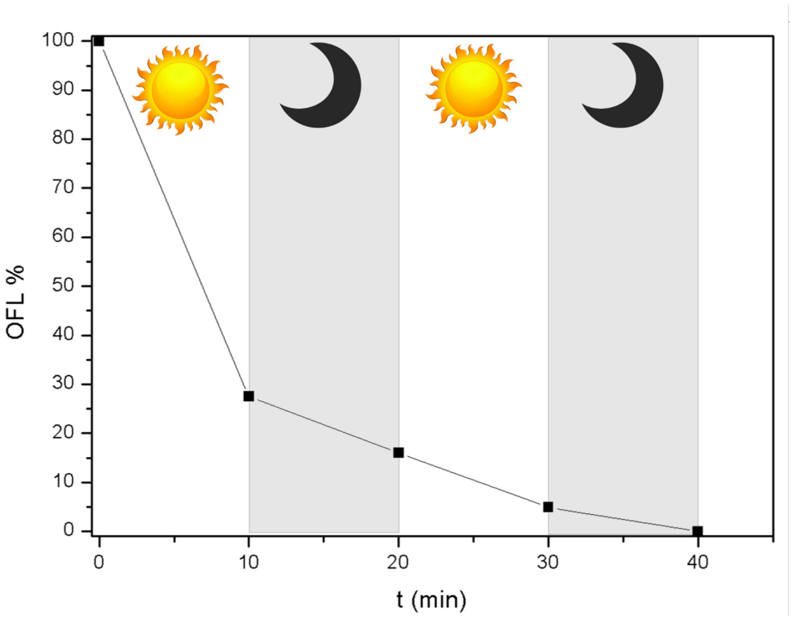

Figure 17: Degradation profile of ofloxacin (20 ppm, 0,5 g/L catalyst) under alternate sunlight/darkness cycles

The antibiotic was quantitatively degraded in just 30 minutes, whose 20 of solar light irradiation and 10 of darkness. According to previous results, in order to reach the same degradation value but without the photocatalyst (thus just a photolysis experiment), 110 minutes of direct solar light irradiation were required.

3.1.1.3. Conclusions

A new photocatalytic material based on TiO_2 nanoparticles and supported on a PeL material was synthesized and optimized by a chemometric approach. The activity of the composite systems was tested for the abatement of methylene blue as well as ofloxacin solutions. The optimized sample reached the highest percentage degradation values for the most convenient synthetic conditions after 50 minutes of irradiation and with alternate dark/light cycles. These results demonstrated the potential applicability of this system when no external irradiation can be provided (during the night or in very turbid solutions, e.g. wastewaters).

3.1.2. $CaAl_2O_4$: (La, Nd)$^{3+}$

In order to test a commercial PeL material as a replacement of the synthetic one, the following project was carried out. The $CaAl_2O_4$: (La, Nd)$^{3+}$ PeL material was chosen for its theoretical compatibility between its emission (2,25 – 3,25 eV, corresponding to 551 – 381 nm) and bare anatase TiO_2 absorption. The main aim was to use a greener material, with a different chemical composition, in order to have an eco-friendlier material with the same efficiency in dark conditions highlighted in the previous section. Samples were synthesized according to a chemometric approach 2^3, similar to the one described in Chapter 3.1.1.2.; each sample was tested on its photocatalytic efficiency with kinetic experiments on the percentage degradation of methylene blue solutions and the resulting optimized sample was characterized by means of XRD, SEM-EDS, BET and DLS analyses.

This Project was designed in collaboration with the research group of M. Sturini (University of Pavia).

3.1.2.1. Materials and Methods

PeL commercial material was purchased from Bright Material S.R.L. (Italy) and used without further purifications. TiO_2 was similarly synthesized through the sol-gel synthesis, with 2-Propanol, TTIP and deionized water in a volume ratio respectively of 2:1:5, left under vigorous magnetic stirring for 4 hours and eventually dried in an oven, at 105 °C or 12 hours. Once dried, the xerogel is grinded in an agate mortar and mixed in 20 mL of water with the PeL material powders before being treated in the muffle furnace. According to the chemometric model, the synthesis was designed to monitor the weight ratio, the heating temperature and the treatment time.

After the validation of the model, the resulting optimized sample was physical-chemically characterized: phase identification was performed with a Philips PW1830 Diffractometer (Bragg-Brentano geometry, Co K_α, Ni filtered, range 10-80 2θ, step 0,04 2θ, sampling time 8 s), SEM-EDS images were collected using a Tescan Vega 3 MXL microscope with EDS (Oxford X-Max) and software Aztec 2.4. Brunauer-Emmet-Teller analysis was carried out using an ASAP 2020 Plus 2.00 physisorption porosimeter (Micromeritics Instrument Corp., Norcross, GA, USA). Before the measurement, the sample was pre-treated at 200 °C under vacuum for 12 hours. Dynamic light scattering analyses were acquired with a Zetas Sizer Instrument, Nano Series, working with laser He-Ne at 633 nm, at the temperature of 25 °C and equilibrating time 120 s. Radiation was collected at 90° in triplicate for each sample.

Photocatalytic activity was investigated by testing the percentage degradation of 25 mL of a 0,01 g/L MB solution, in presence of 0,0125 g of photocatalyst. MB was quantified using a Perkin Elmer UV-Vis spectrophotometer LAMBDA 35 (Perkin Elmer, Whaltam, MA, USA), monitoring the λ: 664 nm. Samples were irradiated using solar simulated light (300 W, 16,6 W of UV, Osram Vitalux lamp, OSRAM) placed at 20 cm above the solutions, for 60 minutes.

In order to find out the best experimental conditions for the synthetic process of the photocatalytic material, a similar chemometric approach was chosen to evaluate the significance of the variables involved in the preparation procedure. A multivariate experimental 2^3 factorial design was carried out considering as variables: weight ratio TiO_2/PeL (X_1), temperature (X_2) and time (X_3). In table 4, the experimental domain comprised of the two levels for each variable is shown.

Table 4. Experimental Domain investigated in the Experimental Design 2^3 for $TiO_2/CaAl_2O_4$: *(La, Nd)*$^{3+}$

Variable		**Level codes**	
		+1	*-1*
X_1	*$TiO_2/CaAl_2O_4$: (La, Nd)$^{3+}$ wt. ratio*^{a}	6	1
X_2	*Temperature (°C)*	550	350
X_3	*Time (h)*	6	1

^{a}Amount of PeL: 0,5 g

3.1.2.2. *Results and Discussion*

The photocatalytic activity results obtained from the synthesized samples are expressed as MB percentage degradation and shown in Table 5.

Table 5. MB percentage degradation obtained at different experimental conditions

Sample	**X_1**	**X_2**	**X_3**	**MB Degradation (St. Dev)** $^{n=3}$
1	+1	+1	+1	100 (1) %
2	+1	+1	-1	98 (2) %
3	+1	-1	+1	93 (3) %
4	-1	+1	+1	53 (2) %
5	+1	-1	-1	93 (1) %
6	-1	+1	-1	58 (2) %

7	-1 -1 +1	52 (5) %
8	-1 -1 -1	53 (4) %

Experimental data were preliminarily elaborated according to the equation 27 reported in the previous chapter and according to the obtained results, the significance of the coefficients is similarly reported in Figure 18:

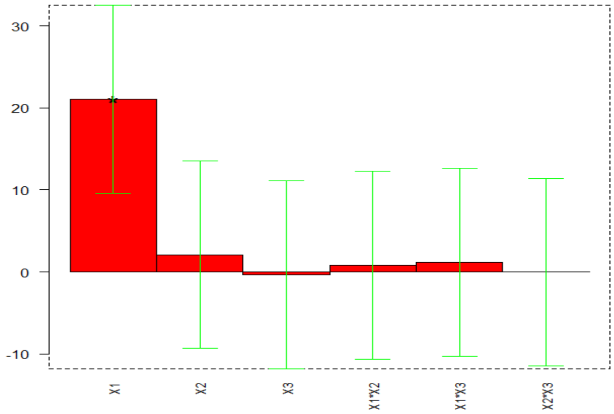

Figure 18: Plot of the coefficients showing the significance of the variables. Confidence interval at *p=0,05

In table 6 the estimated coefficients' values are reported.

Table 6. Estimated coefficients of regression model for dependent variables

	Coefficient	**St. Dev.**
b_0	75,3	0.9
b_1	21,05	0.9
b_2	2,1	0.9
b_3	-0,3	0.9
b_{12}	0,8	0.9
b_{13}	1,1	0.9
b_{23}	-0,04	0.9

The significance of each coefficient was evaluated on usual convention: *p<0,05

Samples 1, 2, 3 and 5 present the highest percentage degradation values among all the synthesized samples as they were synthesized with the highest level of X_1 variable. This variable is strongly significant over the synthesis of this material. It is noteworthy to say that samples with X_1=-1 shown a linear decay over time, resembling a zero-order kinetic while opposite samples shown an exponential decay, suggesting a change in the kinetic behaviour to a first-order or pseudo first-order kinetic.

A test point (X_1=0, X_2=0, X_3=0) was synthesized and tested, in order to compare the theoretical value obtained from the preliminary evaluation to the experimental one, and the experimental degradation reached 80 ± 10%, with respect to the calculated 70 ± 5%. Hence it was possible to state that the optimum and most convenient sample is Sample 5, synthesized with the low values of each non-significant variable; it provides a MB percentage degradation of 93 ± 1% after 60 minutes of irradiation.

Unfortunately, from the dark/light cycles experiments, it was demonstrated that halving the irradiation time led to a decrease of the percentage degradation value for the optimized sample: this suggests that, during darkness cycles, the PeL material doesn’t provide the necessary photons for the activation of the photocatalyst, hence it results to be inactive towards the degradation of MB. In order to investigate the physical-chemical properties of the composite material and in order to justify the absence of activity during dark conditions, the optimized sample was subjected to some characterization techniques.

Surface responses of y (MB percentage abatement) as function of (X_1, X_2, X_3) are reported in Figure 19:

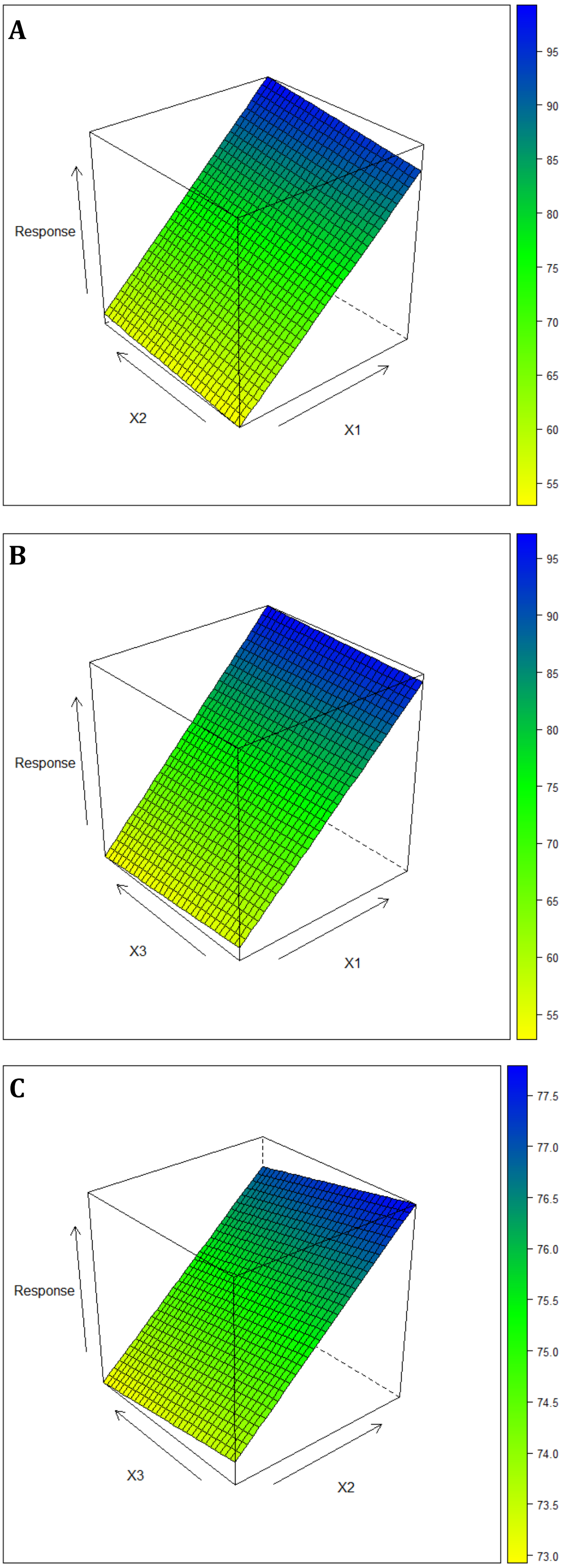
A
Response
X2
X1
95
90
85
80
75
70
65
60
55
B
Response
X3
X1
95
90
85
80
75
70
65
60
55
C
Response
X3
X2
77.5
77.0
76.5
76.0
75.5
75.0
74.5
74.0
73.5
73.0

Figure 19: Response surfaces for the MB percentage abatement: a) $y=f(X_1, X_2)$ and $X_3=0$; b) $y=f(X_1, X_3)$ with $X_2=0$; c) $y=f(X_2, X_3)$ and $X_1=0$

SEM-EDS analyses were performed on the PeL material (treated with the same conditions of Sample 5), as a comparison, and on the optimized sample. These results are reported in Figure 20 and Figure 21.

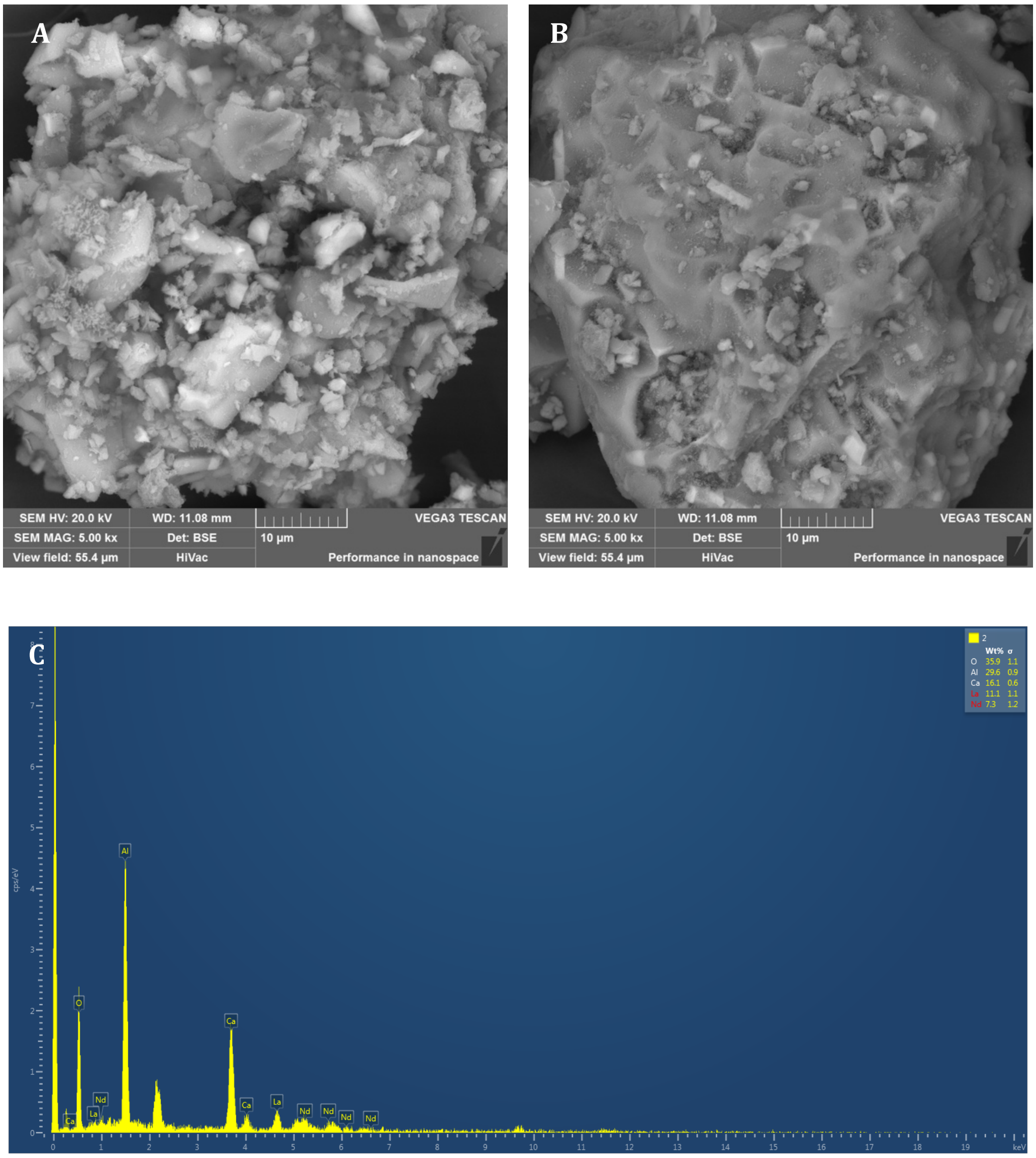

Figure 20: a) SEM image of PeL (5000x, marker 10 μm); b) SEM image of PeL (5000x, marker 10 μm); c) EDS spectrum of PeL (referred to 20a)

From SEM characterization, it is possible to state that the supporting material has a micrometric nature, ranging from tens to hundreds of micrometres. Morphological aspect resembles a typical ceramic aspect, quite irregular, sometimes spongy and filamentous, where particles of very different dimensions are agglomerated together. From EDS spectrum it was possible to confirm the PeL composition, which is made of Ca, Al and O with La and Nd as luminescent dopants (red sign is referred to the proximity to the detection limit).

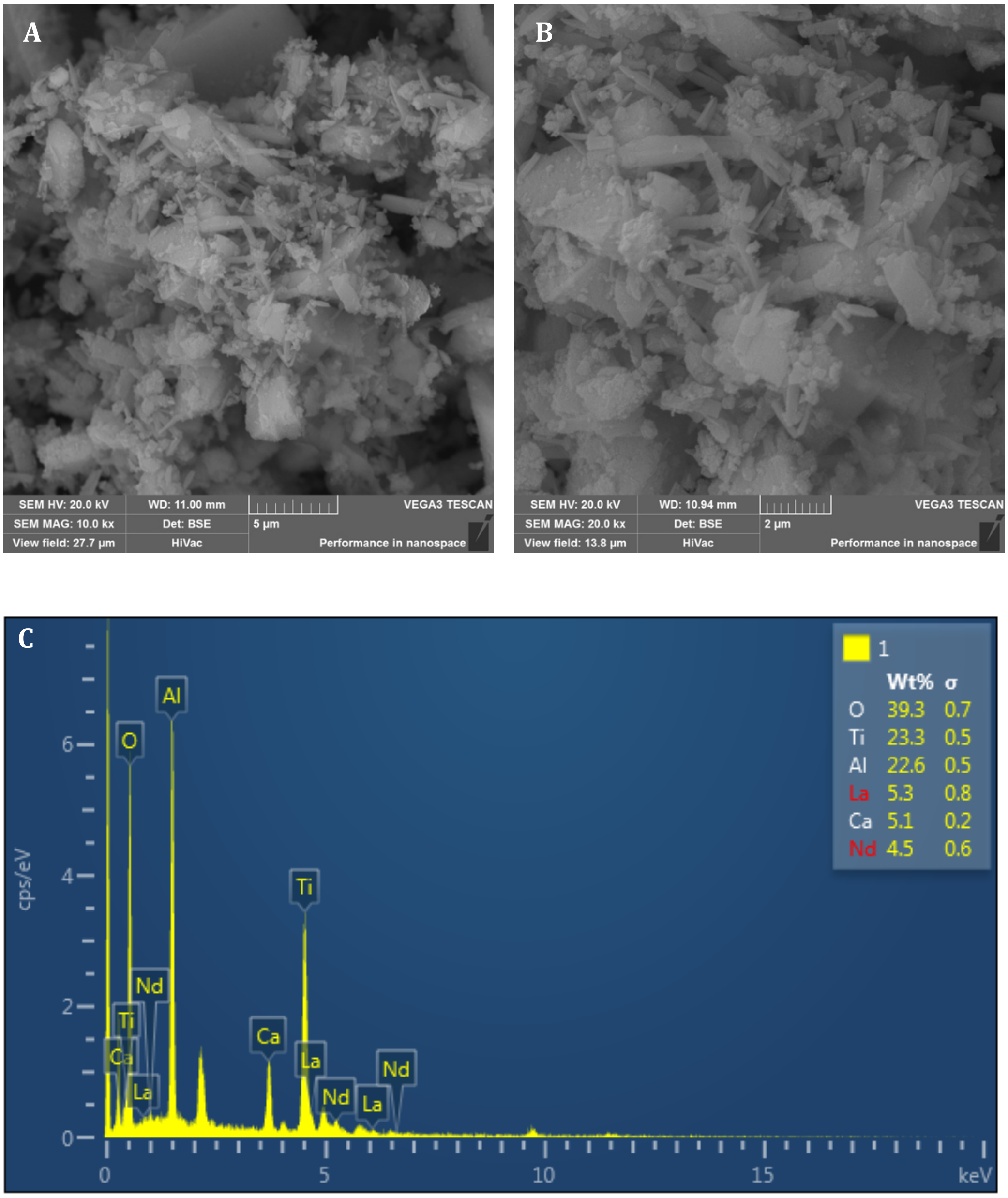

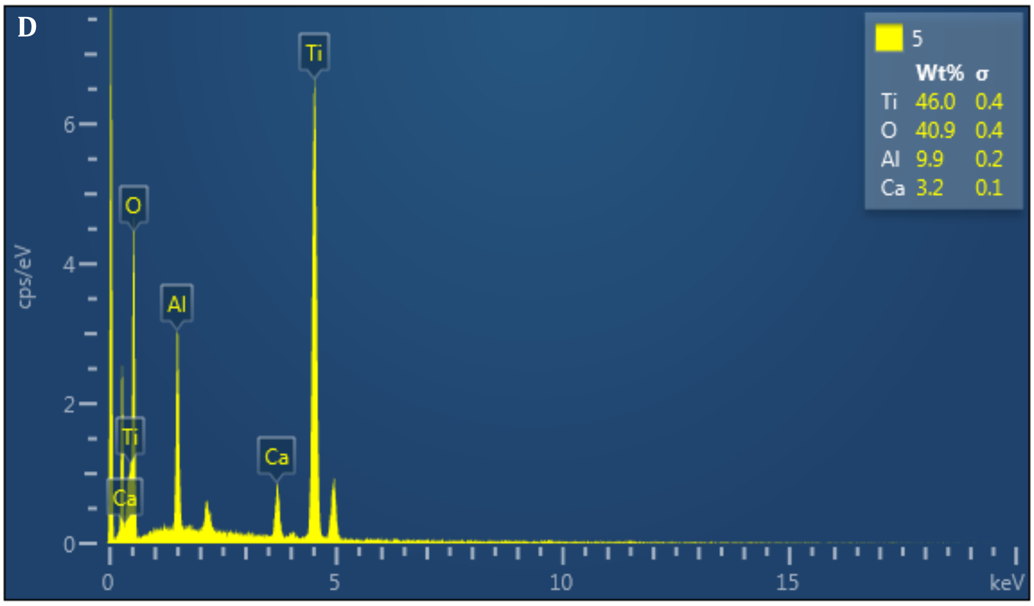

Figure 21: a) SEM image of Sample 5 (10000x, marker 5 μm); b) SEM image of Sample 5 (20000x, marker 2 μm); c) EDS spectrum of Sample 5 on spot 1 (referred to 21a); d) EDS spectrum of Sample 5 on spot 5 (referred to 21a)

Overall morphology of Sample 5 is essentially the same; it is possible yet to distinguish a fraction of smaller particles, with dimensions lower than 1 μm, pretty likely attributable to TiO_2. Elemental analysis confirmed the presence of Ti, O, Ca and Al as main components of the sample (as expected) but with non-neglectable differences in the weight fraction. This fact may be due to an undesired reaction between the support and the photocatalyst, for the diffusion of TiO_2 in the supporting matrix. In order to attribute the change in Ti weight fraction to the undesired reaction, and thus to confirm the hypothesis that the loss of photocatalytic efficiency during the dark conditions could be attributable to a change in the luminescence properties, an XRD characterization was performed. In Figure 22, the XRD patterns of Sample 5, Sample 8 (with X_1=-1), unsupported TiO_2 and PeL are shown while in Figure 23, XRD patterns of untreated and heat treated PeL and Sample 8 are reported.

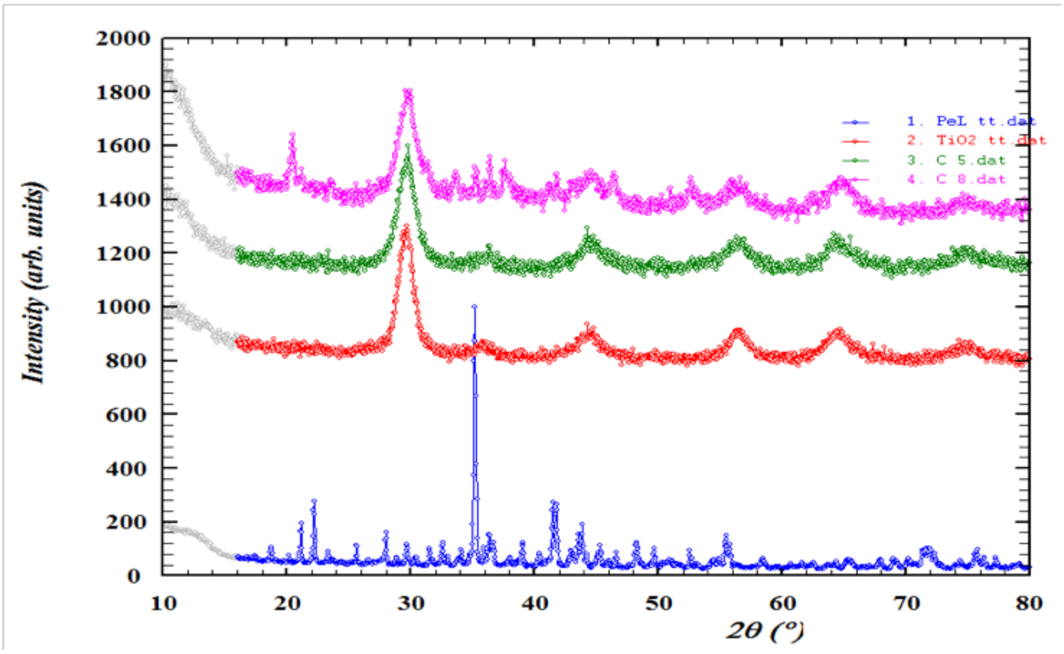

Figure 22: XRD spectra of Sample 8 (purple), Sample 5 (green), unsupported TiO_2 (red) and PeL (blue)

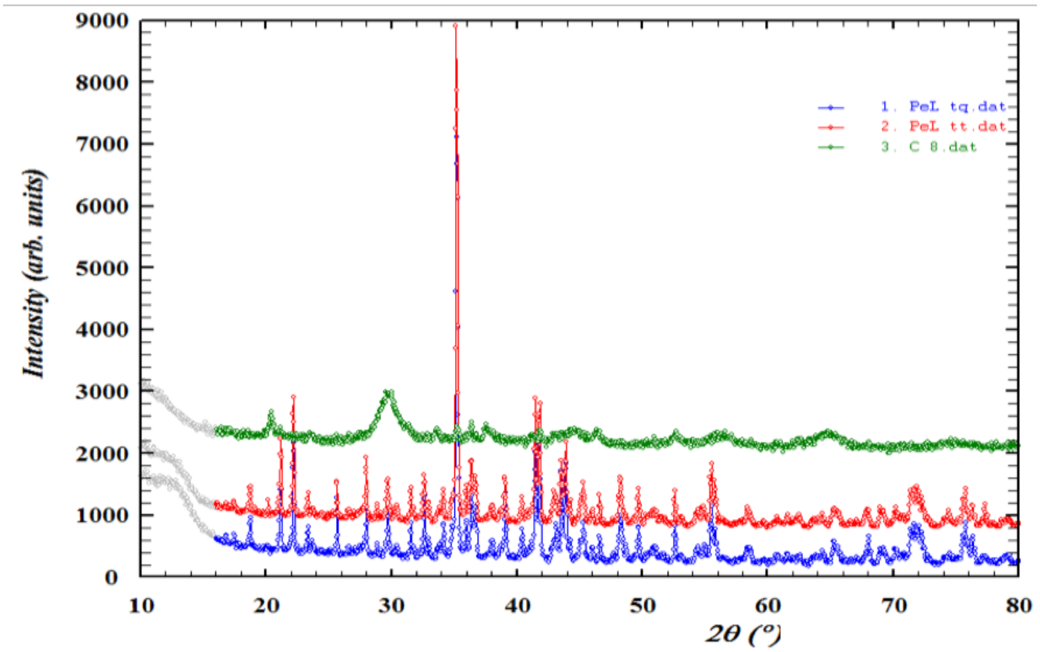

Figure 23: XRD spectra of Sample 8 (green), heat treated PeL (red) and untreated PeL (blue)

From this characterization arises that Sample 5 (X_1=+1) is extremely similar to the pattern of unsupported nanometric TiO_2 (for a wide range of HWFM) while Sample 8 (X_1=-1) pattern shows some extra peaks apart from the anatase ones. These peaks are not comparable with the bare PeL, whose peaks seems to be completely lost after the supporting synthesis (especially the characteristic peak, the most intense). This means that, if the PeL material is heat treated alone, its crystalline structure is not affected at all but, if the material is coupled with TiO_2 at least for the investigated conditions, the crystalline composition of the matrix is strongly affected while the unreacted TiO_2 is still present as anatase nanoparticles.

The optimized sample was subjected to a surface area measurement, which reported a value of 199,8470 ± 0,5 m^2/g. In comparison with general solid-state synthesized samples, this high value of surface area surprises. From SEM images it was possible to note a fine particles fraction in the surface and thus the high BET value should be attributable to this particular feature.

As last characterization, hydrodynamic radius in aqueous suspensions was measured with Dynamic Light Scattering experiments for Sample 5, Sample 8 and bare TiO_2. Results are shown in Table 7.

Table 7. Hydrodynamic radius of Sample 5, Sample 8 and bare TiO_2 in diluted aqueous suspension

	Sample 5	*Sample 8*	*Unsupported TiO₂*
Mean Radius (nm)	102.0	233.3	295.3
St. Dev	19	78	3
P. D. I.	1.000	1.000	0.575

From this analysis, it was possible to draw some conclusions: Poly Dispersion Index “P. D. I.” values are quite high for composite samples, in particular they are equal to 1, sign that the sample is very dispersed in terms of the hydrodynamic radius of suspended aggregates. This may be related to the hand-grinding process in the agate mortar, which evidently brought to a variable range of dimensions (also confirmed by SEM characterization). Furthermore, during the sample preparation for DLS measurements, it was possible to see by eye bigger particles settling down the cuvette. For this reason, it is possible to understand and justify the high P. D. I. value. Once stated the difference in aggregates dimensions, it is also possible to conclude that the bigger fraction of particle has a radius bigger than 10 μm, and this fraction may be related to the composite sample. The smaller fraction of particles is quite likely attributable to unreacted TiO_2, which is stable in a colloidal suspension in aggregate of 300 nm approximately, as visible in Table 7, and composed of small nanoparticles (as suggested from XRD patterns).

3.1.2.3. Conclusions

During this project, a chemometric approach was used to investigate the synthesis of a composite material based on TiO_2 supported on a commercial PeL material. By means of MB degradation, it was possible to highlight the importance of the TiO_2/PeL weight ratio: the best and most convenient sample was Sample 5. During darkness experiments, the experimental outcome highlighted that the supporting material was not able to provide photons to the catalyst, quite likely for the undesired reaction occurred between PeL and TiO_2, evidenced from XRD analysis, which modified the crystalline structure of the composite. Surprising was that the surface area is extremely high, considering that a solid-state synthesis was used, and it may be attributable to the formation of the new crystalline phase on the interface between the support and the catalyst.

3.1.3. *Composite Photocatalysts based on TiO_2/ZnO/PeL*

As a further test on the ability of a PeL material to provide photons to a photocatalyst in absence of an external excitation source, another three-components composite material was projected, based on TiO_2 nanoparticles, ZnO nanoparticles[92,93] and micrometric PeL ($3ZnO:Ga_2O_3:2GeO_2$): Cr^{3+}. The following data are part of a preliminary consideration: the synthesis was not optimized through a chemometric approach and the significance of the synthetic variables was not evaluated. TiO_2 was synthesized trough a sol-gel synthesis, using (2-Propanol:TTIP:H_2O) in a volume ratio of (2:1:5). After 4 hours of magnetic stirring, the gel is dried in an oven for 12 hours at 105 °C and eventually grinded in an agate mortar. ($3ZnO:Ga_2O_3:2GeO_2$): Cr^{3+} is synthesized through a solid-state reaction, by mixing precursors powders (as described in Chapter 3.1.1.1.) and heat treated in a muffle furnace for 2 hours at 900 °C and for other 2 hours at 1100 °C. The preparation of ZnO nanoparticles was performed by the research group of Professor D. Comoretto, Industrial Chemistry Section of University of Genova, according to the following solvothermal process[94]: a methanol solution of KOH and zinc acetate is heated at 63 °C and sonicated for 3 hours. After this time, crystalline ZnO nanoparticles are formed, then purified by five cycles of settling/washing with methanol and finally fried. Composite samples were prepared trough a solid-state treatment in a muffle furnace for 1 hour at 450 °C, changing the weight ratio of each component and preliminary results on the photocatalytic efficiency obtained from the degradation of a 0,01 g/L MB solution under 40 min of solar simulated light irradiation are reported in Table 8 ((a) refers to continuous irradiation; (b) refers to darkness/light cycles)

Table 8. Synthesized samples of TiO_2/ZnO/PeL and MB percentage degradation

Sample	wt. Ratio	% Degradation (a)	% Degradation (b)
ZnO+PeL	1:1	98.8 ± 0.04	81.3 ± 1.4
ZnO+TiO_2+PeL	0,75:0,25:1	96.4 ± 2.7	70.4 ± 7.2
ZnO+TiO_2+PeL	0,5:0,5 :1	94.8 ± 0.2	77.7 ± 3.4

ZnO+TiO_2+PeL	0,25:0,75:1	90.0 ± 4.9	67.0 ± 5.9
TiO_2+PeL	1:1	87.1 ± 1.0	68.8 ± 4.7

It is noteworthy that the degradation in alternate dark/light conditions was good, underlining that supported samples with increasing amount of ZnO resulted to be more efficient with respect to the TiO_2. This fact may be related to the lower E_g value of ZnO (ca. 3 eV) or to the smaller particles' dimensions. As a comparison, a new synthetic method was tested to get ZnO nanoparticles: in particular, a zinc nitrate hexahydrate aqueous solution is prepared at a concentration of 5,78 M as well as a citric acid solution at 0,78 M. Both solutions are heated up to 70 °C for 30 min, under magnetic stirring, and then the zinc nitrate solution is slowly poured into the citric acid one. The mixture is left under stirring until thickening, later dried in an oven at 105 °C for 12 hours and finally treated in muffle furnace for other 12 hours at 500 °C.

As an earliest comparison, the photocatalytic efficiency of ZnO containing samples was tested, and with similar TiO_2 and PeL composition, ZnO from citric acid route resulted to be more efficient than the zinc acetate route.

Hence, a SEM-EDS characterization of the two ZnO samples is reported in Figure 24 and Figure 25.

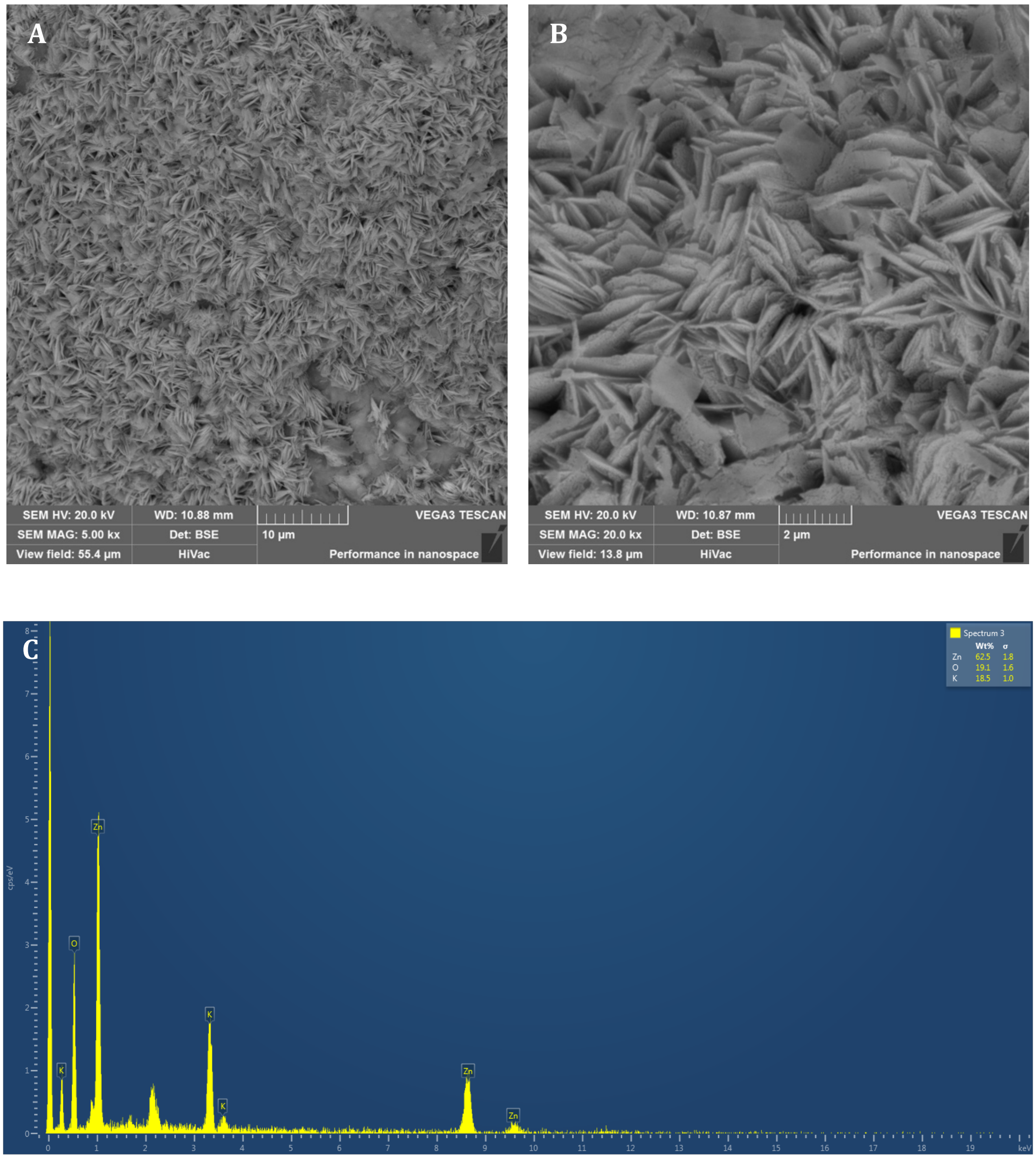

	Wt%	σ
Zn	62.5	1.8
O	19.1	1.6
K	18.5	1.0

Figure 24: a) SEM image of ZnO – zinc acetate route (5000x, marker 10 μm); b) SEM image of ZnO – zinc acetate route (20000x, marker 2 μm); c) EDS spectrum of ZnO – zinc acetate route on spot 3 (referred to 24a)

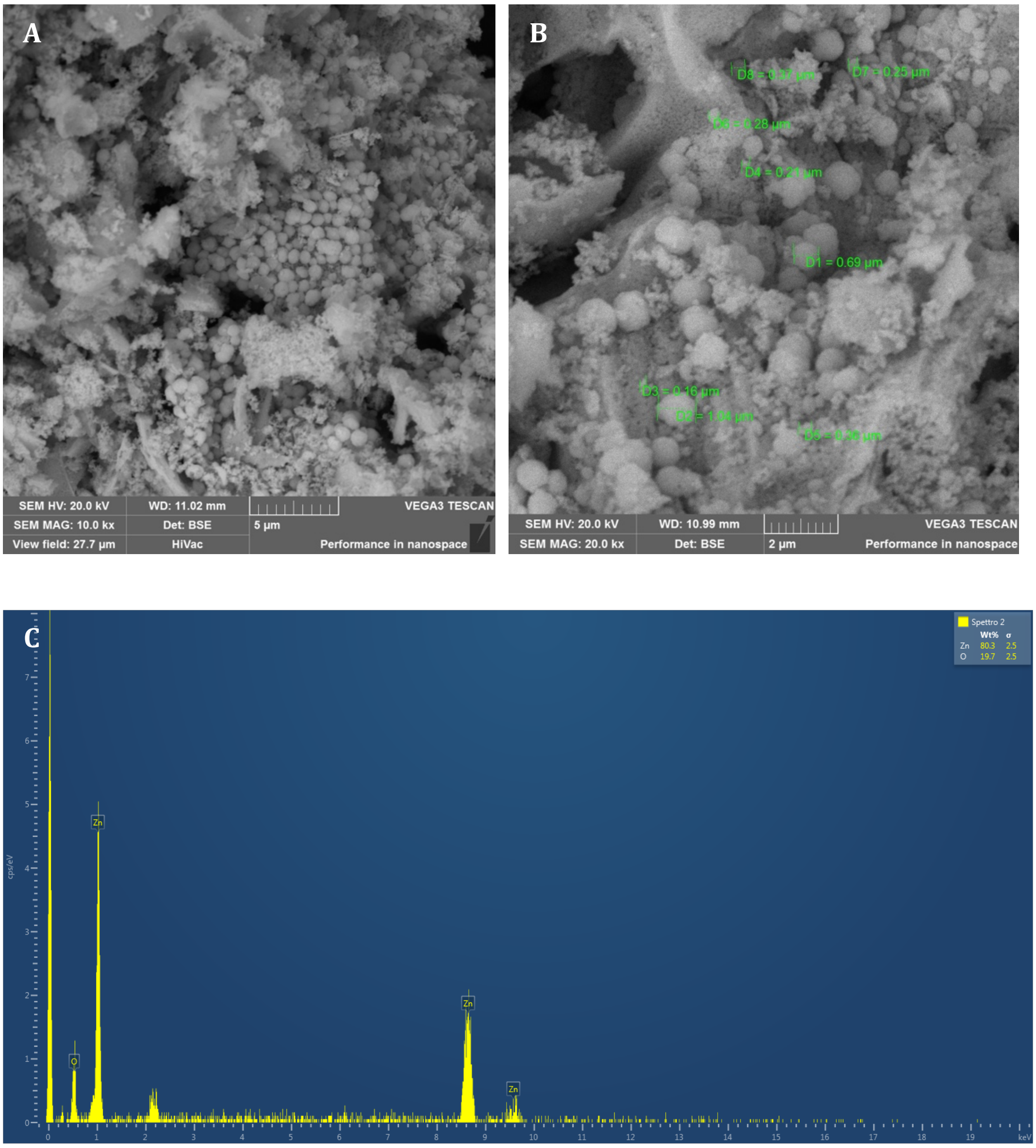

Figure 25: a) SEM image of ZnO – citric acid route (10000x, marker 5 μm); b) SEM image of ZnO – citric acid route (20000x, marker 2 μm) with particles' dimension markers; c) EDS spectrum of ZnO – citric acid route on spot 2 (referred to 25a)

Elemental composition confirms that the citric acid route leads to a homogeneous composition of Zn an O, without the presence of any other impurity, while ZnO – zinc acetate route still presents K impurity due to the synthetic process. The shape of the particles is noteworthy, because the first heat treatments led to a specific platelet arrangement, randomly distributed, with very thin edges showing nanometric to micrometric dimensions, while the second one led to specific spherical shapes, with the same dimensional range (mostly nanometric). Thus, the better photocatalytic efficiency may be imputable to the spherical shape of the second synthetic route. ZnO – citric acid dimensions were confirmed with a DLS test, which reported a mean radius included between 100 and 200 nm, visible in Figure 26.

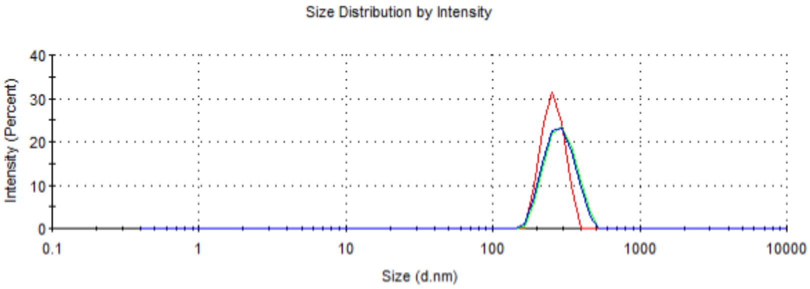

Figure 26: Hydrodynamic radius of ZnO – citric acid route

This part of the research is still ongoing; the presented results are not complete, they need to be widely integrated with further kinetic experiments as well as physical-chemical characterization, in order to be able to get useful information and draw important conclusions. This material was intended to be used in a pilot plant prototype, to test the efficiency of the sample in dark working conditions, aiming for real industrial applications.

3.1.4. Pilot Plant Prototype

As the industrial scale-up of photocatalytic materials was one of the aims of this project, a pilot plant prototype was built to perform preliminary experiments on the efficiency of different catalysts in order to find out the optimal working conditions. This pilot plant, with a processing volume of 1 L, is shown in Figure 27.

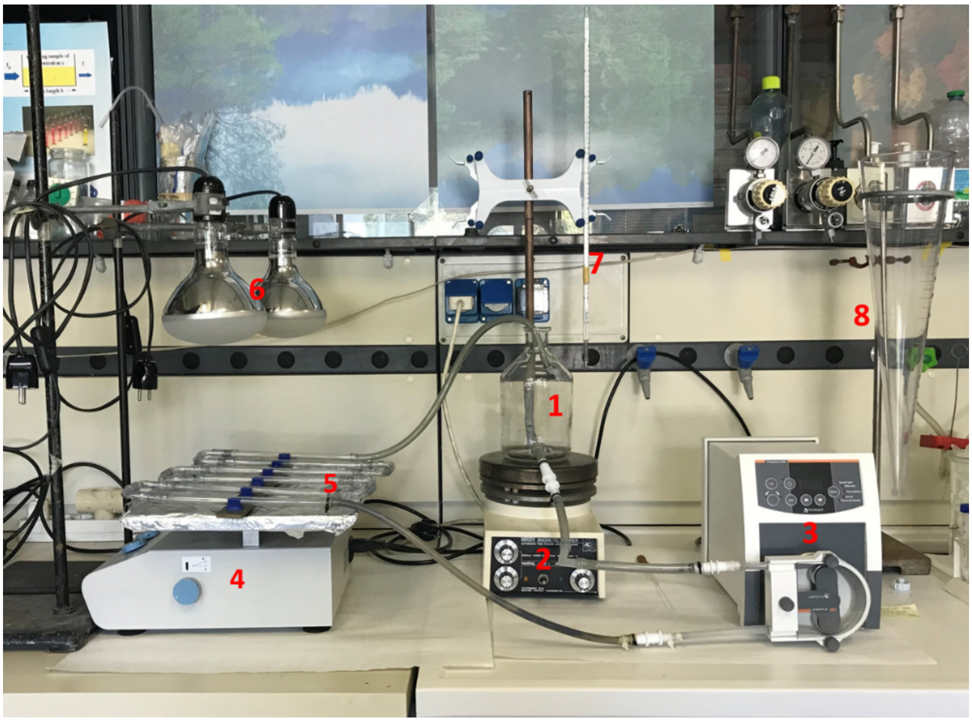

Figure 27: Pilot plant prototype for water treatment

Referring to Figure 27, the description of the apparatus is as follows:

1- 1 L Container

2- Magnetic Stirrer

3- Peristaltic Pump (flow's range from 0,1 to 3,5 L/min)

4- Rocking Plane

5- Glass Coil

6- Solar Simulated Light Lamps

7- Thermometer

8- Imhoff Cone for Settling

The solution to be treated is poured into the container together with the photocatalyst's powders and left during all the experiment under magnetic stirring. The peristaltic pump pushes the solution through the glass coil, which is irradiated with the lamps, placed at 20 cm from it. The glass coil is placed onto a rocking plane, in order to promote the circulation of the suspension. Eventually, the solution is back again in the container in a close circuit. A thermometer allows the temperature control over the experiment duration while the Imhoff cone can be used to recover the photocatalyst and evaluate its settling rate and yield.

3.1.5. Photocatalyst Recovery at pH_{IEP}

This project was performed in collaboration with the research group of Dr. M. O. Amin, of the Department of Chemistry at the University of Kuwait. All the reported data have not been published yet.

Considering the surface charge of TiO_2, it is useful to know the so-called Iso-Electric Point, which corresponds to the pH value of the solution in which TiO_2 is suspended, for which the concentration of OH^- is equal to that of H^+. In these conditions, the colloidal suspension of the catalyst becomes unstable, hence it tends to settle down faster[95]. Otherwise, in other pH conditions, the surface concentration of OH^-/H^+ is unbalanced and so the colloidal suspension remains stable, for charge interactions with the solvent. The possibility to reach pH_{IEP} conditions would lead to the quantitative recovery of the suspended catalyst by just the pH modification of the solution, without the need to support the catalyst on any material. In actual water treatment plants, pH modifications are already used, so it would be reasonable to add the photocatalytic treatment before and then take advantage of the pH modification to recover and reuse the catalyst.

Some TiO_2 based materials were analysed on their pH_{IEP} by means of electrophoretic mobility, later transformed in zeta Potential "ζ" values, with a Zeta Sizer Nano ZS DLS (Malvern Instruments Ltd, Malvern, UK) and on their settling rate, using a Turbidimeter (Turb 550, WTW, Germany) which measures the opacity of the solution and relates it to the presence of suspended solids. Some of the samples subjected to this kind of evaluation are reported in Table 9.

Table 9. Synthetic parameters of samples investigated for pH_{IEP} recovery

Sample	**Composition**	**% wt. Ratio**	**Synthesis**	**Synth. Conditions**
2	TiO_2+PeL*	1:1	Hydrothermal	100 °C – 6 h
3	TiO_2	/	Solid-state	350 °C – 1 h
4	TiO_2+PeL*	1:1	Solid-state	350 °C – 1 h
5	ZnO+TiO_2+PeL*	0,5:0,5:1	Solid-state	350 °C – 1 h

*0,5 g of ($3ZnO:Ga_2O_3:2GeO_2$): Cr^{3+}

Settling efficiency and pH_{IEP} for the investigated samples are reported in Table 10, while turbidity (Nephelometric Turbidity Units “NTU” vs. Time) behaviours are reported in Figure 28.

Table 10. pH_{IEP}, recovery efficiency and recovery time

Sample	**pH_{IEP}**	**Recovery Efficiency (%)**	**Recovery Time (10^3 s)**
2	7,37	85,1	175 (complete in 2 days)
3	8,19	97,3	88,7 (complete in 1 day)
4	5,31 – 6,29 – 6,78	93,3	88,7 (complete in 1 day)
5	5,11 – 5,98 – 7,67	99,3	88,7 (complete in 1 day)

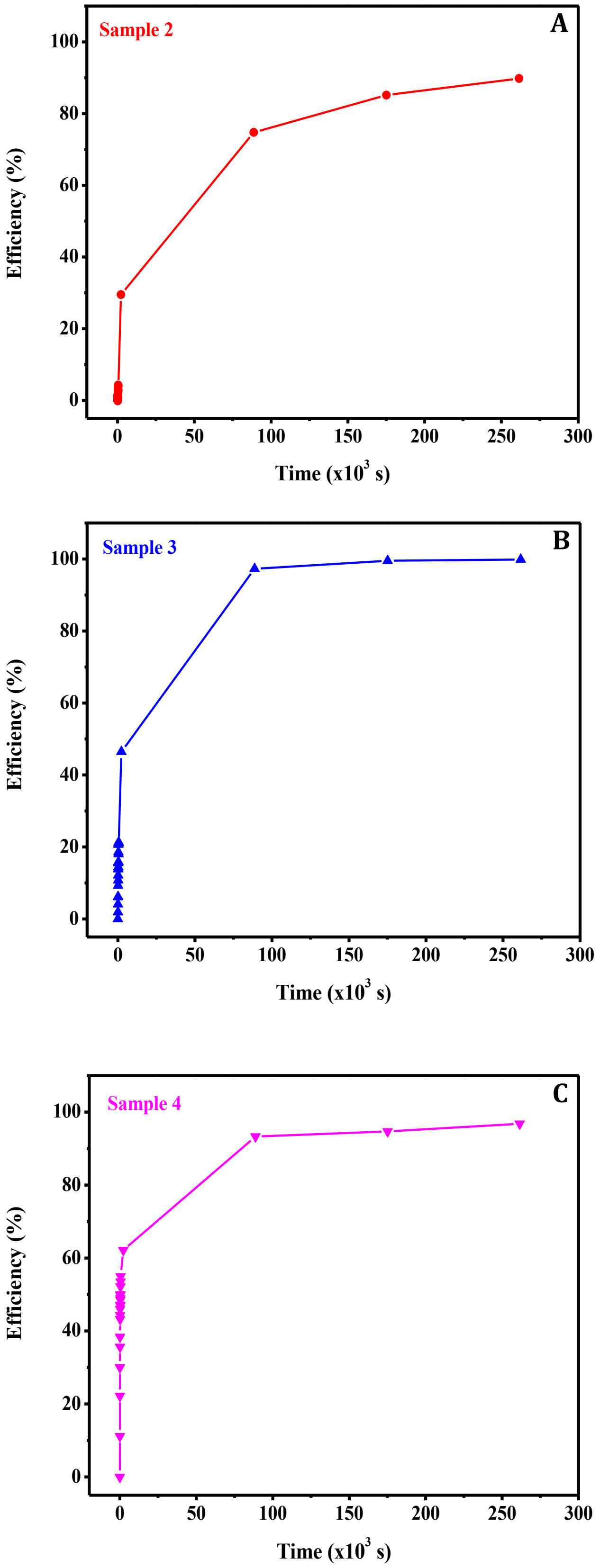
Sample 2
A
Efficiency (%)
0
20
40
60
80
100
0
50
100
150
200
250
300
Time (x10^3 s)
Sample 3
B
Efficiency (%)
0
20
40
60
80
100
0
50
100
150
200
250
300
Time (x10^3 s)
Sample 4
C
Efficiency (%)
0
20
40
60
80
100
0
50
100
150
200
250
300
Time (x10^3 s)

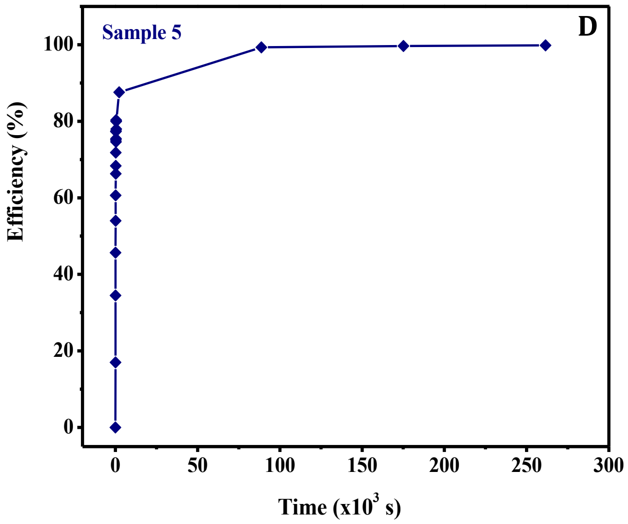

Figure 28: a) Recovery efficiency vs time for Sample 2 (Table 9); b) Recovery efficiency vs time for Sample 3 (Table 9); c) Recovery efficiency vs time for Sample 4 (Table 9) and d) Recovery efficiency vs time for Sample 5 (Table 9)

These data are currently under elaboration: the exploitation of a mathematical model according to a chemometric approach, in particular a D-Optimal screening model, will be used to consider the significance of qualitative and quantitative variables, for the study of the efficiency and the recovery in the pilot plant prototype. Different samples (5 levels), pollutants (3 levels), catalyst amount (3 levels), starting pH conditions (3 levels), reuse cycles (3 levels), treating time (2 levels) and irradiation modes (2 levels) will be the investigated variables, monitored to find out the most significant ones that affect the pre-industrial use and reuse of different catalyst after their recovery at the pH_{IEP}. The following mathematical model will be used to determine the 25 coefficients:

(Eq.**28**) $$y = b_0 + b_1X_1 + b_2X_2 + b_3X_3 + b_4X_4 + b_5X_5 + b_6AX_6A + b_6BX_6B + b_7AX_7A + b_7BX_7B + b_7CX_7C + b_7DX_7D + b_{12}X_1X_2 + b_{13}X_1X_3 + b_{14}X_1X_4 + b_{15}X_1X_5 + b_{23}X_2X_3 + b_{24}X_2X_4 + b_{25}X_2X_5 + b_{34}X_3X_4 + b_{35}X_3X_5 + b_{45}X_4X_5 + b_{11}X_1^2 + b_{22}X_2^2 + b_{33}X_3^2$$

3.2. Synthesis of (Cu, N)-doped TiO_2 and Structural Refinement

Pure, N-doped, Cu-doped and (Cu, N)-double doped TiO_2 samples were synthesized through a sol-gel synthesis in order to investigate the local and average structure of crystalline TiO_2, processed under different pH conditions. Samples resulted mainly composed of anatase phase, even though a low but significant amount of secondary brookite grew in most samples. A detailed structural characterization was performed by means of synchrotron X-Ray elastic scattering experiments; structural data of different samples were gained by means of the pair distribution analysis. The aim of this work was to investigate the crystalline structure of nanosized TiO_2 as a function of the different synthetic conditions tested.

This project was carried out in collaboration with Dr. A. Martinelli of the Institute of Superconducting and other Innovative Materials and Devices of the National Research Council and the research group of Prof. D. Comoretto from Industrial Chemistry Section of University of Genova.

3.2.1. Materials and methods

Six different TiO_2 samples were synthesized by a sol-gel process. Their synthetic conditions are reported in Table 11.

Table 11. Synthetic conditions of the investigated (Cu, N)-doped samples

	Dopant	**Aqueous solution**	**pH**
Sample 1	Cu	H_2O	6
Sample 2	Cu, N	NH_3	8
Sample 3	Cu, N	HNO_3	3
Sample 4	/	H_2O	6
Sample 5	N	NH_3	8
Sample 6	N	HNO_3	3

The first three samples were prepared mixing, under vigorous stirring for 4 hours at T_{room}, TTIP, 2-Propanol and a copper nitrate hexahydrate "CNH" solution, mixed together in a volume ratio of 1:2:5, respectively. Three different CNH solutions were used: an aqueous solution (pH=6), an alkaline 15% (V/V) NH_3 solution (pH=8) and an acidic 0,026 M HNO_3 solution (pH=3). The resulting gel was dried in an oven for 12 hours at 105 °C, in order to remove residual water and organics. Each Cu-doped TiO_2 sample was synthesized with a theoretical molar ratio of 2.0% corresponding to the optimal value found in literature[96]. The remaining samples were synthesized without the Cu doping, therefore without adding the CNH to the different aqueous solutions. All samples were grinded in an agate mort and then thermally treated in a muffle furnace from T_{room} to 400 °C in 20 min, for a total of 3 hours.

X-Ray elastic scattering experiments were carried out at the ID11 beamline of the European Synchrotron Radiation Facility (ESRF, Grenoble, France), λ= 0,3544 Å, T = 25 °C. These data were used for both structural refinements, according to the Rietveld Method and Pair Distribution Function "PDF" analysis; in the first case the information about the long-range structure is obtained, whereas in the second case the average local structural distortion can be investigated.

Structural refinement was carried out, according to Rietveld Method[97], using FullProff[98] and a file describing the instrumental resolution function. In particular, the coherent diffraction domain size as well as the lattice strain are evaluated by fitting the FWHM parameters. In the final cycle, the following parameters were refined: the scale factor, the zero point of detector, the background (parameters of 5th order polynomial function), the unit cell parameters, the atomic displacement parameters, the anisotropic strain parameters and the size parameter. The microstructural properties were inspected by using the refined anisotropic strain parameters and analysing the broadening of diffraction lines by means of the Williamson-Hall plot method[99]. Generally, in the case where the micro-strain is anisotropic, a straight line passing through all the points in the plot and through the origin has to be observed, where the slope provides the micro-strain: the higher the slope, the higher the micro-strain. If the broadening is not isotropic, size and strain effects along particular crystallographic directions can be obtained by considering different orders of the same reflection.

Data from an empty capillary were collected to subtract the container scattering. Reduction of the total scattering data to obtain *G(r)*, the PDF function, was achieved by the PDFgetX3 software using Q_{max} = 30.0 $Å^{-1}$, a sufficient range for an accurate analysis (Q represents the modulus of the scattering vector). Full-profile fitting of the G(r) function was carried out using the PDFgui software and the parameters obtained from the Rietveld method refinements as starting structural models. In the last fitting cycle, the following parameters were refined: the scale factor, the lattice parameters, the atomic positions not constrained by symmetry, the anisotropic atomic displacement parameters, the dynamic correlation factor, a parameter describing experimental resolution effects "Q_{damp}".

Elemental composition of the synthesized samples was evaluated by means of ICP-AES, with a Thermo Fisher Icap 7400 Duo Full MCF, in particular according to UNI EN ISO 13657:2004 + EPA 6010D 2014 for copper amount assessment and BS EN 13654-1:2001, further with the help of a steam current distiller Velp UDK 127, for the nitrogen amount. The residual water content was, instead, measured by Diffuse Reflectance Infrared Fourier Transform Spectroscopy "DRIFTS", collected for all the TiO_2 samples under the same experimental conditions. The data were collected with a Bruker FT-IR spectrometer Vertex V70 (resolution 2 cm^{-1}) equipped with Bruker DRIFTS accessories, in the range between 4000 and 1400 cm^{-1}, where no absorption bands from TiO_2 are expected[100–102]. Indeed, both Ti-O stretching and Ti-O-Ti bridging stretching modes are usually detectable below 1000 cm^{-1}.

Photocatalytic experiments were performed on 0,01 g/L MB solutions with 0,0125 g of each synthesized catalyst; aliquots were analysed by means of UV-Vis spectrophotometry.

3.2.2. Results and Discussion

In Figure 29 the X-Ray diffraction patterns of the analysed samples are compared; invariably, anatase constitutes the main phase, whereas a faint peak at 2,15 Å^{-1} reveals the presence of brookite as secondary phase in most samples. Remarkably, the amount of brookite is very reduced or almost negligible in Sample 2 and Sample 5 (both synthesized in ammonia solution). Figure 30 shows the refinement plot obtained for the Sample 6, selected as representative.

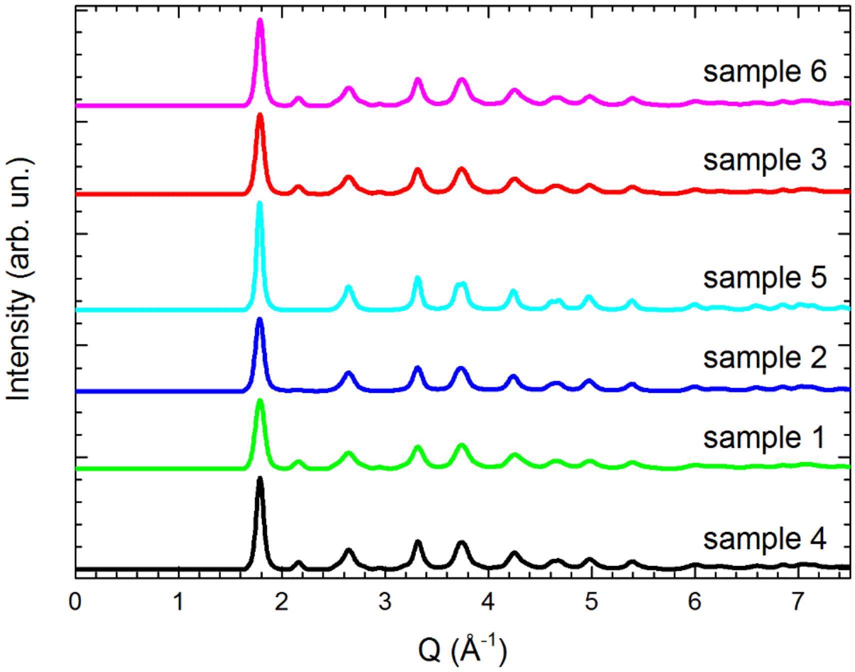

Figure 29: X-Ray powder diffraction patterns of the analysed TiO_2 samples; Q represents the modulus of the scattering vector

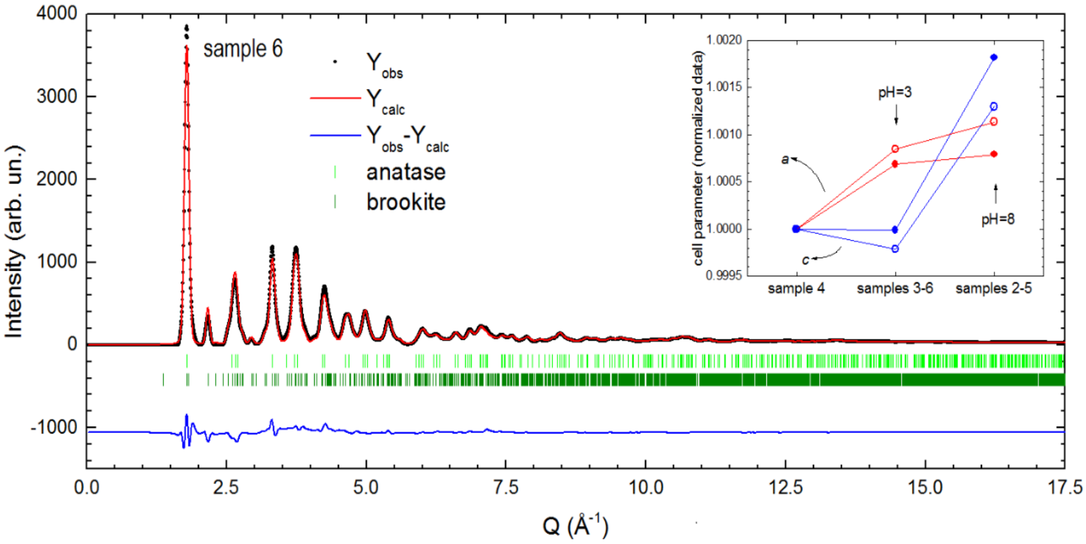

Figure 30: Rietveld refinement plot of Sample 6. The inset shows the evolution of the cell parameters of the samples prepared at pH 3 and 8 (normalized data; full symbols: N-doping; open symbols: (Cu, N)-doping)

Table 12 resumes the structural and microstructural data for anatase synthesized under different conditions as obtained by Rietveld refinements.

Table 12. Structural and microstructural (coherent diffraction domain size) properties of anatase synthesized under different conditions

Sample	***a* (Å)**	***c* (Å)**	**Size (nm)**	**Anatase % (mass)**
Sample 1	3.7880(1)	9.4675(2)	53(1)	72.1(5)
Sample 2	3.7868(1)	9.4787(1)	20(1)	91.4(5)
Sample 3	3.7857(1)	9.4644(1)	91(1)	74.1(5)
Sample 4	3.7825(1)	9.4664(1)	66(1)	78.9(5)
Sample 5	3.7855(1)	9.4836(1)	74(1)	100
Sample 6	3.7851(1)	9.4663(1)	128(1)	75.1(5)

All the substituted samples display a significant increase of *a* axis compared to the undoped sample (Sample 4), suggesting an effective degree of substitution. Unfortunately, it is not possible to rationalize the trend of the cell parameters on account of the complicated and tangled interplay of the type of doping and synthesis conditions. For example, for the N-doped samples it is observed that the sample 6 exhibits a significant increase of the parameter *a*, whereas the parameter *c* is almost unaffected by doping; conversely, Sample 5 displays a similar size for the parameter *a*, but a notable increase of the parameter *c*. In the corresponding (Cu, N)-double doped samples (Sample 2 and 3). The increase of the lattice parameter *a* is coupled with a significant decrease of *c*. The situation is depicted in the inset of Figure 30, where the cell parameters of the aforementioned samples are reported (for the sake of clarity, data are normalized to the values of the undoped Sample 4).

In any case, by these data it is not possible to recognize if N is interstitial or located at the O site. On the other hand, on basis of their crystalline and chemical properties, the substitution of Cu at the Ti site can be predicted, in agreement with previous studies on Cu-substituted TiO_2[103]. Interestingly, the length of the *c* axis exhibits an abrupt change for Sample 2 and Sample 5 that are both synthesized in NH_3. Remarkably, the amount of secondary brookite decreases as the length of the anatase *c* axis increase, as illustrated in Figure 31.

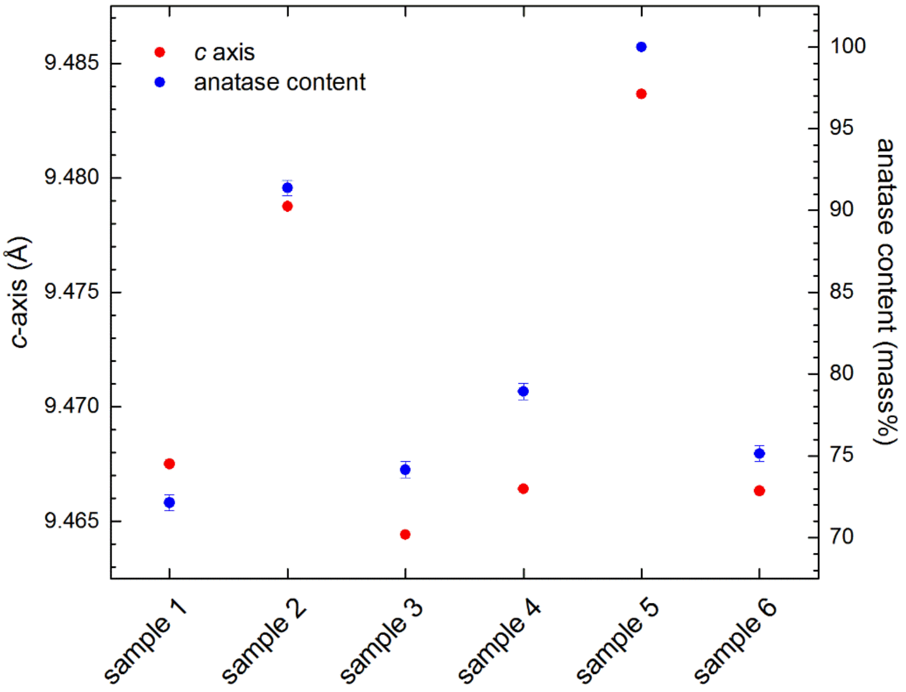

Figure 31: Relationship between the anatase *c* axis and the amount of anatase constituting each sample

This result can be explained by an accurate comparison of both crystal structures. In anatase, O atoms are arranged in order to approach a cubic-closest packing arrangement, whereas in brookite they approximately form double hexagonal closest packing arrangement. In particular, these two structures can be regarded as simply polytypes of TiO_2, based on different stacking of octahedral slabs. These slabs lie in the (112) and (040) planes in the anatase and brookite structures, respectively; in particular, the (112) interplanar spacing of anatase is significantly larger than the corresponding (040) in brookite. Therefore, the crystal structure of anatase results less dense, thus explaining why its amount scales with the c axis length.

Figure 32 shows the comparison of the Williamson-Hall plots obtained for the different samples; the slanting lines on the right represent the linear fit for each set of data extrapolated at high d* in order to highlight the difference degree of lattice strain which characterizes the samples. It is evident that Sample 2 and Sample 5 (both synthesized in NH_3) are less affected by lattice strain, likely due to the absence of secondary brookite. Moreover, the double doped samples display higher lattice strain than the corresponding single doped ones (Samples 2-5 and Samples 3-6), clearly evidencing how Cu substitution determines a notable lattice distortion.

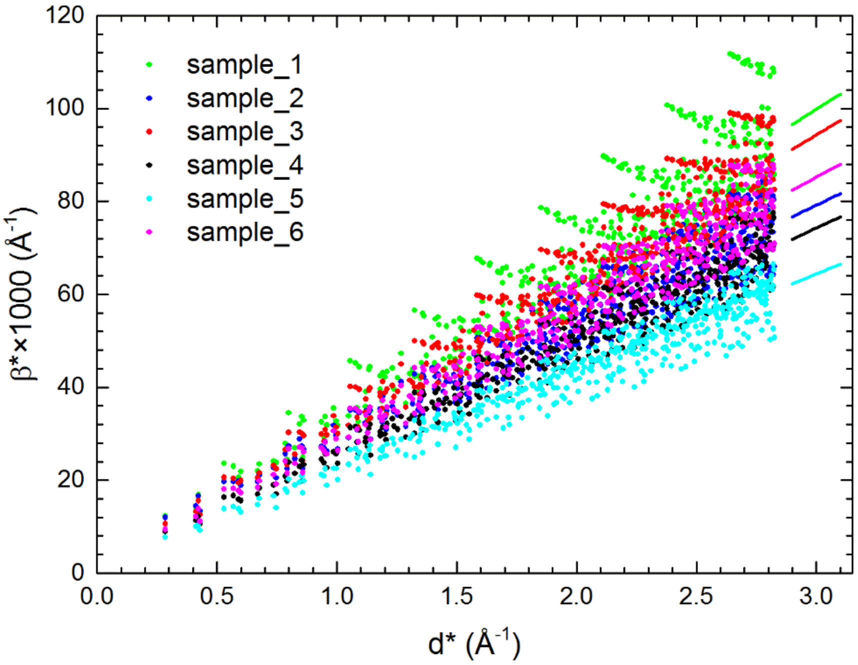

Figure 32: Williamson-Hall plots for the analysed samples

The PDF Function *G(r)* yields the probability of finding pairs of atoms separated by a distance *r*; in the investigated samples the *G(r)* shows sharp features up to quite long distances, indicating a high degree of crystallinity of the nanometric particle. Figure 33 shows the difference curves calculated subtracting the function *G(r)* of the pure sample from the *G(r)* function of the substituted samples; in this way, the structural deviation at the local scales are emphasized. It is evident that samples synthesized with NH_3 (Samples 2 and 5) display the more notable difference; this behaviour can be safely ascribed to the fact that the unsubstituted TiO_2 sample actually contains a significant amount of secondary brookite, whose amount is very reduced or almost negligible in Sample 2 and Sample 5.

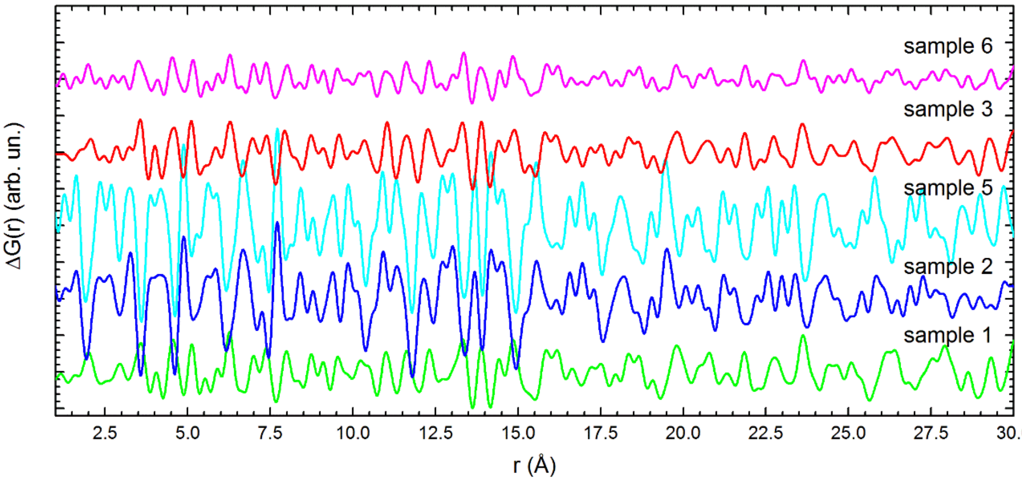

Figure 33: Difference curves obtained by subtracting the *G(r)* function of each substituted sample minus the *G(r)* function of pure TiO2

Figure 34 shows *G(r)* function of Sample 6, fitted with a structural model foreseeing the presence of both anatase and brookite in the analysed sample.

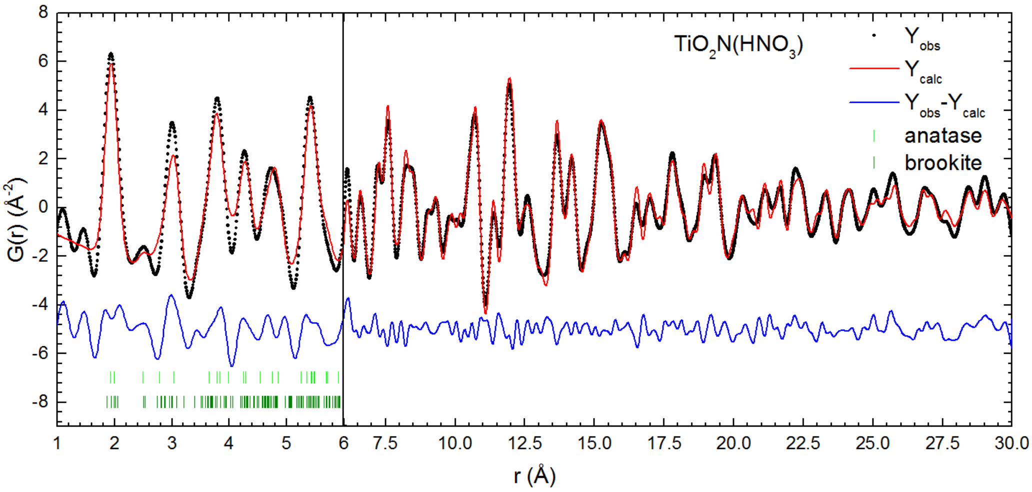

Figure 34: Fit of the *G(r)* function of Sample 6; vertical bars in the lower field indicates bond lengths lower than 6 Å in anatase and brookite

Figure 35, on the left, shows an enlarged view of the low *r* region of the experimental *G(r)* function.

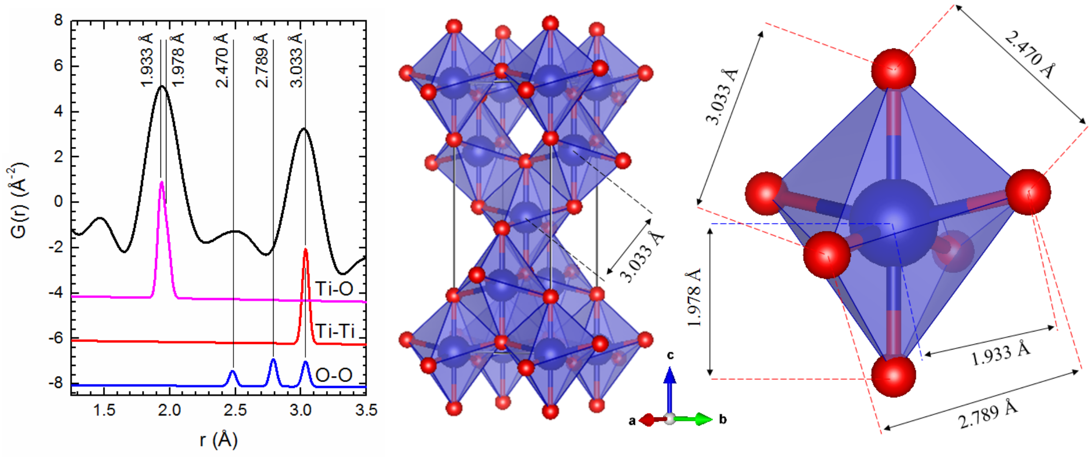

Figure 35: Comparison of low *r* region of the experimental *G(r)* function (Sample 5) with the computed partial PDFs containing only selected contributions of atomic pairs (on the left); on the right: representation of the crystal structure of anatase with main interatomic distances listed

The peak at 2 Å corresponds to the next-neighbour Ti-O distances (Figure 35, right), whereas the shortest Ti-Ti bonds mainly contribute to the peak at 3 Å. Unfortunately, the presence of secondary brookite in the other samples prevents a more detailed analysis and comparison of the local structure. On the other hand, the difference observed in the *G(r)* functions of Sample 3 and Sample 6, being prepared under the same experimental conditions and containing about the same amount of secondary brookite, can be reliably ascribed to the effect of Cu substitution.

The panel on the left of Figure 36 evidences that Cu-substitution (Sample 3) determines an almost negligible effect on the geometry of the octahedra.

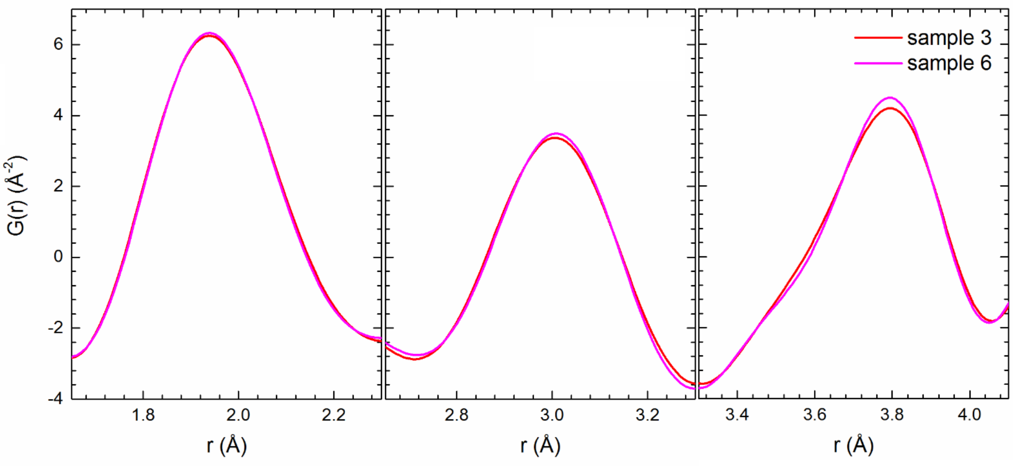

Figure 36: Enlarged view on selected regions of the *G(r)* functions for the Sample 3 and Sample 6 in the *r* ranges pertaining to the nearest Ti-O and Ti-Ti interatomic distances

Conversely, a more pronounced effect can be detected in the peaks mainly originated by Ti-Ti pairs, as those at 3.0 Å and 3,8 Å. Remarkably, all the peaks mainly produced by Ti-Ti pairs display a significant difference in these samples, suggesting that Cu substitution rearranges the cationic sub-lattice to some extent, whereas the anionic sub-lattice is almost unaffected by substitution.

In order to compare the local structure of anatase obtained by PDF analysis with the average structure calculated by Rietveld refinement, the variance σ^2 of the lattice parameter was evaluated as:

$$\sigma^2 = \Sigma_i (\chi_{PDF} - \chi_{RTV})_i^2$$

Where χ_{PDF} and χ_{RTV} represent the cell parameters as obtained by PDF (local structure) and Rietveld refinement (average structure), respectively. Figure 37 shows the variance for the different samples; as expected, Sample 2 and Sample 5 display the more reduced deviation of the local structure from the average one.

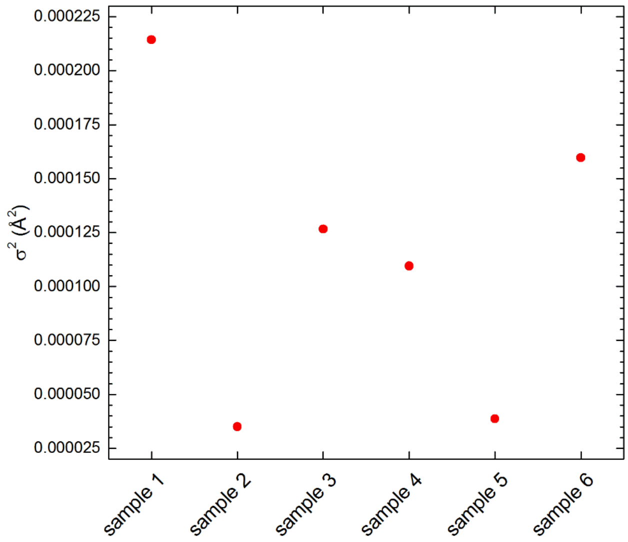

Figure 37: Deviation of the local structure from the average one evaluated by the variance of the lattice parameters

The degree of local disorder in anatase measured by σ^2 roughly scales with the amount of secondary brookite, evidencing that the competing formation of this latter phase induces lattice defects in anatase. In order to gain insights about the location of N atoms inside the anatase structure, three different structural models were calculated together with their corresponding *G(r)* functions. In the first structural model, 20% of O atoms are substituted by N atoms (N atoms located at the *8e* site); in the second structural model, 20% of Ti atoms are substituted by N atoms (N atoms located at the *4a* site); in the third structural model 20% of the largest voids in the anatase crystal structure are occupied by N atoms (N atoms located at the *8d* atomic site). With the same boundary conditions applied for the calculation, the *G(r)* functions of these hypothetical structural models and the *G(r)* functions of anatase in the different analysed samples were calculated using the structural data obtained by fitting the experimental pair distribution functions (derived structural models); in this way, all the instrumental effects and other spurious contributions can be cut out. Finally, in order to evaluate the effect of chemical substitution, the *G(r)* functions of the substituted samples were subtracted from the corresponding *G(r)* of the unsubstituted one for both the hypothetical and derived structural models.

Figure 38 shows the comparison of the different plots obtained for Sample 6; the black line is the *G(r)* difference obtained by subtracting *G(r)* function of Sample 6 from that of Sample 4 (bare TiO_2), whereas the remaining curves are the *G(r)* difference obtained by subtracting the *G(r)* functions of the afore-mentioned three hypothetical models from that of pure TiO_2. It is evident that the structural model foreseeing the N substitution at the O site best matches the difference curve, thus suggesting that N actually replaces O in anatase.

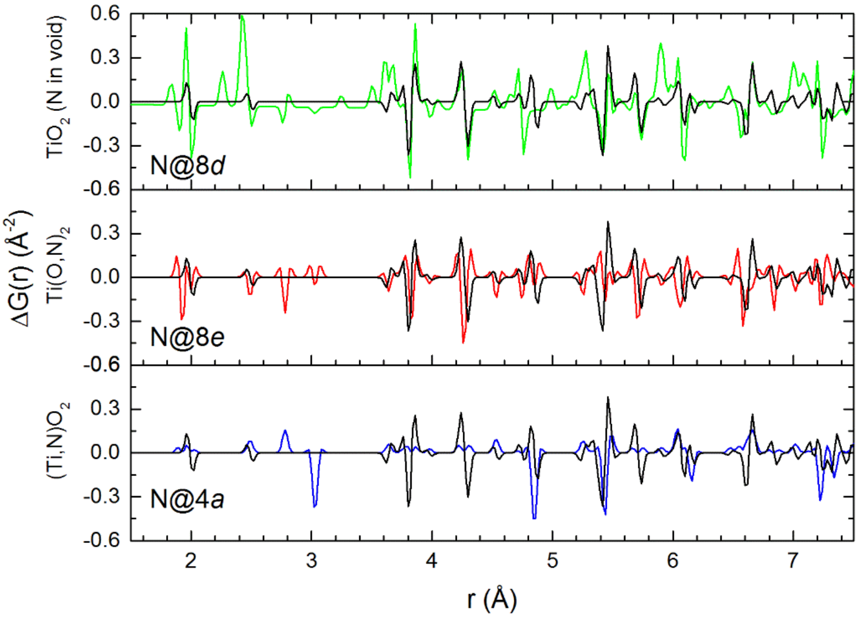

Figure 38: *G(r)* difference plots obtained for different structural models foreseeing N atoms located at different structural sites

This result is in agreement with a recent neutron powder diffraction investigation on N-doped TiO_2 samples, demonstrating a partial occupation of the O site by N atoms[104].

Copper and Nitrogen amount is reported in Table 13. Results suggest that alkaline conditions, which are actually linked to a greater *c* axis distortion, are responsible for an easier location of the dopants within the structure, while acidic and neutral conditions do not strictly influence lattice parameters as well as the dopants content.

Table 13. ICP-AES results for copper and nitrogen amount. L.O.D. for Cu (4 ppm) and N (0,1 ppm)

Sample	pH	Copper (ppm)	Nitrogen (ppm)
Sample 1	6	440	< L.O.D.
Sample 2	8	982	30000
Sample 3	3	736	732
Sample 4	6	< L.O.D.	< L.O.D.
Sample 5	8	< L.O.D.	32800
Sample 6	3	< L.O.D.	1680

It can be seen that Sample 2 and Sample 5, which have been synthesized in alkaline conditions and do not have secondary brookite within the structure, show the major elongation of the *c* axis and, in light of the elemental composition, this features can be thus related to the easier dissolution of N into titania structure which reflects into simpler insertion of dopants along this preferential direction, likely sustained by the presence of hydroxyl ions, actin as bridges between Ti-O bonds, which can be exchanged with other ions easier. In order to definitively exclude the direct dependence of the cell parameters to the water presence, DRIFTS spectra were collected and shown in Figure 39. All the spectra show a large band positioned between 3700 and 2700 cm^{-1}. In the same spectral region, a sharp peak is also detected at 3690 cm^{-1}. As well-known, these bands are assigned to the stretching vibration modes ν_1 and ν_3 of the water molecules[105]. A sharp band at 1631 cm^{-1} assigned to the ν_3 bending is also visible in the short frequency side of the spectra[101,105]. Panel b of Figure 39 shows the ratio signal collected in correspondence of the three spectral features described above, at 1631, 3350 and 3690 cm^{-1}. These data were calculated as the ratio between the intensity collected for the reference Sample 4 and those of the other samples, so that, for $I_{S4}/I_{Si} > 1$ the intensity of the peak is larger for the reference sample and vice-versa. Data are compared with the pH of the synthesis solution (blue squares in Panel b). It can be noticed that there is not a regular correlation between pH value and water content, as we can see that for samples synthesized in alkaline conditions, the relative amount of residual water is both smaller and greater with respect to reference Sample 4. It has to be noticed that this analysis cannot provide information on the absolute water content in the powders.

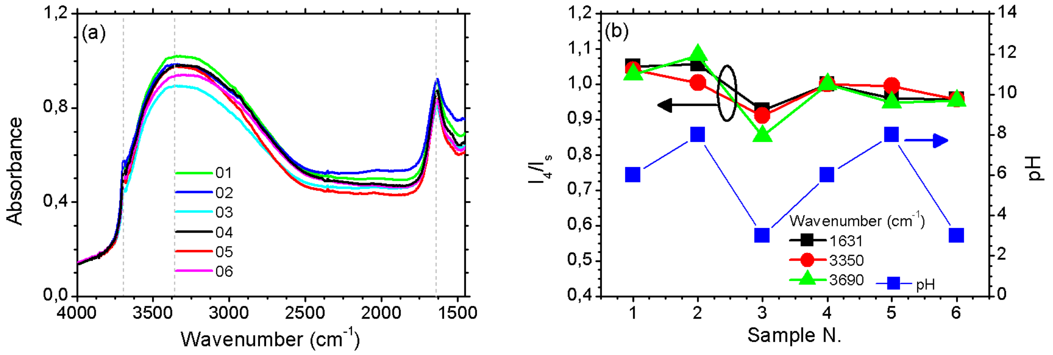

Figure 39: a) DRIFT spectra collected for the six samples; b) Absorbance ration I_4/I_i retrieved from DRIFT spectra at 1631 cm^{-1} (black), 3350 cm^{-1} (red) and 3690 cm^{-1} (green) for the six samples (left axis) compared with the pH values of the solution (right axis, blue)

Eventually, experimental photocatalytic results of the six samples are reported in Table 14 together with the hydrodynamic radius' values of the aggregates suspended in water.

Table 14. MB percentage degradation of the six (Cu, N)-doped samples and mean hydrodynamic radius

Sample	**MB Degradation (%)**	**St. Dev**	**Hydrodynamic Radius (nm)**	**St. Dev**
Sample 1	39,55	1,5	403,1	146,3
Sample 2	44,61	8,9	543,7	76,21
Sample 3	21,78	10,9	326,3	112,2
Sample 4	98,68	0,3	690,4	162,0
Sample 5	98,83	0,2	464,3	48,8
Sample 6	98,74	0,6	434,1	138,7

It is well evident that the Cu-doping, in the investigated conditions within this project, completely brings to the opposite outcome with respect to the expected one: its presence has a detrimental effect of the activity of the catalysts, while on the other side, the synthesis of N-doped samples with inorganic species (HNO_3,

NH_3) led instead to a sharp increase of their photocatalytic efficiency. Hydrodynamic radius measurements, instead, didn't bring useful information, as tested samples provided very similar values of colloidal suspensions dimensions, proof that the synthetic route investigated, mainly for pH conditions, led to stable aggregates of several hundreds of nanometres.

3.2.3. Conclusions

Cu substitution at the Ti site determines a remarkable lattice distortion, larger than that observed for N substitution. In particular, Cu substitution determines a significant rearrangement of the cationic sub-lattice, which could also be related to the photocatalytic efficiency loss; conversely, the anionic sub-lattice appears almost unaffected by the light replacement of Cu for Ti. Local structure analysis suggests that N actually replaces O in anatase, rather than being located in structural voids. In any case, the synthesis in NH_3 solution hinders or even prevents the formation of secondary brookite and this particular synthetic condition also led to the greater *c* axis distortion, with respect to the other samples. This distortion seems to be linked to the capability of the crystalline structure to easier locate dopants in this crystallographic direction. This is relevant, since the competing growth of brookite determines the formation of a large number of structural defects within anatase.

TiO_2 synthesis in presence of nitrogen-containing species seems to be a favourable synthetic condition in order to obtain an effective catalyst, likely for doping-related effects as well as advantageous consequences on the crystalline anatase lattice.

3.3. Hydrothermal synthesis of TiO_2 in presence of Ferrite Nanoparticles as Nucleation Seeds.

In the present work, the crystallization of anatase TiO_2 nanoparticles using different ferrite nanoparticles with different chemical composition, dimensions and shape as nucleation seeds was investigated. In particular, $CoFe_2O_4$, $NiFe_2O_4$ and Fe_3O_4 NPs with a volume ratio equal to 1:1000 with respect to the TiO_2 amount, were used in order to investigate the synthesis of nanocrystalline tetragonal anatase TiO_2 by hydrothermal treatment. In addition, Lu_2O_3 nanoparticles were also used to detect the effect of non-magnetic NP on the synthesis and crystallization of titania[106]. For each sample, a deep physical-chemical characterization was performed by means of XRD and Rietveld refinement, FE-SEM, STEM, TEM, DSC and BET surface area measurements. Furthermore, some samples were subjected to photocatalytic tests for MB solutions degradation. The hydrothermal synthesis was performed in a closed steel vessel, for 3 hours at 150 °C, under a natural pressure of 9 bars. The used temperature results to be much lower than usual temperatures exploited to get the anatase phase, hence indicating that the mere presence of a nucleation seed, without any particular need in terms of composition/morphology, simplifies the crystallization of anatase.

This project was carried out with the collaboration of the research group of Prof. G. Singh of the Department of Materials Science and engineering, Norwegian University of Science and Technology, and of Dr. A Martinelli of the Institute of Superconducting and other Innovative Materials and Devices of the National Research Council.

3.3.1. Materials and Methods

All the syntheses were performed under oxygen-free conditions in a Schlenk line using Iron (III) acetylacetonate "$Fe(acac)_3$" (97%), cobalt (II) acetylacetonate "$Co(acac)_2$" (97%), nickel (II) acetylacetonate "$Ni(acac)_3$" (95%), all purchased from Sigma Aldrich; oleic acid (technical grade, 90%), oleylamine (technical grade, 70%), 1,2-hexadecanediol (90%), benzyl ether (99%), toluene, 2-Propanol and acetone (all from Sigma Aldrich) without any further purification. In Table 15 a brief summary on the characteristics of the different nanoparticles that will be used as nucleation seeds is reported.

Table 15. Chemical composition, size, shape and crystallographic structure of the nucleation seeds used in this project

Sample	Chemical composition	Size (nm)	Shape	Crystalline structure
Sample 1	$NiFe_2O_4$	30 ± 5.2	Cubic	cF56 – Fd-3m
Sample 2	$NiFe_2O_4$	8.8 ± 1.2	Spherical	cF56 – Fd-3m
Sample 3	$CoFe_2O_4$	8.6 ± 2.1	Spherical	cF56 – Fd-3m
Sample 4	$CoFe_2O_4$	17.2 ± 3.4	Cuboctahedron	cF56 – Fd-3m
Sample 5	Fe_3O_4	7.2 ± 1.2	Spherical	cF56 – Fd-3m
Sample 6	Lu_2O_3	19 ± 6	Distorted spherical	cI180 – Ia-3

In brief, the synthesis of Sample 2, Sample 3 and Sample 5: 2 mmol of $Fe(acac)_3$, 1 mmol of $Co(acac)_2$, 10 mmol of 1,2-hexadecanediol, 6 mmol of oleic acid, 6 mmol of oleylamine and 20 mL of benzyl ether were mixed and magnetically stirred under Ar atmosphere. The mixture was heated up to 200 °C for 100 min (5 °C/min) and then heated to reflux at 300 °C (5 °C/min) for 60 min. The black-coloured mixture was left to cool to T_{room} and magnetically washed overnight with toluene and isopropanol. For the synthesis of Sample 1 and Sample 4, the procedure was modified: 2 mmol of $Fe(acac)_3$, 1 mmol of $Ni(acac)_3$/$Co(acac)_3$ and 6 mmol of oleic acid were added to 20 mL of benzyl ether solution. After degassing the solution at T_{room}, the reaction mixture was slowly heated, at 5 °C/min, to 290 °C under Ar atmosphere and kept for 30 min. After cooling the solution, NPs were precipitated with toluene and isopropanol. The NPs were washed two times with toluene and acetone before dispersing them into toluene. Furthermore, we decided to perform the same synthesis in the presence of non-magnetic NPs, to state if any difference would occur. We used Lu_2O_3 NPs which were prepared according to the co-precipitation method[107]: lutetium chloride (Alpha Aesar) was dissolved in a 13% (V/V) HCl (Sigma-Aldrich) solution at 25 °C, then an oxalic acid solution (Alfa Aesar) was added in a stoichiometric ratio equal to 1:2, respectively. Lutetium oxalate, once precipitated, was filtered and washed with deionized water; subsequently, it was calcined at 600 °C for 6 hours, in order to obtain the corresponding nanometric lutetium oxide. For the synthesis of amorphous TiO_2, the sol-gel route was employed. A given amount of each specie reported in Table 14 was dispersed in 10 mL of 2-Propanol by sonicating for 5 min at 30% power, with an OMNI Sonic Ruptor Ultrasonic Homogenizer (Omni International, Atlanta, GA, USA). Later, the dispersion was transferred to a solution of 2-Propanol and TTIP to the final volume of 200 mL. Finally, deionized water was added to the solution to obtain the gel, in a volume ratio of 34:1:5, respectively for 2-Propanol, TTIP and water. The gel is left under magnetic stirring for 4 hours and then 25 mL of this were taken and transferred in the hydrothermal Teflon vessel, to be closed within the steel vessel and eventually put in a silicon oil bath for 3 hours at 150 °C. The pressure naturally evolved within the vessel during the heat treatment reached the value of 9 bar. The treated gel was then split into two aliquots, one kept as it was and the other dried in an oven for 12 hours at 105 °C.

X-Ray Diffraction "XRD" analysis was performed on dried NPs by a Philips PW1830 diffractometer (Philips, Amsterdam, The Netherlands) using the Bragg-Brentano geometry, with Cu Kα (λ= 0,15406 nm), Ni filtered, while Lu_2O_3 NPs were collected with Co Kα radiation (λ= 0,17889 nm). Data were collected in the 10 – 80 2θ range, with a step of 0,023 2θ and a sampling time of 20 s. From XRD patterns, structural refinement was carried out according to the Rietveld Method, using the FullProf software. Microstructural analysis was also performed by refining the anisotropic strain parameters: at this scope, refinements were carried out using an instrumental resolution file and the diffraction lines were modelled by a Thompson-Cox-Hastings pseudo Voigt convoluted with axial divergence asymmetry function. Field Emission – Scanning Electron Microscopy "FE-SEM" analyses were performed using a ZEISS SUPRA 40VP Microscope (Carl Zeiss AG, Oberkochen, Germany) equipped with an energy dispersive X-Ray spectrometer (EDXS OXFORD "INCA Energie 450x3", Oxford Instrument, Abingdon, UK) for microanalysis, using the low voltage (5 kV) mode. The analyses were performed collecting the signal by means of the In-Lens Detector. Scanning Transmission Electron Microscopy "STEM" images were collected with Hitachi S5500, operating at 30 kV. For both analyses, after ultrasonic vibrations used to decrease the aggregation, a drop of the resultant mixture in toluene was deposited on a copper grid covered with a thin carbon layer and then carefully dried in air before the analysis. Transmission Electron Microscopy "TEM" images were collected on a JEOL 3010 High Resolution TEM operating at 300 kV. Specimens were prepared by dispersing the sample by sonication in isopropanol. Differential Scanning Calorimetry "DSC" measurements were carried out with a Mettler Toledo 821e calorimeter (Mettler Toledo, Columbus, OH, USA) in O_2 atmosphere (20 mL/min), using aluminium crucibles. Data were collected in the 40 - 500 °C range, at a heating rate of 10 °C/min. Brunauer-Emmet-Teller "BET" analyses were performed to get the surface area of the samples by nitrogen adsorption isotherms, acquired using an ASAP 2010 physisorption analyser (Micromeritics Instrument Corp., Norcross, GA, USA). Before the measurement, each sample was pre-treated at 200 °C in vacuum for 12 hours.

The photocatalytic activity was measured for each sample by adding 0,0125 g of the catalyst in 25 mL of a 0,04 g/L MB solution. Before irradiation, the suspension is kept for 20 min stirring in the dark, to ensure adsorption/desorption equilibrium between photocatalyst and the dye. The suspensions were then exposed to the solar simulated light irradiation (300 W, OSRA, Munich, Germany), for 2 hours at T_{room}. 1,5 mL aliquots were withdrawn from starting to end time every 20 min. Collected samples were centrifuged by a Centrifuge 5410 (Eppendhorf, Hamburg, Germany) at 13200 rpm for 5 min to separate NPs from the solution; the latter was analysed by means of a UV-Vis spectrophotometer (Lambda 35, Perkin Elmer, Whaltam, MA, USA), monitoring λ = 664 nm.

3.3.2. Results and Discussion

In Figure 40, STEM and TEM images of the NPs are reported.

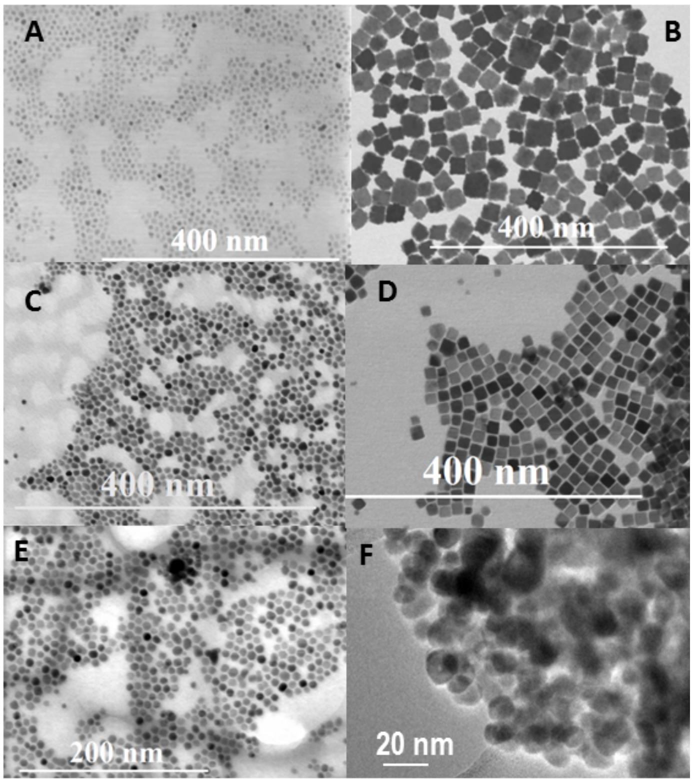

Figure 40: STEM images of Nickel ferrite seeds (A-B), Cobalt ferrite seeds (C-D), Fe_3O_4 seeds (E) and TEM image of Lu_2O_3 seeds (F)

It can be noticed that the different nucleation seed have different morphological aspects, as the NPs possess different dimensions and shapes: nanoparticles' size ranges from 8 to 30 nm, with cubic or spherical shapes. Figure 41 shows the XRD patterns of $CoFe_2O_4$, $NiFe_2O_4$, Lu_2O_3, highlighting the crystal lattice of some of the nucleation seeds.

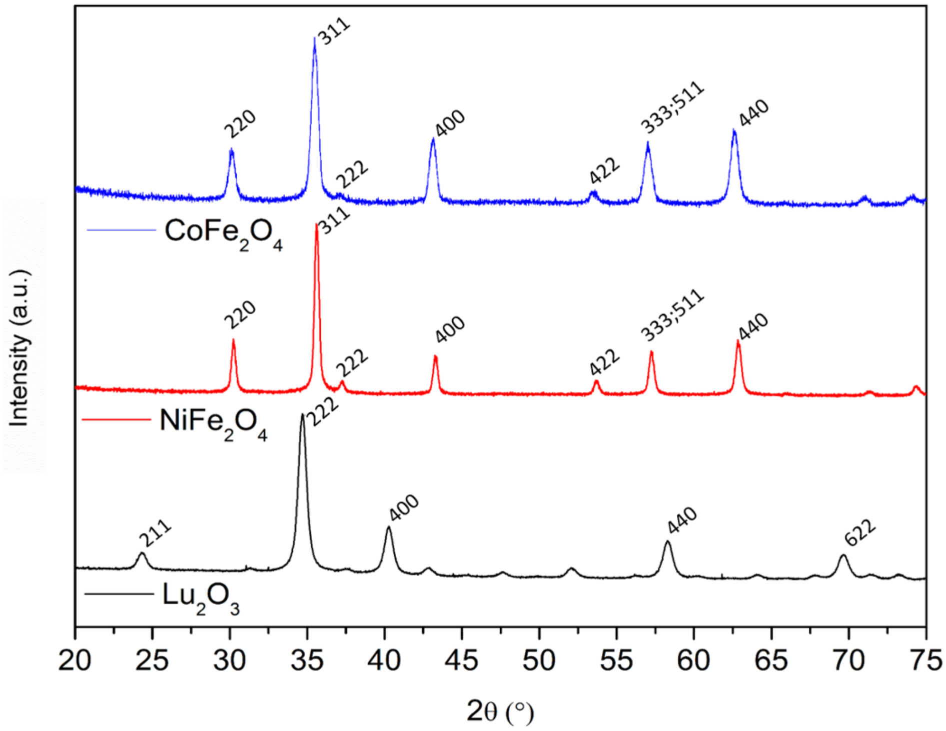

Figure 41: XRD patterns and respective Miller indices of the $NiFe_2O_4$, $CoFe_2O_4$ and Lu_2O_3 NPs used for the synthesis of Sample 1, 4 and 6 respectively.

Figure 42, instead, shows the XRD patterns of the synthesized samples.

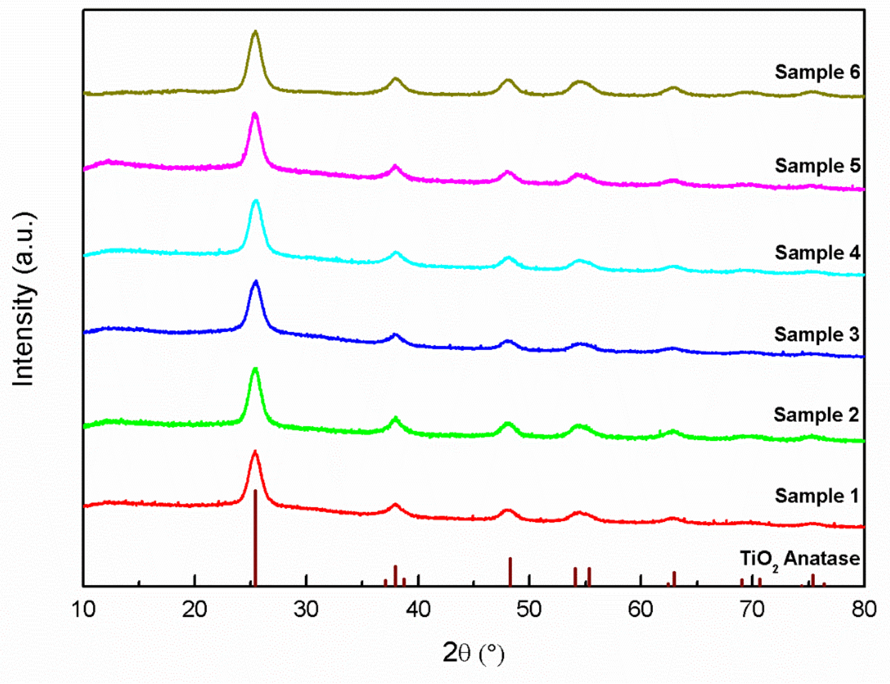

Figure 42: XRD patterns of the synthesized samples and the anatase TiO_2 reference pattern (line pattern) got from Pearson's Crystal Data Software

With reference to the TiO_2 anatase diffraction pattern, presented as a line pattern in the same figure, it is possible to state that the temperature and pressure conditions reached within the hydrothermal synthesis are able to make TiO_2 crystallize from amorphous to anatase, thanks to the presence of the nucleation seeds, even in a concentration 1000 times lower than that of titania. In fact, for each synthesized sample, it is possible to easily identify the main anatase peak, without any other signal ascribable to secondary phases. The only slight difference that can be detected (but unfortunately not quantifiable) is the presence of amorphous TiO_2, which can be roughly estimated from the goodness of the baseline. We couldn't show a comparison with a blank sample as the absence of nucleation seeds within the reactor didn't bring the crystallization of titania, thus the XRD pattern couldn't be registered. Structural Rietveld refined data are displayed in Table 16.

Table 16. Structural and microstructural properties of synthesized TiO_2 samples with nucleation seeds

Sample	***a* (Å)**	***c* (Å)**	**z_O**	**Size (nm)**
Sample 1	3.7912(1)	9.4829(3)	0.2008(1)	3.9
Sample 2	3.7921(1)	9.4876(3)	0.2041(1)	4.3
Sample 3	3.7932(1)	9.4883(4)	0.1989(1)	3.8
Sample 4	3.7920(1)	9.4877(3)	0.2020(1)	4.0
Sample 5	3.7906(1)	9.4875(3)	0.2007(1)	4.6
Sample 6	3.7936(1)	9.4839(2)	0.2045(1)	3.9

Microstructural properties of the six samples are very similar for each one. These lack of differences could be assigned to the unspecific mechanism of the nucleation, as the ferrite NPs act as nucleation seeds for other TiO_2 NPs: titania doesn't grow homogeneously on the ferrite's surface but it begins to crystallize in certain spots of this surface an then the crystallization propagates on other formed TiO_2 crystalline domains.

As a comparison, microstructural properties of a solid-state treated TiO_2 are reported (for the impossibility to compare data from amorphous hydrothermal treated TiO_2), in particular after a 400 °C and 3 hours heat treatment in a muffle furnace. Cell parameters resulted to be *a*= 3,7825(1) Å and *c*= 9,4664(1) Å, with mean crystallites' size of 66(1) nm, which is reasonably higher with respect to hydrothermal treatment for the promotion of grains growth. Furthermore, it is reported in literature that ferrites NPs possess cell parameters of *a*= 10,3929 Å, 8,3457 Å and 8,3873 Å for Lu_2O_3, $NiFe_2O_4$ and $CoFe_2O_4$, respectively, quite comparable with the TiO_2 *c* parameter length.

In Figure 43, surface morphology of synthesized samples is presented.

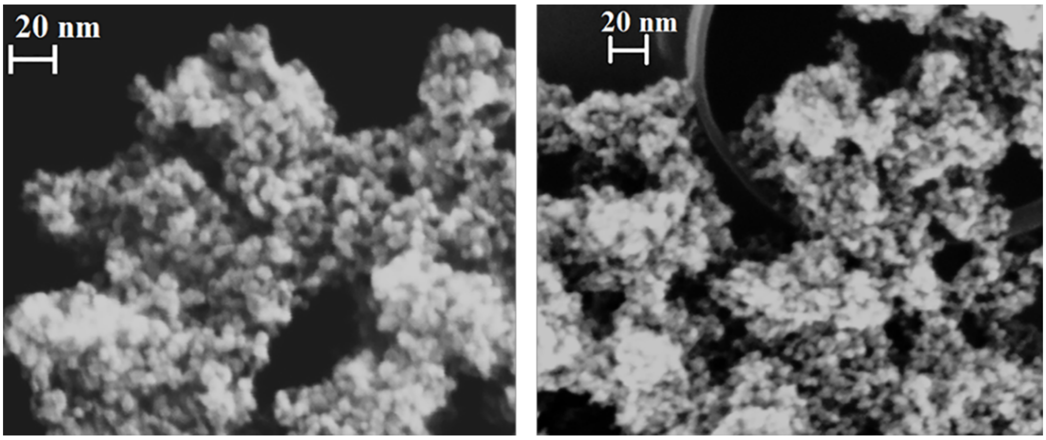

Figure 43: FE-SEM images taken at 20 kV of Sample 3 (left) and of Sample 4 (right)

For the fact that all samples shown a similar morphology only Sample 3 and Sample 4 FE-SEM images were reported. The appearance is quite spongy for the agglomerates but with a closer look it is possible to note very small particles, ranging from 5 to 15 nm, forming the micrometric aggregates.

In figure 44 the thermal behaviour of the samples is reported.

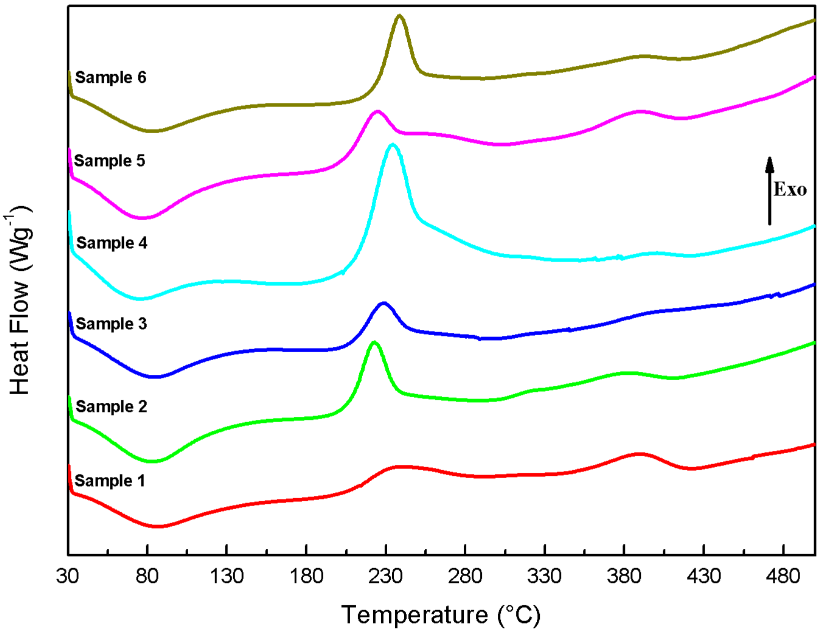

Figure 44: Thermal behavior of the different synthesized samples investigated under O_2 flow (20 mL/min) between T_{room} and 500 °C

Each sample shows a similar trend, with a first endothermic peak, due to the desorption of water, starting around 80 °C. Then, an exothermic signal is visible for each sample at a T_{onset} of 210 °C, with slight differences in the subtended area, which can be ascribed to residual 2-Propanol (from synthesis), adsorbed in the bulk TiO_2 and burnt under O_2 flow during the thermal analysis. A second small but broad exothermic peak, centred at a temperature of 380 °C, related to the phase transition from amorphous titania to anatase, can be detected in every sample. From this last signal, we could state the difference of action among the nucleation seeds, which led to different (but always small) amounts of amorphous phase. This fraction can be anyway neglected with respect to the crystalline portion, as highlighted from XRD analysis.

In table 17, results from photocatalytic results are reported.

Table 17. Photocatalytic efficiency of synthesized samples

Sample	***Degradation (%)*** ***(120 min)***	***St. Dev.*** ***(n=3)***
Sample 1	98.71	1.38
Sample 2	95.36	4.01
Sample 3	97.94	1.26
Sample 4	97.11	2.10
Sample 5	98.78	0.59
Sample 6	96.88	0.10

The activity of all the synthesized samples results to be practically the same: considering the standard deviation over the three replicates, the percentage degradation value fit in the same range for each sample, thus indicating that the different nucleation seed didn't affect the photocatalysts' efficiency.

Hence, the different thermal behaviours highlighted with DSC analyses, compared to the percentage degradation values, may be explained by different surface areas characterizing the bulk samples. In fact, through the hydrothermal synthesis used for these samples, BET measurements brought to values of 200,23 ± 0,5 (1) m^2/g and 218,30 ± 0,5 (1) m^2/g for Sample 3 and Sample 4, respectively. These values, compared to usual solid-state thermal treatments, result very high (usual surface areas of 50-100 m^2/g for calcined samples[108]), indeed they can also explain the high photocatalytic efficiency. With lower temperature conditions, it is reasonable to think that the sintering of particles, due to diffusion mechanisms, is hindered, thus leaving crystalline samples with very high surface areas.

These values can also justify the thermal behaviours presented in Figure 44, that show little differences between the subtended areas, thus ascribable to different surface areas.

3.3.3. Conclusions

In this work it was possible to demonstrate that crystalline anatase TiO_2 can be obtained at significantly lower temperature, in presence of nanoparticles seeds, with respect to usual thermal treatments. The presence of small amounts of ferrite nanoparticles in the hydrothermal reactor, with a ratio equal to 1:1000, allows to obtain crystalline titanium dioxide, as these nanoparticles actually act as nucleation seed for the crystallization. The nucleation starts onto the ferrite nanoparticle surface, likely growing towards a preferential direction (the lattice parameter with comparable length), and thus an anatase crystalline seed is formed, which in turn will act itself as a new nucleation spot. It was proven that the nucleation can proceed in any case, without noticeable differences in the synthesized samples due to the different seeds used: XRD patterns, surface area values, thermal behaviours and photocatalytic efficiency were essentially the same for all the samples. Eventually, it was demonstrated that also non-ferrite structured nanoparticles (Lu_2O_3) could act as nucleation seeds.

3.4. Synthesis of PDMS Membranes loaded with N-doped TiO_2 through Electrospinning Process

TiO_2 was prepared via sol-gel synthesis and subjected to a hydrothermal treatment in presence of a minimum amount (1:1000) of nanoparticles in order to act as nucleation seeds. Concurrently, high pH so-gel syntheses were performed with increasing NH_3 concentrations in order to compare samples' antibacterial activity. Polydimethylsiloxane was chosen as supporting material for TiO_2 nanoparticles, for its high surface area and stability against TiO_2 photoactivity. They were both processed with the electrospinning technique: it was possible to disperse titania among PDMS fibres and to obtain detachable polymeric membranes with the appearance of white soft sheets. These membranes show antibacterial activity under fluorescent light; hence they may be used as coating film for several kind of surfaces. Synthesized samples were controlled and characterized by means of rheological measurements, SEM-EDS images, DSC analyses, E_g calculation by means of diffuse reflectance (Kubelka-Munk plot), recycling photocatalytic experiments and bacterial inactivation with *Escherichia Coli* colonies.

This project was carried out in collaboration with the research group of Prof. M. Castellano and S. Vicini of the Industrial Chemistry Section of University of Genova.

3.4.1. Materials and Methods

TTIP, 2-Propanol and deionized water were used as sol-gel precursors for the photocatalyst synthesis. NH_3 solutions were prepared by diluting a parent solution (28-32%, VWR Chemicals) with deionized water and used for doped samples. The same experimental synthetic procedure described in Chapter 3.3.1. was used, in order to obtain a crystalline TiO_2 gel at a concentration of 3,99 g/L; instead, TiO_2 powders are too unstable to be firmly dispersed in an organic solvent (in fact, the suspension settles down too fast, with respect to the time and the flow rates employed during the electrospinning process). N-doped samples were synthesized with the same experimental procedure, with the only exception of the aqueous solution, which is replaced by NH_3 solution at three different concentrations (1, 5, 15 % V/V).

Two different hydroxyl-terminated PDMS prepolymers (PDMS-Low-Weight, viscosity= 18000-22000 cSt and PDMS-High-Weight, viscosity= 50000 cSt) with two different molecular weights, were used a precursors for the polymeric support; anhydrous tetrahydrofuran “THF”, with 250 ppm of butylated hydroxytoluene “BHT” as inhibitor (≥ 99,9%), was used as solvent, tetraethyl orthosilicate “TEOS” (reagent grade 98%) was added as cross-linking multifunctional agent and eventually HNO_3 (69%), used as acidic catalyst for the hydrolysis reaction. Dibutyltin dilaurate “DBTDL” (95%) was used as curing agent. All products were supplied by Sigma Aldrich and used as received. The two prepolymers were mixed at a ratio of 20:80 for respectively PDMS-HW and PDMS-LW: precisely, 0,88 g of PDMS-HW and 3,52 g of PDMS-LW were dissolved in 8,34 mL of THF. Later, 0,54 mL of TEOS were added. Each precursor is added in a twin-neck RB flask and left for 15 minutes before each addition, in order to equilibrate the temperature to 80 °C, controlled by means of a silicon oil bath; 16

μL of HNO_3 were added and then the mixture was left for 20 min under reflux conditions with a condenser; once finished, the solution is subjected to three days of aging in an oven at 50 °C, where slight evaporation of the solvent from the gel occurs. During this curing time, the cross-linking process between PMDS and TEOS proceeds, but has to be concluded onto the collector's surface during the electrospinning process. Above-mentioned synthetic conditions were chosen among other different possibilities, reported in Table 18.

Table 18. Synthetic conditions investigated for PDMS solution synthesis (bold numbers represent the optimized values)

PDMS-OH LW	2,23 g	**3,52 g**		
PDMS-OH HW	2,18 g	**0,88 g**		
THF	**8,34 mL**			
TEOS	**0,54 mL**			
HNO_3 (69%)	5 μL	11 μL	**16 μL**	200 μL
DBTDL in THF	5% (V/V)	**10% (V/V)**		
Bath Temperature	50 °C	**80 °C**		
Reflux Time	**20 min**			
Curing Time	24 h	48 h	**72 h**	96 h

Once PDMS solution aged correctly, it was possible to set up the electrospinning apparatus, with the configuration shown in Figure 45[109].

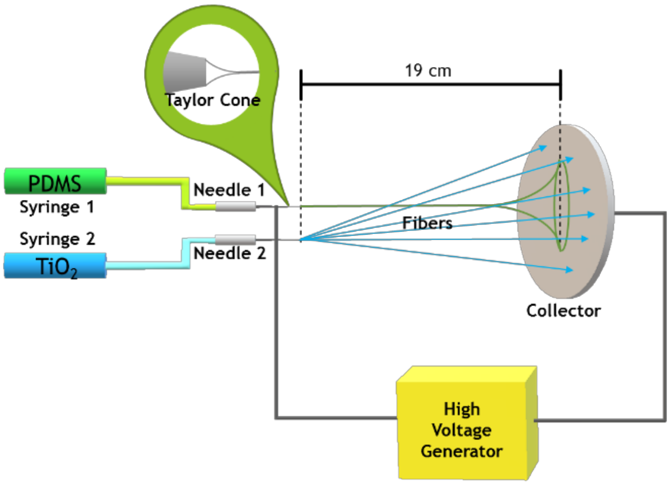

Figure 45: Electrospinning set-up for simultaneous spinning and spraying of PDMS and TiO_2 crystalline gel

Electrospinning was performed under a voltage of 12 kV; the distance between needles and collectors was set to 19 cm. The flow rates were set to 0,065 mL/min for PDMS solution and TiO_2 gel. Before the electrospinning process started, 2 mL of a THF solution of DBTDL (10% V/V), were dabbed onto the collector's surface in order to complete there the cross-linking process. 5 mL of PDMS solution were used to obtain one piece of membrane, with a thickness smaller than 1 mm; TiO_2 was left as obtained from the hydrothermal treatment. When it comes to N-doped TiO_2 gels, processing electrospinning conditions were modified, as the gel conductivity was likely modified by the presence of ammonia. The voltage had to be then raised up to 16 kV, in order to have a proper spray of the gel, while the distance between electrodes and collector, reduced to 15 cm, due to a mutual repulsion of the two jets, which occurred when using doped TiO_2 and hindered the membrane formation: as a matter of fact, it was possible to obtain PDMS membranes only with 1% and 5% of NH_3, while 15% NH_3 resulted to be incompatible with the used apparatus.

All synthesized samples were then physical-chemical characterized by means of rheological measurements, in order to assess the cross-linking degree by evaluating the viscosity values of the PDMS solutions, after different aging times. The dynamic-mechanical analyses were carried out using an Anton Paar Physica MCR 301 Rheometer. Tests were performed in Time Sweep "TS" mode, with constant strain of 10% (value within the linear viscoelasticity region, evaluated by preliminary Amplitude Sweep "AS" tests), enforcing a deformation frequency of 1 Hz. All measurements were set to 25 °C. After the electrospinning, FE-SEM images were collected in order to state the samples' morphology: EDS spectra were collected to detect Ti signal within the membrane. Fibres mean diameter was assessed with ImageJ 1,51r as statistical distribution measured over 200 fibres.

N-doped TiO_2 samples were investigated on their thermal behaviour by means of DSC analyses, in the range between 30 and 600 °C in air atmosphere. Last, diffuse reflectance spectra were collected using a CM-2600d spectrophotometer (Konica Minolta) equipped with an integrating sphere, in order to extrapolate the E_g values from the graphical representation, in the spectral range of 400-700 nm, with the Kubelka-Munk method[110].

Photocatalytic experiments were performed using 20 mL of 0,01 g/L MB solution: these recycling tests were performed in order to preliminarily prove that the interaction between the catalyst and support was strong enough to keep the particles attached to the PDMS, thus the photocatalytic activity against the dye wouldn't show any reduction. Experimentally, MB solution was poured into a Petri capsule (at the bottom of which a piece of TiO_2 loaded membrane was put), placed under the solar simulated light lamp and left under irradiation for 30 min. Aliquots of the MB solution were taken at fixed times and analysed by means of UV-Vis spectrophotometry at λ= 664 nm. Each membrane was subjected to three consecutive cycles of photocatalytic experiments.

Antibacterial experiments were conducted on *Escherichia Coli* ATCC®1775 (1000 CFU, Cat #: RQC01707 – 10EA), purchased from Fluka Analytical, a gram-negative bacterium. A solution with E. Coli was diluted with sterilized 0,9% NaCl solution, in order to have known number of colonies (50 CFU) and transferred onto the polymeric membranes (4 cm^2). The membranes were then irradiated for 30, 60, 90 and 120 min with a neon fluorescent lamp (300-700 nm, 50 Hz, Neon L36W/640, 36 W). The membranes were then put in agar plates and placed inside an incubator and left for 24 hours at 37 °C[111]. Data were eventually analysed with a mixed-effect linear model, including time and treatment (TiO_2 and N-doped TiO_2 versus control) as fixed effects with an interaction term, and experiment batch as random effect (statistical analysis was performed with R 3.2.3.)

3.4.2. Results and Discussion

The correct aging time for the PDMS solution was measure by dynamic mechanical analysis, TS tests, by studying the viscoelastic behaviour with the evaluation of the storage modulus G' and the loss modulus G'' of the polymer, in order to assess the change from viscous to elastic behaviour. In Figure 46 the viscoelastic behaviour of three differently aged solutions is presented.

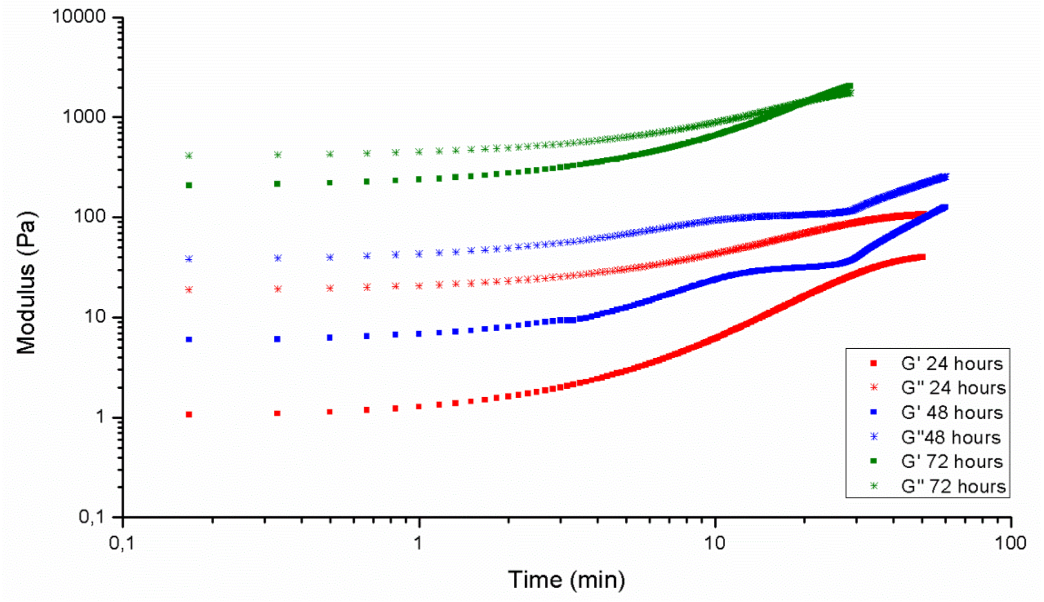

Figure 46: Viscoelastic behaviour of: ■) Storage modulus G' and •) Loss modulus G'' of three samples aged for 24 hours (red), 48 hours (blue) and 72 hours (green)

Thanks to this characterization, it was possible to state that an aging time equal to 72 hours at least is mandatory to get the cross-linking point (i.e. the change from a viscous liquid-like behaviour to an elastic solid-like one) in the right time, in order to reach the end of the cross-linking process during the electrospinning. The crossover between G' and G'' appears in a reasonable time: 20,5 min with 72 hours of curing while it doesn't appear if the aging time is not sufficient for a sufficient cross-linking degree.

The following SEM images (Figure 47, Figure 48 and Figure 49) show the different morphologies obtained with the different aging times.

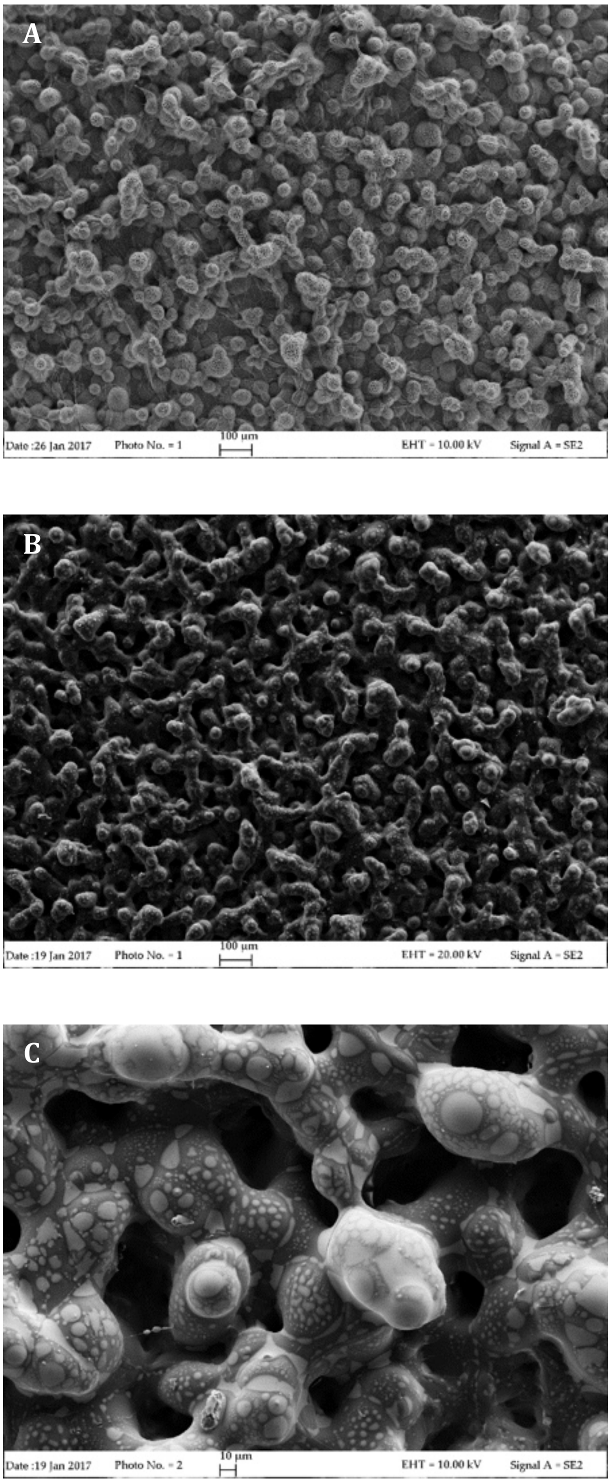

Figure 47: a-b) Different FE-SEM images for PDMS solutions cured for 24 hours (segment 100 μm); c) FE-SEM images for PDMS solution cured for 24 hours (segment 10 μm)

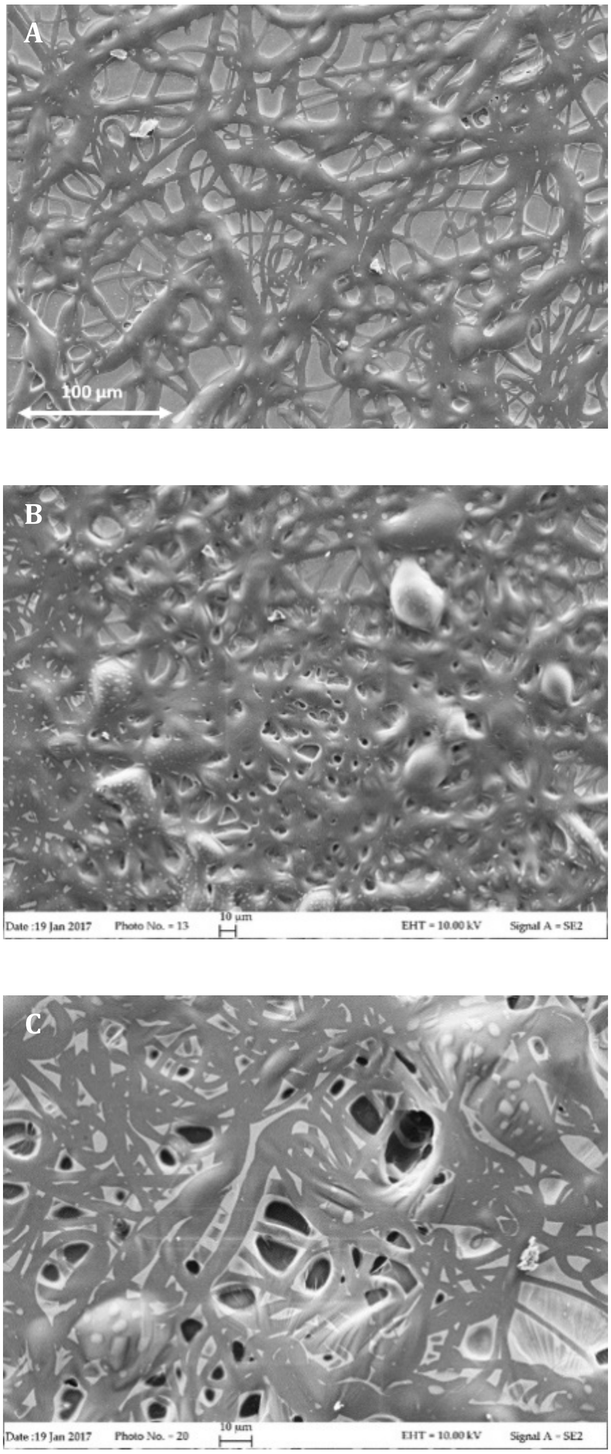

Figure 48: a) Different FE-SEM images for PDMS solution cured for 48 hours (segment 100 μm); b-c) FE-SEM images for PDMS solutions cured for 48 hours (segment 10 μm)

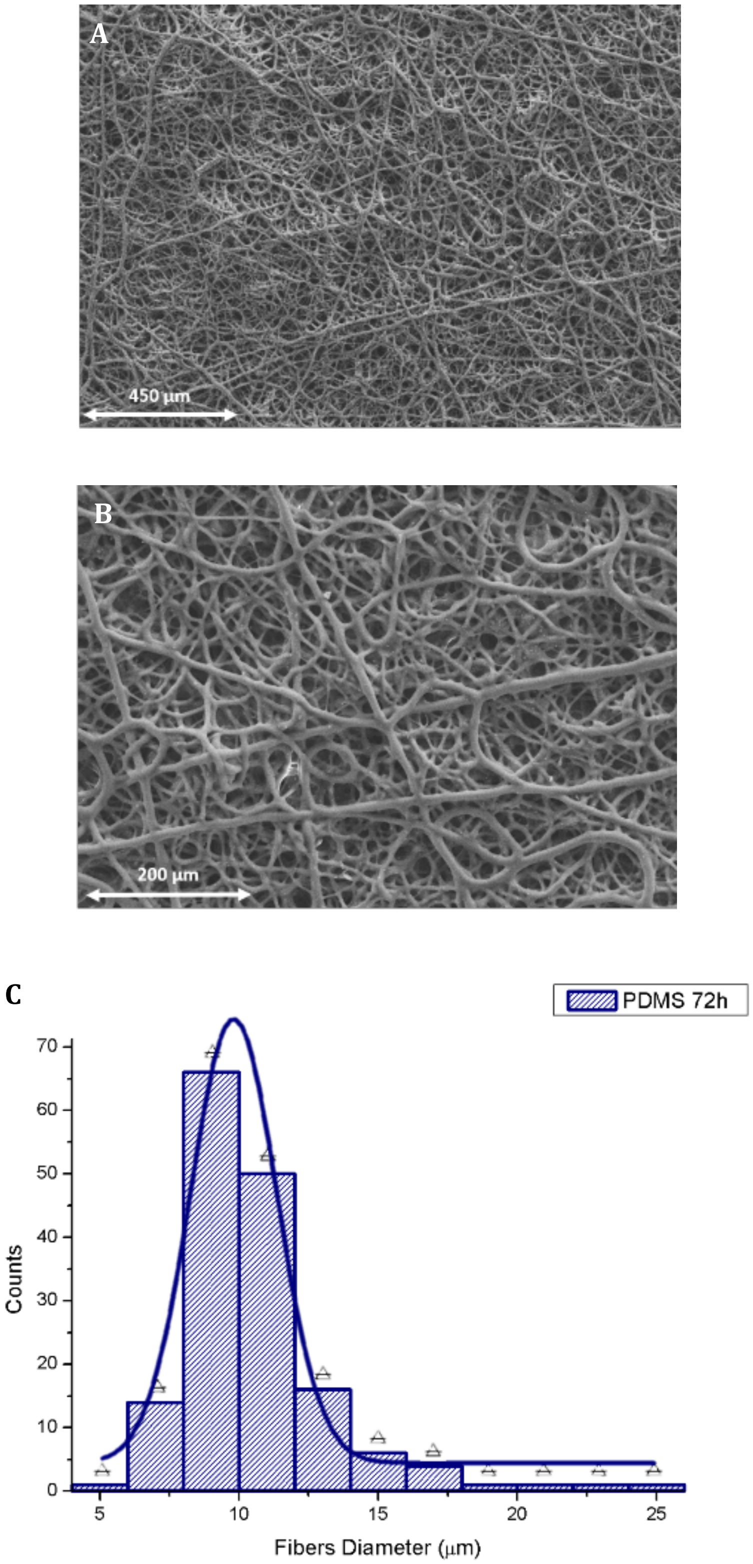
A
450 µm
B
200 µm
C
PDMS 72h
Counts
0
10
20
30
40
50
60
70
5
10
15
20
25
Fibers Diameter (µm)

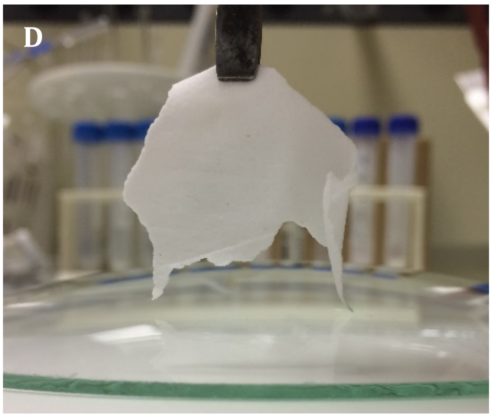

Figure 49: a) FE-SEM images for PDMS solution cured for 72 hours (segment 450 μm); b) FE-SEM images for PDMS solution cured for 72 hours (segment 200 μm); c) Statistical distribution histogram and Gaussian fitting curve of the PDMS fibres mean diameter; d) Single piece of membrane as obtained after electrospinning

It is clear how important the aging time of the PDMS solution is for the cross-linking process: every sample cured for a time lower than three days could not reach the elastic solid-like feature, indeed the membrane morphology show agglomeration of polymers, phase separations, blurred sizes and bi-dimensional films.

With the optimized parameter it was instead possible to obtain a white slim piece of PDMS membrane, with average micrometric fibres dimensions equal to 9,76 ± 3,13 μm, as calculated on 200 fibres.

The presence of standard and N-doped TiO_2 within the polymeric network was assessed by means of SEM-EDS images; indeed, EDS spectra highlighted the presence of the Ti signal above the main Si one. In Figure 50 it is possible to see the homogeneous distribution of TiO_2 NPs.

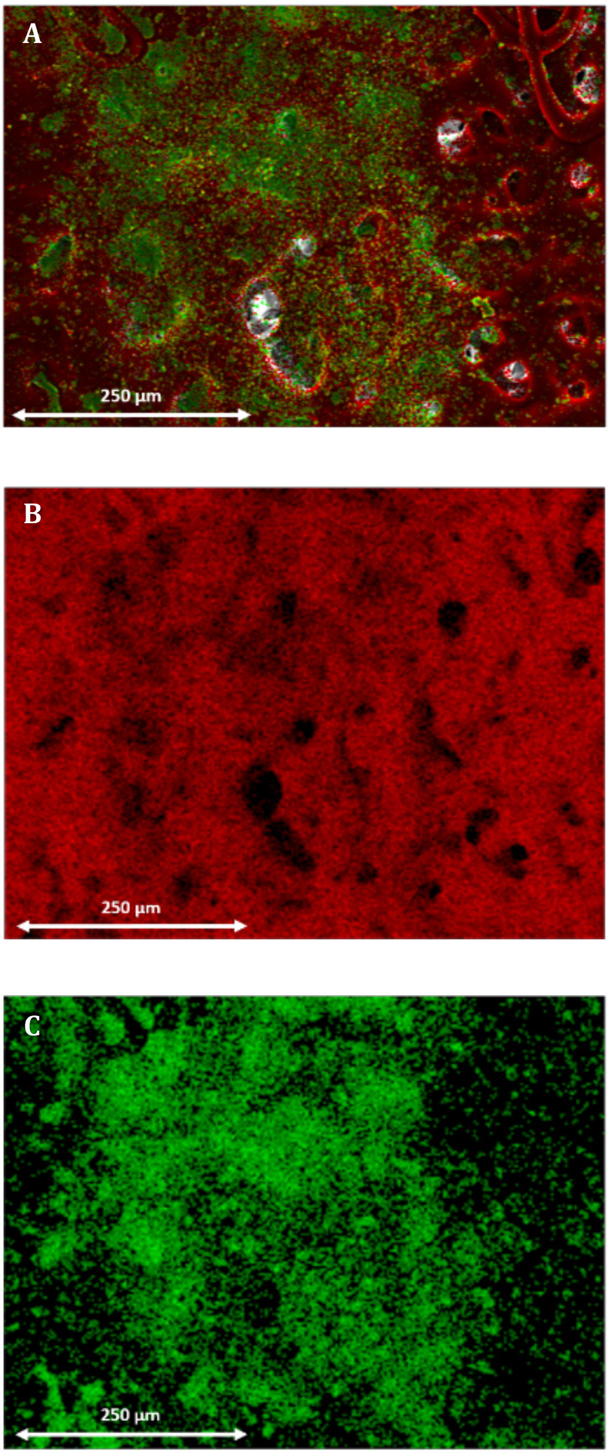

Figure 50: a-c) Elemental maps (Si red, Ti green) overlapped to SEM images; Si in b) and Ti in c) (segment 250 µm)

When the colloidal gel is synthesized with NH_3, as already mentioned, the processing electrospinning conditions had to be changed towards higher voltage values and closer electrodes distance, so that PDMS fibers as well as N-doped TiO_2 dispersion varied. The main problem occurred with ammonia samples, was the incompatibility between the two jets subjected to the voltage, due to a reciprocal repulsion, increasing with increasing NH_3 concentration. In Figure 51 it is possible to see the different samples' morphology due to the different synthetic conditions.

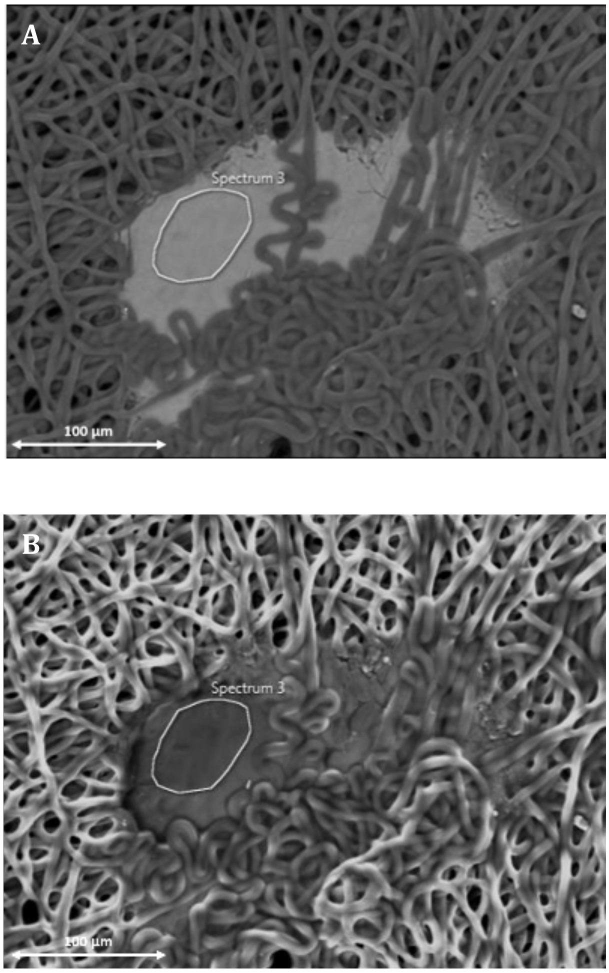

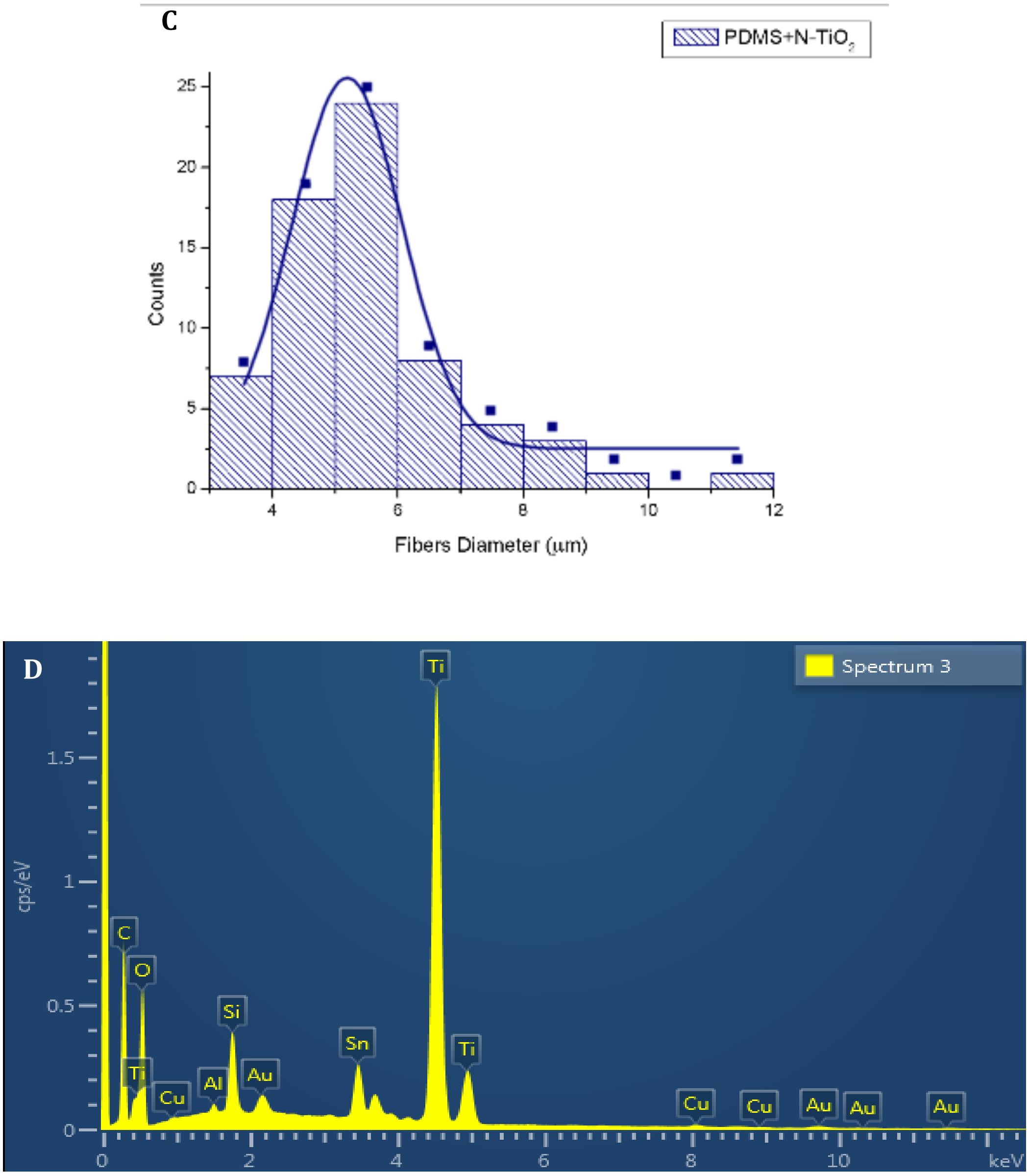

Figure 51: a-b) SEM images of N-doped TiO_2/PDMS with 5% NH_3, collected on BSE and SE; c) Statistical distribution histogram and Gaussian fitting curve of the same membrane; d) EDS spectrum collected in the highlighted region

Fibres mean diameter resulted to be mildly reduced in the range of 5,17 ± 1,78 µm, even if it fits the first dimensional range found for the unloaded PDMS fibres. It has to be noted that the N-doped TiO_2 dispersion has changed towards micrometric agglomerates rather than homogeneous interspersion within the matric. In addition, EDS spectrum lacks in N signal, pointing out that the doping maybe didn't occur properly through the hydrothermal synthesis.

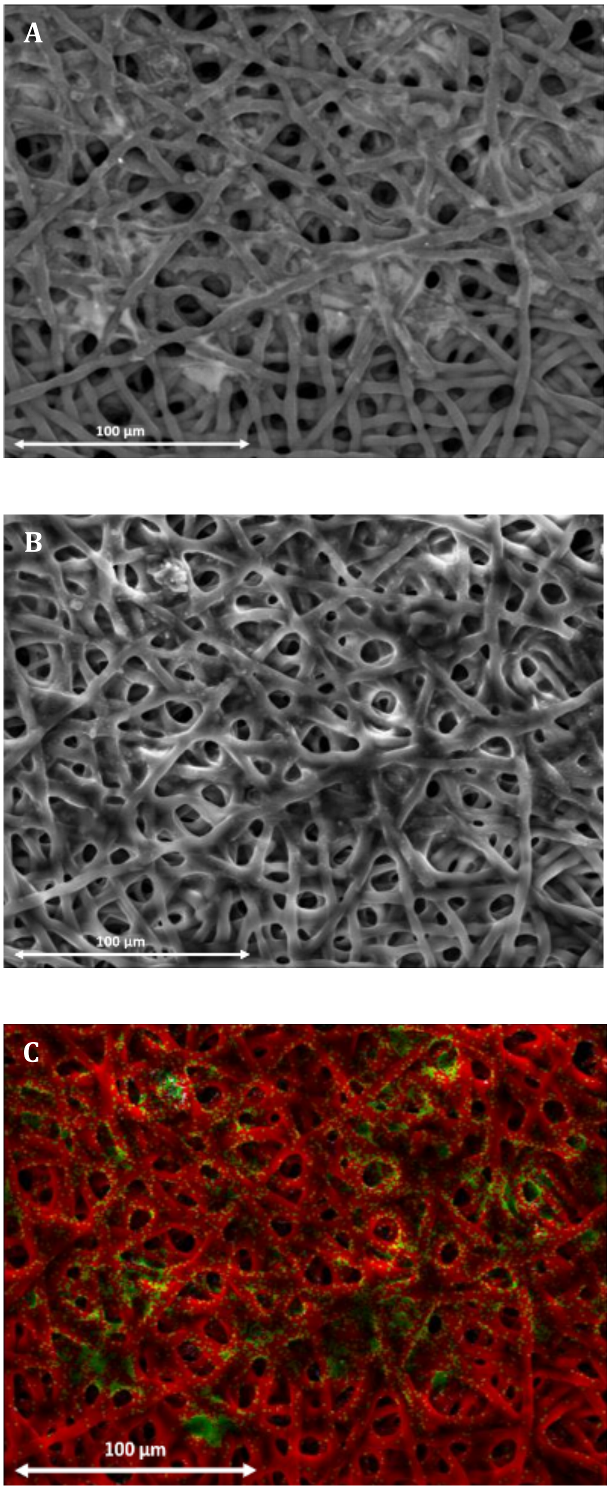

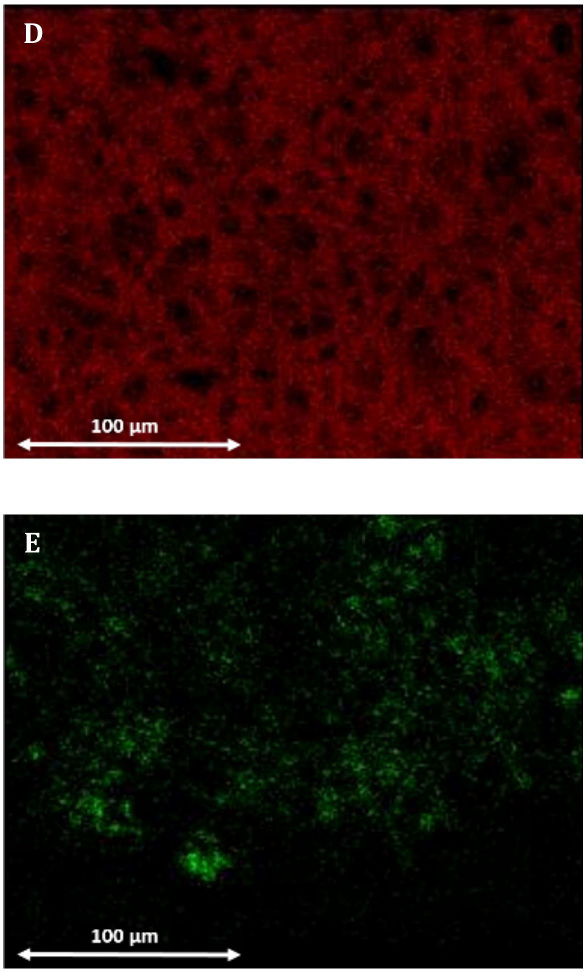

Figure 52: a-b) Other SEM images of N-doped TiO_2 (NH_3 5%)-PDMS collected on BSE and SE signals (segment 100 µm) respectively; c-e) Elemental maps (Si red, Ti green) overlapped to SEM images; Si in d) and Ti in e) (segment 100 µm)

Figure 52 confirms that the catalyst is not properly distributed throughout the membrane, despite its signal is still present in the elemental mapping, suggesting that strong alkaline conditions for the hydrothermal process are not suitable for an effective doping of the lattice as much as incompatible with the voltage electrospinning conditions. In order to highlight the different behaviour of the N-doped TiO_2 samples, we compared their thermal curves with respect to the standard TiO_2 obtained with the help of nano-seeds during the hydrothermal process, by means of DSC analysis, presented in Figure 53.

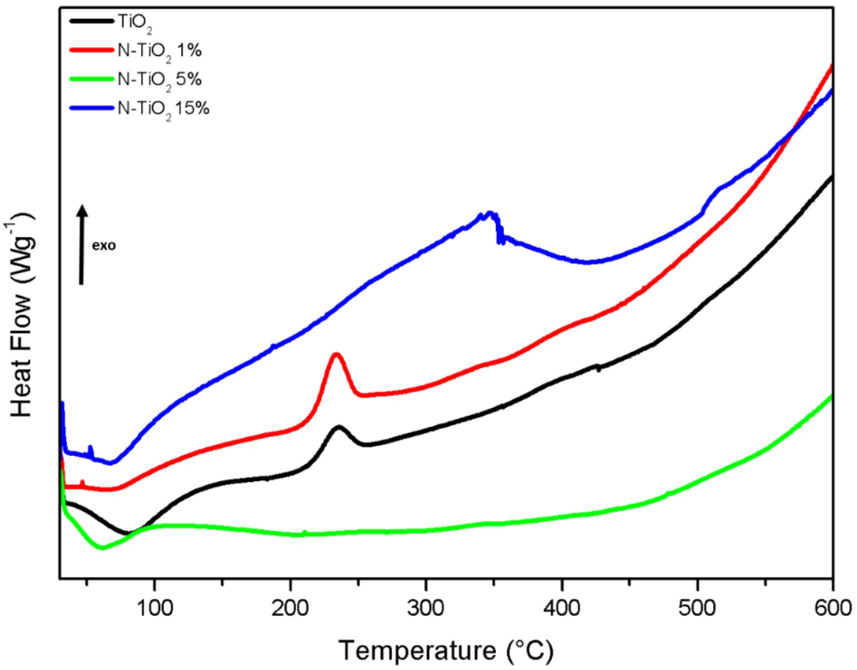

Figure 53: Thermal behaviours of the synthesized samples: standard-TiO_2 (black), N(1%)-doped TiO_2 (red), N(5%)-doped TiO_2 (green) and N(15%)-doped TiO_2 (blue)

It is possible to note from DSC analysis that standard and N-doped (NH_3 1%) TiO_2 are similar in their thermal behaviour, as they both display the first endothermic peak below 100 °C, due to the volatilization of residual water, as well as the exothermic peak due to the desorption and oxidation of residual organics, around 240 °C. The phase transformation peak, for the crystallization from amorphous to anatase phase, expected to be around 350 °C, in not visible for these two samples, prof the crystallization properly occurred during synthesis. It must be noticed that samples with increasing ammonia concentrations are, instead, quite different with respect to the previous ones. In particular, N-doped (NH_3 5%) TiO_2 sample seems to have reduced affinity for the organic compound adsorption, as the first exothermic peak has disappeared, while on the contrary, N-doped (NH_3 15%) TiO_2 shows some unexpected exothermic peaks (that may be ascribable to phase transformations from amorphous to anatase, or from anatase to rutile or even other Ti-N compounds).

Another important issue is semiconductor photocatalysis is E_g shift due to the dopant presence, which is intended to enhance the photons absorption in the visible range and thus to increase its activity in more eco-sustainable conditions.

In Figure 54, the diffuse reflectance spectra of the hydrothermal treated samples were compared, with also two reference of N-doped TiO_2 samples subjected to a solid-state synthesis (350 °C, 1 hour). The optical method of visible diffuse reflectance spectra (400-700 nm) was used to calculate the E_g using the Kubelka-Munk method, based on the following equation:

$$\textit{(Eq. }\mathbf{29}\textit{)} \qquad F(R) = \frac{(1-R)^2}{2R}$$

For the graphic representation, we have plotted $(F(R)*h\nu)^n$ versus hν, using n=2 for indirect allowed transitions, as reported in literature.

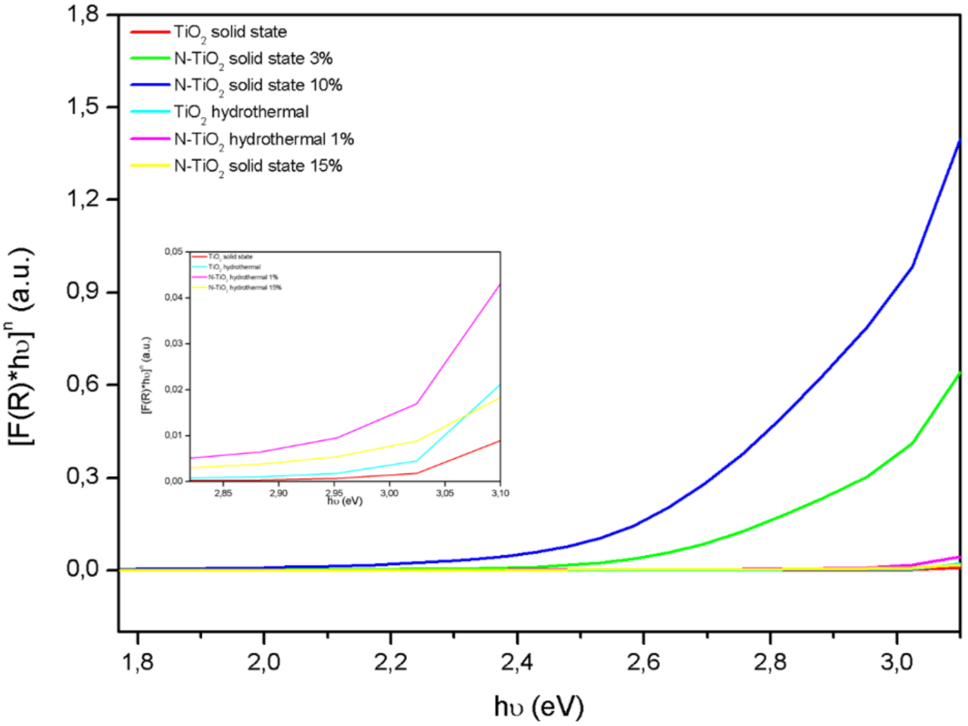

Figure 54: Kubelka-Munk graphic representation plot for the E_g measurements. Inset shows an enlargement of the range 2,80 to 3,10 eV)

These analyses highlighted that the hydrothermal treatment doesn't affect samples' Eg value, with respect to the solid-state reference samples, reported in blue and green. In the enlarged frame it is possible to see very slight difference in the position of the reflectance signals, proof that the NH_3 presence, in different concentrations, along with the hydrothermal process, do not considerably shift the gap between the bands and thus the activity is not improved.

In Figure 55 it is possible to see the degradation results of a 0,01 g/L MB solution as a comparison between PDMS membranes with and without standard-TiO_2 nanoparticles. The results demonstrate that the bare PDMS membrane shows an average abatement of 30% of the MB solution, likely for the direct photolysis of the dye due to the proximity of the lamp to the Petri plates. These analyses highlighted that the re-use of the same membranes lead to the same abatement degree (values within the standard deviation) without any noticeable activity loss, sign that the interaction between PDMS and standard-TIO_2 is stable enough to resist to at least 3 consecutive recycling experiments in aqueous medium.

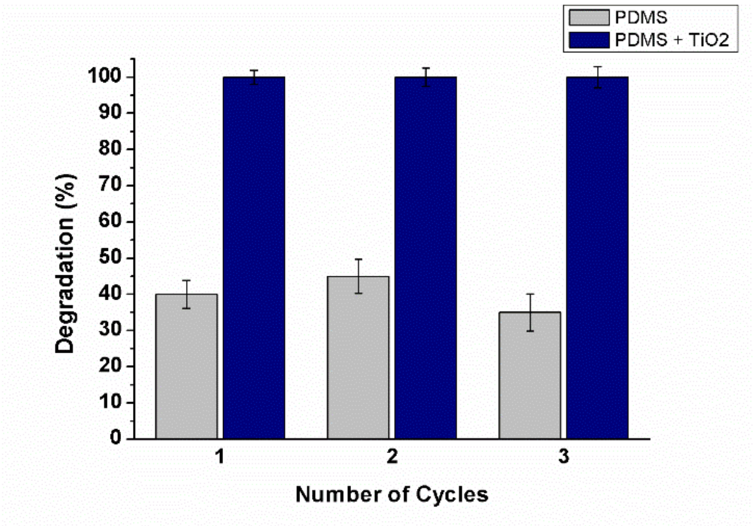

Figure 55: MB percentage degradation results for 3 consecutive cycles

N-doped TiO_2 loaded membranes were not subjected to recycling experiments in favour of the antibacterial activity experiments. This was evaluated by the inactivation of *E. Coli* cultures, after different irradiation intervals with a fluorescent lamp and results are shown as a comparison between load and unloaded membranes. In particular, a starting inoculum of *E. Coli* is prepared from a parent LB-Agar solution, diluted with physiological solution (NaCl 0,9%, sterile) down to 100 CFU. 1 mL of the inoculum is poured onto the different synthesized membranes and then each sample is subjected to different times of irradiation. After this, the membrane is placed above a Petri dish, filled with EMB Agar medium, and left growing overnight at 37 °C in an incubator. At the mixed linear model analysis, a significant effect of time, treatment and interaction ($p < 0,001$) was observed. All time-points from 30 to 120 min had a lower CFU count compared to baseline, with a significantly lower CFU count in the samples treated with the TiO_2 and N-doped TiO_2 (NH_3 5%) membranes. No differences were observed between doped and undoped TiO_2 at any time-point. Antibacterial activity results are reported in Figure 56.

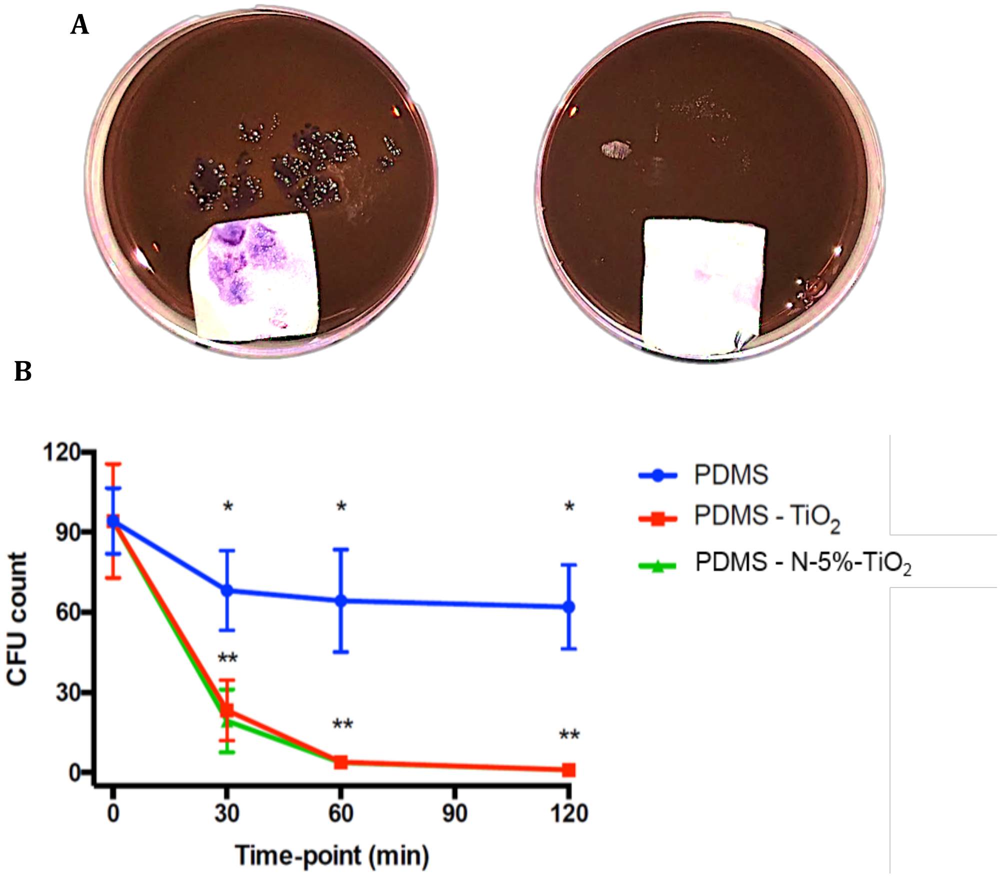

Figure 56: a) E. Coli growth in PDMS membrane (left) and in PDMS-standard-TiO_2 membrane (right); b) CFU count at the difference time-points with control membrane (control) or TiO_2-loaded membrane (TiO_2). *Significantly lower compared to baseline in all treatment arms (p< 0,001); **TiO_2 and N-doped TiO_2 significantly lower than control (p< 0,001). Dots represent mean value; bars represent the standard error of the mean

3.4.3. Conclusions

A composite material with important antibacterial features was successfully synthesized, as the porous structure of the PDMS membrane, joined with the macroscopic manoeuvrability of the sheet itself, allows a satisfying TiO_2 surface activity against *E. Coli* cultures. This material can be employed in a wide range of fields: it can be applied to several surfaces, it is easily activated under artificial light and it can be detached without difficulties; furthermore, as highlighted with recycling tests, the composite is recyclable. TiO_2 activity is not limited by the support because it has a very high surface area and the interaction between PDMS fibres and the catalyst is strong enough to avoid the dispersion of the TiO_2, as highlighted with MB recycling experiments, for at least 3 consecutive cycles. N-doped TiO_2 samples didn't behave as forecast, because the hydrothermal synthesis did not provide the proper conditions to dope effectively the catalyst's lattice, with respect to the solid-state treatment. In fact, the E_g wasn't affected at all by the different NH_3 concentrations and the electrospinning conditions changed towards an increasing incompatibility between PDMS and TiO_2 jets corresponding to more concentrated ammonia solutions. Furthermore, the antibacterial activity was not improved for the alkaline conditions, so it is finally feasible to state that, for this purpose, it is possible to get a satisfying antibacterial activity with just standard low-temperature crystallized TiO_2. Lastly, the composite material's synthesis was chosen in order to be easily scaled up towards the industrial production, indeed, the electrospinning process fits in this choice for its easy handling and process parameters' control.

3.5. Synthesis of TiO_2 supported on Magnetic Zeolite obtained from Industrial Waste

In the current work, a new nanometric TiO_2-based magnetic catalyst has been developed from an innovative material obtained from the treatment of iron and steel industrial waste, i.e. Fly Ash. This magnetic material contains iron in the chemical-mineralogical composition, and it represents an excellent example of circular economy: the industrial waste is converted into a high technological valued product. Through a one-step hydrothermal activation, the precursor is transformed in a zeolite with good magnetic properties. These features could be exploited in the environmental field, such as the degradation of emerging pollutants in aqueous media by coupling it with a photocatalyst. In particular, TiO_2 NPs are synthesized with a sol-gel technique and then mixed with the magnetic material by means of ultrasounds, in different pH conditions: acidic (0,1 M HNO_3), neutral and alkaline (0,1 M NaOH). Afterwards, the composite is subjected to a mild heat treatment to reinforce the interaction. The synthesized materials are characterized by means of XRD and SEM-EDS while their photocatalytic activity is evaluated through the abatement of MB solutions, testing also the possibility to magnetically recover the suspension and reuse the catalyst.

This project was carried out in collaboration with the research group of C. Belviso from Institute of Methodologies for Environmental Analysis of the National Research Council and the research group of Prof. D. Peddis from the Institute of Matter Structure of the National Research Council.

3.5.1. Materials and Methods

Synthesized samples are reported in Table 19.

Table 19: Synthesized samples and treatment conditions of TiO_2/F.A. samples

Sample	**Mixing Method**	**TiO_2:FA:H_2O**	**Thermal Treatment**	**pH**
FA-USN	Ultrasound (35 kHz)	2:1:20	Oven – 100 °C	Neutral
FA-USB	Ultrasound (35 kHz)	2:1:20	Oven – 100 °C	Alkaline
FA-USA	Ultrasound (35 kHz)	3:1:20	Oven – 100 °C	Acidic
FA-MSN	Magnetic Stirring (1000 rpm)	3:1:20	Oven – 100 °C	Neutral

TiO_2 is synthesized through the sol-gel route, with TTIP: 2-Propanol and deionized water used as precursors in a volume ratio of 1:2:5, respectively. 0,1 M HNO_3 and 0,1 M NaOH were prepared with deionized water and used for acidic and alkaline synthetic conditions. All products are supplied by Sigma Aldrich and used as received.

Fly Ash zeolite is synthesized by means of a low temperature hydrothermal synthesis, after a pre-treatment fusion with NaOH. In detail, Fly Ash precursor, got from a thermoelectric power plant, is grinded for few minutes in a mortar with NaOH at a weight ratio equal to 1:1,2, respectively. The resulting mixture is then heated up to 550 °C for 1 hour and the resulting solid is grinded again to obtain powders. Deionized water is added to the powders and the solution is kept under vigorous stirring overnight. After being stirred, the solution is incubated in hydrothermal reactor for 4 days at 35 °C and later centrifuged in order to separate the solid zeolite, which is eventually rinsed with distilled water and dried at 80 °C for 12 hours. Other specifications about the synthesis can be found in previous works[112,113].

In the current project, zeolite is used as prepared from the abovementioned process. In particular, TiO_2 powders, obtained from the sol-gel process, once dried and grinded, are heat treated in a muffle furnace for 1 hour at 350 °C, in order to let the phase transformation from amorphous to anatase. Crystallized catalyst's powders are now mixed, for 15 min, with the magnetic zeolite, according to the ratios and the synthetic conditions reported in Table 19.

Synthesized samples are physical-chemical characterized: XRD analyses were performed with a Philips PW1830 diffractometer (Bragg Brentano, Co Kα, Ni filter, 20-80 2θ, step 0,025 2θ, sampling time 10 s). SEM-EDS images were collected using a Leica Cambridge S530, coupled with an EDS Oxford X-Max 20 detector. Photocatalytic experiments were performed with 25 mL of a 0,05 g/L MB (for screening tests) and 25 mL of a 0,01 g/L MB (for recycling tests), using 0,0125 g of each catalyst. Experimentally, samples were placed under solar simulated light, at 20 cm above the solution, and left under magnetic stirring for 20 min in dark conditions. Later, the irradiation source was switched on and left for 60 min, while 1 mL aliquots were taken at fixed times. Percentage degradation was evaluated by means of UV-Vis spectrophotometry, at λ= 664 nm.

3.5.2. Results and Discussion

Figure 57 shows the Fly Ash precursor morphology and its elemental composition.

A

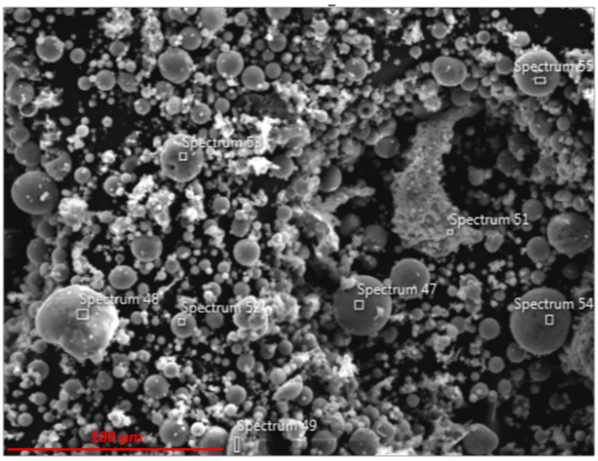

B

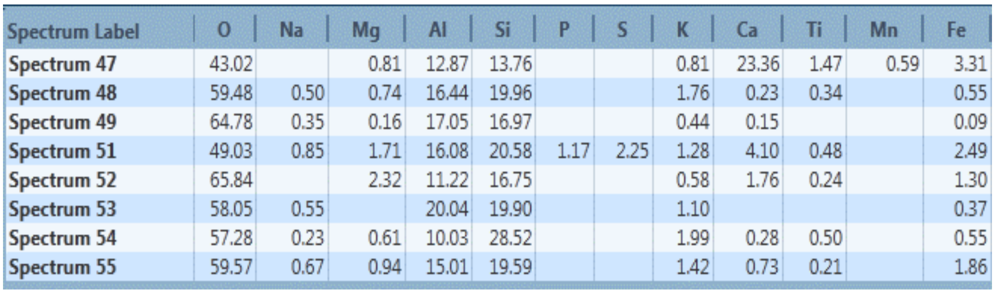

Spectrum Label	O	Na	Mg	Al	Si	P	S	K	Ca	Ti	Mn	Fe
Spectrum 47	43.02		0.81	12.87	13.76			0.81	23.36	1.47	0.59	3.31
Spectrum 48	59.48	0.50	0.74	16.44	19.96			1.76	0.23	0.34		0.55
Spectrum 49	64.78	0.35	0.16	17.05	16.97			0.44	0.15			0.09
Spectrum 51	49.03	0.85	1.71	16.08	20.58	1.17	2.25	1.28	4.10	0.48		2.49
Spectrum 52	65.84		2.32	11.22	16.75			0.58	1.76	0.24		1.30
Spectrum 53	58.05	0.55		20.04	19.90			1.10				0.37
Spectrum 54	57.28	0.23	0.61	10.03	28.52			1.99	0.28	0.50		0.55
Spectrum 55	59.57	0.67	0.94	15.01	19.59			1.42	0.73	0.21		1.86

Figure 57: a) SEM image of the Fly Ash precursors morphology, before hydrothermal synthesis (segment 100 μm); b) Elemental composition of different spots selected in the SEM image

Main constituents of this material are Si, Al and O, suggesting that high amounts of SiO_2 and Al_2O_3 are present in the sample. This is the reason why Fly Ash was used as zeolite precursor. All particles have a spherical shape, with a dimensional range comprising few to tens micrometres; local composition significantly varies according to the investigated spot, proof of inhomogeneity of the precursor.

SEM-EDS images of the titania-supported magnetic zeolite are instead reported in Figure 58, where it is possible to note the local elemental composition in Al, Si and Fe of the supporting material together with the Ti from TiO_2 signal.

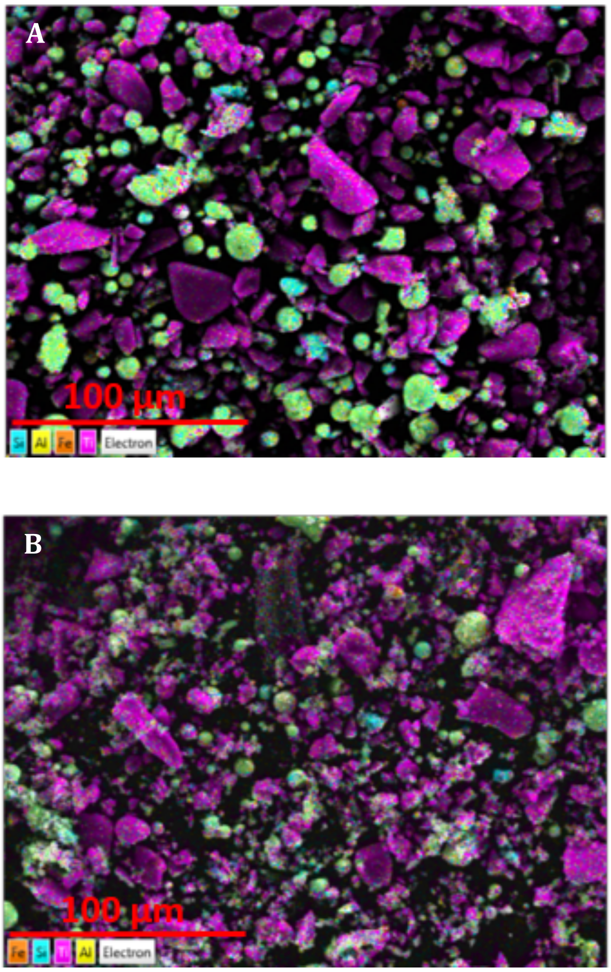

Figure 58: a) Elemental mapping overlapped to a SEM image for catalyst FA-USA (Si light blue, Al yellow, Fe orange, Ti purple) (marker 100 μm); b) Elemental mapping overlapped to a SEM image for catalyst FA-USB (Si light blue, Al yellow, Fe orange, Ti purple) (marker 100 μm)

From this characterization it is possible to underline that the different synthetic conditions mainly led to two different morphological features: the acidic synthesis, FA-USA, led to an inhomogeneous recovery of TiO_2 onto the magnetic support, highlighting that some spots lack in Ti signal. Alkaline conditions, instead, led to a better covering of the supporting material. This fact may be due to surface interactions occurring between FA-zeolite and TiO_2: titania surface is functionalized by the alkaline medium of the synthesis with a negative charge that can interact with the zeolite support in a stronger way with respect to the positively charged TiO_2 (acidic). In both cases, morphology slightly changed from spherical to a mixed spherical-rectangular shape, with respect to the precursor, but comparing acidic and alkaline conditions, it seems that the latter led to a smaller particle size.

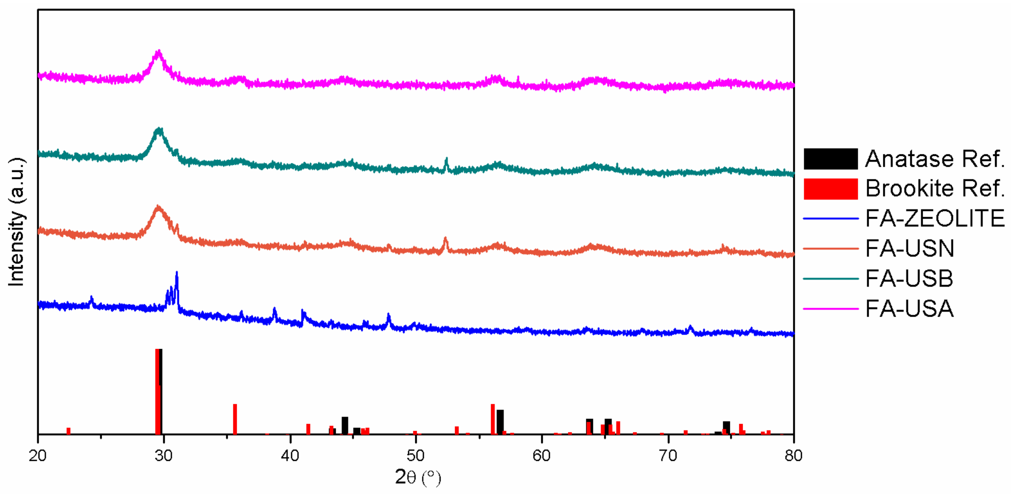

Figure 59: XRD spectra of anatase (black) and brookite (red) TiO_2 (Reference from Pearson's Crystal Data), FA-Zeolite (blue), FA-USN (orange), FA-USB (dark cyan) and FA-USA (magenta)

Figure 59 shows the normalized XRD spectra, which were performed in order to investigate if some visible crystalline structure modifications occurred in the material due to the different synthetic conditions. As reference, anatase and brookite TiO_2 polymorphs and unsupported FA-zeolite spectra are reported. At a first glance, no remarkable differences were detected: each composite sample has the most intense peak centred around 30 2θ and its width could be related to different reasons: nanometric size of crystallites, superimpositions of signals deriving from different crystalline phases (anatase, brookite and zeolite) or eventually a low crystallinity degree. With respect to reference spectra, all three supported samples seem to resemble the anatase crystallographic structure, together with some brookite-attributable peaks. Furthermore, Samples FA-USA and FA-USN show some extra peaks around 52 2θ which can be ascribed to the beginning of some other structure transformations, apart from the one abovementioned. Indeed, it is reported in literature that alkaline conditions and high temperature may lead to the formation of geopolymer superstructures, i.e. zeolites' hydrolysis products with a different crystalline habitus and thus adsorbent capacities, which could be much more alike towards TiO_2 adsorption, rather than acidic conditions[114].

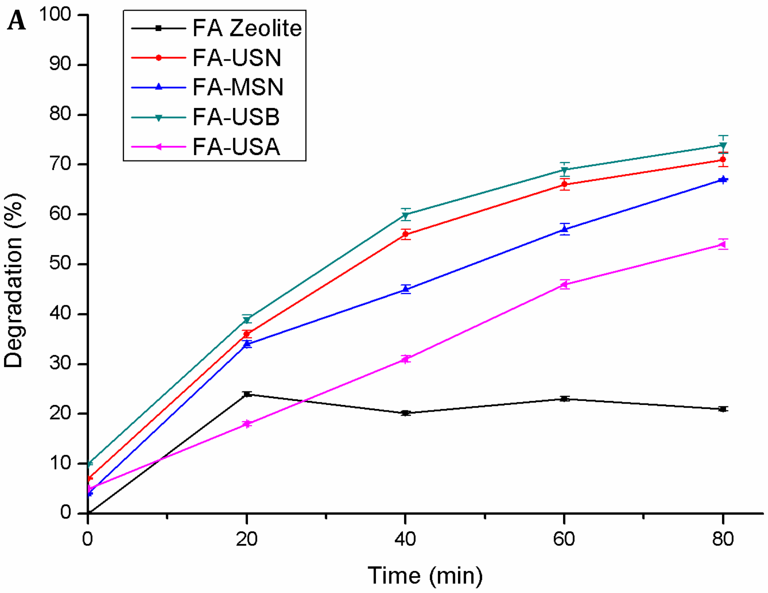

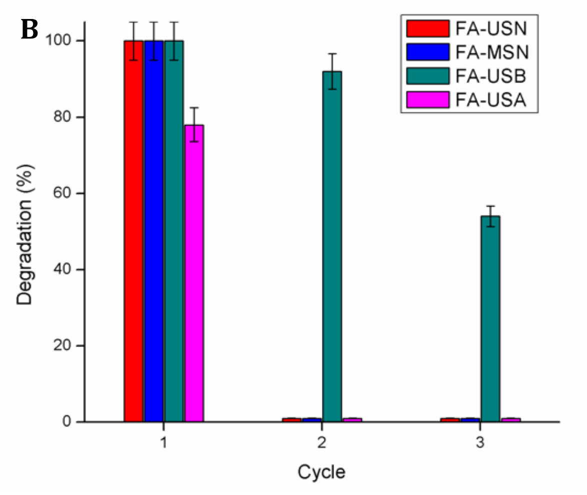

Figure 60: a) Percentage degradation of 0,05 g/L MB solution by Samples FA-zeolite (black), FA-USN (red), FA-MSN (blue), FA-USB (dark cyan) and FA-USA (magenta); b) Percentage degradation of 0,01 g/L MB solution for 3 recycling tests.

At last, in Figure 60, the photocatalytic behaviour of the synthesized samples is reported, all experiments were performed in the dark for 20 min (in order to ensure the adsorption-desorption equilibrium between the composite and the dye) and then irradiated with solar simulated light for 60 min. Figure 60 a) shows the photocatalytic test made on a very concentrated MB solution (0,05 g/L), carried out as a screening test in order to compare their activity at the beginning. It has to be noticed that unsupported FA-zeolite is able to absorb up to 20% of initial mb concentration, proof that its surface area is wide enough to make it a suitable supporting material; FA-USA and FA-MSN, despite the overall MB degradation was quite good, resulted to be the worst catalysts among the investigated ones, in terms of adsorption and efficiency. This suggested that the magnetic stirring and the acidic conditions are not favourable for this composite's synthesis. FA-USN and FA-USB show a similar behaviour towards MB degradation (as suggested by XRD measurements), but the largest extent in the dye bleaching is reached by the sample synthesized in alkaline conditions. Once differentiated the different activities, recycling photocatalytic experiments were performed over a 0,01 g/L MB solution, in order to give evidence for the magnetic recovery of the colloidal suspension and, mainly, the reuse of the catalyst (a Nd-based magnet with a reported surface magnetic induction of 1,43 T was used; settling was carried out overnight and followed by a short thermal treatment at 30 °C under vacuum to dry the recovered powders before reuse). Even though all samples could be collected by magnetic settling, it is more than evident that only FA-USB, according to results reported in Figure 60 b), could be exploited for recycling experiments. An activity loss occurred among the three cycles, proof that the interaction between the catalyst and the supporting material is not strong enough and thus should be improved.

3.5.3. Conclusions

It was possible to state that in this work we could show an excellent example of circular economy, as an industrial waste was successfully transformed in an advanced supporting material used for environmental purposes for its promising magnetic properties and porous zeolite-type structure. The TiO_2-based composite material was used as an advanced oxidation process for the photocatalytic degradation of a model pollutant. This represent the possibility to extend the use of photocatalysis as tertiary process, because the magnetic material has strongly enhanced the recovery of the colloidal suspension. This result could only be obtained when the synthesis of the material was performed in alkaline conditions, because the crystalline structure and the surface properties obtained in these conditions led to a good photocatalytic efficiency and, moreover, to the possibility to reuse the catalyst (for at least 3 cycles).

4. Analytical Approach to Emerging Pollutants

In this chapter, the instrumental analytical approach used to study some specific emerging pollutants is reported and deepened. In particular, there will be three chapters, each of them divided as a scientific paper, dealing with the study on Parabens, Nicotine and Salbutamol: specifically, chromatographic techniques coupled to mass spectrometry and/or diode array detectors are exploited to study the fate of each specific contaminant as well as the matrix conditions affecting the oxidation process. The big part of this study was undertaken during the abroad period of four months and a half spent at the Water Lab of the Department of Environmental Engineering Department, (Technical University of Crete), under the supervision of Professor Elia Psillakis.

The main goal of this analytical approach was to make a comparison between photolysis and photocatalysis features, specifically on the different rate of degradation of emerging pollutants and the potential by-products formation. After preliminary considerations on the feasibility of AOPs application, the work should have directed towards the comparison of the activity of different synthesized samples (some of the ones presented in Section 3.). Furthermore, everything was intended to be studied according to the different matrix compositions, in order to get closer, eventually, to the application on real samples and to have a better knowledge on the behaviour of these pollutants in the environment.

Unfortunately, these results are presented incomplete, because it was not possible to finish the experimental set in the prearranged time. In particular, the project on parabens (Chapter 4.1) was abandoned because it was not possible to obtain significant differences between the photolysis and photocatalysis (within the investigated conditions) thus it was decided to continue with the project on nicotine (Chapter 4.2), which instead led to very interesting results but limited to the photolysis experiments, for a matter of time. Throughout this section, some analytical characterizations are mentioned but not reported, because they still have to be performed at the put in writing date. Anyway, the presented data have not been published yet, but they will be included in a paper as soon as the missing experimental set of data will be finished by Professor Psillakis' research group.

4.1. Parabens

Aqueous solutions of a mixture of four parabens were subjected to photolysis experiments under different processing conditions. As an example, the general structure of a para-hydroxybenzoate "paraben" is reported (R- stands for the different substituting agent: $-CH_3$, $-C_2H_5$, $-C_3H_7$, $-C_4H_9$ respectively for Methyl Paraben "MP", Ethyl Paraben "EP", Propyl Paraben "PP" and Butyl Paraben "BP") in Figure 61.

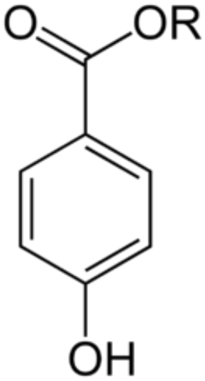

Figure 61: Structure of a generic para-hydroxybenzoate

This class of compounds is considered to belong to the emerging pollutants' class because they are employed for cosmetical preparations as well as food and pharmaceutical products, mainly for antibacterial and preservative purposes. These compounds are characterized by a good water solubility, chemical and photo-chemical stability; it was reported (even though it has still to be confirmed) that the presence of trace amounts of this class' compounds could get to undesired oestrogenic outcomes for living organism; thus they were chosen as subject for the study of the application of advanced oxidation processes[115–117].

Effectively, this project was started in order to evaluate different aspects on the degradation of the parabens' mixture: first of all, to study the possibility to exploit photolysis and later photocatalysis as advanced oxidation processes to degrade these compounds from water; furthermore, to study the formation of probable degradation by-products in relation to the matrix composition and eventually to study the significant parameters affecting the degradation process, such as: pH effect, initial parabens concentration, undesired dissolved species (tert-butanol, humic acid) and catalyst's concentration. The final aim was to study the degradation of these species in real matrices, i.e. wastewater, river water and tap water.

This project was carried out in the Water Lab of the Environmental Engineering Department, at the Technical University of Crete, under the supervision and with the help of Professor Elia Psillakis.

4.1.1. Materials and Methods

Aqueous solutions of parabens mixture were prepared using a methanol stock solution, previously prepared from the solid reactants at the concentration of 2000 ppm for each paraben, kept in the fridge at -20 °C. The proper amount of the stock solution was withdrawn with a micropipette and transferred to a volumetric flask. With a gentle nitrogen flow, methanol was removed from the volumetric flask; water was then added to reach the final volume and finally the solution was homogenised using an ultrasonic bath for 10 minutes. Fresh solutions were prepared daily before each experiment. pH modifications (from neutral solutions) were performed using buffer solutions based on ammonium acetate (also used as one of the two mobile phases), with CH_3COOH (pH 4,9) and NH_3 (pH 11) additions.

Experimentally, 8 mL of the aqueous solution of the parabens' mixture were transferred in a quartz vial, which in turn was put in a home-made laboratory photoreactor (26 cm × 26 cm × 26 cm), used for all photolysis and photocatalysis experiments. The photoreactor was equipped with two 8 W low-pressure mercury lamps (OSRAM Puritec Germicidal Lamp HNS 8W G8T5), each mounted on opposing sidewall of the photoreactor and having a strong emission line at 254 nm. The distance between each lamp and the quartz vial used in the experiments was set to 13 cm. The quartz vial was placed on a magnetic stirrer, switched on during each experiment. 50 μL aliquots were taken at fixed times during each experiment, transferred in 250 μL glass inserts, placed in 2 mL glass autosampler vials equipped with septum caps, and subjected to the chromatographic separation (in case of suspended powders, centrifugation step for 10 min at 13200 rpm was added). The initial mixture of the parabens was analysed by means of a HPLC-DAD Agilent 1200 Series, equipped with a binary pump, a degasser, autosampler and thermostated compartment for the column. Chromatographic column used was a C18 thermo-Electron Betasil (Whaltam, MA, USA) of 2,1 mm ID x 100 mm, with 5 μm particles. The chromatographic run was performed with two mobile phases: A_1 was an ultrapure H_2O solution of 5 mM NH_4OAc while B_1 was pure MeOH. The flow was set to 0,2 mL/min and column temperature to 25 °C, while the overall analysis time was 29 min. The Diode Array Detector was set to λ= 256,4 nm to measure the pollutants' amount[118].

4.1.2. *Results and Discussion*

The solvents' gradient program used with the HPLC is reported in Table 20, while Figure 62 shows the calibration curves calculated for each paraben as well as the chromatogram of the resolved mixture, together with the experimental retention time of each pollutant, within the method.

Table 20: Gradient elution program used in the HPLC-DAD for parabens elution

Time (min)	% B_1
0,00	*40,0*
5,00	*55,0*
11,00	*55,0*
13,00	*100,0*
21,00	*40,0*

29,00	*40,0*

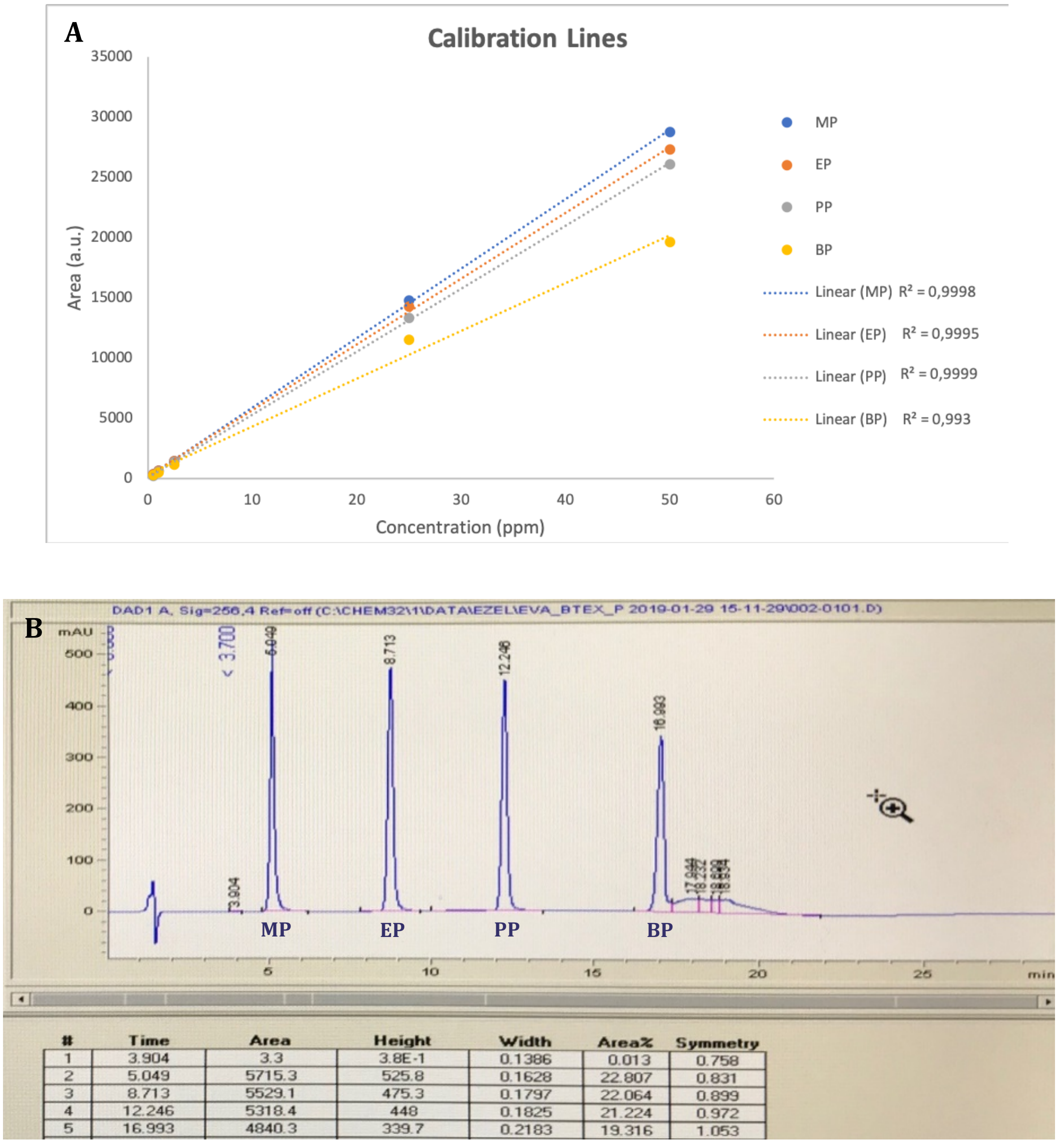

#	Time	Area	Height	Width	Area%	Symmetry
1	3.904	3.3	3.8E-1	0.1386	0.013	0.758
2	5.049	5715.3	525.8	0.1628	22.807	0.831
3	8.713	5529.1	475.3	0.1797	22.064	0.899
4	12.246	5318.4	448	0.1825	21.224	0.972
5	16.993	4840.3	339.7	0.2183	19.316	1.053

Figure 62: a) Calibration curves of all the four studied parabens, using HPLC-DAD; b) Chromatographic separation of the parabens' mixture and retention times' table of each species

Once stated the linearity of the instrument's response, together with the quantification limit, as well as the possibility to have a good separation of each component, it was possible to start with photolysis experiments, where the parabens' solutions, at different starting conditions, were subjected to UV irradiation. These experiments were performed in order to give a comparison with the subsequent photocatalytic tests.

Figure 63 shows the plots of the concentration variation with time, for different parabens concentrations. It has to be noticed that all the following results are related to buffered solutions at pH 4,9, obtained with 5 mM NH_4OAc and CH_3COOH aqueous solutions, because it was found to be the best pH condition to get a satisfying abatement degree (this is also in agreement with literature data[117]). Reported C_0 is equal to the concentration of each single paraben in the mixture (e.g. C_0= 10 ppm means that the mixture contains concurrently 10 ppm of each single paraben, thus MP= 10 ppm + EP= 10 ppm + PP= 10 ppm + BP= 10 ppm).

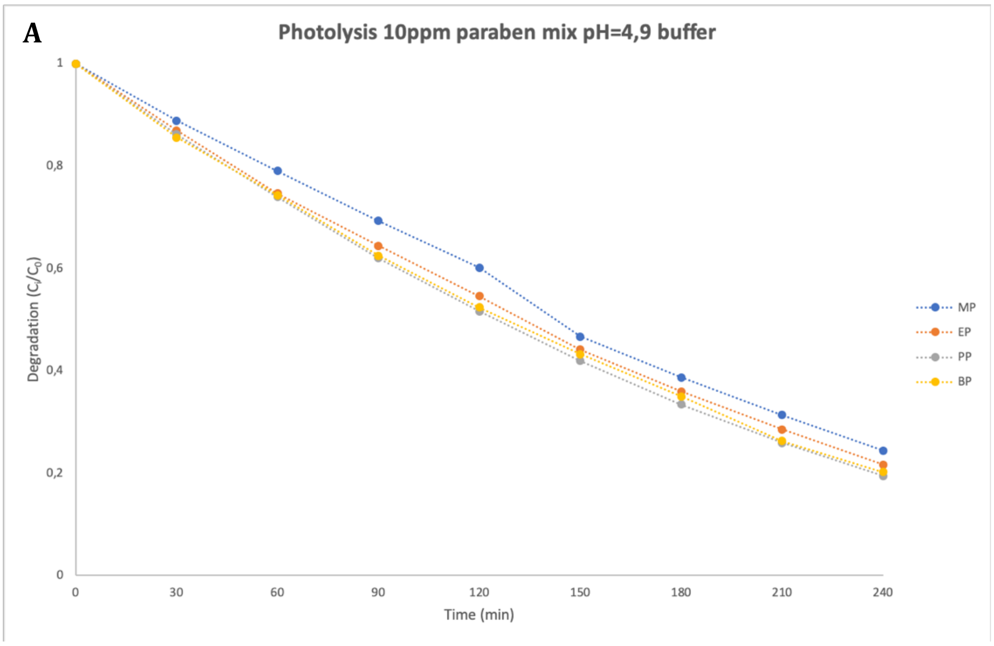

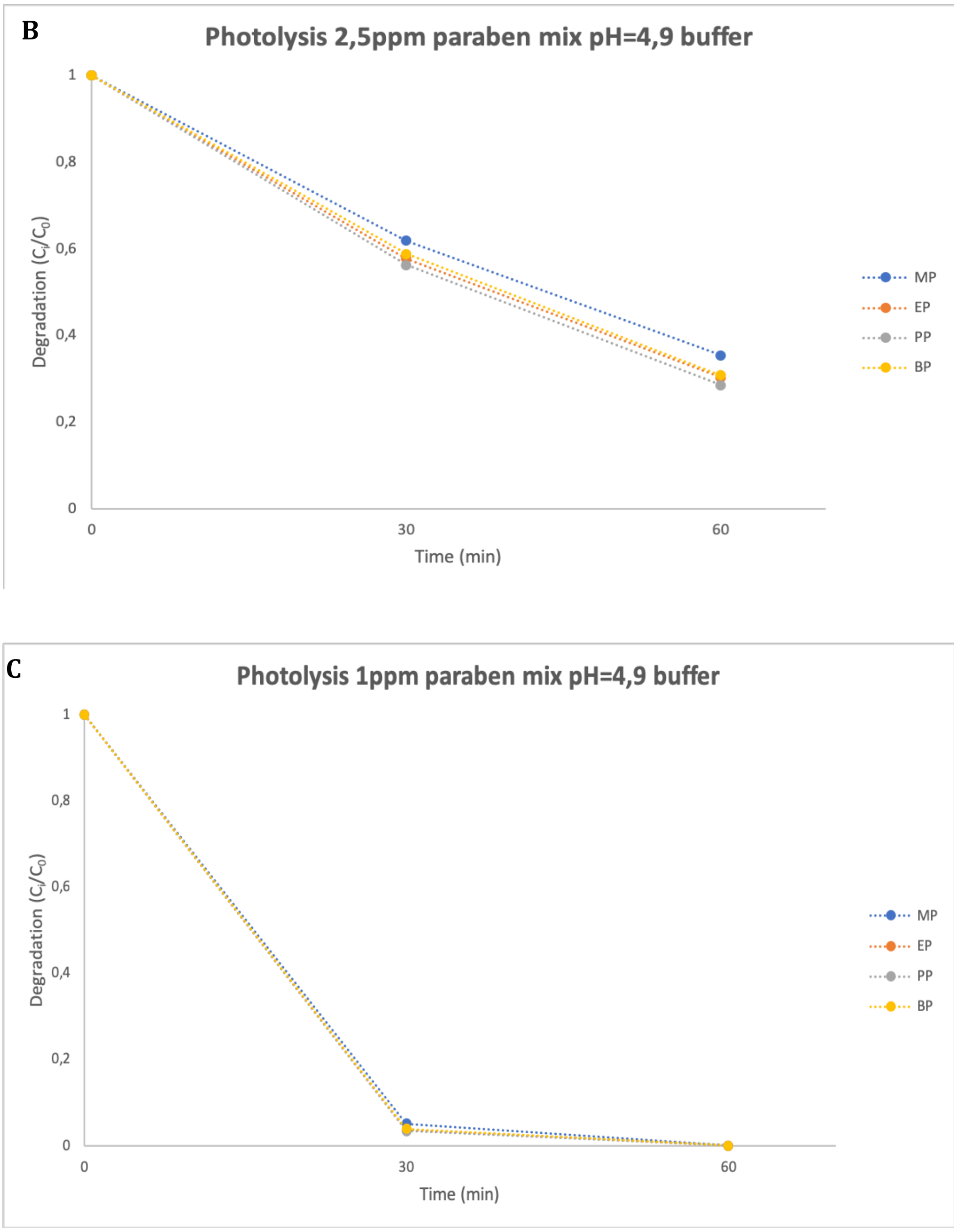

Figure 63: Photolytic degradation of the parabens mixture, a) C_i/C_0 versus time trend of a buffered parabens mixture solution at C_0= 10 ppm; b) C_i/C_0 versus time trend of a buffered parabens mixture solution at C_0= 2,5 ppm; c) C_i/C_0 versus time trend of a buffered parabens mixture solution at C_0= 1 ppm

It is possible to see that the parabens result to be slowly but steadily degraded by the UV source, with a linear trend for all the experiments except the one with C_0=1 ppm. In this last experiment, the degradation rate seems to be increased, resembling a first/pseudo-first order fashion. Unfortunately, only with very diluted concentrations it was possible to obtain this rate, which is the condition to aim for to get a good decrease yield in a short time.

Anyway, it has to be remembered that these experimental results, apart from specific features of the considered pollutants, may be also ascribable to the investigated experimental conditions (reactor configuration, lamps power, photon flux) which could not be optimized for a matter of time.

The same kind of experiments were performed using the TiO_2/PeL-based photocatalysts (specifically the optimized one, described in chapter 3.1.1.), in order to demonstrate the possibility to speed up the degradation rate of the parabens. In Figure 64 the photocatalytic results are reported (C_0 was chosen equal to 2,5 ppm in order to have, possibly, a clear evidence of the different rate between the two processes).

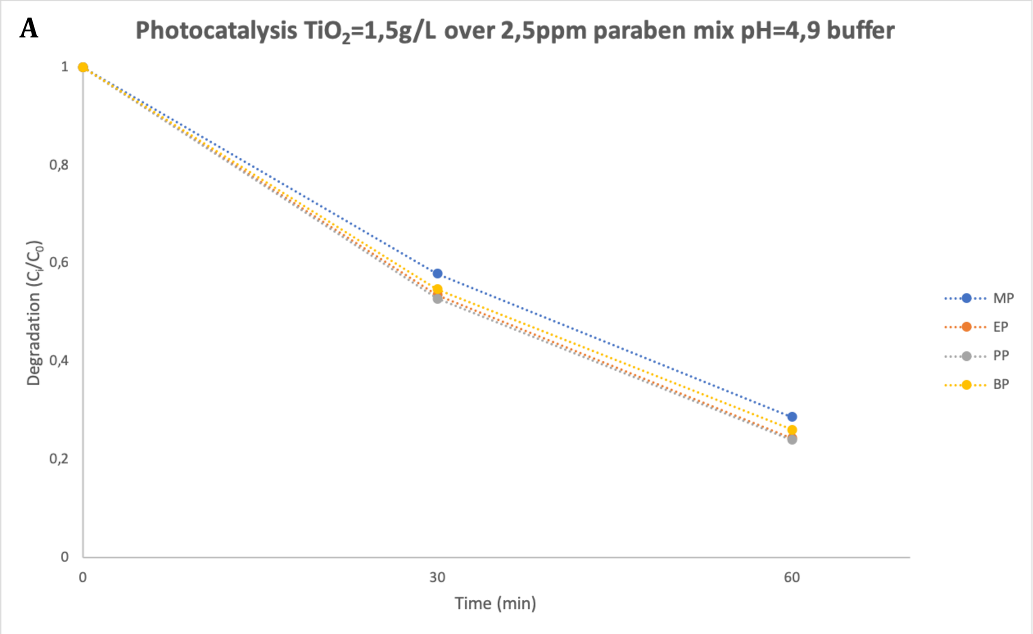

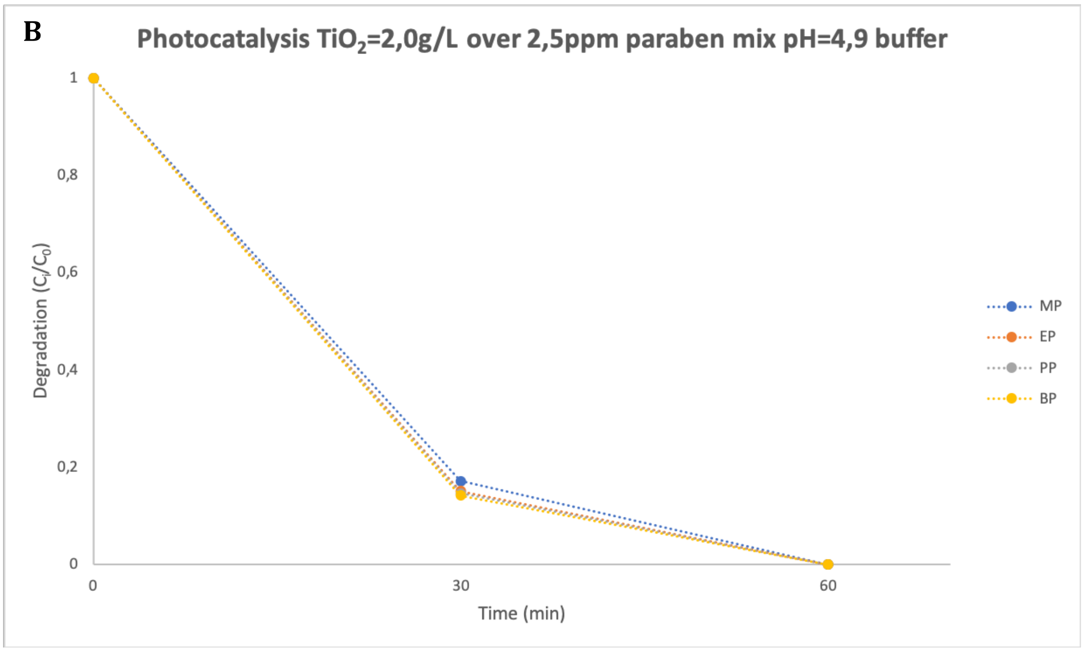

Figure 64: Photocatalytic degradation of the parabens mixture a) C_i/C_0 versus time trend of a buffered parabens mixture solution at C_0= 2,5 ppm and TiO_2 concentration of 1,5 g/L; b) C_i/C_0 versus time trend of a buffered parabens mixture solution at C_0= 2,5 ppm and TiO_2 concentration of 2,0 g/L

The two different catalyst's concentrations had a different influence on the degradation trend. To make a comparison between the photolysis experiment (Fig. 63 b) and the photocatalysis experiment (Fig. 64 a), the overall degradation after 60 min of UV irradiation brought to a slight increase in the yield, anyway too low to be significant, thus the catalyst's activity could be considered as none; comparing the two different catalyst's concentration, a significant increase in the degradation yield was instead noticed. This could be likely ascribable to a critical catalyst's concentration (2,0 g/L), within the investigated system, which has a positive effect on the degradation on the parabens. In order to confirm that this TiO_2 concentration was the minimum amount required to degrade these pollutants, the same photocatalytic experiment was performed with a starting parabens' concentration equal to 10 ppm. Results are reported in Figure 65.

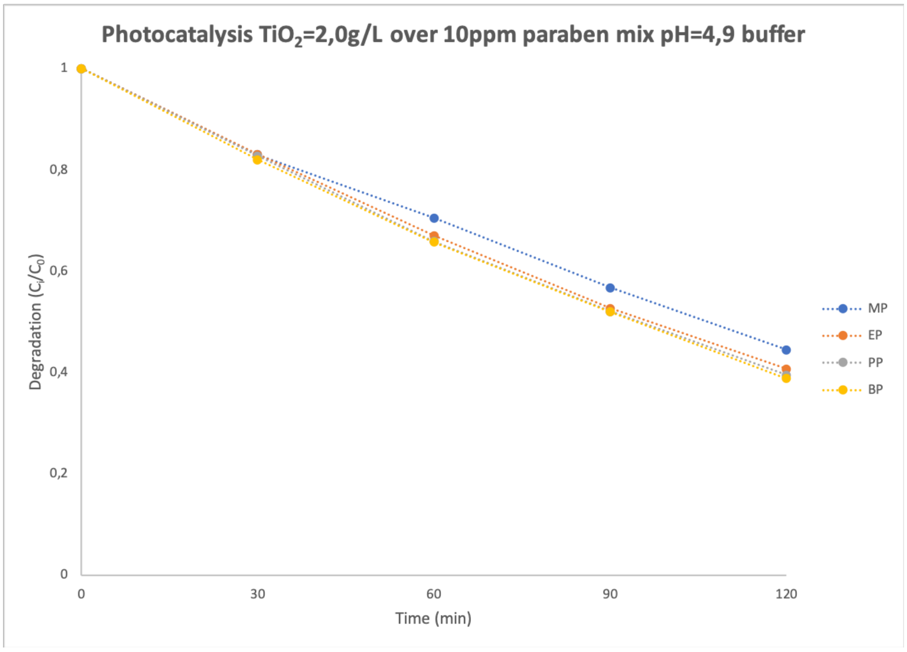

Figure 65: Photocatalytic degradation of the parabens, C_i/C_0 versus time trend of a buffered parabens mixture solution at C_0= 10 ppm and TiO_2 concentration of 2,0 g/L

From experimental results it was possible to see that the different starting parabens concentration was too high to be degraded by TiO_2 with a first order-like trend; a slight increase in the percentage yield was measured (with respect to photolysis experiment highlighted in Fig. 63 a) but the same consideration is not valid regarding the kinetic.

Unfortunately, it was not possible to increase TiO_2 amount, both because the catalyst's suspension would have been too thick to let the irradiation penetrate through the solvent and also because using such a big amount would have been economically unfavourable.

4.1.3. Conclusions

For the experimental results obtained from this project, in particular the inability to speed up the degradation process with the photocatalyst (within the chosen experimental conditions) and further taking into consideration the short time available at the Water Lab facilities, it was decided not to continue; thus, all the experiments on the matrix effect and the degradation by-products were not performed.

Some considerations may be done on the displayed behaviour: the mixture of all parabens could likely undergo radiation quenching processes among all the molecules, hence substituting bonds cleavage with energy dissipation which involves vibrational and rotational energy levels. The presence of the photocatalyst, activated by UV light, didn't really improve the degradation and this fact may be ascribable to a poor interaction between the catalyst's surface and the pollutants (maybe for missing charge interactions) as well as a remarkable stability of the mixture of these pollutants. The mechanism of the parabens' photocatalytic degradation should be clarified, in order to put in evidence which mechanisms are involved in the mineralization and which ones are responsible for the low photocatalytic activity. Anyway, as reported in literature, different but effective AOPs can be employed (e.g. an hard AOP: ozonation[119]) against parabens, even if the energetic demand is higher, because they can have more energy available to degrade the mixture of these compounds and thus overcome the limitations highlighted with photocatalysis.

4.2. Nicotine

Nicotine is a highly toxic alkaloid, deriving from the tobacco consumption, that is found to be ubiquitous in wastewater effluent. Cigarette smoking has well-documented negative effects on human health and environment[120]. Its principle alkaloid is composed of a pyridine ring and a pyrrolidine ring. The structure is reported in Figure 66.

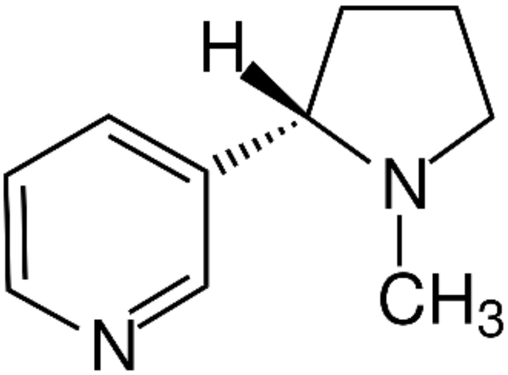

Figure 66: (–)-Nicotine molecular structure

The U.S. Environmental Protection Agency has included nicotine in its Toxic Release Inventory since 1995, as the annual global consumption is estimated to be around 50.000 tons. This pollutant is highly soluble in water and most of it is indeed found in the aqueous environment. The primary point sources are the effluents from municipal wastewater treatment plants, because the incomplete degradation of nicotine results in a concentration undesired effect up to hundreds of ppb. Further, 76% of consumed cigarettes (16 billion per day, globally) are actually thrown away unproperly, so it must be added to the overall contamination from cellulose acetate the contribution of Polycyclic Aromatic Hydrocarbons, heavy metals, nicotine and its by-products. Nicotine related danger is well known for humans, but its highest danger arises in the aquatic environment, where its presence is lethal for the aquatic life. It's highly related to anthropologic pollution, in fact nicotine and its metabolites are used as chemical markers for water contamination and for population size assessment[121,122].

After the experimental results obtained with photocatalysis with the previous project (Chapter 4.1), it was decided to proceed with photolysis experiments to state the feasibility of the project. Luckily, it was possible to exploit photolysis as AOP to degrade nicotine[123], so it was possible to determine the different effects that influenced the process: starting pollutant concentration, pH effect, matrix effect (tert-butanol, humic acid and sodium chloride presence) and eventually different aqueous matrices (sea water, river water, tap water, wastewater and rain water). At last, nicotine degradation from aqueous leachates obtained with four different cigarettes configurations was studied: conventional and IQOS cigarettes, shown in Figure 67, were used bare and smoked by a smoking machine. The photocatalytic experiments, as a comparison with the photolysis results, could not be performed for a matter of time.

Figure 67: Conventional cigarette (left) and IQOS cigarette and burner

Analytical methods employed for the study of this complex system were different, according to the different samples composition; HPLC-DAD-MS, GC-FID and GC-MS.

This project was carried out in the Water Lab of the Environmental Engineering Department, at the Technical University of Crete, under the supervision and with the help of Professor Elia Psillakis. These data are currently under consideration for a future publication; therefore, they are reported confidentially at the put in writing date.

4.2.1. Materials and Methods

(-) Nicotine PESTANAL® at analytical standard grade was purchased from Supelco. Acetonitrile for LC/MS was obtained by Carlo Erba Reagents. Sodium Chloride (99,9%, Penta), humic acid from Fluka Analytical and tert-butanol (assay GC ≥ 99%) from Fisher Chemicals (Pittsburgh, Pennsylvania). Ammonium acetate puriss p.a. was obtained from Fluka Analytical (assay ≥90%); formic acid was supplied by Fluka Chemie GmbH (Bucks, Switzerland).

When stated in the text, aqueous solutions of HCl or NaOH (Honeywell-Riedel-de Haen-Fluka) were used to adjust the pH for non-buffered solutions while acetic acid (100%) anhydrous GR for analysis and boric acid (99.8%), supplied by Merck, KGaA (Darmstadt, Germany); potassium phosphate dibasic trihydrate Reagent Plus (≥ 99.0%) (T) from Sigma-Aldrich (Steinheim, Germany), sodium acetate trihydrate (Ultra ≥ 99.5%) (NT) and potassium dihydrogen phosphate (assay ≥ 99.5%) (T) both by Fluka BioChemika (Germany), were all used for buffered solutions when pH effect was investigated. Ultra-pure water was prepared by using an EASYpure RF water purification system supplied by Barnstead/Thermolyne Corporation (Dubuque, IA, USA).

Aqueous standards as well as working solutions were prepared daily from an aqueous stock solution containing 9,5 g/L (9499ppm) of (−)-Nicotine, stored at 4 °C in a brown bottle covered with aluminium foil. The matrix effect on nicotine degradation was studied using: fresh water sampled from the river Koiliaris at Kyani Akti (Kalyves, Crete, Greece) pH 7,99; tap water collected form the laboratory sink (T.U.C., Chania, Crete, Greece) pH 7,80; secondary treated wastewater effluent (WWTP Effluent) from the municipal wastewater treatment plant of Chania (Crete, Greece, serving approximately 70,000 inhabitants) pH 7,85; sea water sampled near the beach of Koum Kapi (Chania, Crete, Greece) pH 7,91 and rain water collected during the month of February, 2019 (Chania, Crete, Greece) pH 6,44. Real matrixes water samples were filtered on 0,45 μm sterile MCE gridded membrane filters (MS) and stored in the dark at 4 °C before use. All samples were initially analysed and found free of nicotine.

A home-made laboratory photoreactor (26 cm × 26 cm × 26 cm) was used for all experiments. The photoreactor was equipped with two 8 W low-pressure mercury lamps (OSRAM Puritec Germicidal Lamp HNS 8W G8T5), with a strong emission line at 254 nm. The set-up is the same as the one described in Chapter

4.1.1. The rate of the incident UV light intensity entering the solution (I_0, given in E/L·s, where E=Einstein) was determined to be $I_0 = (1.65 \pm 0.06) \cdot 10^{-5}$ E/L·s, using H_2O_2 as a chemical actinometer. The concentration of the aqueous H_2O_2 solution (0.15 M) was sufficiently high to assume that the actinometer absorbed all incident light and that the direct photolysis of the reactant followed zero-order kinetics.

In all photolysis experiments, 10 mL of a (–)-Nicotine aqueous solution at a fixed concentration and a certain matrix composition were introduced in a tailor-made quartz vial (2.0 cm outer diameter × 4.5 cm height). The vial was then capped and submitted to UV irradiation for a pre-set time. The inner diameter of the quartz vial (1.3 cm) was used as the optical path length of radiation. After UV-exposure, samples 50 µL samples were collected and directly injected in the HPLC-MS without pre-treatments. Dark tests were run in parallel by placing the spiked water samples inside the photoreactor with the lamps switched off, so as to ensure that any decrease in the analytical signal was due to the action of photons alone. All experiments were run at least in duplicates.

A UV-Vis spectrophotometer was used, in a scan mode between 150 and 500 nm, in order to investigate the maximum absorbance of a 10 ppm (–)-Nicotine aqueous solution, with different pH conditions (HCl/NaOH). The absorbance of natural and engineered water samples at 254 nm was measured using a single-beam UV-visible spectrophotometer (UVmini-240, Shimadzu, Tokyo Japan), equipped with quartz cuvettes having a 1 cm optical path length.

All analyses on standard nicotine were carried out using an Agilent 1200 Series high-performance liquid chromatography “HPLC” system equipped with a binary pump, autosampler, degasser and thermostated column compartment coupled to a diode array detector “DAD” and an Agilent 6110 single quadrupole LC-MS system equipped with a multimode ionization source. For the analysis, 50 µL of the sample were added in 250 µL glass inserts placed in 2 mL glass autosampler vials equipped with septum caps, all purchased from Agilent (Palo

Alto, USA). A Thermo-Electron Betasil C18 column (Waltham, MA, USA) of dimensions 2.1 mm ID × 100 mm length and 5 μm particle size was used for separation. The mobile phase consisted of solvent A_2 ultrapure water containing 0.1% formic acid (V/V) and B_2 acetonitrile containing 0.1% formic acid (V/V). The LC gradient method used was 2% B_2 for the first 1 min, then linearly increased to 100% B_2 in 10 min where it was held for 2 min, followed by a 0,5 min ramp to 2% B_2 where it was held for the rest of the analysis. These conditions are summarized in Table 21.

Table 21: Gradient elution program used in the HPLC-MS-DAD for nicotine elution

Tempo (min)	**% B_2**
0,00	*2,0*
1,00	*2,0*
11,00	*100,0*
13,00	*100,0*
13,50	*2,0*
20,00	*2,0*

Column temperature was set to 30 °C and the flow rate of the mobile phase was 300 μL/min, while the total analysis time was 20 min. Injection depth was set to 6 mm within the autosampler vials and the volume of each analysis was 20 μL. The MS conditions were: drying gas flow 8 L/min; drying gas temperature 250 °C; nebulizer pressure 30 psi; collector capillary voltage 4.0 kV; fragmentor voltage 70 V; scan range (m/z) of 100-1000 amu for signal n°1 and scan range (m/z) 160-165 for signal n°2. The mass spectrometry data were recorded using the positive electrospray ionization “ESI” mode. The DAD signal, set at 260 nm, was used at all times for monitoring nicotine while mass spectrometry was used to assign the mass/charge ration to the eluting peaks.

Once standard nicotine experiments were completed, cigarettes leachates were prepared to start the experimental part on the real matrices. Cigarettes and cigarette butts were put in contact with aqueous solutions in order to have a solid to liquid ratio equal to 10 and left on a rocking plane for 24 h at 180 rpm. After extraction time, the solutions were filtered with 0,45 μm before chromatographic separation. In order to find out the nicotine concentration in each different leachate, a hexane extraction was performed in order to measure the samples at the GC-FID, injecting 1 μL of samples and using a pre-existing method. Taking into account the resulting concentrations, real leachates were diluted to the final concentration of 5 ppm for the degradation experiments.

For headspace SPME, a 100 μm PDMS, Fused Silica, 24Ga PDMS fibre equipped with a manual SPME holder was used to preconcentrate nicotine from cigarettes leachates in ultrapure water. 10 mL of the diluted leachate, brought to a final concentration of 5 ppm, were subjected to UV irradiation for different times (0-2.5-5-10-15 minutes); the whole sample subjected to photolysis was placed in a 15 mL crimp top amber glass vial containing a stirring bar and fitted with a septum cap, then salted (5% wt. NaCl) and eventually alkalized with 0.1 mL of a concentrated NaOH solution (final pH=13). Magnetic stirring at 700 rpm was applied before extraction for 5 min (allowing thus equilibrium to be attained between the aqueous and gaseous phases) as well as during extraction (30 min), under a thermostated temperature of 60 °C, attained with a water bath and a thermometer. It should be mentioned here, that in order to eliminate volatilisation losses, all aqueous samples were freshly prepared before photolysis and headspace SPME extraction. After the extraction time, the fibre was withdrawn within the holder and then immediately transferred to the heated injection port of the gas chromatograph-mass spectrometer “GC-MS” for analysis.

All analyses were carried-out on a Shimadzu GC-17A, Version 3, QP-5050A Gas Chromatograph/Mass Spectrometer system (Shimadzu Corporation, Kyoto, Japan) equipped with a 30 m × 0.25 mm 0.25 μm HP-5MS capillary column (Agilent Technologies). The injector was maintained at 250 °C and operated with a split ration equal to 12. Helium (> 99.999% pure) was used as carrier gas at a flow rate of 1.0 mL/min. The column oven was initially set at 50 °C for 3 min, programmed to 280 °C at a 10 °C/min, where it was held for 2 min, until the end of the program time, set at 28 min. The interface temperature was set at 300 °C and the detector voltage at 1.80 kV. The ionization mode was electron impact (70 eV). The full scan mode (m/z 50-350) was used for identification of all target compounds based on their mass spectra and GC retention times as well as for monitoring the decrease in nicotine's signal along UV irradiation time.

4.2.2. Results and Discussion

At first, the absorbance of a 10 ppm nicotine solution as a function of the pH was recorded and reported in Figure 68.

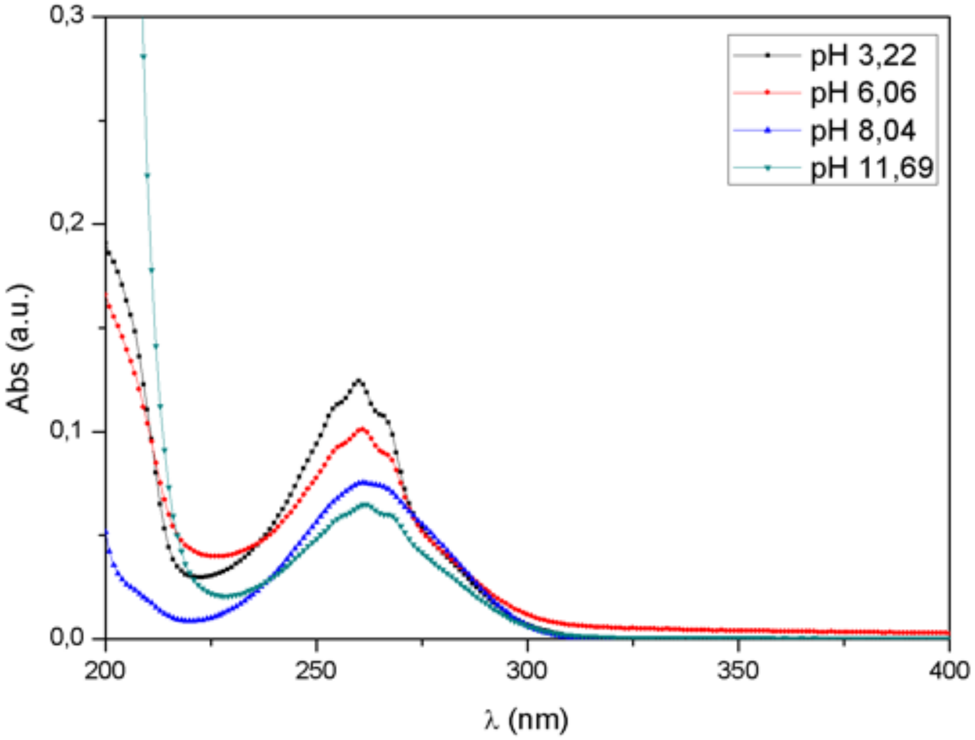

Figure 68: pH effect on UV-Vis absorbance of 10 ppm (–)-nicotine aqueous solution

It was possible to demonstrate that the absorbance of nicotine didn't remarkably change along with the pH modifications, assessing around 260 ± 2 nm, thus it was possible to set the wavelength at this value for the diode array detector.

All the investigated matrix effects affecting the photolysis experiments are reported in Figure 69, respectively for: concentration effect (a), pH effect (b), presence of 100 ppm of tert-butanol (c), presence of 2,5 ppm of humic acid (d), presence of 3,5% wt. of NaCl (e) and aqueous matrix concentration (f).

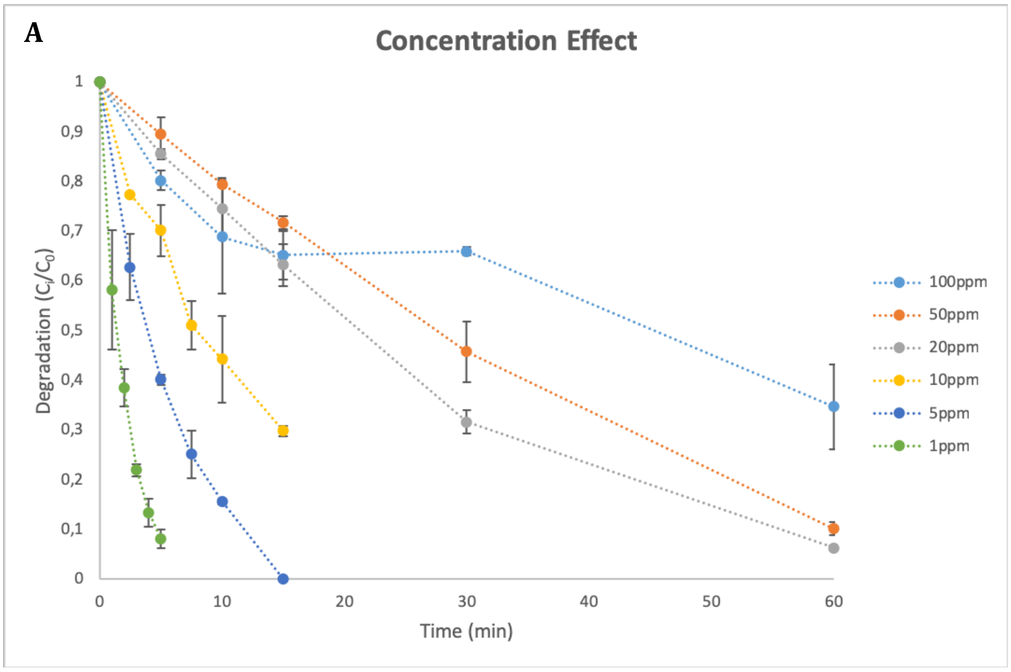

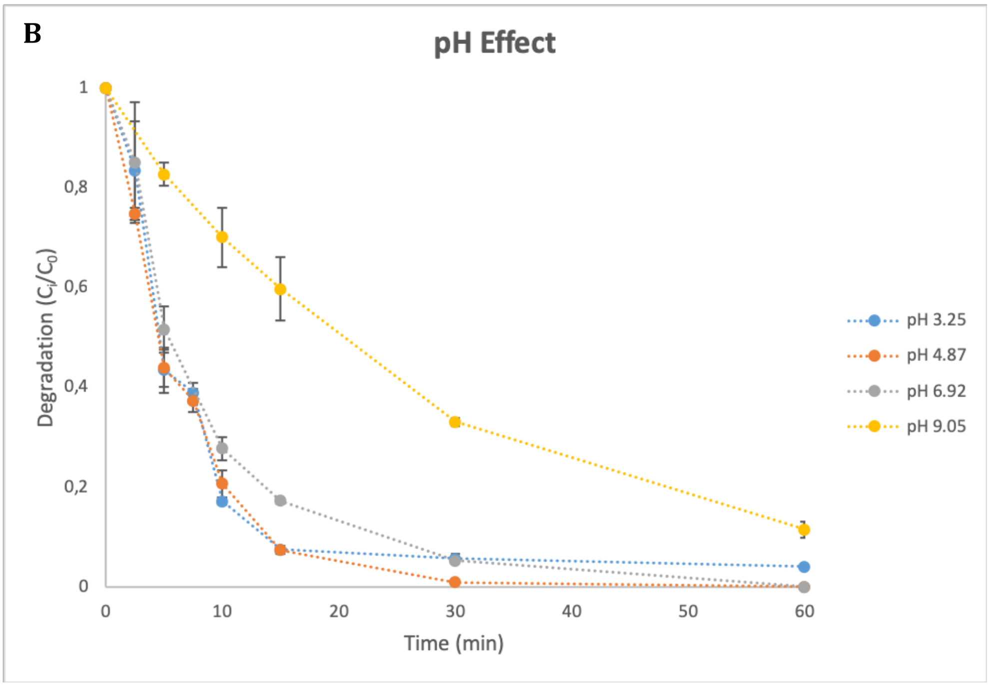

C

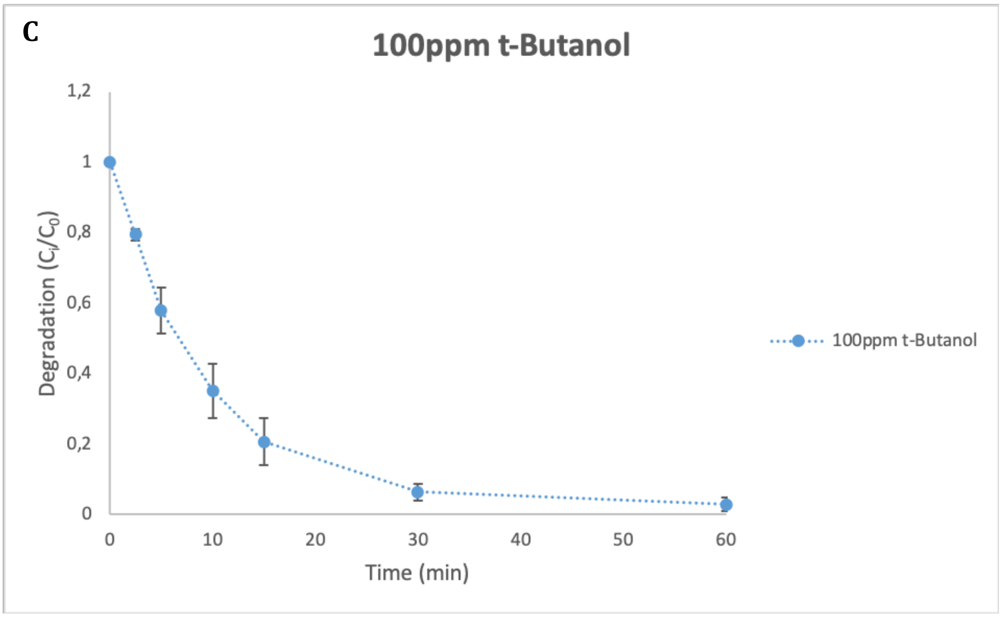
100ppm t-Butanol
Degradation (C_i/C_0)
1,2
1
0,8
0,6
0,4
0,2
0
0
10
20
30
40
50
60
Time (min)
100ppm t-Butanol

D

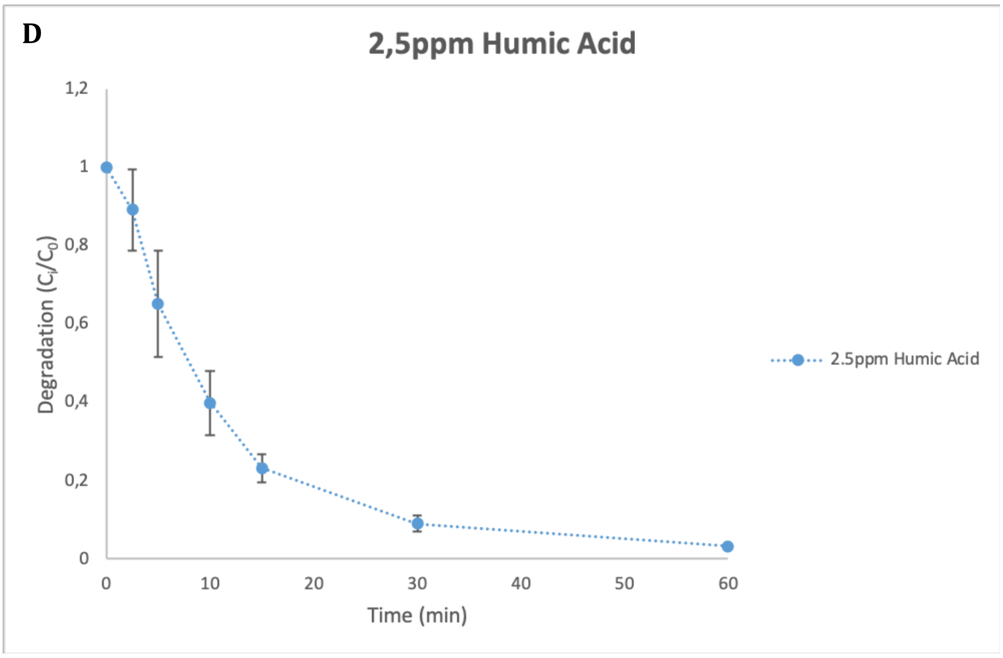
2,5ppm Humic Acid
Degradation (C_i/C_0)
1,2
1
0,8
0,6
0,4
0,2
0
0
10
20
30
40
50
60
Time (min)
2.5ppm Humic Acid

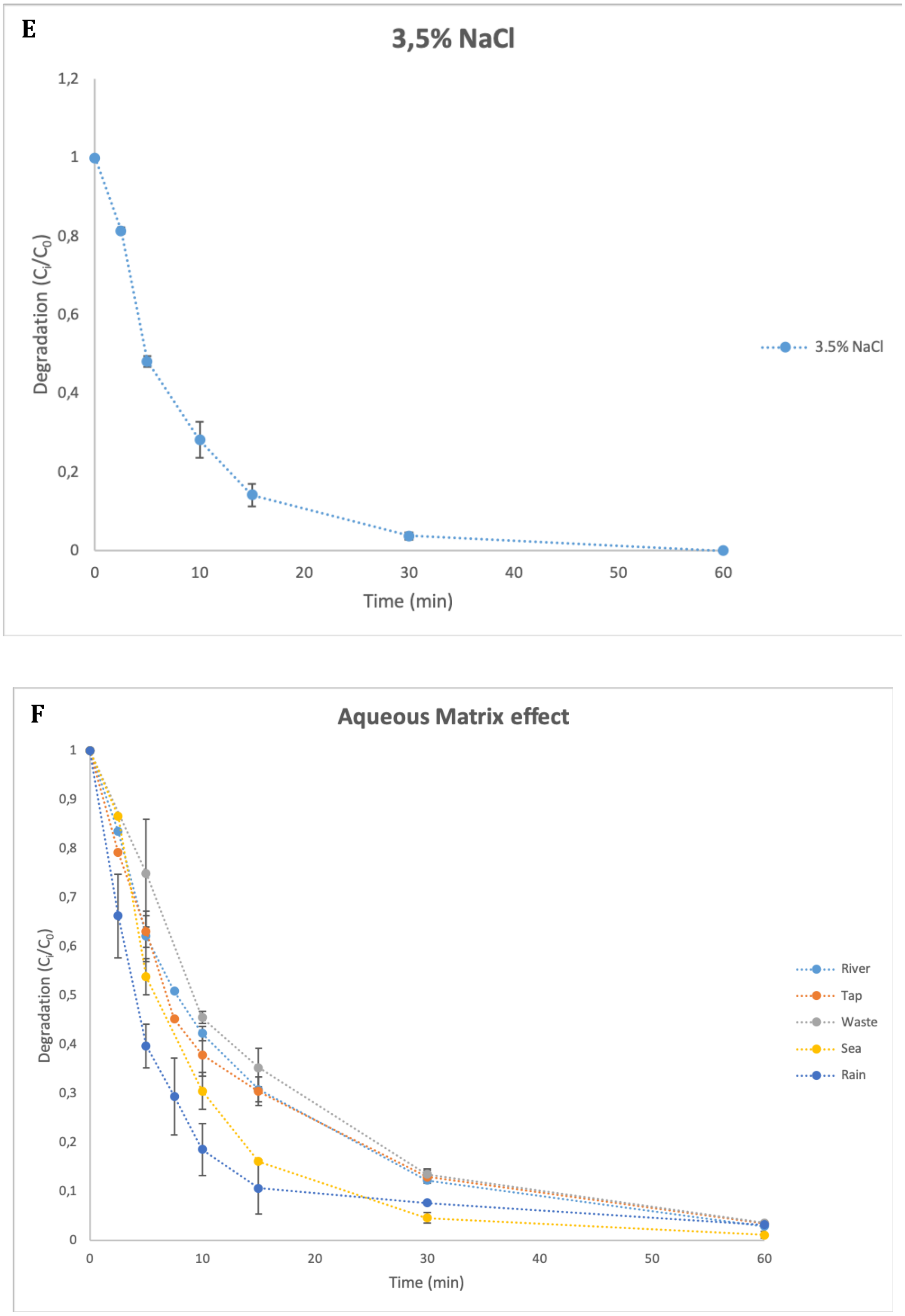

Figure 69: Photolysis experiments**:** a) initial concentration effect (from 1 to 100 ppm), b) pH effect (buffered values of 3, 5, 7 and 9), c) presence of 100 ppm of tert-butanol, d) presence of 2,5 ppm of humic acid, e) presence of 3,5% wt. of NaCl, f) effect of aqueous matrix (river black, tap red, waste blue, sea green and rain purple)

From experimental results it was possible to state that a starting 10 ppm concentration was adequate to have a significant pollutant degradation in a short time (resembling a first order-like kinetic), with respect to higher starting amounts, which could be degraded in 60 min of irradiation but with a linear trend over time. The study thus continued to investigate the best pH conditions and it is clear from results that alkaline conditions are detrimental for the abatement, while neutral to acidic conditions are able to speed up the reaction. The presence of scavengers species (tert-butanol, humic acid and sodium chloride) didn't affect the process, it was indeed possible to obtain the same degradation yield with these conditions, proof that an advanced oxidation process like UV photolysis could be useful in real conditions for the degradation of the nicotine load. Eventually, the different aqueous matrices were investigated with the nicotine standard to state the real feasibility of the AOP application. It is possible to see that none of the investigated matrices brought to a decrease in the activity, on the contrary rainwater and sea water appeared to be enhancing the degradation process. Maybe this trend could be ascribable to the characteristics of the matrix, where the acidic behaviour of the rain water enhanced the degradation of the pollutant as well as the presence of sodium chloride led to a positive effect (but it should be clarified if the positive effect is related to the degradation itself or to the instrumental signal).

All of these considerations helped to recognise the opportunity to degrade nicotine in real water matrices, highlighting that no particular conditions were detrimental for its abatement, apart from alkaline pH, thus the subsequent experiments were performed on diluted real leachates as a final step to understand how the leachates' complexity (issues related to the brown-coloured solution and the rich organics' compositions) could worsen the degradation outcome. Results are reported in Figure 70.

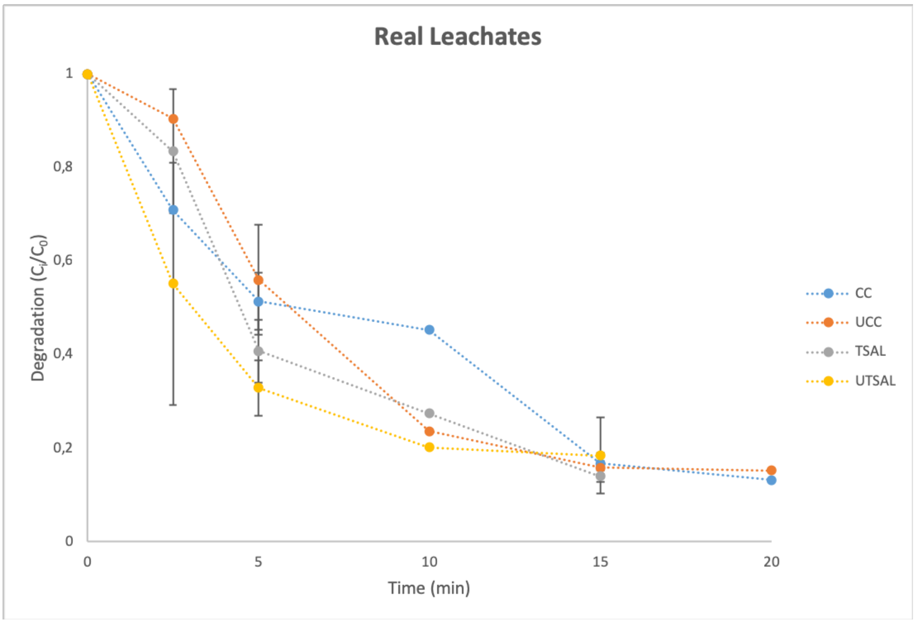

Figure 70: Nicotine degradation study on diluted real leachates samples (C_0 c.a. 5 ppm). CC= conventional cigarette, UCC= smoked conventional cigarette, TSAL= IQOS tobacco stick, UTSAL= smoked IQOS tobacco stick

Real leachates are characterized by a complex composition and thus the preliminary photolysis experiments show a big data variability (taking also into account the difficulty of the extraction procedure); it is anyway possible to see that nicotine can be degraded in about 20 min of irradiation, despite the presence of other polluting matter within the solution.

4.2.3. Conclusions

Experimental results on the degradation of this ubiquitous pollutant by means of photolysis were successful, because it was possible to demonstrate that nicotine itself can be degraded in different matrix conditions, from simple to complex cases like the ones of real leachates. In particular, it was found that acidic conditions were favourable to have a successful and fast degradation of nicotine, while the presence of other dissolved species didn't bring to negative effects on the process. This behaviour suggests that the use of photocatalysis as oxidation process could be really effective on the improvement of the degradation rate and yield of nicotine.

Further studies and characterizations still need to be done for what concerns the total organic carbon "*T.O.C.*" content of the real leachates after the photolysis experiments and mainly the identification of transformation by-products formed during the process. All recorded spectra are indeed characterized by a wide variety of secondary signals, in relation to the photolysis time, which have to be characterized and confirmed by means of literature and database comparison. This step is clearly the most complicated, especially for the real leachates' samples, because the composition of the matrix gets the interpretation of spectra more complicated. Eventually, toxicity tests on nicotine and its by-products are on the go, in order to be included in the final work together with the rest of the expected characterizations. As already mentioned, these data are not included in the current thesis because they're not available yet, but they will be included in a scientific publication as soon as they will be ready.

4.3. Salbutamol

The pharmaceutical Salbutamol, also known as albuterol, is mainly used for lungs related diseases, as it helps to open up the medium and large airways of the organism and thus it helps to treat people with asthma. It is a short-acting β_2 adrenergic receptor agonist and it works by causing relaxation of airway smooth muscle. In the U.S., this pharmaceutical was prescribed with more than 47 million prescriptions during 2016.

Salbutamol molecular structure is characterized by different hydroxyl groups, one amino group and a tert-butyl group. According to pH conditions, salbutamol will be locally ionized with different resulting charges. The proposed scheme for the micro-ionizations of salbutamol as well as the related constants are visible in Figure 71[124].

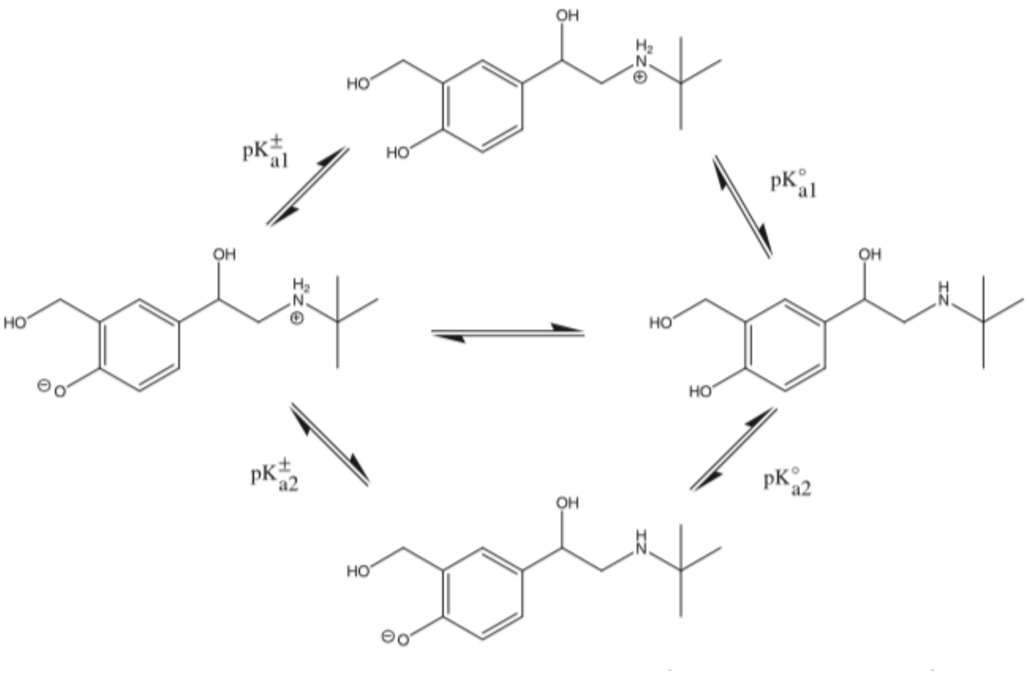

Figure 71: Micro-ionization scheme proposed for salbutamol and micro-ionization constants: pK$_{a1}^{\pm}$ = 9,22; pK$_{a1}^{\circ}$= 9,60; pK$_{a2}^{\pm}$= 9,60; pK$_{a2}^{\circ}$= 9,84 .[124]

Salbutamol can be considered as an emerging pollutant for consumption and structure characteristics; thus, it was object of the current project. The evaluation of the degradation rate of salbutamol in water was assessed by means of UV-Vis spectra acquired in second derivative and some preliminary confirmations were obtained with HPLC-MS/MS and used to validate the procedure[125].

Further studies will be conducted on the degradation by-products that can be obtained during the photocatalytic degradation process. This project was performed in collaboration with the Analytical Chemistry Section of the University of Genova, with the help of Prof. M. Di Carro.

4.3.1. Materials and Methods

Salbutamol aqueous solutions were prepared using a parent solution of salbutamol sulphate (Sigma-Aldrich, 98%), at a concentration of 1,6 g/L. All photolysis and photocatalysis experiments were performed on a 10 ppm salbutamol solution. 25 mL of the solutions were put under solar simulated light lamps (OSRAM, 300 W), placed 20 cm above, and irradiated for 60 min; photocatalysis experiments were performed with 0,0125 g of photocatalyst and the irradiation period was preceded by 20 min of equilibrating time in dark conditions. Aliquots of 1,5 mL were withdrawn at fixed times, centrifuged in presence of the catalyst and then evaluated. Each experiment was performed in triplicate.

The degradation of salbutamol was analysed by means of UV-Vis spectrophotometry, using a direct spectrum recording as well as second derivative recording, calculated from the direct spectrum by the software. The used instrument was a Lambda 35 Perkin Elmer (Whaltam, MA, USA) and spectra were recorded in the 200-500 nm range, at a scan speed of 240 nm/min and scan step of 1 nm.

The photocatalytic degradation was compared using two different catalysts: in particular, $TiO_2/(3ZnO:Ga_2O_3:2GeO_2)$: Cr^{3+} and $TiO_2/CaAl_2O_4$: $(La, Nd)^{3+}$, the ones described in Chapter 3.1.1. and Chapter 3.1.2, respectively.

As a proof of the experimental results obtained with the spectrophotometer, a HPLC-MS/MS (HPLC 1200 SL Agilent Technologies coupled with 6430 MSD Triple Quadrupol) was employed. In particular, the fragmentation mass spectrum of salbutamol was acquired and compared with literature data, in order to confirm the composition of the parent solution and then the amount of salbutamol after photolysis and photocatalysis experiments was compared with the results obtained with the UV-Vis spectra. It has to be underlined that HPLC-MS characterization was just a preliminary test, thus a scientific proof of the experimental evidence has still to be accurately confirmed by other tests. Experimentally, the HPLC chromatographic run was performed using two different mobile phases: A_3 acetonitrile and B_3 0,1% CH_3COOH aqueous solution, at a ratio of 50:50, with an isocratic flow of 0,2 mL/min. 10 μL of the samples were automatically injected in the instruments by the autosampler. A biphenyl column was used while the source was an electrospray ionization "ESI". Prior to analysis, samples at known concentrations were diluted to a final concentration of 500 ppb while samples subjected to photolysis and photocatalysis were diluted accordingly. Salbutamol fragmentation was investigated with the scan mode, within the analysis range of 100-400 m/z whilst the salbutamol concentration, after degradation experiments, was measured using the Multiple Reaction Monitoring "MRM" mode, selecting the fragment at 222,2 m/z, obtained from the pseudo-molecular $(M+1)^+$ characteristic fragment of the analyte, at 240,2 m/z.

4.3.2. Results and Discussion

First, the calibration line of different concentrations of salbutamol solution was calculated both in the direct and derivative spectrum, in order to be able to correlate the absorbance values to the unknown concentrations. In figure 72 it is possible to see the UV-Vis spectra of the different salbutamol solutions, in the range of 200-500 nm.

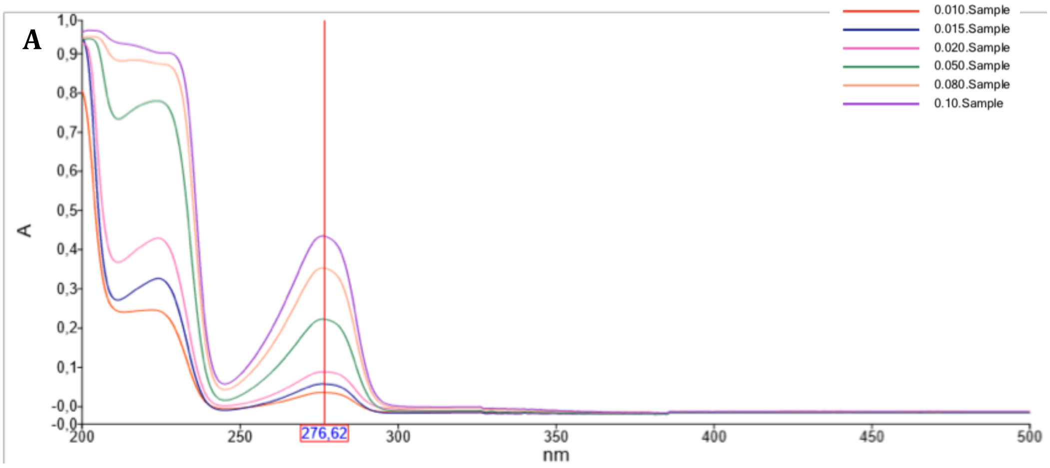

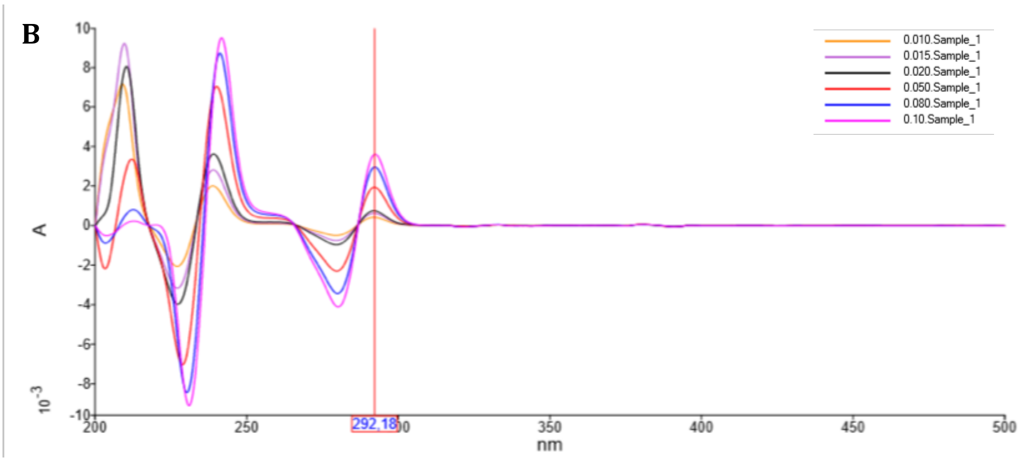

Figure 72: a) Direct UV-Vis spectra of different salbutamol solutions at six different concentrations; b) Second derivative UV-Vis spectra of six different salbutamol solutions

Both spectra recordings enabled to correlate the different absorbance intensity to the different salbutamol concentration (in order to apply Lambert-Beer law): in particular, absorbance in the direct spectra was measured on the λ= 276,62 nm signal while in the derivative spectra, signals at λ= 280,03 nm and λ= 292,18 nm were identified and used for calibration purposes. Calculated equations are reported respectively:

(Eq. ***30****)* Direct (λ= 276,62 nm) $y = 4{,}3548x + 0{,}006$; R^2= 0,9982

(Eq. ***31****)* Derivative (λ= 280,03 nm) $y = -0{,}0392x - 0{,}0002$; R^2= 0,9967

(Eq. ***32****)* Derivative (λ= 292,18 nm) $y = 0{,}0348x + 0{,}00009$; R^2= 0,9984

Photolysis and photocatalysis experiments were performed in order to state the possibility to use these advanced oxidation processes against this pharmaceutical. Dark equilibration tests didn’t bring to a significant decrease in salbutamol concentration; thus, it was possible to use 20 min as equilibrating time.

After calibration, photolysis and photocatalysis experiments were performed and direct UV-Vis spectra were recorded and reported in Figure 73.

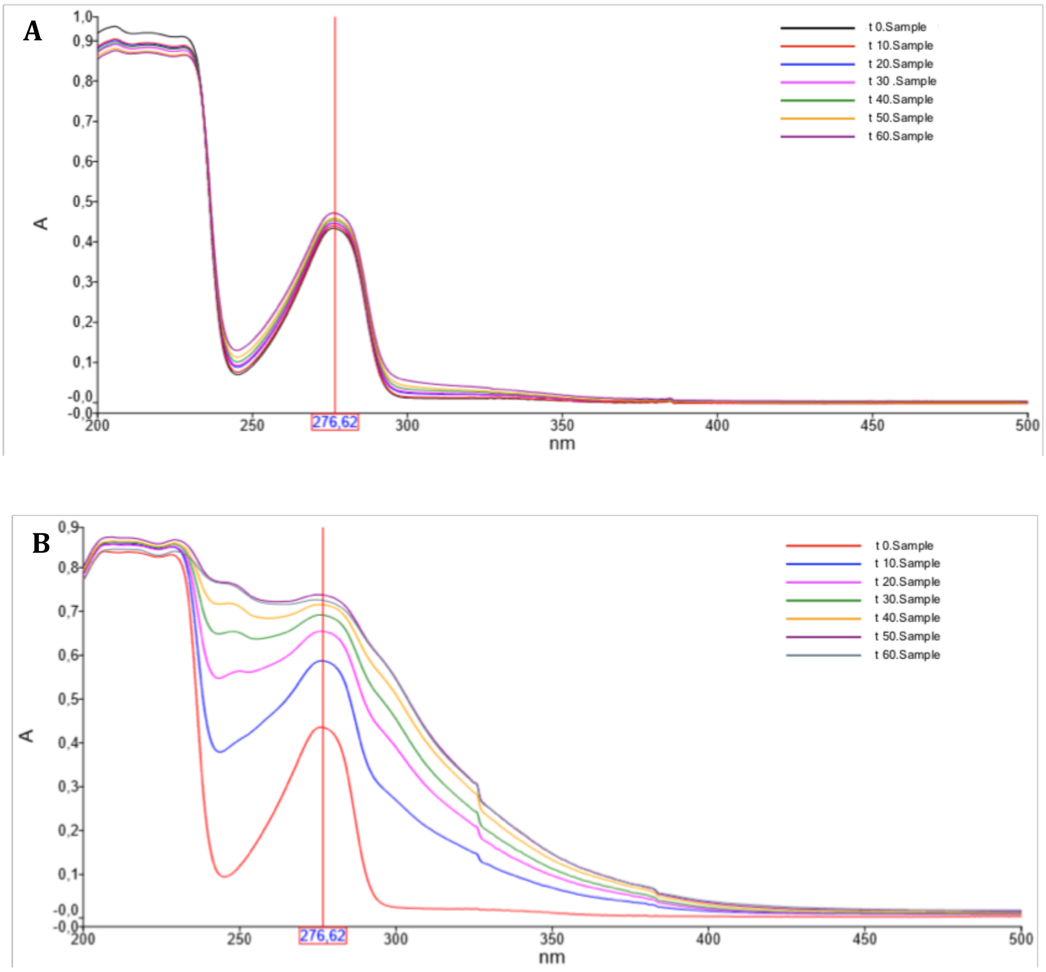

Figure 73: a) Direct UV-Vis spectra of different aliquots withdrawn for photolysis experiment; b) Direct UV-Vis spectra of different aliquots withdrawn for photocatalysis experiment

According to experimental results, it seemed that both photolysis and photocatalysis experiments were not able to degrade salbutamol; on the contrary, the monitored signals at fixed wavelengths shown an unexpected increasing trend. In order to establish whether this trend would have been addressed to the impossibility to degrade salbutamol with these techniques or to the formation of degradation products and/or molecular adducts involving salbutamol which had similar electronic properties to those of the pure pharmaceutical, the same aliquots were then acquired in second derivative acquisition mode. The contribution of salbutamol and other possible by-products to the direct UV-Vis peaks should have been then clarified. In Figure 74 these results are described.

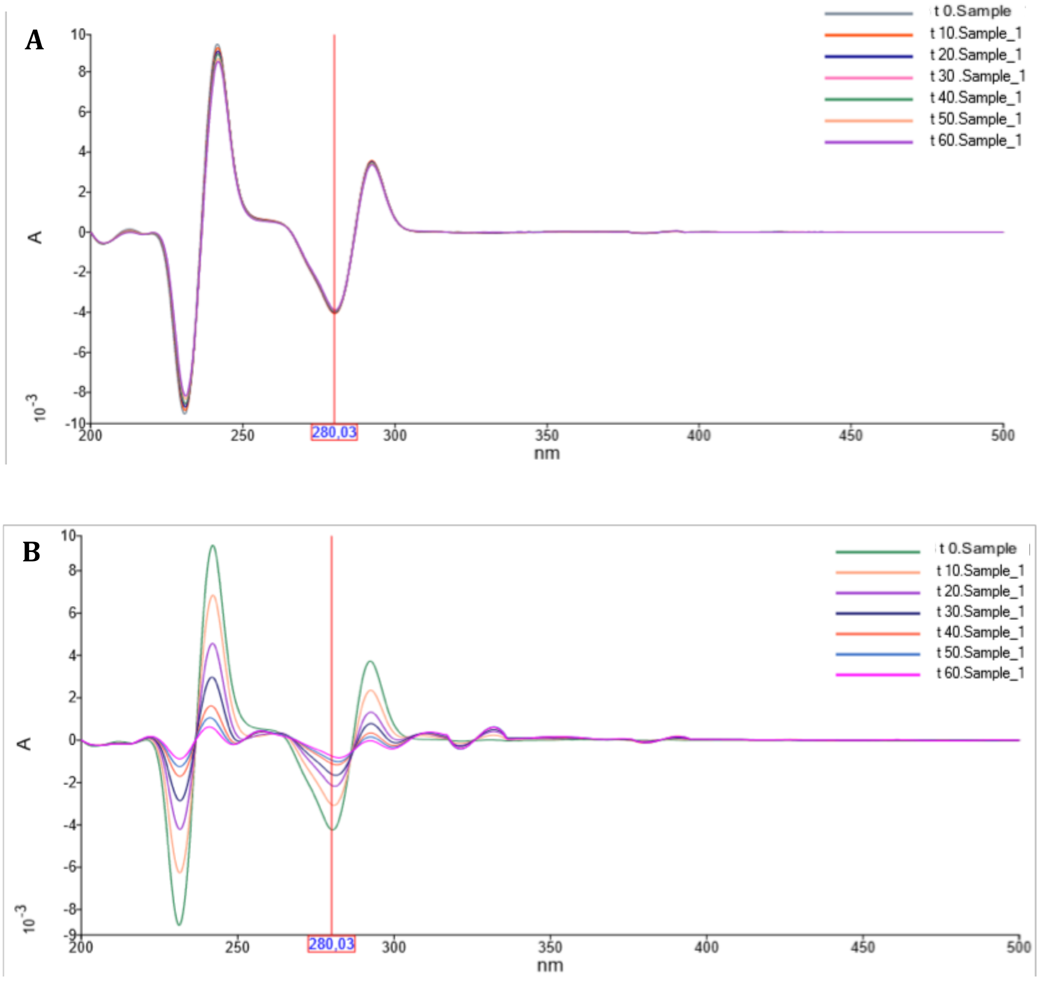

Figure 74: a) Second derivative UV-Vis spectra of different aliquots withdrawn for photolysis experiment; b) Second derivative UV-Vis spectra of different aliquots withdrawn for photocatalysis experiment

These results helped to explain the different activity of photolysis and photocatalysis which couldn't be visible with direct spectra. Photolysis seems to leave the sample unchanged, proof that these techniques is not powerful enough to bring to bonds cleavage as well as to the formation of degradation products; photocatalysis instead led to a modification of the monitored signals (both 280,03 nm and 292,18 nm), highlighting the decrease of salbutamol intensity and the appearance of new signals (according to the experiment time), which is a reasonable outcome for photocatalytic tests.

Thus, the activity's comparison between the two catalysts was performed using the derivative signal and degradation results are reported in Figure 75.

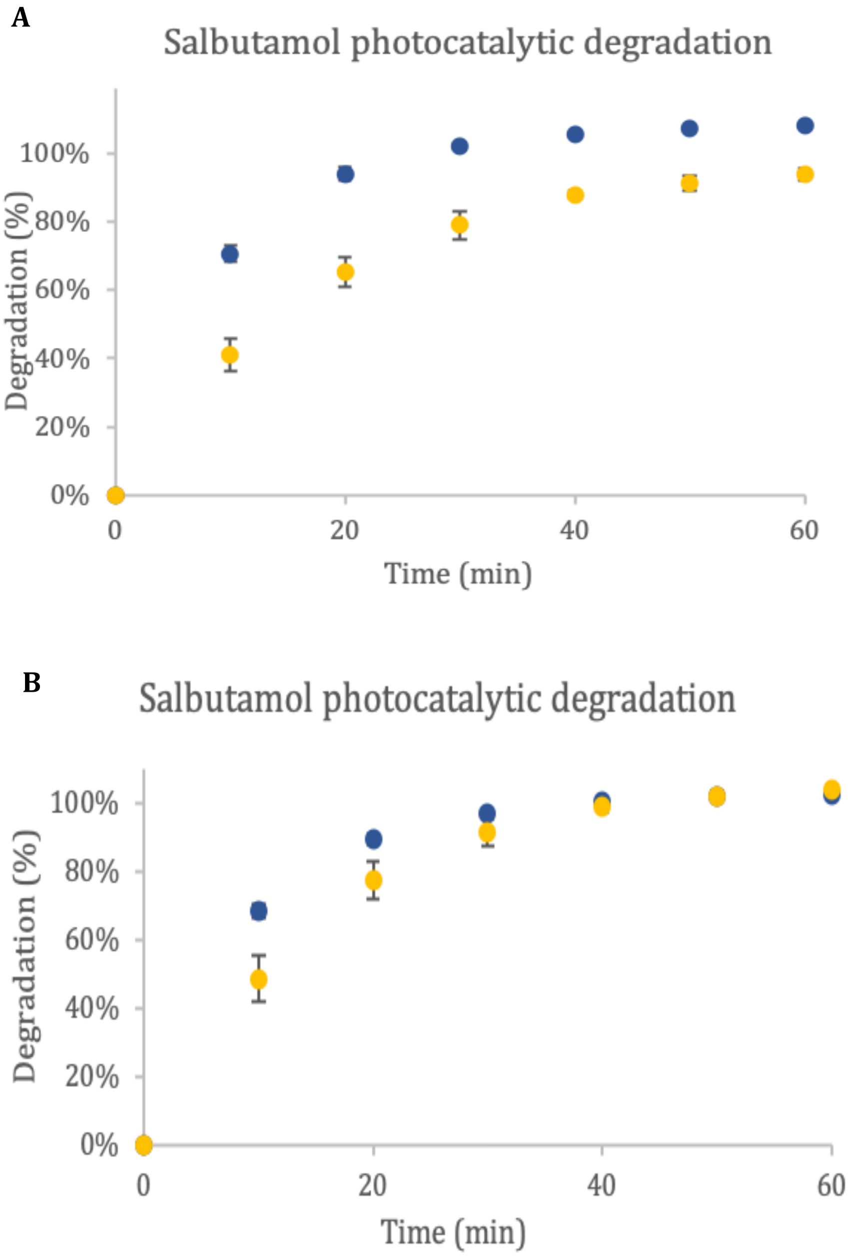

Figure 75: Salbutamol percentage degradation during 60 min of photocatalytic test under irradiation for $TiO_2/(3ZnO:Ga_2O_3:2GeO_2)$: Cr^{3+} (yellow) and $TiO_2/CaAl_2O_4$: (La, Nd)$^{3+}$ (blue) acquired at a) λ= 280,03 nm and b) λ= 292,18 nm

It is possible to see some difference in the reported graphs: $TiO_2/(3ZnO:Ga_2O_3:2GeO_2)$: Cr^{3+} sample shows a minor photocatalytic activity (between 10 and 20 %) towards salbutamol with respect to $TiO_2/CaAl_2O_4$: (La, Nd)$^{3+}$ sample and this fact could be ascribable to the different crystalline and surface feature of the two different catalysts; furthermore it is well evident the difference between the two monitored signals, in particular λ= 280,03 nm shows a pronounced dissimilarity of activity for all test points while, for λ= 292,18 nm, the intensity decrease is different only for the first test points.

As final proof to confirm the accuracy of this analytical approach, bare salbutamol and treated solutions were analysed by means of liquid chromatography coupled to mass spectrometry technique. Results are reported in Figure 76.

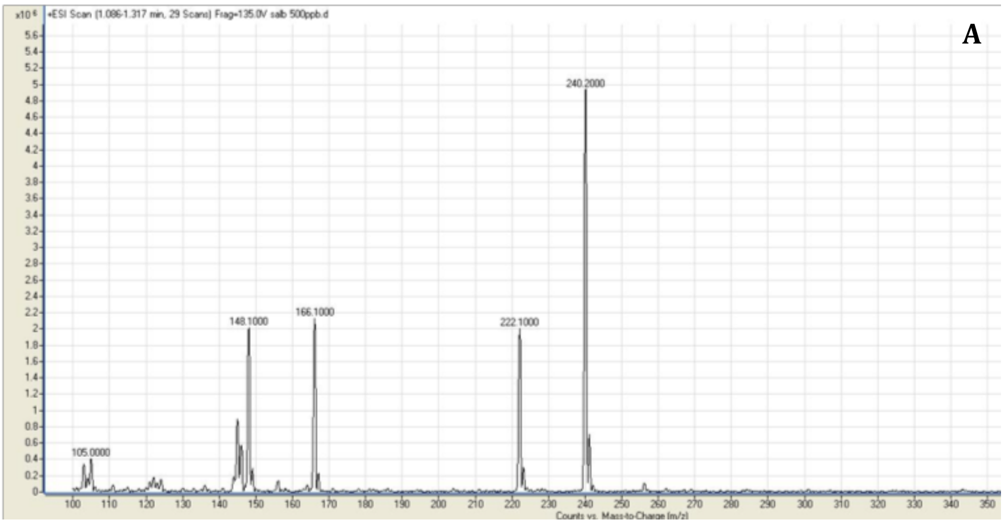

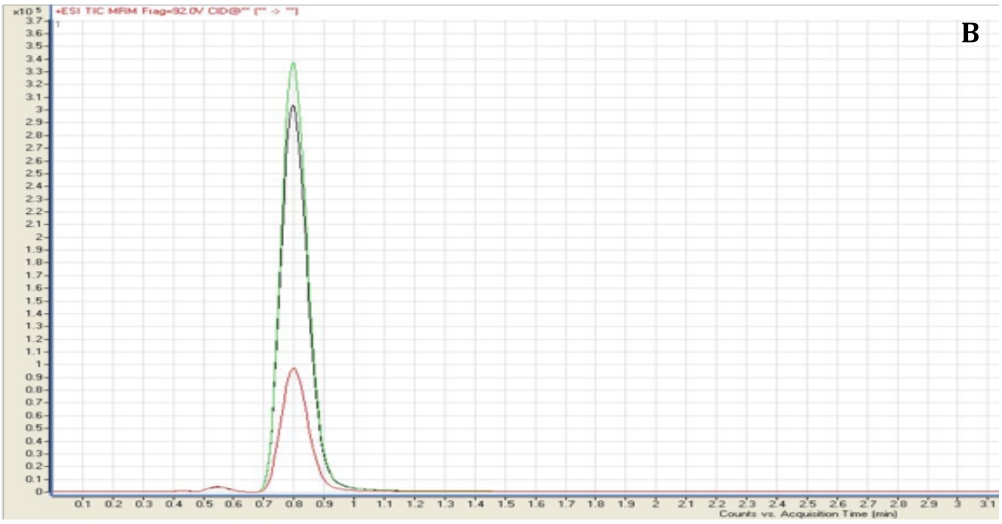

Figure 76: a) Intensity vs m/z ratio recorded for pure salbutamol solution at 500 ppb; b) Chromatogram of pure salbutamol (black), salbutamol subjected to 60 min of photolysis (green) and salbutamol subjected to 60 min of photocatalysis (red)

From literature data it was possible to confirm the nature of the salbutamol parent solution, as it is perfectly comparable with reference spectrum. In addition, elution time of all samples is the same, within the same method, proof that the eluted compound is the identical; the different subtended area are instead different: the sample subjected to photocatalysis is significantly lower than that of pure salbutamol and this of course can be related to the degradation obtained with the photocatalyst. Sample subjected to photolysis shows instead a bigger area than the one of pure salbutamol, (thus confirming the trend highlighted with UV-Vis spectra), but it still remains an unexpected and strange behaviour that could be likely justified with a calibration of the MS signal (hence the difference should be included within the instrumental error).

4.3.3. Conclusions

As a conclusion, it is possible to say that photocatalysis was successfully employed to degrade the pharmaceutical salbutamol, using solar simulated irradiation, below at least the detection limit of the instrument. Furthermore, it was possible to measure the concentration change using the second derivative

UV-Vis spectra rather than direct spectra, which couldn't be used for kinetic evaluation as the signal of interest increased along time. These results could also be confirmed by preliminary HPLC-MS/MS tests, which highlighted the drop in MS signal of the salbutamol solution subjected to photocatalysis with respect to the untreated one. It remains to be confirmed the strange trend shown for the photolysis experiments, which reasonably cannot induce transformations in salbutamol but hardly can provoke an increase in the MS signal, fact that could be validated with a calibration of the method with more experimental repetitions.

5. Concluding Remarks

During the three years of the PhD, I had the chance to deepen the knowledge on photocatalysis as Advanced Oxidation Process in the wastewater treatment field. The project was mainly focused on the chemistry of TiO_2, comprehending the synthesis, the application and the characterization of this system. National and International collaborations gave me the possibility to enhance the scientific value of the research as well as to learn a lot about this particular area of expertise.

Titanium dioxide was synthesized by means of sol-gel process while the investigated processing syntheses were different, e.g. solid-state synthesis, hydrothermal treatment and electrospinning technique. It was possible to find suitable synthetic solutions to support the nanometric powders on the different materials.

It seems that photocatalysis can be advantageously employed to degrade contaminants of emerging concern, in particular nicotine, ofloxacin and salbutamol (excluding model pollutants from this category as already well established). It didn't demonstrate as much effective with parabens, which ended to be recalcitrant to this kind of process within the investigated experimental conditions. Hence, it's reasonable to think that the activity of different AOPs together could be the right choice to have the highest efficiency against the biggest number of micropollutants possible. The upgrade of actual WWTP with the sum of these tertiary processes seems to be promising to act fast against the spread of this new class of pollution.

From experimental evidence obtained during the research, it seems that TiO_2-based photocatalytic materials are more suitable for bacteria disinfection rather than water treatment, because the risk of photocatalyst's powders dispersion is too high in water solutions rather than on coating surfaces. Even if the action mechanism is the same, the adhesion of titania on a solid support which is not dispersed in a liquid medium enables to prevent its diffusion, which is also the main cause of activity failure.

In addition, the exploitation of a chemometric approach on the synthesis of TiO_2-based materials was found to be successful, because it helped to perform the least number of experiments while getting the most information out of it (among all information, the optimized synthetic conditions). Persistent luminescence materials proved to be a good supporting material, especially for the ability to lengthen the activity in dark and or turbid situations. The coupling with another semiconductor material (ZnO) also proved to be a good choice to increment the photocatalytic efficiency; the magnetic zeolite-type material obtained from industrial waste recovery is, as well, very promising, especially considering the innovative synthesis, which fits in the circular economy frame, and the magnetic behaviour of the sample, which can be easily recovered from a suspension. The synthesis of N-doped TiO_2 confirmed the possibility to extend the absorption edge of the semiconductor towards the visible region but the doping conditions often led to a sharp decrease of the activity (likely for lattice rearrangements), thus the doping process needs to be finely controlled and optimized. Among all investigated synthesis processes, hydrothermal treatment led to the crystalline samples with the highest surface to volume ratio and also gave the possibility to exploit pressure and nucleation seeds to promote titania crystallization with lower temperature conditions with respect to usual synthetic paths. Eventually, this hydrothermal synthesis allowed to couple titania to electro-spun PDMS fibres, resulting in a very interesting antibacterial material activated by fluorescent light.

The best instrumental analytical approaches, applied to identify degradation by-products and to quantify the concentration of monitored pollutants during advanced oxidation experiments, were surely chromatographic techniques coupled with the sensitive mass spectrometry method, otherwise, it wouldn’t have been possible to accurately control their fate. Even if the project on nicotine is still ongoing, MS spectra (not reported in the current thesis) have already revealed the presence of signals ascribable to degradation by-products, that have only to be characterized. The study on the degradation of salbutamol highlighted the possibility to exploit a cheap and fast spectroscopic technique, that is the UV-Vis spectroscopy, by the acquisition of second derivative spectra, to monitor the pollutant's concentration over time, regardless of the complicated direct spectra. Finally, it can be stated that the study on the degradation of emerging pollutants cannot be divided from instrumental analytical techniques.

Scientific research on titanium dioxide is more than mature to say that this technology has still too many drawbacks, with respect to benefits, to be industrially used. Certain is that, as materials science is progressing, it is reasonable to think that new materials, with suitable properties and features, will be likely found and they will allow to overcome TiO_2 main disadvantages resulting in the industrial application in WWTPs of these materials.

In general, it can be concluded that advanced oxidation processes represent for sure an effective tool for emerging pollution remediation and their application would be able to prevent as fast as possible the spread of contaminants in the environment as well as their related diseases, like for example multidrug resistance, sexual/endocrine modification and long-term chronic exposure on humans.

6. Thesis Summary

This PhD thesis deals with the exploitation of heterogeneous photocatalysis, as an Advanced Oxidation Process, for environmental issues related to the emerging pollution: in particular for wastewater remediation and bacterial decontamination purposes. During this project, several photocatalytic materials have been synthesized by coupling semiconductor (TiO_2) nanoparticles (both bare and doped) to different supporting materials, e.g. persistent luminescence materials ($3ZnO:Ga_2O_3:2GeO_2$: Cr^{3+}; $CaAl_2O_4$: $(La, Nd)^{3+}$), magnetic and porous materials (ferrite nanoparticles, magnetic zeolite obtained from industrial waste) and polymeric materials (based on polydimethylsiloxane “PDMS”). In addition, an analytical approach to the study on the abatement and quantification of emerging pollutants was considered, an important part of which was carried out at the Water Lab of the Environmental Engineering Department at Technical University of Crete, under the supervision of Professor Elia Psillakis.

Specifically, TiO_2 was synthesized through the sol-gel technique, both in the undoped and doped form (for example with Cu and N), while its crystallization on several supporting materials was obtained with different synthetic techniques such as: sol-gel synthesis, solid-state synthesis, hydrothermal/solvothermal synthesis and electrospinning technique. Some of the synthesized materials were investigated using a chemometric approach, that is the possibility to exploit an Experimental Design mathematical model in order to investigate the optimal synthetic conditions to get enhanced photocatalytic efficiency (within the experimental domain) for the materials.

All samples synthesized within the current project were subjected to a physical-chemical characterization, by means of: X-Ray Diffraction “XRD” and crystallographic refinements (Rietveld, Pair Distribution Function “PDF”, Williamson-Hall plot), Scanning and Transmission Electron Microscopy-Energy Dispersive X-Ray Spectrometry “SEM-EDS”, “TEM”, Porosimetry Brunauer-Emmett-Teller “BET”, Dynamic Light Scattering “DLS”, Differential Scanning

Calorimetry “DSC”, Diffuse Reflectance (Kubelka-Munk plots for Energy Gap “E_g”), Rheological Measurements, Luminescence Properties, Turbidimetry, Inductively Coupled Plasma – Atomic Emission Spectroscopy “ICP-AES”, Diffuse Reflectance Infrared Fourier Transform Spectroscopy “DRIFTS” and antibacterial properties with *E. Coli* cultures. Above all, a kinetic characterization in terms of photocatalytic efficiency evaluation was always performed for synthesized samples. In particular, kinetic behaviour of the photocatalysts was evaluated by means of Methylene Blue “MB” aqueous solutions degradation, studied as a function of time, with different initial concentrations (as required by ISO NORM 10678:2010). For MB quantification, a UV-Vis spectrophotometer was used, and experiments were usually performed in triplicate. Furthermore, during the first part of the project, a Pilot Plant Prototype was assembled (with a processing volume equal to 1L) and used for preliminary evaluations on a potential industrial scale-up. All tests and characterizations achieved were adapted according to the specific supporting material employed.

Eventually, considering the nature of emerging micro-pollutants, an analytical approach to the determination of their concentration in aqueous systems was employed. Specifically, chromatographic tests were performed with liquid and gas chromatography techniques, often coupled with mass spectrometry, for some specific emerging pollutants (Ofloxacin, Parabens, Nicotine, Salbutamol). Matrix effects were also considered in the evaluation of the pollutants’ degradation during the advanced oxidation tests.

This task wouldn’t have been possible without valuable National and International collaborations, which gave an essential help to the development of the project for what concerns a part of the reported characterization. My acknowledgements are directed to: Department of Chemistry and Industrial Chemistry - University of Genova (Analytical, Industrial, Physical Sections), Analytic and Photochemistry Section of the Department of Chemistry - University of Pavia; Department of Chemistry - University of Kuwait; Department of Environmental Engineering - Technical University of Crete; Institute of

Methodologies of Environmental Analysis, Institute of Matter and Institute of Superconducting and other Innovative Materials and Devices - National Research Council. Each individual contribute will be highlighted in each dedicated section, throughout the manuscript.

Emerging pollutants are defined, according to the Environmental Protection Agency "EPA" definition, as all those compounds which are not subjected to precise environmental regulation and their impact on the environment and human health is still poorly understood and known[8,9]; it's a matter of thousands of synthetic compounds with heterogeneous physical-chemical properties and unknown environmental behaviour. Among all, the most alarming substances are pharmaceuticals and drugs, together with their transformation by-products, as they are designed to have a biological response. Despite the concentration of the overall class is still quite low (ppm to ppt), they're administered and used in large quantities (the estimated annual trade of these compounds ranges from 100.000 to 200.000 tons); hence they are continuously replenished in the environment[11,12].Unfortunately, actual wastewater treatment plants are not designed to face these specific pollutants because they are not equipped with effective technologies (average percentage abatement sets up to about 2%)[22]; for this reason the current PhD project dealt with advanced oxidation process, because they represent a solid option to face this threat. Nowadays, the problem involves whole Earth[14,15] but still there is not a single complete solution established for each micropollutant.

Among all the emerging pollutants, the most concerning are pharmaceuticals, together with their degradation and metabolization by-products, because they are designed to have high chemical stability, high water solubility and strong biological interaction, even in low concentrations[16,17]. The variety of pharmaceuticals available today is as huge as the variety of medical effects that can be obtained and the presence in the aquatic environment of all these compounds together may even represent a bigger and more dangerous threat, as the simultaneous action can likely be synergic and thus affect in unknown ways living organisms. Multidrug resistance represents an effect of the presence of antibiotics: it is due to the ability of bacteria to grow and reproduce quickly, accumulating favourable genetic mutations to adapt to the continuous alterations of their living environment[26]. For this reason, some bacteria strains have developed a resistance to the commonly used pharmaceuticals (mainly antibiotics): the enormous hazard relies in the fact that, since antibiotics are no longer active in counteracting bacterial infections, even common and harmless diseases could eventually lead to the worst outcomes[28].

Advanced oxidation processes[31] have a higher affinity to emerging contaminants and they can also be exploited with eco-friendly and cheaper energy sources[32–36]. Heterogeneous photocatalysis was chosen because semiconductors like TiO_2 have high oxidizing powers, able to completely mineralize a huge spectrum of organic micropollutants to nontoxic molecules[60,75]. The engineering of the photocatalytic material represented the main part of this project, because through the synthetic process is possible to control the characteristics of the photocatalytic materials and so overcome those drawbacks which actually hinder its industrial application.

As a first part of the project, a photocatalytic material based on TiO_2 and ($3ZnO:Ga_2O_3:2GeO_2$): Cr^{3+} "PeL" material was produced and the synthesis was optimized using a chemometric approach. Nanometric powders of anatase TiO_2 were synthesized through the sol-gel technique, while PeL material was synthesized through a solid-state treatment. Each sample was characterized by means of XRD, SEM and BET analyses, while the photocatalytic activity was evaluated testing the percentage degradation of a methylene blue aqueous solution. In particular, the optimized sample was subjected to two kind of kinetic experiments: continuous irradiation and alternate dark/light cycles. It was demonstrated that the supporting PeL material could provide photons for the photocatalytic process during the absence of light. The synthesis of the composite material was planned through an Experimental Design 2^3, were the weight ratio between TiO_2/PeL, the heating temperature and the processing time were investigated as variables upon two levels. The evaluation of the model led to the conclusions that the monitored variables didn't affect the synthesis; thus, the most convenient values of the variables could be exploited to have an optimized sample. Eventually, the best one was tested for the degradation of a real emerging pollutant, i.e. the antibiotic ofloxacin, in tap water under simulated sunlight. The activity of the optimized sample reached the highest percentage degradation values for the most convenient synthetic conditions after 50 minutes of alternate dark/light irradiation cycle. These results demonstrated the potential applicability of this system when no external irradiation can be provided (during the night or in very turbid solutions, e.g. wastewaters). The Project was performed in collaboration with the section of Analytical and Photo- Chemistry of the Department of Chemistry of the University of Pavia, in particular with the research group of M. Sturini. The photocatalytic material was optimized by the chemometric approach.

As a second part of the project, in order to test a commercial PeL material as a replacement of the synthetic one, the $CaAl_2O_4$: (La, Nd)$^{3+}$ PeL material was chosen for its theoretical compatibility between its emission (2,25 – 3,25 eV, corresponding to 551 – 381 nm) and bare anatase TiO_2 absorption. The main aim was to use a greener material, with a different chemical composition, in order to have an eco-friendlier material with the same efficiency in dark conditions highlighted in the previous section. Samples were synthesized according to a chemometric approach 2^3; each sample was tested on its photocatalytic efficiency with kinetic experiments on the percentage degradation of methylene blue solutions and the resulting optimized sample was characterized by means of XRD, SEM-EDS, BET and DLS analyses. By means of MB degradation, it was possible to highlight the importance of the TiO_2/PeL weight ratio. During darkness experiments, the experimental outcome highlighted that this supporting material was not able to provide photons to the catalyst, quite likely for the undesired side-reaction occurred between PeL and TiO_2, evidenced from XRD analysis, which modified the crystalline structure of the composite. Surprising was that the surface area is extremely high, considering that a solid-state synthesis was used, and it may be attributable to the formation of the new crystalline phase on the interface between the support and the catalyst. The project was designed in collaboration with the research group of M. Sturini (University of Pavia).

As a third part of the project, a three-components composite material was projected, based on TiO_2 nanoparticles, ZnO nanoparticles[92,93] and micrometric PeL ($3ZnO:Ga_2O_3:2GeO_2$): Cr^{3+}. The preparation of ZnO nanoparticles was performed in two ways: via zinc citrate, by the research group of Professor D. Comoretto, Industrial Chemistry Section of University of Genova, and via zinc nitrate. Preliminary results on the photocatalytic efficiency were obtained from the degradation of a 0,01 g/L MB solution under 40 min of solar simulated light irradiation. Elemental composition confirmed that the zinc nitrate route lead to a homogeneous composition of Zn an O, without the presence of any other impurity, while zinc acetate route still presented K impurity due to the synthetic process. The shape of the particles is noteworthy, because the first heat treatments led to a specific platelet arrangement, randomly distributed, with very thin edges showing nanometric to micrometric dimensions, while the second one led to specific spherical shapes, with the same dimensional range (mostly nanometric). This part of the research is still ongoing; the presented results are not complete, and they need to be widely integrated with further kinetic experiments as well as physical-chemical characterization, in order to be able to get useful information and draw important conclusions.

As a fourth part of the project, a pilot plant prototype (with a processing volume of 1 L) was built to perform beginning experiments on the efficiency of different synthesized catalysts. Considering the surface charge of TiO_2, it is useful to know the so-called Iso-Electric Point, which corresponds to the pH value of the solution in which TiO_2 is suspended, for which the concentration of OH^- is equal to that of H^+. In these conditions, the colloidal suspension of the catalyst becomes unstable, hence it tends to settle down faster[95]. Some TiO_2 based materials were analysed on their pH_{IEP} by means of electrophoretic mobility, later transformed in "ζ" Potential values and on their settling rate. This project was performed in collaboration with the research group of Dr. M. O. Amin, of the Department of Chemistry at the University of Kuwait. All the reported data have not been published yet. These data are currently under elaboration: the exploitation of a mathematical model according to a chemometric approach, in particular a D-Optimal screening model, will be used to consider the significance of qualitative and quantitative variables, for the study of the efficiency and the recovery in the pilot plant prototype

As a fifth part of the project, pure, N-doped, Cu-doped and (Cu, N)-double doped TiO_2 samples were synthesized through a sol-gel synthesis in order to investigate the local and average structure of crystalline TiO_2, processed under different pH conditions. Samples resulted mainly composed of anatase phase, even though a low but significant amount of secondary brookite grew in most samples. A detailed structural characterization was performed by means of synchrotron X-Ray elastic scattering experiments; structural data of different samples were gained by means of the pair distribution function analysis. The aim of this work was to investigate the crystalline structure of nanosized TiO_2 as a function of the different synthetic conditions tested. As a result, Cu substitution at the Ti site determines a remarkable lattice distortion, larger than that observed for N substitution. In particular, Cu substitution determines a rearrangement of the cationic sub-lattice, which can also be related to the photocatalytic efficiency loss; conversely, the anionic sub-lattice appears almost unaffected by the light replacement of Cu for Ti. Local structure analysis suggests that N actually replaces O in anatase, rather than being located in structural voids. In any case, the synthesis in NH_3 solution hinders or even prevents the formation of secondary brookite. This is relevant, since the competing growth of brookite determines the formation of a large number of structural defects within anatase. This project was carried out in collaboration with Dr. A. Martinelli of the Institute of Superconducting and other Innovative Materials and Devices of the National

Research Council and the research group of Prof. D. Comoretto from Industrial Chemistry Section of University of Genova.

As a sixth part of the project, the hydrothermal crystallization of anatase TiO_2 nanoparticles using different ferrite nanoparticles with different chemical composition, dimensions and shape as nucleation seeds was investigated. In particular, $CoFe_2O_4$, $NiFe_2O_4$ and Fe_3O_4 NPs with a volume ratio equal to 1:1000 with respect to the TiO_2 amount, were used. In addition, Lu_2O_3 nanoparticles were also used to detect the effect of non-magnetic NP on the synthesis and crystallization of titania[106]. For each sample, a deep physical-chemical characterization was performed by means of XRD and Rietveld refinement, FE-SEM, STEM, TEM, DSC and BET surface area measurements. Furthermore, some samples were subjected to photocatalytic tests for MB solutions degradation. The hydrothermal synthesis was performed in a closed steel vessel, for 3 hours at 150 °C, under a natural pressure of 9 bars. The used temperature resulted to be significantly lower than usual temperatures exploited to get the anatase phase, hence indicating that the mere presence of a nucleation seed, without any particular need in terms of composition/morphology, simplifies the crystallization of anatase. The nucleation starts onto the ferrite nanoparticle surface, likely growing towards a preferential direction (the lattice parameter with comparable length), and thus an anatase crystalline seed is formed, which in turn will act itself as a new nucleation spot. It was proven that the nucleation can proceed in any case, without noticeable differences in the synthesized samples due to the different seeds used: XRD patterns, surface area values, thermal behaviours and photocatalytic efficiency were essentially the same for all the samples. Eventually, it was demonstrated that also non-ferrite structured nanoparticles (Lu_2O_3) could act as nucleation seeds. This project was carried out with the collaboration of the research group of Prof. G. Singh of the Department of Materials Science and engineering, Norwegian University of Science and Technology, and of Dr. A Martinelli of the Institute of Superconducting and other Innovative Materials and Devices of the National Research Council

As a seventh part of the project, polydimethylsiloxane was chosen as supporting material for TiO_2 nanoparticles, for its high surface area and stability against TiO_2 photoactivity. TiO_2 was prepared via sol-gel synthesis and subjected to a hydrothermal treatment in presence ferrite nanoparticles in order to act as nucleation seeds; concurrently, high pH so-gel syntheses were performed with increasing NH_3 concentrations in order to compare samples' antibacterial activity. They were both processed with the electrospinning technique: it was possible to disperse titania among PDMS fibres and to obtain detachable polymeric membranes with the appearance of white soft sheets. These membranes show antibacterial activity under fluorescent light; hence they may be used as coating film for several kind of surfaces. Synthesized samples were controlled and characterized by means of rheological measurements, SEM-EDS images, DSC analyses, E_g calculation by means of diffuse reflectance (Kubelka-Munk plot), recycling photocatalytic experiments and bacterial inactivation with *Escherichia Coli* colonies. The supporting synthesis was successful, as the porous structure of the PDMS membrane, joined with the macroscopic manoeuvrability of the sheet itself, allows a satisfying TiO_2 surface activity. This material can be employed in a wide range of fields: it can be applied to several surfaces, it is easily activated under artificial light and it can be detached without difficulties; furthermore, as highlighted with recycling tests, the composite is recyclable. TiO_2 activity is not limited by the support because it has a very high surface area and the interaction between PDMS fibres and the catalyst is strong enough to avoid the dispersion of the TiO_2, as highlighted with MB recycling experiments, for at least 3 consecutive cycles. N-doped TiO_2 samples didn't behave as forecast, because the hydrothermal synthesis did not provide the proper conditions to dope effectively the catalyst's lattice, furthermore, the antibacterial activity was not improved for the alkaline conditions. Lastly, the composite material's synthesis was chosen in order to be easily scaled up towards the industrial production, indeed, the electrospinning process fits in this choice for its easy handling and process parameters' control. This project was carried out in collaboration with the research group of Prof. M. Castellano and S. Vicini of the Industrial Chemistry Section of University of Genova.

As an eighth part of the project, a new nanometric TiO_2-based magnetic catalyst has been developed from an innovative material obtained from the treatment of iron and steel industrial waste, i.e. Fly Ash. This magnetic material contains iron in the chemical-mineralogical composition, and it represents an excellent example of circular economy: the industrial waste is converted into a high technological valued product. Through a one-step hydrothermal activation, the precursor is transformed in a zeolite with good magnetic properties. These features could be exploited in the environmental field, such as the degradation of emerging pollutants in aqueous media by coupling it with a photocatalyst. In particular, TiO_2 NPs are synthesized with a sol-gel technique and then mixed with the magnetic material by means of ultrasounds, in different pH conditions: acidic (0,1 M HNO_3), neutral and alkaline (0,1 M NaOH). Afterwards, the composite is subjected to a mild heat treatment to reinforce the interaction. The synthesized materials are characterized by means of XRD and SEM-EDS while their photocatalytic activity is evaluated through the abatement of MB solutions, testing also the possibility to magnetically recover the suspension and reuse the catalyst. The TiO_2-based composite material was used as an advanced oxidation process for the photocatalytic degradation of a model pollutant. This represent the possibility to extend the use of photocatalysis as tertiary process, because the magnetic material has strongly enhanced the recovery of the colloidal suspension. This result could only be obtained when the synthesis of the material was performed in alkaline conditions, because the crystalline structure and the surface properties obtained in these conditions led to a good photocatalytic efficiency and, moreover, to the possibility to reuse the catalyst (for at least 3 cycles). This project was carried out in collaboration with the research group of C. Belviso from Institute of Methodologies for Environmental Analysis of the National Research Council and the research group of Prof. D. Peddis from the Institute of Matter Structure of the National Research Council.

Conversely, during the PhD, an instrumental analytical approach was also studied to investigate some specific emerging pollutants. In particular, the study dealt with the identification of parabens, nicotine and salbutamol by means of chromatographic techniques coupled to mass spectrometry and/or diode array detectors. Also, matrix conditions affecting the oxidation process were considered. The big part of this study was undertaken during the abroad period of four months and a half spent at the Water Lab of the Department of Environmental Engineering Department, (Technical University of Crete), under the supervision of professor Elia Psillakis. All presented data and results have not been published yet.

As a ninth part of the project, aqueous solutions of a mixture of four parabens (MP, EP, PP, BP) were subjected to photolysis experiments under different processing conditions. These compounds are characterized by a good water solubility, chemical and photo-chemical stability; thus they were chosen as subject of the study[115–117]. Effectively, this project was performed in order to evaluate different aspects on the degradation of the parabens' mixture: first of all, to study the possibility to exploit photocatalysis as advanced oxidation process to degrade these compounds from water; furthermore, to study the formation of probable degradation by-products in relation to the matrix composition and eventually to study the significant parameters affecting the degradation process, such as: pH effect, initial parabens concentration, undesired dissolved species (tert-butanol, humic acid) and catalyst's concentration. The final aim was to study the degradation of these species in real matrices, i.e. wastewater, river water and tap water. This project was carried out in the Water Lab of the Environmental Engineering Department, at the Technical University of Crete, under the supervision and with the help of Professor Elia Psillakis. For the experimental results obtained from this project, in particular the inability to speed up the degradation process with the photocatalyst (within the chosen experimental conditions) and further taking into consideration the short time available at the Water Lab facilities, it was decided not to continue; thus, all the experiments on the matrix effect and the degradation by-products were not performed. Some considerations may be done on the displayed behaviour: the mixture of all parabens could likely undergo radiation quenching processes among all the molecules, hence substituting bonds cleavage with energy dissipation which involves vibrational and rotational energy levels. The presence of the photocatalyst, activated by UV light, didn't really improve the degradation and this fact may be ascribable to a poor interaction between the catalyst's surface and the pollutants (maybe for missing charge interactions) as well as a remarkable stability of the mixture of these pollutants. The mechanism of the parabens' photocatalytic degradation should be clarified, in order to put in evidence which mechanisms are involved in the mineralization and which ones are responsible for the low photocatalytic activity. Anyway, as reported in literature, different but effective AOPs can be employed (e.g. an hard AOP: ozonation[119]) against parabens, even if the energetic demand is higher, because they can have more energy available to degrade the mixture of these compounds and thus overcome the limitations highlighted with photocatalysis.

As a tenth part of the project, nicotine, a highly toxic alkaloid deriving from the tobacco consumption that is found to be ubiquitous in wastewater effluent, was used as subject of the oxidation process. Luckily, it was possible to exploit photolysis as AOP to degrade nicotine[123], thus it was possible to determine the different effects that influenced the process: starting pollutant concentration, pH effect, matrix effect (tert-butanol, humic acid and sodium chloride presence) and eventually different aqueous matrices (sea water, river water, tap water, wastewater and rain water). At last, nicotine degradation from aqueous leachates obtained with four different cigarettes configurations was studied: conventional and IQOS cigarettes were used bare and smoked by a smoking machine. Analytical methods employed for the study of this complex system were different, according to the different samples composition; HPLC-DAD-MS, GC-FID and GC-MS. Experimental results were successful, because it was possible to demonstrate that nicotine itself can be degraded in different matrix conditions, from simple to complex cases like the ones of real leachates. In particular, it was found that acidic conditions were favourable to have a successful and fast degradation of nicotine, while the presence of other dissolved species didn't bring to negative effects on the process. This behaviour suggests that the use of photocatalysis as oxidation process could be really effective on the improvement of the degradation rate and yield of nicotine. Further studies and characterizations still need to be done for what concerns the total organic carbon "*T.O.C.*" content of the real leachates after the photolysis experiments and mainly the identification of transformation by-products formed during the process. All recorded spectra are indeed characterized by a wide variety of secondary signals, in relation to the photolysis time, which have to be characterized and confirmed by means of literature and database comparison. This step is clearly the most complicated, especially for the real leachates' samples, because the composition of the matrix gets the interpretation of spectra more complicated. Eventually, toxicity tests on nicotine and its by-products are on the go, in order to be included in the final work together with the rest of the expected characterizations. As already mentioned, these data are not included in the current thesis because they're not available yet, but they will be included in a scientific publication as soon as they will be ready.

As an eleventh and last part of the project, the pharmaceutical salbutamol, prescribed in the U.S. more than 47 million times per year, was object of the analytical study. The evaluation of the degradation rate of salbutamol in water was assessed by means of UV-Vis spectra acquired in second derivative and preliminary confirmations with HPLC-MS were used to validate the procedure[125]. Further studies will be conducted on the degradation by-products that can be obtained during the photocatalytic degradation process. As a conclusion, photocatalysis was successfully employed to degrade the analyte, using solar simulated irradiation, below at least the detection limit of the instrument. Furthermore, it was possible to measure the concentration change using the second derivative UV-Vis spectra rather than direct spectra, which couldn't be used for kinetic evaluation as the signal of interest increased along time. These results could also be confirmed by preliminary HPLC-MS tests, which highlighted the drop in MS signal of the salbutamol solution subjected to photocatalysis with respect to the untreated one. This project was performed in collaboration with the Analytical Chemistry Section of the University of Genova, with the help of Prof. M. Di Carro.

It's reasonable to think that the activity of different AOPs together could be the right choice to have the highest efficiency against the biggest number of micropollutants possible. The upgrade of actual WWTP with the sum of these tertiary processes seems to be promising to act fast against the spread of this new class of pollution. Scientific research on titanium dioxide is more than mature to say that this technology has still too many drawbacks, with respect to benefits, to be industrially used. Certain is that, as materials science is progressing, it is realistic that new materials, with suitable properties and features, will be likely found and they will allow to overcome TiO_2 main disadvantages resulting in the industrial application in WWTPs of these materials. In general, it can be concluded that advanced oxidation processes represent for sure an effective tool for emerging pollution remediation and their application would be able to prevent as fast as possible the spread of contaminants in the environment as well as their related diseases.

Riassunto della Tesi

L'oggetto della presente tesi di dottorato è stato l'utilizzo della fotocatalisi eterogenea in quanto Processo di Ossidazione Avanzata, per applicazioni ambientali legate all'inquinamento emergente: in particolare per la bonifica delle acque reflue e la decontaminazione batterica. Durante questo progetto, sono stati sintetizzati diversi materiali fotocatalitici accoppiando nanoparticelle di un materiale semiconduttore (TiO_2, sia tal quale che drogato) a diversi materiali di supporto, come ad esempio: materiali a luminescenza persistente ($3ZnO:Ga_2O_3:2GeO_2$: Cr^{3+}; $CaAl_2O_4$: $(La, Nd)^{3+}$), materiali magnetici e porosi (nanoparticelle di ferrite, zeolite magnetica ottenuta da rifiuti industriali) e materiali polimerici (membrane a base di polidimetilsilossano "PDMS"). Inoltre, è stato preso in considerazione un approccio analitico strumentale, applicato allo studio sull'abbattimento degli inquinanti emergenti e la loro quantificazione; di questo progetto, la parte più importante è stata condotta presso il *Water Lab* del Dipartimento di Ingegneria Ambientale dell'Università Politecnica di Creta, sotto la supervisione della Professoressa Elia Psillakis.

In particolare, il TiO_2 è stato sintetizzato attraverso la tecnica sol-gel, sia in forma non drogata che drogata (ad esempio con Cu e N), mentre la sua cristallizzazione su differenti materiali di supporto è stata ottenuta con diverse tecniche, quali: sintesi sol-gel, sintesi allo stato solido, sintesi idrotermale/solvotermale e tecnica *elettrospinning*. Alcuni dei dispositivi sintetizzati sono stati studiati utilizzando un approccio chemiometrico, ovvero sfruttando un modello matematico, sul quale è stata progettata la parte sperimentale, al fine di studiare le condizioni sintetiche ottimali per ottenere una maggiore efficienza fotocatalitica (all'interno del dominio sperimentale indagato).

Tutti i campioni sintetizzati nell'ambito del presente progetto sono stati sottoposti a una caratterizzazione chimico-fisica, mediante: Diffrattometria a Raggi X "XRD" e affinamenti strutturali (Rietveld, Pair Distribution Function

"PDF", Williamson-Hall Plot), Microscopia a Scansione e Trasmissione Elettronica - Spettrometro a Raggi X a Dispersione di Energia "SEM-EDS", "TEM", Porosimetria Brunauer-Emmett-Teller "BET", Dynamic Light Scattering "DLS", Calorimetria a Scansione Differenziale "DSC", Riflettanza Diffusa (grafici Kubelka-Munk per Energy Gap "E_g"), Misure Reologiche, Proprietà di Luminescenza, Turbidimetria, Plasma Accoppiato Induttivamente - Spettroscopia di Emissione Atomica "ICP-AES", Spettroscopia in Riflettanza Diffusa nell'Infrarosso a Trasformata di Fourier "DRIFTS" e Attività Antibatterica con colture di *Escherichia Coli*. Per la maggior parte dei campioni sintetizzati è stata effettuata una caratterizzazione cinetica in termini di valutazione dell'efficienza fotocatalitica; in particolare: il comportamento cinetico dei fotocatalizzatori è stato valutato mediante la degradazione di soluzioni acquose di blu di metilene "MB", studiata in funzione del tempo, con diverse concentrazioni iniziali (come richiesto dalla Norma ISO 10678: 2010). Per la quantificazione del MB, è stato utilizzato uno spettrofotometro UV-Vis e gli esperimenti sono stati generalmente eseguiti in triplicato. Inoltre, durante la prima parte del progetto, è stato assemblato un prototipo di un impianto pilota (con un volume processabile pari a 1L), utilizzato per effettuare valutazioni preliminari su un potenziale *scale-up* industriale. Tutti i test e le caratterizzazioni effettuate sono stati adattati in base allo specifico materiale di supporto impiegato.

Infine, considerando la natura dei microinquinanti emergenti, è stato impiegato un approccio analitico strumentale per la determinazione della loro concentrazione in sistemi acquosi. In particolare, sono stati eseguiti dei test analitici con tecniche di cromatografia liquida e gassosa, spesso accoppiate alla spettrometria di massa, per alcuni inquinanti emergenti specifici, tra cui ofloxacina, parabeni, nicotina e salbutamolo. Sono stati presi in considerazione anche gli effetti matrice nella valutazione della degradazione degli inquinanti durante i test di ossidazione avanzata.

Questo compito non sarebbe stato possibile senza le preziose collaborazioni nazionali e internazionali che hanno dato un aiuto essenziale allo sviluppo del progetto per quanto riguarda una parte della caratterizzazione riportata. I miei ringraziamenti vanno a: Dipartimento di Chimica e Chimica Industriale - Università degli Studi di Genova (Sezione di Chimica Analitica, Industriale e Chimica-Fisica), Sezione di Chimica Analitica e Fotochimica del Dipartimento di Chimica - Università degli Studi di Pavia; Dipartimento di Chimica - Università del Kuwait; Dipartimento di Ingegneria Ambientale - Università Politecnica di Creta; Istituto di Metodologie per l'analisi Ambientale, Istituto di Struttura della Materia e Istituto di Materiali e Dispositivi Superconduttori e altri Materiali Innovativi – Consiglio Nazionale delle Ricerche. Ogni singolo contributo viene evidenziato nell'elaborato scritto, in ogni sezione dedicata.

Gli inquinanti emergenti sono definiti, secondo la definizione dell'Agenzia statunitense per la Protezione Ambientale, come tutti quei composti che non sono soggetti a una precisa regolamentazione ambientale, il cui impatto sull'ambiente e sulla salute umana risulta ancora poco conosciuto[8,9]; si tratta di migliaia di composti sintetici con proprietà chimico-fisiche eterogenee e comportamento ambientale sconosciuto. Nonostante la concentrazione della classe sia complessivamente ancora piuttosto bassa (dalle ppm alle ppt), questi composti vengono amministrati e utilizzati in grandi quantità (il commercio annuo stimato varia dalle 100.000 alle 200.000 tonnellate) e pertanto vengono continuamente immessi nell'ambiente[11,12]. Sfortunatamente, gli attuali impianti di trattamento delle acque reflue non sono progettati per affrontare questi specifici inquinanti perché non sono dotati di tecnologie abbastanza efficaci (la percentuale media di abbattimento raggiunge circa il 2%)[22]; per questo motivo i processi di ossidazione avanzata sono stati oggetto del presente progetto di Dottorato, in quanto rappresentano una solida opzione per affrontare questa minaccia. Al giorno d'oggi, il problema risulta di rilevanza mondiale[14,15], ma ciononostante non esiste ancora una soluzione completa per ogni micro-inquinante.

Tra tutti gli inquinanti emergenti, i più preoccupanti risultano essere i prodotti farmaceutici, insieme ai loro sottoprodotti di degradazione e metabolizzazione, in quanto progettati per avere un'elevata stabilità chimica, una elevata solubilità in acqua e una forte interazione biologica, anche a basse concentrazioni[16,17]. La varietà di farmaci disponibili oggi è tanto grande quanto la varietà di effetti medici che possono essere ottenuti. La concomitante presenza, nell'ambiente acquatico, di tutti questi composti insieme può rappresentare una minaccia persino più grande e più pericolosa, poiché la loro azione simultanea potrebbe essere sinergica e influenzare in modo sconosciuto gli organismi viventi. La resistenza ai farmaci rappresenta un effetto collegato alla presenza di antibiotici: è legata alla capacità dei batteri di crescere e riprodursi molto rapidamente, accumulando mutazioni genetiche favorevoli per adattarsi alle continue alterazioni del loro ambiente di vita[26]. Per questo motivo, alcuni ceppi batterici hanno sviluppato una resistenza ai prodotti farmaceutici di uso comune (principalmente gli antibiotici, appunto): l'enorme pericolo dipende dal fatto che, poiché gli antibiotici non risultano più attivi nel contrastare le infezioni batteriche, anche le malattie più comuni e innocue potrebbero infine portare a i risultati peggiori[28].

I processi di ossidazione avanzata[31] hanno una maggiore affinità con i contaminanti emergenti e possono anche essere sfruttati con fonti di energia sostenibili ed economiche[32–36]. È stata scelta la fotocatalisi eterogenea perché i semiconduttori come il TiO_2 hanno elevati poteri ossidanti, in grado di mineralizzare completamente un ampio spettro di micro-inquinanti organici in specie chimiche non tossiche[60,75]. L'ingegneria del materiale fotocatalitico ha rappresentato la parte principale di questo progetto, perché attraverso il processo di sintesi è stato possibile controllare le caratteristiche dei dispositivi fotocatalitici e superare così gli inconvenienti che ne ostacolano effettivamente l'applicazione industriale.

Come prima parte del progetto, è stato prodotto un dispositivo fotocatalitico basato sul TiO_2 e il materiale luminescente "PeL" ($3ZnO:Ga_2O_3:2GeO_2$): Cr^{3+} e la sintesi è stata ottimizzata utilizzando un approccio chemiometrico. Le polveri nanometriche di anatasio TiO_2 sono state sintetizzate attraverso la tecnica sol-gel, mentre il materiale PeL è stato sintetizzato attraverso un trattamento allo stato solido. Ciascun campione è stato caratterizzato mediante analisi XRD, SEM e BET, mentre l'attività fotocatalitica è stata valutata testando la degradazione percentuale di una soluzione acquosa di blu di metilene. In particolare, il campione ottimizzato è stato sottoposto a due tipi di esperimenti cinetici: irraggiamento continuo e irraggiamento alternato luce/buio. È stato dimostrato che il materiale PeL di supporto può fornire i fotoni necessari al processo fotocatalitico durante l'assenza di luce proveniente da una fonte esterna. La sintesi del materiale composito è stata pianificata attraverso un disegno sperimentale 2^3, in cui sono state indagate come variabili il rapporto in peso tra TiO_2/PeL, la temperatura del trattamento e il tempo di trattamento, utilizzando due livelli di studio. La valutazione del modello ha portato alla conclusione che le variabili in oggetto non sono risultate significative per la sintesi, pertanto i valori più convenienti delle variabili (livello -1) possono essere impiegati per avere un campione efficiente. Infine, il campione ottimizzato è stato testato per la degradazione di un vero inquinante emergente, ovvero l'antibiotico ofloxacina, nell'acqua del rubinetto sotto luce solare simulata. L'attività del campione ottimizzato ha raggiunto i più alti valori di abbattimento percentuale, con le condizioni sintetiche più convenienti, dopo 50 minuti di irraggiamento in ciclo alternato. Questi risultati hanno dimostrato la potenziale applicabilità di questo sistema quando non è possibile disporre di una fonte esterna (durante la notte o in soluzioni molto torbide, come ad esempio le acque reflue). Il progetto è stato realizzato in collaborazione con la sezione di Chimica Analitica e fotochimica del Dipartimento di Chimica dell'Università di Pavia, in particolare con il gruppo di ricerca di M. Sturini.

Come seconda parte del progetto, al fine di testare un materiale “PeL” commerciale in sostituzione di quello sintetico, il materiale a base di $CaAl_2O_4$: (La, Nd)$^{3+}$ è stato scelto per la sua compatibilità teorica tra l’emissione (2,25 - 3,25 eV, corrispondente a 551 - 381 nm) e l’assorbimento del TiO_2. L'obiettivo principale era quello di utilizzare un materiale più ecologico, con una diversa composizione chimica, al fine di avere un dispositivo eco-compatibile con la stessa efficienza mostrata nelle condizioni di assenza di luce dal dispositivo descritto nel capitolo precedente. I campioni sono stati sintetizzati secondo un approccio chemiometrico 2^3; ogni campione è stato testato sulla sua efficienza fotocatalitica con esperimenti cinetici sulla degradazione percentuale del blu di metilene e il campione ottimizzato risultante è stato caratterizzato mediante analisi XRD, SEM-EDS, BET e DLS. Mediante la degradazione del MB, è stato possibile evidenziare l'importanza del rapporto in peso tra TiO_2 e “PeL”. Durante gli esperimenti al buio, i risultati sperimentali hanno evidenziato che questo materiale non è stato in grado di fornire fotoni al catalizzatore, molto probabilmente per la reazione indesiderata avvenuta tra il PeL e il TiO_2 evidenziata dall'analisi XRD, che ha modificato la struttura cristallina del composito. L’area superficiale è risultata, sorprendentemente, molto elevata, considerando che è stata utilizzata una sintesi allo stato solido, ma ciò può essere attribuibile alla formazione della nuova fase cristallina all'interfaccia tra il supporto e il catalizzatore. Il progetto è stato svolto in collaborazione con il gruppo di ricerca di M. Sturini (Università di Pavia).

Come terza parte del progetto, è stato progettato un materiale composito a tre componenti, basato su nanoparticelle di TiO_2, nanoparticelle di ZnO[92,93] e PeL micrometrico ($3ZnO:Ga_2O_3:2GeO_2$): Cr^{3+}. La preparazione delle nanoparticelle di ZnO è stata eseguita in due modi: via citrato di zinco, dal gruppo di ricerca del professor D. Comoretto, Sezione di Chimica Industriale dell'Università di Genova, e via nitrato di zinco. I risultati preliminari sull'efficienza fotocatalitica sono stati ottenuti dall’abbattimento di una soluzione di MB alla concentrazione di 0,01 g/L, in 40 minuti di irraggiamento con luce solare simulata. La composizione elementare ha confermato che la via del nitrato di zinco porta a una composizione omogenea di Zn e O, senza la presenza di altre impurità, mentre la via dell'acetato di zinco presenta ancora impurezze di K, provenienti dalla sintesi. La forma delle particelle è degna di nota, perché il primo trattamento termico ha portato ad una forma particolare tipo piastrina, con orientazioni casuali e bordi molto sottili, che mostra dimensioni variabili tra i nanometri a micrometri; la seconda ha invece portato a forme sferiche, appartenenti allo stesso intervallo dimensionale (principalmente nanometrico). Questa parte della ricerca è ancora in corso; i risultati presentati non sono completi e devono essere integrati con ulteriori esperimenti cinetici e caratterizzazioni chimico-fisiche, al fine di poter ottenere informazioni utili e trarre conclusioni significative.

Come quarta parte del progetto, è stato costruito un prototipo di un impianto pilota (con un volume processabile di 1L) per eseguire esperimenti preliminari sull'efficienza dei diversi catalizzatori sintetizzati. Considerando la carica superficiale di TiO_2, è utile conoscere il cosiddetto punto isoelettrico, che corrisponde al valore del pH della soluzione in cui il TiO_2 è sospeso, per il quale la concentrazione sulla superficie degli OH^- è uguale a quella degli H^+. In queste condizioni, la sospensione colloidale del catalizzatore diventa instabile, quindi tende a precipitare più rapidamente[95]. Alcuni dispositivi basati sul TiO_2 sono stati analizzati sul loro pH_{IEP} per mezzo della mobilità elettroforetica, successivamente trasformati in valori di "ζ *potential",* e sulla loro velocità di sedimentazione. Questo progetto è stato realizzato in collaborazione con il gruppo di ricerca del Dr. M. O. Amin, del Dipartimento di Chimica dell'Università del Kuwait. Tutti i dati riportati non sono ancora stati pubblicati e sono attualmente in fase di elaborazione: l’uso di un modello matematico (approccio chemiometrico), in particolare un modello di screening D-Optimal, sarà utilizzato per considerare l’importanza delle variabili qualitative e quantitative che influenzano il processo a livello preindustriale, per lo studio sull'efficienza fotocatalitica e l’efficienza del recupero nel prototipo dell'impianto pilota costruito.

Come quinta parte del progetto, sono stati sintetizzati dei campioni di TiO_2 puro, drogato con N, drogato con Cu e doppiamente drogato con (Cu, N). È stata impiegata la tecnica sol-gel al fine di studiare la struttura cristallina locale e media del TiO_2, processato in diverse condizioni di pH. I campioni risultano principalmente composti dalla fase anatasio, sebbene una quantità bassa ma significativa di brookite secondaria viene riscontrata nella maggior parte dei campioni. Una caratterizzazione strutturale dettagliata è stata eseguita mediante esperimenti di *scattering* elastico a raggi X con luce di sincrotrone; i dati strutturali di diversi campioni sono stati ottenuti mediante l'analisi della *Pair Distribution Function*. I risultati sperimentali hanno evidenziato che la sostituzione di Cu nel sito del Ti determina una notevole distorsione reticolare, maggiore di quella osservata per la sostituzione di N. In particolare, la sostituzione di Cu determina un riarrangiamento del reticolo cationico, che può anche essere correlato alla perdita di efficienza fotocatalitica misurata; viceversa, il reticolo anionico sembra quasi non esser stato influenzato dalla leggera sostituzione di Cu per Ti. L'analisi della struttura locale suggerisce che N si sostituisca effettivamente all'O nell'anatasio, piuttosto che trovarsi nei vuoti strutturali. In ogni caso, la sintesi nella soluzione di NH_3 ostacola o addirittura impedisce la formazione di brookite secondaria. Ciò è rilevante, poiché la crescita concorrenziale della brookite determina la formazione di un gran numero di difetti strutturali all'interno dell'anatasio. Questo progetto è stato realizzato in collaborazione con il Dr. A. Martinelli dell'Istituto di Materiali e Dispositivi Superconduttori e altri Materiali Innovativi del CNR e con il gruppo di ricerca del Prof. D. Comoretto della Sezione di Chimica Industriale dell'Università di Genova.

Come sesta parte del progetto, è stata studiata la cristallizzazione idrotermale di nanoparticelle di anatasio usando diverse nanoparticelle di ferrite come germi di nucleazione con composizione chimica, dimensioni e forma diverse. In particolare, sono state impiegate delle nanoparticelle di $CoFe_2O_4$, $NiFe_2O_4$ e Fe_3O_4 con un rapporto in volume rispetto alla quantità di TiO_2 pari a 1:1000. Inoltre, sono state utilizzate anche delle nanoparticelle non magnetiche di Lu_2O_3 per valutarne l'effetto sulla sintesi e la cristallizzazione della titania[106]. Per ogni campione, è stata eseguita una caratterizzazione chimico-fisica approfondita mediante analisi XRD e affinamento Rietveld, analisi FE-SEM, STEM, TEM, DSC e BET. Inoltre, alcuni campioni sono stati sottoposti a test fotocatalitici per l'abbattimento delle soluzioni di MB. La sintesi idrotermale è stata eseguita in un reattore di acciaio chiuso e condotta per 3 ore a 150 °C, a una pressione naturale di 9 bar. La temperatura utilizzata è risultata essere significativamente più bassa delle normali temperature solitamente usate per ottenere la fase anatasio, indicando quindi che la semplice presenza di un germe di nucleazione, senza particolari necessità in termini di composizione/morfologia, possa facilitare la cristallizzazione del TiO_2. La nucleazione inizia sulla superficie della nanoparticella di ferrite, probabilmente crescendo verso una direzione preferenziale (ad esempio il parametro reticolare con lunghezza comparabile), da cui si forma un seme cristallino di anatasio che a sua volta fungerà da nuovo punto di nucleazione. È stato dimostrato che la nucleazione può procedere in ogni caso, senza differenze evidenti causate dai diversi semi utilizzati: gli spettri XRD, i valori di area superficiale, i comportamenti termici e l'efficienza fotocatalitica sono risultati essenzialmente gli stessi per tutti i campioni. Alla fine, è stato dimostrato che anche le nanoparticelle a struttura non ferritica (Lu_2O_3) potrebbero agire come germi di nucleazione. Questo progetto è stato realizzato con la collaborazione del gruppo di ricerca del Prof. G. Singh del Dipartimento di Scienza e Ingegneria dei Materiali, Università Norvegese di Scienza e Tecnologia, e del Dr. A Martinelli dell'Istituto di Materiali e Dispositivi Superconduttori e altri Materiali Innovativi del CNR.

Come settima parte del progetto, il polidimetilsilossano è stato scelto come materiale di supporto per le nanoparticelle di TiO_2, vista la sua elevata area superficiale e stabilità contro la foto-attività del catalizzatore. Il biossido di titanio è stato preparato mediante sintesi sol-gel e sottoposto a un trattamento idrotermale, in presenza di nanoparticelle di ferrite in quanto germi di nucleazione; contemporaneamente, sono state eseguite sintesi sol gel ad alto pH, aumentando la concentrazione di NH_3 per confrontare l'attività antibatterica dei campioni. Entrambi sono stati elaborati con la tecnica dell'*elettrospinning*: è stato possibile disperdere la titania tra le fibre di PDMS e ottenere membrane polimeriche removibili, dall'aspetto di fogli bianchi morbidi. Queste membrane mostrano attività antibatterica sotto luce fluorescente; quindi possono essere usate come film di rivestimento per diversi tipi di superfici in diversi tipi di ambienti illuminati. I campioni sintetizzati sono stati controllati e caratterizzati mediante misure reologiche, immagini SEM-EDS, analisi DSC, Riflettanza diffusa (diagramma di Kubelka-Munk), esperimenti fotocatalitici di riciclo e inattivazione batterica con colonie di *E. Coli*. La sintesi di supporto ha avuto successo, poiché la struttura porosa della membrana PDMS, unita alla manovrabilità macroscopica del foglio stesso, ha consentito una soddisfacente attività superficiale del TiO_2. Questo materiale può essere potenzialmente impiegato per una vasta gamma di applicazioni: può essere applicato su più superfici, si attiva facilmente con luce artificiale e può essere staccato senza difficoltà; inoltre, come evidenziato dai test di riutilizzo, il composito è effettivamente riciclabile. L'attività del TiO_2 non è limitata dal supporto perché ha una superficie molto elevata e l'interazione tra le fibre di PDMS e il catalizzatore è abbastanza forte da evitare la dispersione del TiO_2, come evidenziato dagli esperimenti di riciclo con il MB (per almeno 3 cicli consecutivi). I campioni di TiO_2 drogati con N non si sono comportati come previsto, poiché la sintesi idrotermale non ha fornito le condizioni adeguate a drogare efficacemente il reticolo del catalizzatore e inoltre l'attività antibatterica non è stata migliorata dalle condizioni di sintesi basiche. Infine, la tecnica di sintesi è stata anche scelta per essere facilmente adattata alla produzione industriale in quanto il processo di *elettrospinning* permette una facile gestione e controllo dei parametri di processo, nonché una elevata automazione. Questo progetto è stato realizzato in collaborazione con il gruppo di ricerca della Prof.ssa M. Castellano e Prof.ssa S. Vicini della Sezione di Chimica Industriale dell'Università di Genova.

Come ottava parte del progetto, un nuovo catalizzatore magnetico a base di nanoparticelle di TiO_2 è stato sviluppato da un materiale innovativo ottenuto dal trattamento dei rifiuti industriali di ferro e acciaio, ovvero il *Fly Ash*. Questo materiale magnetico contiene ferro nella composizione chimico-mineralogica e rappresenta un eccellente esempio di economia circolare: i rifiuti industriali vengono convertiti in un prodotto ad alto valore aggiunto attraverso un trattamento idrotermale effettuato in un solo passaggio, per cui il precursore viene trasformato in una zeolite dalle buone proprietà magnetiche. Queste caratteristiche potrebbero essere sfruttate nel campo ambientale, come l’abbattimento degli inquinanti emergenti nel comparto idrico, accoppiandolo con un fotocatalizzatore. In particolare, le nanoparticelle di TiO_2 vengono sintetizzate con la tecnica sol-gel e quindi miscelate con il materiale magnetico mediante ultrasuoni, in diverse condizioni di pH: acido (0,1 M HNO_3), neutro e basico (0,1 M NaOH). Successivamente, il composito viene sottoposto a un leggero trattamento termico per rafforzare l'interazione. I *device* sintetizzati sono stati caratterizzati da XRD e SEM-EDS mentre la loro attività fotocatalitica è stata valutata attraverso l'abbattimento di soluzioni di MB, testando anche la possibilità di recuperare magneticamente la sospensione e riutilizzare il catalizzatore. Questa sintesi ha rappresentato la possibilità di estendere l'uso della fotocatalisi come processo terziario, poiché il materiale magnetico ha fortemente migliorato il recupero della sospensione colloidale: questo risultato può essere ottenuto solo quando la sintesi del materiale viene eseguita in condizioni basiche, poiché la struttura cristallina e le proprietà superficiali ottenute in queste condizioni han portato ad una buona efficienza fotocatalitica e alla possibilità di riutilizzare il catalizzatore (per almeno 3 cicli), contrariamente a quanto osservato con le condizioni acide. Questo progetto è stato realizzato in collaborazione con il gruppo di ricerca di C. Belviso dell'Istituto di Metodologie per l'Analisi Ambientale del CNR e con il gruppo di ricerca del Prof. D. Peddis dell'Istituto di Struttura della Materia del CNR.

Durante il Dottorato è stato possibile applicare anche un approccio analitico strumentale allo studio di alcuni inquinanti emergenti specifici. In particolare, lo studio ha coinvolto le seguenti specie chimiche: i parabeni, la nicotina e il salbutamolo ed è stato effettuato mediante tecniche cromatografiche accoppiate a spettrometria di massa e/o rilevatore ad arrangiamento di diodi. Sono inoltre stati considerati gli effetti matrice che hanno influenzato il processo di ossidazione. La maggior parte di questo progetto è stata svolta durante il periodo all'estero di quattro mesi e mezzo trascorsi presso il *Water Lab* del Dipartimento di Ingegneria Ambientale (Università Politecnica di Creta), sotto la supervisione della Professoressa Elia Psillakis. Tutti i dati e i risultati presentati non sono ancora stati pubblicati.

Come nona parte del progetto, le soluzioni acquose dei quattro parabeni (MP, EP, PP, BP) in miscela sono state sottoposte a esperimenti di fotolisi in diverse condizioni. Questi composti sono caratterizzati da una buona solubilità in acqua, stabilità chimica e fotochimica; per questo sono stati scelti come oggetti dello studio[115–117]. In effetti, questo progetto è stato svolto al fine di valutare diversi aspetti della degradazione della miscela di parabeni: prima di tutto, per studiare la possibilità di sfruttare la fotocatalisi come processo di ossidazione avanzata per degradare questi composti dall'acqua; successivamente, per studiare la formazione di probabili sottoprodotti derivanti dalla degradazione in relazione alla composizione della matrice. Infine, si volevano studiare i parametri significativi che influenzano il processo di degradazione, quali: effetto del pH, concentrazione iniziale dei parabeni, specie dissolte indesiderate (t-butanolo, acido umico) e concentrazione del catalizzatore. L'obiettivo finale era studiare il degrado di queste specie in matrici reali, ovvero acque reflue, acqua di fiume e acqua di rubinetto. Questo progetto è stato realizzato sotto la supervisione della Prof.ssa Elia Psillakis. Per i risultati sperimentali ottenuti da questo progetto, in particolare l'incapacità di accelerare il processo di degradazione con il fotocatalizzatore (nelle condizioni sperimentali scelte) e tenendo ulteriormente conto del breve tempo disponibile presso le strutture del *Water Lab*, si è deciso di non proseguire; pertanto, non sono stati condotti tutti gli esperimenti sugli effetti matrice e sui sottoprodotti di degradazione. Alcune considerazioni possono essere fatte sul comportamento mostrato: la miscela di parabeni potrebbe subire processi di *quenching* della radiazione per interazioni tra tutte le molecole, sostituendo così la scissione dei legami con la dissipazione di energia coinvolgendo livelli energetici vibrazionali e rotazionali. La presenza del fotocatalizzatore attivato da luce UV non ha realmente migliorato l'abbattimento e ciò può essere attribuibile ad una scarsa interazione tra la superficie del catalizzatore e gli inquinanti. Ad ogni modo, come riportato in letteratura, si possono impiegare AOP diversi ma efficaci (come ad es. un AOP *hard*: ozonazione[119]) contro i parabeni, anche se la richiesta di energia risulta essere maggiore, perché possono disporre di un maggior potere ossidante per degradare la miscela e quindi superare i limiti evidenziati con la fotocatalisi.

Come decima parte del progetto, la nicotina, un alcaloide altamente tossico derivante dal consumo di tabacco che risulta ormai essere ubiquitario nelle acque reflue, è stata utilizzata come oggetto del processo di ossidazione. Fortunatamente, in questo caso, è stato possibile sfruttare la fotolisi come AOP per degradare l'inquinante[123], quindi è stato possibile determinare i diversi effetti che hanno influenzato il processo: concentrazione iniziale del composto, effetto pH, effetto matrice (t-butanolo, acido umico e presenza di cloruro di sodio) ed infine diverse matrici acquose (acqua di mare, acqua di fiume, acqua di rubinetto, acque reflue e acqua piovana). Alla fine, è stata studiata la degradazione della nicotina da percolati acquosi reali ottenuti con quattro diverse configurazioni di sigarette: le sigarette convenzionali e sigarette IQOS usate tal quali e fumate (i mozziconi, dunque) da una *smoking machine*. I metodi analitici impiegati per lo studio di questo sistema complesso sono stati diversi, in base alla diversa composizione dei campioni; HPLC-DAD-MS, GC-FID e GC-MS. I risultati sperimentali si sono dimostrati positivi, perché è stato possibile provare che la nicotina stessa possa essere degradata in diverse condizioni, da casi semplici a complessi come quelli dei veri e propri percolati. In particolare, è stato scoperto che le condizioni acide sono risultate favorevoli per avere una degradazione della nicotina rapida ed efficace mentre la presenza di altre specie disciolte non ha prodotto effetti negativi sul processo. Questo comportamento suggerisce che l'uso della fotocatalisi come processo di ossidazione potrebbe essere davvero efficace sul miglioramento della velocità e della resa di degradazione della nicotina. Ulteriori studi e caratterizzazioni sono attualmente in corso per quanto riguarda il contenuto di carbonio organico totale "*T.O.C.*" sui percolati, successivamente agli esperimenti di abbattimento, e principalmente l'identificazione dei sottoprodotti di trasformazione formati durante il processo.

Tutti gli spettri registrati sono infatti caratterizzati da un'ampia varietà di segnali secondari emergenti, in relazione al tempo di fotolisi, che devono essere caratterizzati e confermati mediante confronto con la letteratura. Questo passaggio risulta chiaramente essere il più complicato, specialmente per i campioni reali, in quanto la composizione della matrice rende più complicata l'interpretazione degli spettri. Infine, sono tutt’ora in corso i test di tossicità sulla nicotina e sui suoi derivati, al fine di essere inclusi nel lavoro finale insieme al resto delle caratterizzazioni attese (come già accennato questi dati non sono inclusi nell’attuale lavoro di tesi perché non ancora disponibili). Questo progetto è stato realizzato nel *Water Lab*, con l'aiuto della Professoressa Psillakis. I presenti dati saranno inclusi in una pubblicazione scientifica non appena completi, pertanto vengono riportati confidenzialmente alla data della stesura.

Come undicesima e ultima parte del progetto, il farmaco salbutamolo (prescritto negli Stati Uniti più di 47 milioni di volte l'anno), è stato scelto come oggetto dello studio analitico. La valutazione del tasso di degradazione del salbutamolo in acqua è stata determinata mediante spettrofotometria UV-Vis, acquisendo gli spettri in derivata seconda e i risultati sono stati convalidati preliminarmente mediante analisi HPLC-MS/MS[125]. Ulteriori studi saranno condotti sui sottoprodotti della degradazione che possono essere ottenuti durante il processo di degradazione fotocatalitica. In conclusione, la fotocatalisi è stata impiegata con successo per degradare l'analita (almeno al di sotto del limite di rilevabilità dello strumento) usando luce solare simulata. È stato inoltre possibile misurare la variazione di concentrazione utilizzando gli spettri UV-Vis acquisiti in derivata anziché gli spettri diretti. Questi risultati sono stati confermati dai test preliminari mediante HPLC-MS/MS, che hanno evidenziato la diminuzione del segnale MS del salbutamolo sottoposto a fotocatalisi, rispetto a quello non trattato. Questo progetto è stato realizzato in collaborazione con la Sezione di Chimica Analitica dell'Università di Genova, con l'aiuto della Prof.ssa M. Di Carro.

È ragionevole pensare che l'attività di diversi AOP insieme possa rappresentare la scelta giusta per avere la massima efficienza rispetto al maggior numero possibile di microinquinanti. L'adeguamento degli attuali impianti di trattamento delle acque con l'insieme di questi processi terziari sembrerebbe essere promettente per poter agire rapidamente contro la diffusione di questa nuova classe di inquinanti. La ricerca scientifica sul biossido di titanio è più che matura per affermare che questa tecnologia ha ancora troppi inconvenienti, rispetto ai benefici, per essere utilizzata a livello industriale. Certo è che, al progredire della scienza dei materiali, sembra realistico pensare di trovare nuovi materiali, con proprietà e caratteristiche adeguate, che consentiranno di superare i principali svantaggi del TiO_2 con la conseguente applicazione industriale. In generale, si può concludere che i processi di ossidazione avanzata rappresentano sicuramente uno strumento efficace per la bonifica di molti inquinanti emergenti e la loro applicazione sarebbe in grado di prevenire il più rapidamente possibile la diffusione di questi contaminanti nell'ambiente e delle malattie a loro correlate.

7. Appendix

Scientific Publications

1. “*Synthesis and characterization of a new photocatalyst based on TiO_2 nanoparticles supported on a magnetic zeolite obtained from iron and steel industrial waste*” – S. Alberti, V. Caratto, D. Peddis, C. Belviso, M. Ferretti – Journal of Alloys and Compounds 2019, 797, 820-825 - DOI 10.1016/j.jallcom.2019.05.098

2. “*Systematic study on TiO_2 crystallization via hydrothermal synthesis in the presence of different ferrite nanoparticles as nucleation seeds*” – S. Alberti, S. Villa, G. Singh, F. Seland, A. Martinelli, M. Ferretti, F. Canepa, V. Caratto –Journal of Nanoscience and Nanotechnology 2019, 9:8, 4994-4999 – DOI 10.1166/jnn.2019.16787

3. “*Porous Polydimethylsiloxane membranes loaded with low-temperature crystallized TiO_2 NPs for detachable antibacterial films*” – S. Alberti, M. Ferretti, S. Vicini, M. Castellano, V. Caratto - Journal of Materials Science – 2018, 54(2), 1665-1676 – DOI 10.1007/s10853-018-2881-4

4. “*Photocatalysis in darkness. Optimization of sol-gel synthesis of NP-TiO_2 supported on a persistent luminescence material and its application for the removal of Ofloxacin from water*” – S. Alberti, F. Locardi, M. Sturini, A. Speltini, F. Maraschi, G.A. Costa, M. Ferretti, V. Caratto –Journal of Nanomedicine and Nanotechnology 2018, 9:3, 501– DOI 10.4172/2157-7439.1000501

5. “*Structural studies on copper and nitrogen doped nanosized anatase*” – A. Martinelli, S. Alberti, V. Caratto, P. Lova, F. Locardi, G. Pampararo, S. Villa, M. Ferretti currently in press in Zeitschrift fuer Kristallographie – Crystalline Materials, 2018, 233(12), 867-876 DOI: https://doi.org/10.1515/zkri-2017-2143

6. “*Different sol–gel preparations of iron-doped TiO_2 nanoparticles: characterization, photocatalytic activity and cytotoxicity*” – V. Caratto, F. Locardi, S. Alberti, S. Villa, E. Sanguineti, A. Martinelli, T. Balbi, L. Canesi, M. Ferretti – Journal of Sol-Gel Science and Technology, 2016, 80, 152–159 - DOI:10.1007/s10971-016-4057-5

7. “*Enhancement of TiO_2 NPs Activity by Fe_3O_4 Nano-Seeds for Removal of Organic Pollutants in Water*” – *S.* Villa, V. Caratto, F. Locardi, S. Alberti, M. Sturini,

A. Speltini, F. Maraschi, F. Canepa, M. Ferretti – Materials, 2016, 9,9, 771 - DOI:10.3390/ma9090771

8. *"Antibacterial activity of standard and N-doped titanium dioxide-coated endotracheal tubes: an in vitro study"* – V. Caratto, L. Ball, E. Sanguineti, A. Insorsi, I. Firpo, S. Alberti, M. Ferretti, P. Pelosi - Revista Brasileira de Terapia Intensiva. 2017; 29(1): 55-62 – DOI:10.5935/0103-507X.20170009

Congress Communications

1. ORAL *"Synthesis of a TiO_2-based photocatalyst supported on a magnetic zeolite obtained from industrial waste for environmental remediation"* - S. Alberti, V. Caratto, D. Peddis, C. Belviso, M. Ferretti - CDCF19 - University "Sapienza" of Roma, Roma – Italy – July 1-4, 2019

2. ORAL *"Porous PDMS membranes loaded with bare and N-doped TiO_2 NPs for antibacterial coatings"* – S. Alberti, I. Basciu, A. Saperdi, S. Vicini, M. Castellano, M. Ferretti, V. Caratto - CABC2018 - Genova – Italy, June 24-27, 2018

3. ORAL *"Porous PDMS membranes loaded with TiO_2 NPs for detachable antibacterial coatings"* – S. Alberti, I. Basciu, S. Vicini, M. Castellano, M. Ferretti, V. Caratto – GIFC18 – Genova – Italy, April 16-18, 2018

4. ORAL *"PDMS membranes loaded with TiO_2 NPs for antibacterial activity"* – S. Alberti, V. Caratto, I. Basciu, M. Mauri, S. Vicini, M. Castellano, M. Ferretti – ANNIC2017 – Roma, October 18-20, 2017

5. ORAL *"Removal of pollutants of emerging concern and the treatment of turbid wastewaters: optimization of the synthesis of NP-TiO_2 supported on a persistent luminescence material"* – S. Alberti, V. Caratto, F. Locardi, M. Ferretti, G.A. Costa, M. Sturini, A. Speltini, F. Maraschi – ICCE2017 – Oslo, June 18-22, 2017

6. POSTER *"Synthesis and characterization of a new photocatalyst based on TiO_2 nanoparticles supported on magnetic materials from iron and steel industrial waste"* – M. Ferretti, V. Caratto, S. Alberti, D. Peddis, M. Sturini, A. Speltini, F. Maraschi, C. Belviso – ISMANAM2018 – Roma – July Italy, 2-6, 2018

7. POSTER *"NPs TiO_2 supported on sepiolites: a photocatalytic tool for emerging pollution"* – F. Fossati, S. Alberti, M. Ricci, M. Sturini, A. Speltini, F. Maraschi, V. Cartto, M. Ferretti - CABC2018 - Genova - Italy, June 24-27, 2018

8. POSTER *"Synthesis and characterization of a new photocatalyst based on TiO_2 nanoparticles supported on magnetic materials from iron and steel industrial* *waste"* – M. Ferretti, V. Caratto, S. Alberti, P. Rizzo, D. Sangaletti, D. Peddis, M. Sturini, C. Belviso, A. Speltini - CABC2018 - Genova - Italy, June 24-27, 2018

9. POSTER *"PDMS membranes loaded with TiO_2 NPs: antibacterial activity and self-cleaning properties"* - S. Alberti, V. Caratto, I. Basciu, M. Mauri, S. Vicini, M. Castellano, M. Ferretti – CNSCI17 – Paestum, September 10-14, 2017

10. POSTER *"Efficiency improvement of the TiO_2 – ZnO NPs photocatalytic coupled system supported on a persistent luminescence material"* – V. Caratto, S. Alberti, G. Pampararo, F. Locardi, P. Lova, D. Comoretto, M. Sturini, F. Maraschi, A. Speltini, A. Profumo, G.A. Costa, M. Ferretti - CNSCI17 – Paestum, September 10-14, 2017

11. POSTER *"TiO_2 NPs supported on sepiolites: a photocatalytic tool for emerging pollution"* – F. Fossati, S. Alberti, M. Sturini, A. Speltini, F. Maraschi, V. Caratto, M. Ferretti - CNSCI17 – Paestum, September 10-14, 2017

12. POSTER *"A new method for cleaning frescoes paintings"* – G. Torrielli, V. Caratto, F. Fossati, S. Alberti, M. Ferretti - CNSCI17 – Paestum, September 10-14, 2017

13. POSTER *"Synthesis optimization and efficiency improvement of a catalytic coupled system of NPs TiO_2 - NPs ZnO supported on a persistent luminescence material"* – P. Lova, S. Alberti, V. Caratto, F. Locardi, M. Ferretti, D. Comoretto - European Materials Research Society Fall Meeting – Varsavia, September 18-21, 2017.

8. List of Tables and Figures

Table 1. *Experimental Domain investigated in the Experimental Design 2^3 for $TiO_2/(3ZnO:Ga_2O_3:2GeO_2)$: Cr^{3+}* Page 40

Table 2. *MB percentage degradation obtained at different experimental conditions* Page 41

Table 3. *Estimated coefficients of regression model for dependent variables* Page 42

Table 4. *Experimental Domain investigated in the Experimental Design 2^3 for $TiO_2/CaAl_2O_4$: $(La, Nd)^{3+}$* Page 49

Table 5. *MB percentage degradation obtained at different experimental conditions* Page 49

Table 6. *Estimated coefficients of regression model for dependent variables* Page 50

Table 7. *Hydrodynamic radius of Sample 5, Sample 8 and bare TiO_2 in diluted aqueous suspension* Page 57

Table 8. *Synthesized samples of $TiO_2/ZnO/PeL$ and MB percentage degradation* Page 59

Table 9. *Synthetic parameters of samples investigated for pH_{IEP} recovery* Page 62

Table 10. *pH_{IEP}, recovery efficiency and recovery time* Page 62

Table 11. *Synthetic conditions of the investigated (Cu, N)-doped samples* Page 69

Table 12. *Structural and microstructural (coherent diffraction domain size) properties of anatase synthesized under different conditions* Page 73

Table 13. *ICP-AES results for copper and nitrogen amount. L.O.D. for Cu (4 ppm) and N (0,1 ppm)* Page 82

Table 14. *MB percentage degradation of the six (Cu, N)-doped samples and mean hydrodynamic radius* Page 83

Table 15. *Chemical composition, size, shape and crystallographic structure of the nucleation seeds used in this project* Page 86

Table 16. *Structural and microstructural properties of synthesized TiO_2 samples with nucleation seeds* Page 91

Table 17. *Photocatalytic efficiency of synthesized samples* Page 94

Table 18. *Synthetic conditions investigated for PDMS solution synthesis (bold numbers represent the optimized values)* Page 97

Table 19. *Synthesized samples and treatment conditions of TiO_2/F.A. samples* Page 116

Table 20. *Gradient elution program used in the HPLC-DAD for parabens elution* Page 126

Table 21. *Gradient elution program used in the HPLC-MS-DAD for nicotine elution* Page 138

Figure 1	*Scheme of Classic pollutants spread in the atmosphere and transport/reaction processes involving these molecules*	Page 10
Figure 2	*Distribution of synthetic chemicals and main transformations in the environment and the techno-sphere*	Page 12
Figure 3	*Routes of pharmaceuticals entering the environment*	Page 14
Figure 4	*Scheme of a wastewater treatment plant*	Page 17
Figure 5	*Main features of the hydroxyl radical*	Page 20
Figure 6	*Schematic representation of an electrical double layer when the surface of a solid is exposed to an electrolyte*	Page 24
Figure 7	*Crystal structure of principal* TiO_2 *polymorphs: a) Anatase, b) Rutile, c) Brookite*	Page 27
Figure 8	e^-/h^+ *redox potentials for some semiconductor materials, in comparison with some redox reference potentials*	Page 29
Figure 9	*Mechanisms involved in the persistent luminescence phenomenon*	Page 34
Figure 10	*a) Emission spectrum of* $(3ZnO:Ga_2O_3:2GeO_2)$*:* Cr^{3+} *excited with RX source; b) Decay time of emission intensity*	Page 36
Figure 11	*a) Intensity of Radioluminescence and Persistent Luminesce of* $CaAl_2O_4$*: (La, Nd)*$^{3+}$*; b) Charge/Discharge duration of persistent emission*	Page 37
Figure 12	*Plot of the coefficients of the model showing the significance of the variables considered in the chemometric study. Error bars indicate the confidence intervals at* $p=0.05$	Page 41
Figure 13	*Response surfaces for the MB percentage abatement: a)* $y=f(X_1, X_2)$*; b)* $y=f(X_2, X_3)$*; c)* $y=f(X_1, X_3)$	Page 43
Figure 14	*XRD spectra of the reference anatase* TiO_2 *(from Pearson's Crystal Data n° 1024705); PeL material (PeL) and Sample 2 (*TiO_2*/PeL)*	Page 44
Figure 15	*Behavior of the emission intensity, in darkness, of the PeL material and of Sample 2 (solar simulated light excitation source). Pictures recorded with Fujifilm – Finepix*	Page 45

Figure 16	*a) BSE image of a spot of Sample 2; b) EDS spectrum of Ti signal (red) recorded on the same spot*	Page 45
Figure 17	*Degradation profile of ofloxacin (20 ppm, 0,5 g/L catalyst) under alternate sunlight/darkness cycles*	Page 46
Figure 18	*Plot of the coefficients showing the significance of the variables. Confidence interval at *p=0,05*	Page 50
Figure 19	*Response surfaces for the MB percentage abatement: a) $y=f(X_1, X_2)$ and $X_3=0$; b) $y=f(X_1, X_3)$ with $X_2=0$; c) $y=f(X_2, X_3)$ and $X_1=0$*	Page 52
Figure 20	*a) SEM image of PeL (5000x, marker 10 μm); b) SEM image of PeL (10000x, marker 5 μm); c) EDS spectrum of PeL (referred to 18a)*	Page 53
Figure 21	*a) SEM image of Sample 5 (10000x, marker 5 μm); b) SEM image of Sample 5 (20000x, marker 2 μm); c) EDS spectrum of Sample 5 on spot 1 (referred to 19a); d) EDS spectrum of Sample 5 on spot 5 (referred to 19a)*	Page 55
Figure 22	*XRD spectra of Sample 8 (purple), Sample 5 (green), unsupported TiO_2 (red) and PeL (blue)*	Page 56
Figure 23	*XRD spectra of Sample 8 (green), heat treated PeL (red) and untreated PeL (blue)*	Page 56
Figure 24	*a) SEM image of ZnO – zinc acetate route (5000x, marker 10 μm); b) SEM image of ZnO – zinc acetate route (20000x, marker 2 μm); c) EDS spectrum of ZnO – zinc acetate route on spot 3 (referred to 22a)*	Page 61
Figure 25	*a) SEM image of ZnO – citric acid route (10000x, marker 5 μm); b) SEM image of ZnO – citric acid route (20000x, marker 2 μm) with particles' dimension markers; c) EDS spectrum of ZnO – citric acid route on spot 2 (referred to 23a)*	Page 62
Figure 26	*Hydrodynamic radius of ZnO – citric acid route*	Page 63
Figure 27	*Pilot plant prototype for water treatment*	Page 64
Figure 28	*a) Recovery efficiency vs time for Sample 2 (Table 8); b) Recovery efficiency vs time for Sample 3 (Table 8); c) Recovery efficiency vs time for Sample 4 (Table 8) and d) Recovery efficiency vs time for Sample 5 (Table 8)*	Page 68
Figure 29	*X-Ray powder diffraction patterns of the analysed TiO_2 samples; Q represents the modulus of the scattering vector*	Page 72

Figure 30	*Rietveld refinement plot of Sample 6. The inset shows the evolution of the cell parameters of the samples prepared at pH 3 and 8 (normalized data; full symbols: N-doping; open symbols: (Cu, N)-doping)*	Page 73
Figure 31	*Relationship between the anatase c axis and the amount of anatase constituting each sample*	Page 75
Figure 32	*Williamson-Hall plots for the analysed samples*	Page 76
Figure 33	*Difference curves obtained by subtracting the G(r) function of each substituted sample minus the G(r) function of pure TiO_2*	Page 77
Figure 34	*Fit of the G(r) function of Sample 6; vertical bars in the lower field indicates bond lengths lower than 6 Å in anatase and brookite*	Page 77
Figure 35	*Comparison of low r region of the experimental G(r) function (Sample 5) with the computed partial PDFs containing only selected contributions of atomic pairs (on the left); on the right: representation of the crystal structure of anatase with main interatomic distances listed*	Page 78
Figure 36	*Enlarged view on selected regions of the G(r) functions for the Sample 3 and Sample 6 in the r ranges pertaining to the nearest Ti-O and Ti-Ti interatomic distances*	Page 79
Figure 37	*Deviation of the local structure from the average one evaluated by the variance of the lattice parameters*	Page 80
Figure 38	*G(r) difference plots obtained for different structural models foreseeing N atoms located at different structural sites*	Page 81
Figure 39	*a) DRIFT spectra collected for the six samples; b) Absorbance ration I_4/I_i retrieved from DRIFT spectra at 1631 cm^{-1} (black), 3350 cm^{-1} (red) and 3690 cm^{-1} (green) for the six samples (left axis) compared with the pH values of the solution (right axis, blue)*	Page 83
Figure 40	*STEM images of Nickel ferrite seeds (A-B), Cobalt ferrite seeds (C-D), Fe_3O_4 seeds (E) and TEM image of Lu_2O_3 seeds (F)*	Page 89
Figure 41	*XRD patterns and respective Miller indices of the $NiFe_2O_4$, $CoFe_2O_4$ and Lu_2O_3 NPs used for the synthesis of Sample 1, 4 and 6 respectively*	Page 90
Figure 42	*XRD patterns of the synthesized samples and the anatase TiO_2 reference pattern (line pattern) got from Pearson's Crystal Data Software*	Page 90
Figure 43	*FE-SEM images taken at 20 kV of Sample 3 (left) and of Sample 4 (right)*	Page 92

Figure 44	*Thermal behavior of the different synthesized samples investigated under O_2 flow (20 mL/min) between T_{room} and 500 °C*	Page 93
Figure 45	*Electrospinning set-up for simultaneous spinning and spraying of PDMS and TiO_2 crystalline gel*	Page 97
Figure 46	*Viscoelastic behaviour of: ■) Storage modulus G’ and •) Loss modulus G’’ of three samples aged for 24 hours (red), 48 hours (blue) and 72 hours (green)*	Page 100
Figure 47	*a-b) Different FE-SEM images for PDMS solutions cured for 24 hours (segment 100 μm); c) FE-SEM images for PDMS solution cured for 24 hours (segment 10 μm)*	Page 101
Figure 48	*a) Different FE-SEM images for PDMS solution cured for 48 hours (segment 100 μm); b-c) FE-SEM images for PDMS solutions cured for 48 hours (segment 10 μm)*	Page 102
Figure 49	*a) FE-SEM images for PDMS solution cured for 72 hours (segment 450 μm); b) FE-SEM images for PDMS solution cured for 72 hours (segment 200 μm); c) Statistical distribution histogram and Gaussian fitting curve of the PDMS fibres mean diameter; d) Single piece of membrane as obtained after electrospinning*	Pp. 103-104
Figure 50	*Figure 50: a-c) Elemental maps (Si red, Ti green) overlapped to SEM images; Si in b) and Ti in c) (segment 250 μm)*	Page 105
Figure 51	*a-b) SEM images of N-doped TiO_2/PDMS with 5% NH_3, collected on BSE and SE; c) Statistical distribution histogram and Gaussian fitting curve of the same membrane; d) EDS spectrum collected in the highlighted region*	Pp. 106-107
Figure 52	*a-b) Other SEM images of N-doped TiO_2 (NH_3 5%)-PDMS collected on BSE and SE signals (segment 100 μm) respectively; c-e) Elemental maps (Si red, Ti green) overlapped to SEM images; Si in d) and Ti in e) (segment 100 μm)*	Pp. 108-109
Figure 53	*Thermal behaviours of the synthesized samples: standard-TiO_2 (black), N(1%)-doped TiO_2 (red), N(5%)-doped TiO_2 (green) and N(15%)-doped TiO_2 (blue)*	Page 110
Figure 54	*Kubelka-Munk graphic representation plot for the E_g measurements. Inset shows an enlargement of the range 2,80 to 3,10 eV)*	Page 111
Figure 55	*MB percentage degradation results for 3 consecutive cycles*	Page 112
Figure 56	*a) E. Coli growth in PDMS membrane (left) and in PDMS-standard-TiO_2 membrane (right); b) CFU count at the difference time-points with control membrane (control) or TiO_2-loaded membrane (TiO_2). *Significantly lower compared to baseline in all treatment arms ($p < 0,001$); **TiO_2 and N-doped TiO_2*	Page 113

	significantly lower than control ($p< 0,001$). Dots represent mean value; bars represent the standard error of the mean	
Figure 57	*a) SEM image of the Fly Ash precursors morphology, before hydrothermal synthesis (segment 100 μm); b) Elemental composition of different spots selected in the SEM image*	Page 117
Figure 58	*a) Elemental mapping overlapped to a SEM image for catalyst FA-USA (Si light blue, Al yellow, Fe orange, Ti purple) (marker 100 μm); b) Elemental mapping overlapped to a SEM image for catalyst FA-USB (Si light blue, Al yellow, Fe orange, Ti purple) (marker 100 μm)*	Page 118
Figure 59	*XRD spectra of anatase (black) and brookite (red) TiO_2 (Reference from Pearson's Crystal Data), FA-Zeolite (blue), FA-USN (orange), FA-USB (dark cyan) and FA-USA (magenta)*	Page 119
Figure 60	*a) Percentage degradation of 0,05 g/L MB solution by Samples FA-zeolite (black), FA-USN (red), FA-MSN (blue), FA-USB (dark cyan) and FA-USA (magenta); b) Percentage degradation of 0,01 g/L MB solution for 3 recycling tests.*	Pp. 120-121
Figure 61	*Structure of a generic para-hydroxybenzoate*	Page 124
Figure 62	*a) Calibration curves of all the four studied parabens, using HPLC-DAD; b) Chromatographic separation of the parabens' mixture and retention times' table of each species*	Page 127
Figure 63	*Photolytic degradation of the parabens mixture, a) C_i/C_0 versus time trend of a buffered parabens mixture solution at C_0= 10 ppm; b) C_i/C_0 versus time trend of a buffered parabens mixture solution at C_0= 2,5 ppm; a) C_i/C_0 versus time trend of a buffered parabens mixture solution at C_0= 1 ppm*	Pp. 128-129
Figure 64	*Photocatalytic degradation of the parabens mixture a) C_i/C_0 versus time trend of a buffered parabens mixture solution at C_0= 2,5 ppm and TiO_2 concentration of 1,5 g/L; b) C_i/C_0 versus time trend of a buffered parabens mixture solution at C_0= 2,5 ppm and TiO_2 concentration of 2,0 g/L*	Pp. 130-131
Figure 65	*Photocatalytic degradation of the parabens, C_i/C_0 versus time trend of a buffered parabens mixture solution at C_0= 10 ppm and TiO_2 concentration of 2,0 g/L*	Page 132
Figure 66	*(–)-Nicotine molecular structure*	Page 134
Figure 67	*Conventional cigarette (left) and IQOS cigarette and burner*	Page 135
Figure 68	*pH effect on UV-Vis absorbance of 10 ppm (–)-nicotine aqueous solution*	Page 140

Figure 69	*Photolysis experiments: a) initial concentration effect (from 1 to 100 ppm), b) pH effect (buffered values of 3, 5, 7 and 9), c) presence of 100 ppm of tert-butanol, d) presence of 2,5 ppm of humic acid, e) presence of 3,5% wt. of NaCl, f) effect of aqueous matrix (river black, tap red, waste blue, sea green and rain purple)*	Pp. 141-143
Figure 70	*Nicotine degradation study on diluted real leachates samples (C_0 c.a. 5 ppm). CC= conventional cigarette, UCC= smoked conventional cigarette, TSAL= IQOS tobacco stick, UTSAL= smoked IQOS tobacco stick*	Page 145
Figure 71	*Micro-ionization scheme proposed for salbutamol and micro-ionization constants: $pK_{a1}^{\pm} = 9,22$; $pK_{a1}^{\circ}= 9,60$; $pK_{a2}^{\pm}= 9,60$; $pK_{a2}^{\circ}= 9,84$*	Page 147
Figure 72	*a) Direct UV-Vis spectra of different salbutamol solutions at six different concentrations; b) Second derivative UV-Vis spectra of six different salbutamol solutions*	Pp. 149-150
Figure 73	*a) Direct UV-Vis spectra of different aliquots withdrawn for photolysis experiment; b) Direct UV-Vis spectra of different aliquots withdrawn for photocatalysis experiment*	Page 151
Figure 74	*a) Second derivative UV-Vis spectra of different aliquots withdrawn for photolysis experiment; b) Second derivative UV-Vis spectra of different aliquots withdrawn for photocatalysis experiment*	Page 152
Figure 75	*Salbutamol percentage degradation during 60 min of photocatalytic test under irradiation for $TiO_2/(3ZnO:Ga_2O_3:2GeO_2)$: Cr^{3+} (yellow) and $TiO_2/CaAl_2O_4$: $(La, Nd)^{3+}$ (blue) acquired at a) $\lambda= 280,03$ nm and b) $\lambda= 292,18$ nm*	Page 153
Figure 76	*a) Intensity vs m/z ratio recorded for pure salbutamol solution at 500 ppb; b) Chromatogram of pure salbutamol (black), salbutamol subjected to 60 min of photolysis (green) and salbutamol subjected to 60 min of photocatalysis (red)*	Pp. 154-155

9. References

1. Noman, M. T., Ashraf, M. A. & Ali, A. *Synthesis and applications of nano-TiO_2: a review*. Environmental Science and Pollution Research (2018) doi:10.1007/s11356-018-3884-z.

2. Deblonde, T., Cossu-Leguille, C. & Hartemann, P. *Emerging pollutants in wastewater: A review of the literature.* International Journal of Hygiene and Environmental Health 214, 442–448 (2011).

3. Ratola, N., Alves, A. & Psillakis, E. *Biomonitoring of Polycyclic Aromatic Hydrocarbons Contamination in the Island of Crete Using Pine Needles.* Water, Air, & Soil Pollution 215, 189–203 (2011).

4. Byrne, J. A., Eggins, B. R., Brown, N. M. D., McKinney, B. & Rouse, M. *Immobilisation of TiO_2 powder for the treatment of polluted water*. Applied Catalysis B: Environmental 17, 25–36 (1998).

5. Jung, Y. *et al.* NO_x *and* N_2O *emissions over a Urea-SCR system containing both* V_2O_5 -WO_3/TiO_2 *and Cu-zeolite catalysts in a diesel engine*. Chemical Engineering Journal 326, 853–862 (2017).

6. Pozzo, R. L., Baltanas, M. A. & Cassano, A. E. *Supported titanium oxide as photocatalyst in water decontamination: state of the art*. Catalysis Today 39, 219–231 (1997).

7. Segner, H. *et al.* I*dentification of endocrine-disrupting effects in aquatic vertebrates and invertebrates: report from the European IDEA project.* Ecotoxicology and Environmental Safety 54, 302–314 (2003).

8. Bolong, N., Ismail, A. F., Salim, M. R. & Matsuura, T. *A review of the effects of emerging contaminants in wastewater and options for their removal.* Desalination 239, 229–246 (2009).

9. Zuccato, E., Calamari, D., Natangelo, M. & Fanelli, R. *Presence of therapeutic drugs in the environment.* The Lancet 355, 1789–1790 (2000).

10. Richardson, S. D. & Kimura, S. Y. *Water Analysis: Emerging Contaminants and Current Issues*. Analytical Chemistry 88, 546–582 (2016).

11. Zuccato, E., Castiglioni, S., Fanelli, R. & Bagnati, R. *Inquinamento da farmaci: le evidenze*. 7 (2007).

12. Farré, M. la, Pérez, S., Kantiani, L. & Barceló, D. *Fate and toxicity of emerging pollutants, their metabolites and transformation products in the aquatic environment.* TrAC Trends in Analytical Chemistry 27, 991–1007 (2008).

13. Barbosa, M. O., Moreira, N. F. F., Ribeiro, A. R., Pereira, M. F. R. & Silva, A. M. T. *Occurrence and removal of organic micropollutants: An overview of the watch list of EU Decision 2015/495*. Water Research 94, 257–279 (2016).

14. Liu, J.-L. & Wong, M.-H. *Pharmaceuticals and personal care products (PPCPs): A review on environmental contamination in China*. Environment International 59, 208–224 (2013).

15. Gelband, H. *et al. The state of the world's antibiotics 2015*. Wound Healing Southern Africa 8, 30–34 (2015).

16. Papageorgiou, M., Zioris, I., Danis, T., Bikiaris, D. & Lambropoulou, D. *Comprehensive investigation of a wide range of pharmaceuticals and personal care products in urban and hospital wastewaters in Greece*. Science of The Total Environment 694, 133565 (2019).

17. Wang, J. & Wang, S. *Removal of pharmaceuticals and personal care products (PPCPs) from wastewater: A review.* Journal of Environmental Management 182, 620–640 (2016).

18. Petrie, B., Barden, R. & Kasprzyk-Hordern, B. *A review on emerging contaminants in wastewaters and the environment: Current knowledge, understudied areas and recommendations for future monitoring*. Water Research 72, 3–27 (2015).

19. Boxall, A. B. A. *The environmental side effects of medication*. EMBO Rep 5, 1110–1116 (2004).

20. Nannou, C. *et al. Analytical strategies for the determination of antiviral drugs in the aquatic environment.* Trends in Environmental Analytical Chemistry 24, e00071 (2019).

21. Nannou, C. *et al. Antiviral drugs in aquatic environment and wastewater treatment plants: A review on occurrence, fate, removal and ecotoxicity*. Science of The Total Environment 699, 134322 (2020).

22. Prieto-Rodriguez, L. *et al. Treatment of emerging contaminants in wastewater treatment plants (WWTP) effluents by solar photocatalysis using low* TiO_2 *concentrations*. Journal of Hazardous Materials 211–212, 131–137 (2012).

23. Krzeminski, P. *et al. Performance of secondary wastewater treatment methods for the removal of contaminants of emerging concern implicated in crop uptake and antibiotic resistance spread: A review*. Science of The Total Environment 648, 1052–1081 (2019).

24. Behra-Miellet, J. *et al. Antibiotic resistance among anaerobic Gram-negative bacilli: lessons from a French multicentric survey*. Anaerobe 9, 105–111 (2003).

25. Duquette, R. A. & Nuttall, T. J. *Methicillin-resistant Staphylococcus aureus in dogs and cats: an emerging problem?* Journal of Small Animal Practice 45, 591–597 (2004).

26. Schuetz, A. N. *Antimicrobial Resistance and Susceptibility Testing of Anaerobic Bacteria.* Clinical Infectious Diseases 59, 698–705 (2014).

27. Caratto, V. *et al. Antibacterial activity of standard and N-doped titanium dioxide-coated endotracheal tubes: an in vitro study*. Revista Brasileira de Terapia Intensiva 29, (2017).

28. Santo, E., Salvador, M. M. & Marin, J. M. *Multidrug-resistant urinary tract isolates of Escherichia coli from Ribeirão Preto, São Paulo, Brazil*. Brazilian Journal of Infectious Diseases 11, 575–578 (2007).

29. Patel, D. K. K. & Patel, D. S. *Multidrug-resistant Escherichia coli urinary isolates from cases of UTI*. 5 (2015).

30. https://ambiente.provincia.bz.it/acqua/%20funzionamento-impianto-depurazione.asp.

31. García-Ballesteros, S. *et al.* A *new methodology to assess the performance of AOPs in complex samples: Application to the degradation of phenolic compounds by O_3 and O_3/UV-A–Vis*. Chemosphere 222, 114–123 (2019).

32. von Gunten, U. *Oxidation Processes in Water Treatment: Are We on Track?* Environmental Science & Technology 52, 5062–5075 (2018).

33. Aziz, A. A. & Ibrahim, S. *Preparation of Activated Carbon/N-doped Titania Composite for Synergistic Adsorption-photocatalytic Oxidation of Batik Dye*. IOP Conference Series: Materials Science and Engineering 358, 012014 (2018).

34. Miklos, D. B. *et al. Evaluation of advanced oxidation processes for water and wastewater treatment – A critical review*. Water Research 139, 118–131 (2018).

35. Atanassova, D. *et al. Sonochemical reduction of the antioxidant activity of olive mill wastewater*. Environment International 31, 281–287 (2005).

36. Mantzavinos, D. & Psillakis, E. *Enhancement of biodegradability of industrial wastewaters by chemical oxidation pre-treatment*. Journal of Chemical Technology & Biotechnology 79, 431–454 (2004).

37. Martinez-Haya, R. *et al. Time-resolved kinetic assessment of the role of singlet and triplet excited states in the photocatalytic treatment of pollutants at different concentrations*. Applied Catalysis B: Environmental 203, 381–388 (2017).

38. Iakovides, I. C. *et al. Continuous ozonation of urban wastewater: Removal of antibiotics, antibiotic-resistant Escherichia coli and antibiotic resistance genes and phytotoxicity.* Water Research 159, 333–347 (2019).

39. Liu, S.-Q. *Magnetic semiconductor nano-photocatalysts for the degradation of organic pollutants*. Environmental Chemistry Letters 10, 209–216 (2012).

40. Anandan, S., Ikuma, Y. & Niwa, K. *An Overview of Semi-Conductor Photocatalysis: Modification of TiO_2 Nanomaterials*. Solid State Phenomena 162, 239–260 (2010).

41. Dong, S. *et al. Recent developments in heterogeneous photocatalytic water treatment using visible light-responsive photocatalysts: a review*. RSC Advances 5, 14610–14630 (2015).

42. Bonetta, S., Bonetta, S., Motta, F., Strini, A. & Carraro, E. *Photocatalytic bacterial inactivation by TiO_2-coated surfaces.* AMB Express 3, 59 (2013).

43. https://commons.wikimedia.org/wiki/File:Electric_double-layer_(BMD_model)_NT.PNG#filelinks.

44. Grehs, B. W. N. *et al.* R*emoval of microorganisms and antibiotic resistance genes from treated urban wastewater: A comparison between aluminium sulphate and tannin coagulants*. Water Research 166, 115056 (2019).

45. Koltsakidou, A., Katsiloulis, Ch., Evgenidou, E. & Lambropoulou, D. A. *Photolysis and photocatalysis of the non-steroidal anti-inflammatory drug Nimesulide under simulated solar irradiation: Kinetic studies, transformation products and toxicity assessment.* Science of The Total Environment 689, 245–257 (2019).

46. Moreira, N. F. F. *et al. Photocatalytic ozonation of urban wastewater and surface water using immobilized* TiO_2 *with LEDs: Micropollutants, antibiotic resistance genes and estrogenic activity.* Water Research 94, 10–22 (2016).

47. Biancullo, F. *et al. Heterogeneous photocatalysis using UVA-LEDs for the removal of antibiotics and antibiotic resistant bacteria from urban wastewater treatment plant effluents*. Chemical Engineering Journal 367, 304–313 (2019).

48. Leroy, P., Tournassat, C. & Bizi, M. *Influence of surface conductivity on the apparent zeta potential of* TiO_2 *nanoparticles.* Journal of Colloid and Interface Science 356, 442–453 (2011).

49. Azeez, F. *et al. The effect of surface charge on photocatalytic degradation of methylene blue dye using chargeable titania nanoparticles*. Scientific Reports 8, (2018).

50. Diebold, U. T*he surface science of titanium dioxide*. Surface Science Reports 48, 53–229 (2003).

51. Manhique, A. J., Focke, W. W. & Madivate, C. T*itania recovery from low-grade titanoferrous minerals.* Hydrometallurgy 109, 230–236 (2011).

52. Sabacky, J. & Victor, D. E. George West-Sells, Vancouver (CA); Timothy Malcome Spitler, Fernley, NV (US); Andrew Vince, Moranbah (AU); James R. Burkholder; 19.

53. Carp, O. *Photoinduced reactivity of titanium dioxide.* Progress in Solid State Chemistry 32, 33–177 (2004).

54. Chen, H., Nanayakkara, C. E. & Grassian, V. H. *Titanium Dioxide Photocatalysis in Atmospheric Chemistry.* Chemical Reviews 112, 5919–5948 (2012).

55. Fujishima, A., Rao, T. N. & Tryk, D. A. *Titanium dioxide photocatalysis.* Journal of Photochemistry and Photobiology C: Photochemistry Reviews 1, 1–21 (2000).

56. Siddiqui, H. *Modification of Physical and Chemical Properties of Titanium Dioxide* (TiO_2) *by Ion Implantation for Dye Sensitized Solar Cells*. Ion Beam (IntechOpen, 2019). doi:10.5772/intechopen.83566.

57. Schneider, J. *et al. Understanding* TiO_2 *Photocatalysis: Mechanisms and Materials*. Chemical Reviews 114, 9919–9986 (2014).

58. Li, Z., Cong, S. & Xu, Y. *Brookite vs Anatase TiO_2 in the Photocatalytic Activity for Organic Degradation in Water*. ACS Catalysis 4, 3273–3280 (2014).

59. Ola, O. & Maroto-Valer, M. M. *Review of material design and reactor engineering on TiO_2 photocatalysis for CO_2 reduction.* Journal of Photochemistry and Photobiology C: Photochemistry Reviews 24, 16–42 (2015).

60. Chen, X. & Burda, C. *Photoelectron Spectroscopic Investigation of Nitrogen-Doped Titania Nanoparticles*. The Journal of Physical Chemistry B 108, 15446–15449 (2004).

61. Marugán, J., Christensen, P., Egerton, T. & Purnama, H. I*nfluence of the Synthesis pH on the Properties and Activity of Sol-Gel TiO_2 Photocatalysts*. International Journal of Photoenergy 2008, 1–7 (2008).

62. Pelaez, M. *et al. A review on the visible light active titanium dioxide photocatalysts for environmental applications*. Applied Catalysis B: Environmental 125, 331–349 (2012).

63. Wang, C., Liu, H., Liu, Y., He, G. & Jiang, C. *Comparative activity of TiO_2 microspheres and P25 powder for organic degradation: Implicative importance of structural defects and organic adsorption*. Applied Surface Science 319, 2–7 (2014).

64. Ngamta, S. *et al. A facile synthesis of nanocrystalline anatase TiO_2 from $TiOSO_4$ aqueous solution*. Materials Letters 105, 76–79 (2013).

65. Macwan, D. P., Dave, P. N. & Chaturvedi, S. *A review on nano-TiO_2 sol–gel type syntheses and its applications.* Journal of Materials Science 46, 3669–3686 (2011).

66. Parida, K. M. & Naik, B. *Synthesis of mesoporous $TiO_{2-x}N_x$ spheres by template free homogeneous co-precipitation method and their photo-catalytic activity under visible light illumination*. Journal of Colloid and Interface Science 333, 269–276 (2009).

67. Sundrarajan, M. & Gowri, S. *Green synthesis of titanium dioxide nanoparticles by nyctanthes arbor tristis leaves extract.* 5 (2011).

68. Masuda, Y. & Kato, K. *Nanocrystal Assembled TiO_2 Particles Prepared from Aqueous Solution.* Crystal Growth & Design 8, 3213–3218 (2008).

69. Gao, Y., Masuda, Y., Seo, W.-S., Ohta, H. & Koumoto, K. *TiO_2 nanoparticles* *prepared using an aqueous peroxotitanate solution*. Ceramics International 30, 1365–1368 (2004).

70. Li, W. & Zeng, T. *Preparation of TiO_2 Anatase Nanocrystals by $TiCl_4$ Hydrolysis with Additive H_2SO_4*. PLoS ONE 6, e21082 (2011).

71. Wang, C.-C. & Ying, J. Y. *Sol–Gel Synthesis and Hydrothermal Processing of Anatase and Rutile Titania Nanocrystals*. Chemistry of Materials 11, 3113–3120 (1999).

72. Wang, S., Lian, J. S., Zheng, W. T. & Jiang, Q. *Photocatalytic property of Fe doped anatase and rutile TiO_2 nanocrystal particles prepared by sol–gel technique.* Applied Surface Science 263, 260–265 (2012).

73. Caratto, V., Ferretti, M. & Setti, L. *Synthesis of TiO_2 rutile nanoparticles by PLA in solution*. Applied Surface Science 258, 2393–2396 (2012).

74. Caratto, V. *et al. Synthesis and characterization of nitrogen-doped TiO_2 nanoparticles prepared by sol–gel method.* Journal of Sol-Gel Science and Technology 63, 16–22 (2012).

75. Zhang, G., Song, A., Duan, Y. & Zheng, S. *Enhanced photocatalytic activity of TiO_2/zeolite composite for abatement of pollutants*. Microporous and Mesoporous Materials 255, 61–68 (2018).

76. Malesic-Eleftheriadou, N., Evgenidou, E. N., Kyzas, G. Z., Bikiaris, D. N. & Lambropoulou, D. A. *Removal of antibiotics in aqueous media by using new synthesized bio-based poly(ethyleneterephthalate)-TiO_2 photocatalysts.* Chemosphere 234, 746–755 (2019).

77. MiarAlipour, S., Friedmann, D., Scott, J. & Amal, R. *TiO_2/porous adsorbents: Recent advances and novel applications.* Journal of Hazardous Materials 341, 404–423 (2018).

78. Gomes, J. F. *et al. Noble metal–TiO_2 supported catalysts for the catalytic ozonation of parabens mixtures*. Process Safety and Environmental Protection 111, 148–159 (2017).

79. Rtimi, S. *et al. Supported TiO_2 films deposited at different energies: Implications of the surface compactness on the catalytic kinetics*. Applied Catalysis B: Environmental 191, 42–52 (2016).

80. Eskandarian, M. R., Fazli, M., Rasoulifard, M. H. & Choi, H. *Decomposition of* *organic chemicals by zeolite-TiO_2 nanocomposite supported onto low density polyethylene film under UV-LED powered by solar radiation*. Applied Catalysis B: Environmental 183, 407–416 (2016).

81. El Yadini, A. *et al. Supported TiO_2 on Borosilicate Glass Plates for Efficient Photocatalytic Degradation of Fenamiphos*. Journal of Catalysts 2014, 1–8 (2014).

82. Shen, C., Wang, Y. J., Xu, J. H. & Luo, G. S. *Facile synthesis and photocatalytic properties of TiO_2 nanoparticles supported on porous glass beads*. Chemical Engineering Journal 209, 478–485 (2012).

83. Ökte, A. N. & Sayınsöz, E. *Characterization and photocatalytic activity of TiO_2 supported sepiolite catalysts.* Separation and Purification Technology 62, 535–543 (2008).

84. Pan, Z., Lu, Y.-Y. & Liu, F. *Sunlight-activated long-persistent luminescence in the near-infrared from Cr^{3+}-doped zinc gallogermanates*. Nature Materials 11, 58–63 (2012).

85. Abdukayum, A., Chen, J.-T., Zhao, Q. & Yan, X.-P. *Functional Near Infrared-Emitting Cr^{3+}/Pr^{3+} Co-Doped Zinc Gallogermanate Persistent Luminescent Nanoparticles with Superlong Afterglow for in Vivo Targeted Bioimaging*. Journal of the American Chemical Society 135, 14125–14133 (2013).

86. Allix, M. *et al. Considerable Improvement of Long-Persistent Luminescence in Germanium and Tin Substituted $ZnGa_2O_4$*. Chemistry of Materials 25, 1600–1606 (2013).

87. Hölsä, J. *Persistent luminescence beats the afterglow: 400 years of persistent luminescence.* Electrochem. Soc. Interface 18, 42–45 (2009).

88. Jia, D. & Yen, W. M. *Trapping Mechanism Associated with Electron Delocalization and Tunneling of $CaAl_2O_4$:Ce^{3+}, A Persistent Phosphor*. Journal of the Electrochemical Society 150, H61–H65 (2003).

89. Liu, F., Liang, Y. & Pan, Z. *Detection of Up-converted Persistent Luminescence in the Near Infrared Emitted by the $Zn_3Ga_2GeO_8$: Cr^{3+}, Yb^{3+}, Er^{3+} Phosphor.* Physical Review Letters 113, (2014).

90. Locardi, F. *et al. Photocatalytic activity of TiO_2 nanopowders supported on a new persistent luminescence phosphor*. Catalysis Communications 74, 24–27 (2016).

91. Van Doorslaer, X., Dewulf, J., Van Langenhove, H. & Demeestere, K. *Fluoroquinolone antibiotics: An emerging class of environmental micropollutants*. Science of The Total Environment 500–501, 250–269 (2014).

92. Znaidi, L. *Sol–gel-deposited ZnO thin films: A review.* Materials Science and Engineering: B 174, 18–30 (2010).

93. Sampaio, M. J. *et al. Synergistic effect between carbon nanomaterials and ZnO for photocatalytic water decontamination*. Journal of Catalysis 331, 172–180 (2015).

94. Lova, P. *et al. Hybrid ZnO/polystyrene nanocomposite for all-polymer photonic crystals*. Physica Status Solidi (c) 12, 158–162 (2015).

95. Al-Hetlani, E., Amin, M. O. & Madkour, M. *Detachable photocatalysts of anatase* TiO_2 *nanoparticles: Annulling surface charge for immediate photocatalyst separation.* Applied Surface Science 411, 355–362 (2017).

96. Pongwan, P., Wetchakun, K., Phanichphant, S. & Wetchakun, N. *Enhancement of visible-light photocatalytic activity of Cu-doped* TiO_2 *nanoparticles*. Research on Chemical Intermediates 42, 2815–2830 (2016).

97. Young, R. A. *The Rietveld Method.* (Oxford University Press, 1991).

98. Rodríguez-Carvajal, J. *Recent advances in magnetic structure determination by neutron powder diffraction.* Physica B: Condensed Matter 192, 55–69 (1993).

99. Langford, J. I., Louër, D., Sonneveld, E. J. & Visser, J. W. *Applications of Total Pattern Fitting to a Study of Crystallite Size and Strain in Zinc Oxide Powder.* Powder Diffr. 1, 211–221 (1986).

100. Connor, P. A., Dobson, K. D. & McQuillan, A. J. I*nfrared Spectroscopy of the* TiO_2*/Aqueous Solution Interface*. Langmuir 15, 2402–2408 (1999).

101. Maira, A. J. *et al.* F*ourier Transform Infrared Study of the Performance of Nanostructured* TiO_2 *Particles for the Photocatalytic Oxidation of Gaseous Toluene*. Journal of Catalysis 202, 413–420 (2001).

102. Takeuchi, M., Martra, G., Coluccia, S. & Anpo, M. *Investigations of the Structure of* H_2O *Clusters Adsorbed on* TiO_2 *Surfaces by Near-Infrared Absorption Spectroscopy*. J. Phys. Chem. B 109, 7387–7391 (2005).

103. Reeves-McLaren, N., Ferrarelli, M. C., Tung, Y.-W., Sinclair, D. C. & West, A.

R. *Synthesis, structure and electrical properties of* $Cu_{3.21}Ti_{1.16}Nb_{2.63}O_{12}$ *and the* CuO_x*–*TiO_2*–*Nb_2O_5 *pseudoternary phase diagram*. Journal of Solid State Chemistry 184, 1813–1819 (2011).

104. Legrand, V., Merdrignac-Conanec, O., Paulus, W. & Hansen, T. *Study of the Thermal Nitridation of Nanocrystalline* $Ti(OH)_4$ *by X-ray and in Situ Neutron Powder Diffraction.* J. Phys. Chem. A 116, 9561–9567 (2012).

105. Zobov, N. F., Polyansky, O. L., Le Sueur, C. R. & Tennyson, J. *Vibration-rotation levels of water beyond the Born-Oppenheimer approximation*. Chemical Physics Letters 260, 381–387 (1996).

106. Villa, S. *et al.* E*nhancement of* TiO_2 *NPs Activity by Fe3O4 Nano-Seeds for Removal of Organic Pollutants in Water*. Materials 9, 771 (2016).

107. Locardi, F. *et al. Facile synthesis of NIR and Visible luminescent* Sm^{3+} *doped lutetium oxide nanoparticles.* Materials Research Bulletin 86, 220–227 (2017).

108. Su, C., Hong, B.-Y. & Tseng, C.-M. *Sol–gel preparation and photocatalysis of titanium dioxide.* Catalysis Today 96, 119–126 (2004).

109. Castellano, M., Cantù, R., Mauri, M., Marsano, E. & Vicini, S. *Poly(dimethylsiloxane)/*TiO_2 *Photocatalytic Membranes Obtained by Different Electrospinning Systems*. Journal of Nanoscience and Nanotechnology 16, 6587–6594 (2016).

110. López, R. & Gómez, R. *Band-gap energy estimation from diffuse reflectance measurements on sol–gel and commercial* TiO_2*: a comparative study*. Journal of Sol-Gel Science and Technology 61, 1–7 (2012).

111. Caratto, V. *et al. Inactivation of Escherichia coli on anatase and rutile nanoparticles using UV and fluorescent light*. Materials Research Bulletin 48, 2095–2101 (2013).

112. Belviso, C., Cavalcante, F. & Fiore, S. *Synthesis of zeolite from Italian coal fly ash: Differences in crystallization temperature using seawater instead of distilled water*. Waste Management 30, 839–847 (2010).

113. Belviso, C. *et al. Synthesis of magnetic zeolite at low temperature using a waste material mixture: Fly ash and red mud.* Microporous and Mesoporous Materials 202, 208–216 (2015).

114. Belviso, C. *et al. The crystallisation of zeolite (X- and A-type) from fly ash at*

25 °C in artificial sea water. Microporous and Mesoporous Materials 162, 115–121 (2012).

115. Błędzka, D., Gromadzińska, J. & Wąsowicz, W. *Parabens. From environmental studies to human health*. Environment International 67, 27–42 (2014).

116. Gmurek, M., Rossi, A. F., Martins, R. C., Quinta-Ferreira, R. M. & Ledakowicz, S. *Photodegradation of single and mixture of parabens – Kinetic, by-products identification and cost-efficiency analysis*. Chemical Engineering Journal 276, 303–314 (2015).

117. Gomes, J. F., Lopes, A., Gmurek, M., Quinta-Ferreira, R. M. & Martins, R. C. *Study of the influence of the matrix characteristics over the photocatalytic ozonation of parabens using Ag-*TiO_2*.* Science of The Total Environment 646, 1468–1477 (2019).

118. González-Mariño, I., Quintana, J. B., Rodríguez, I. & Cela, R. *Simultaneous determination of parabens, triclosan and triclocarban in water by liquid chromatography/electrospray ionisation tandem mass spectrometry*. Rapid Communications in Mass Spectrometry 23, 1756–1766 (2009).

119. Fernandes, E., Martins, R. C. & Gomes, J. *Photocatalytic ozonation of parabens mixture using 10% N-*TiO_2 *and the effect of water matrix*. Science of The Total Environment 718, 137321 (2020).

120. Lian, L., Yan, S., Yao, B., Chan, S.-A. & Song, W. *Photochemical Transformation of Nicotine in Wastewater Effluent*. Environmental Science & Technology 51, 11718–11730 (2017).

121. Passananti, M. *et al. Photoenhanced transformation of nicotine in aquatic environments: Involvement of naturally occurring radical sources*. Water Research 55, 106–114 (2014).

122. Poland *et al. The Study on the Photocatalytic Degradation of Nicotine*. Journal of Research & Developments in Chemistry 1–5 (2015) doi:10.5171/2015.157781.

123. de Franco, M. A. E., da Silva, W. L., Bagnara, M., Lansarin, M. A. & dos Santos, J. H. Z. *Photocatalytic degradation of nicotine in an aqueous solution using unconventional supported catalysts and commercial ZnO/*TiO_2 *under ultraviolet radiation.* Science of The Total Environment 494–495, 97–103 (2014).

124. Dodson, L. G., Vogt, R. A., Marks, J., Reichardt, C. & Crespo-Hernández, C. E. *Photophysical and photochemical properties of the pharmaceutical compound salbutamol in aqueous solutions*. Chemosphere 83, 1513–1523 (2011).

125. Cope, M. & Bautista-Parra, F. *The degradation of salbutamol in ethanolic solutions*. Journal of Pharmaceutical and Biomedical Analysis 52, 210–215 (2010).